A Small Perturbation Based Optimization Approach for the Frequency Placement of High Aspect Ratio Wings

A Thesis
Presented to
The Academic Faculty

by

Mandy Goltsch

In Partial Fulfillment
of the Requirements for the Degree
Doctor of Philosophy

School of Aerospace Engineering
Georgia Institute of Technology
May 2009

A Small Perturbation Based Optimization Approach for the Frequency Placement of High Aspect Ratio Wings

Approved by:

Prof. Dimitri N. Mavris
Committee Chair
School of Aerospace Engineering
Georgia Institute of Technology

Prof. Daniel P. Schrage
School of Aerospace Engineering
Georgia Institute of Technology

Prof. Vitali Volovoi
School of Aerospace Engineering
Georgia Institute of Technology

Prof. Olivier A. Bauchau
School of Aerospace Engineering
Georgia Institute of Technology

Prof. Wenbin Yu
Mechanical and Aerospace Engineering
Utah State University

Date Approved: March 2009

To my mother and sister.

ACKNOWLEDGEMENTS

The journey of my dissertation has been a long and arduous one and I could not have succeeded without the help of numerous individuals.

My foremost and sincere thanks go to my advisor and committee chair Dr. Dimitri Mavris who took me under his wings and gave me a home at the Aerospace Systems Design Laboratory. I am very grateful indeed for his continued patience, his lasting support, and his wise words of advice that extended far beyond my scholarly being.

I would like to thank my committee members Dr. Daniel Schrage who was never just critical but always positive; Dr. Vitali Volovoi who remained optimistic and cheerful in even the darkest of times; Dr. Wenbin Yu who assisted me in understanding and implementing VABS; and Dr. Olivier Bauchau who helped me do the same with DYMORE. Dr. Bauchau also spent a considerable amount of time sharing his incredible expertise. His insight and experience greatly contributed to the completion of this thesis and I regret to not have approached him sooner.

I would like to thank Dr. Dewey Hodges for his outside help, and for the sometimes painful lessons during the unfortunately too few encounters on the squash court.

Many genuine hugs to all the old and new friends that at some point or another found themselves living in Room 308. Thank you Simon Briceno, Bjorn Cole, Kyle Collins, Stephane Dufresne, Alex Moodie, Reza Rezvani, Frederic Villeneuve, Henry Won, and Jack Zentner. Thank you for putting up with me, for making me laugh, and for dragging me out of the lab when necessary.

My heartfelt thanks go to Tracy and Irian Ordaz for being there in good times and in bad. I cannot begin to express my gratitude for your friendship. My sincere appreciation extends to both your families that, right from the start, treated me like a daughter and sister. Thank you so much for everything.

A special thanks for my dear friend Oluwasegun Oyewo. Thank you for being part of this endeavor and for putting aside your own problems whenever I came along with mine.

Last but certainly not least I thank my family for never giving up on me and always believing in me. I could not have done it without your unconditional love and support. My singular gratitude is reserved for my sister Aline Azizi Ghanbari. Thank you for being an invariable and invaluable source of hope, inspiration, and encouragement.

Contents

List of Tables

List of Figures

LIST OF ACRONYMS

3AS	Active Aeroelastic Aircraft Structures
ANSYS	Analysis System
ASTROS	Automated Structural Optimization System
BLISS	Bi-Level Integrated System Synthesis
CA	Contributing Analysis
CAS	Circumferentially Asymmetric Stiffness
CFD	Computational Fluid Dynamics
CO	Collaborative Optimization
CSD	Cross Sectional Design
CSSO	Concurrent Subspace Optimization
CUS	Circumferentially Uniform Stiffness
DASA-M	Daimler-Benz Aerospace AG Military Aircraft Division
DOE	Design of Experiments
DOT	Design Optimization Tool Package
DSM	Dynamic Stiffness Method
ELAPS	Equivalent Laminated Plate Solution
ERAST	Environmental Research Aircraft and Sensor Technology
FD	Finite Differences
FEA	Finite Element Analysis
FE	Finite Element
FEM	Finite Element Method
FLOPS	Flight Optimization System
GA	Genetic Algorithm

GP	Gaussian Process
GTGH	Georgia Tech Generic Helicopter
GTGH	Georgia Tech Generic Helicopter
HALE	High Altitude Long Endurance
HSCT	High Speed Civil Transport
IPR	Inverse Perturbation Redesign
LEAP	Large Admissible Perturbations
LQR	Linear Quadratic Regulator Theory
MCS	Monte Carlo Simulation
MDO	Multidisciplinary Design Optimization
MMFD	Modified Method of Feasible Direction
MSC	MacNeal-Schwendler Corporation
NASTRAN	NASA Structural Analysis System
NN	Neural Network
PASCO	Panel Analysis and Sizing Code
PASTA	Proprotor Aeroelastic Stability Analysis
PWAKE	Coupled airframe wake system based on Peters wake theory
RESTRUCT	Redesign of Structures
ROA	Remotely Operated Aircraft
RPV	Remotely Piloted Vehicle
RSE	Response Surface Equation
RSM	Response Surface Methodology
RS	Response Surface
SA	Simulated Annealing

SLP	Sequential Linear Programming
SQP	Sequential Quadratic Programming
SVBT	Saint-Venant Beam Theory
TIPR	Timoshenko refined Inverse Perturbation Redesign
UAV	Unmanned Aerial Vehicle or Uninhabited Air Vehicle
V/STOL	Vertical/Short Takeoff and Landing
VABS	Variational Asymptotic Beam Sectional Analysis
VASCOMP	VTOL Aircraft Sizing and Performance Computer Code
WINGDES	Wing Design program

SUMMARY

Design denotes the transformation of an identified need to its physical embodiment in a traditionally iterative approach of trial and error. Conceptual design plays a prominent role but an almost infinite number of possible solutions at the outset of design necessitates fast evaluations. The corresponding practice of empirical equations and low fidelity analyses becomes obsolete in the light of novel concepts. Ever increasing system complexity and resource scarcity mandate new approaches to adequately capture system characteristics.

Contemporary concerns in atmospheric science and homeland security created an operational need for unconventional configurations. Unmanned long endurance flight at high altitudes offers a unique showcase for the exploration of new design spaces and the incidental deficit of conceptual modeling and simulation capabilities. Structural and aerodynamic performance requirements necessitate light weight materials and high aspect ratio wings resulting in distinct structural and aeroelastic response characteristics that stand in close correlation with natural vibration modes.

The present research effort evolves around the development of an efficient and accurate optimization algorithm for high aspect ratio wings subject to natural frequency constraints. Foundational corner stones are beam dimensional reduction and modal perturbation redesign. Local and global analyses inherent to the former suggest corresponding levels of local and global optimization. The present approach departs from this suggestion. It introduces local level surrogate models to capacitate a methodology that consists of multi level analyses feeding into a single level optimization.

The innovative heart of the new algorithm originates in small perturbation theory. A sequence of small perturbation solutions allows the optimizer to make incremental movements within the design space. It enables a directed search that is free of costly gradients. System matrices are decomposed based on a Timoshenko stiffness effect separation. The formulation of respective linear changes falls back on surrogate models that approximate cross sectional properties. Corresponding functional responses are readily available. Their direct use by

the small perturbation based optimizer ensures constitutive laws and eliminates a previously necessary optimization at the local level.

The scope of the present work is derived from an existing configuration such as a conceptual baseline or a prototype that experiences aeroelastic instabilities. Due to the lack of respective design studies in the traditional design process it is not uncommon for an initial wing design to have such stability problems. The developed optimization scheme allows the effective redesign of high aspect ratio wings subject to natural frequency objectives. Its successful application is demonstrated by three separate optimization studies.

The implementation results of all three studies confirm that the gradient liberation of the new methodology brings about great computational savings. A generic wing study is used to indicate the connection between the proposed methodology and the aeroelastic stability problems outlined in the motivation. It is also used to illustrate an important practical aspect of structural redesign, i.e., a minimum departure from the existing baseline configuration. The proposed optimization scheme is naturally conducive to this practical aspect by using a minimum change optimization criterion. However, only an elemental formulation truly enables a minimum change solution. It accounts for the spanwise significance of a structural modification to the mode of interest. This idea of localized reinforcement greatly benefits the practical realization of structural redesign efforts.

The implementation results also highlight the fundamental limitation of the proposed methodology. The exclusive consideration of mass and stiffness effects on modal response characteristics disregards other disciplinary problems such as allowable stresses or buckling loads. Both are of central importance to the structural integrity of an aircraft but are currently not accounted for in the proposed optimization scheme. The concluding discussion thus outlines the need for respective constraints and/or additional analyses to capture all requirements necessary for a comprehensive structural redesign study.

Chapter I

INTRODUCTION

The following thesis documents the development of a small perturbation based optimization algorithm for the natural frequency placement of high aspect ratio wings. The underlying motivation is essentially twofold.

On one hand there is a contemporary demand for Unmanned Air Vehicles for high altitude and long endurance missions. Operational assignments range from traffic monitoring to border control, from surveillance to reconnaissance, from atmospheric sampling to storm tracking. Structural and aerodynamic requirements necessitate a light weight and high aspect ratio wing with a resultant flexibility that gives rise to distinctive structural and aeroelastic response characteristics.

On the other hand there is a lack of corresponding analysis and optimization capabilities for the conceptual phase of design. Both structures and aeroelasticity have a great impact on vehicle performance, reliability, and cost; and need to become integral part of the conceptual design process. The inability to conduct respective trade studies at the conceptual level disables an adequate assessment of design alternatives. It not only confines design freedom but supports suboptimal or even faulty design solutions.

Finding remedy for potential design problems becomes increasingly difficult and expensive when moving down on the design time line. The rectification of design flaws in the detail phase of design and beyond can only be realized at enormous correctional costs. However, the initial design of a wing commonly experiences stability problems due to the late and detached consideration of aeroelastic analyses. Unconventional configurations as the ones of interest to the present study are particularly and adversely affected by the lack of corresponding experience and design studies.

The present research refrains from the attempt to devise a comprehensive aeroelastic analysis and design environment. Focus of the present work is the composition of an efficient

and accurate optimization algorithm that enables the natural frequency placement of high aspect ratio wings. The proposed optimization algorithm will allow for the effective redesign of an initial wing configuration subject to dynamic instabilities.

Two fundamentally different optimization techniques exist in the form of gradient based and stochastic methods. The former make very informed decisions about the usability and feasibility of local search directions. The latter are essentially random but greatly increase the chances of finding a global optimum. In general there is no assurance that the absolute best solution has been found. Practical implementations resort to multiple starting points and/or the application of hybrid schemes. A common example is the utilization of a stochastic method to scan the entire space for the most promising locations, concluded by a gradient method that climbs down the hill.

The proposed optimization approach is aligned with a directed exploration of the design space. That is, the algorithm has no random elements but rather directs its search based on natural frequency objectives. Unlike gradient based methods, however, it abandons computationally expensive function calls associated with finite difference evaluations required for the identification of the search direction. Instead, each iteration is based on the solution of a small perturbation equation subject to an incremental change in natural frequencies.

The rationale connecting the placement of natural frequencies to the motivational statement lies in the physical significance of natural modes. The dynamic response of a structure depends on exciting forces and modal characteristics. The deformation of a structure can be expressed in terms of natural modes and frequencies. Critical aeroelastic modes stand in a one-to-one correspondence to natural vibration modes. For that reason both structural and aeroelastic analyses are typically performed in the modal space.

While the intent of the present research is not to compose a comprehensive aeroelastic analysis and design framework, the performance of any design environment still depends on the efficiency of the employed optimization. The algorithm developed in the present research effort provides a very efficient means of optimization. Combined with aeroelastic analysis capabilities it could greatly contribute to the ultimate realization of aeroelastic design capabilities at the conceptual level.

Chapter II elaborates on the founding motivation. It gives a brief overview of current design practice and establishes the early importance of structural and aeroelastic parameters to performance, quality, and cost of an aircraft. It gives a brief taste of the exciting possibilities of unmanned and unconventional flight by introducing exemplary vehicles such as the HALE UAV, the tailless sail plane, or the unique Rutan designs.

Chapter III explores past research efforts pertaining to the aeroelastic analysis and design of aerospace vehicles. It touches capability gaps and outlines a need for further improvements. The vast and impressive amount of related research and accomplishments affords the foundational corner stones of the present work. These are the methods of beam dimensional reduction and modal perturbation redesign.

Chapter IV presents the concise definition of the present research objective. It briefly reflects on the underlying motivation before outlining the scope of work and the ultimate contribution to design. The motivational idea behind the present research allows the introduction of a notional concept of the optimization algorithm. Corresponding research questions and hypotheses provide details of the emerging challenges.

Chapter V keeps record of development studies that lead to the final optimization methodology presented in Chapter VI. Chapter VII is dedicated to the presentation of results supporting the accuracy and efficiency of the implemented optimization algorithm. Because the analysis tools used in the present work also serve the validation of optimization results, the correct implementation of the analysis framework receives elaborate attention.

Chapter VIII concludes the documentation of the present work by providing a critical discussion of benefits and limitations of the new optimization algorithm; and by offering incitement and suggestions for future work.

There is an imperative need to increase the fidelity of structural and aeroelastic analyses at the conceptual stage of aircraft design. The introduction of new technologies, novel concepts, and unconventional configurations makes traditional approaches obsolete and inadequate. The inherent absence of related experience and/or data calls for the renouncement of low fidelity analyses and statistical models.

Knowledge drives and guides all design decisions. Conceptual design decisions are particularly prominent because their consequences propagate downstream on the design time line. The present research makes a small contribution to the ultimate goal of conceptual aeroelastic design capabilities. It presents an efficient optimization algorithm for the accurate frequency placement of high aspect ratio wings. The underlying goal, however, is not to devise a comprehensive aeroelastic design environment but rather to propose an effective redesign approach for high aspect ratio wings with aeroelastic stability problems due to the lack of sufficient conceptual analysis and design capabilities.

Chapter II

MOTIVATION

2.1 The Design Process

Every new system starts with the identification of a need that evolves into a set of specific requirements. What separates the initial phase of requirement definition from the actual full scale implementation of the first prototype is the process of design. Design is traditionally conducted in three phases (Figure 2.1). Each phase is characterized by different levels of decisions to be made, analysis studies to be performed, and design tools to be employed.

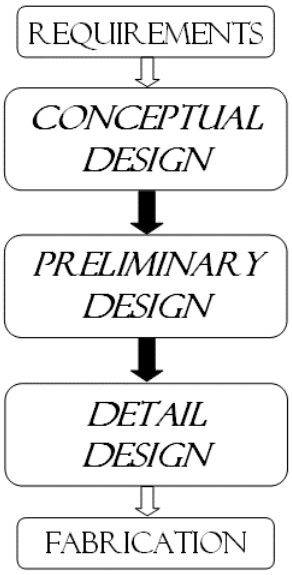

Figure 2.1: The three phases of design
Figure 2.2 in Raymer [152]

Conceptual design is concerned with top level decisions. Foremost, a solution of the basic configuration arrangement needs to be found. Numerous trade studies have to be performed using initial estimates of size, weight, and performance parameters. Given the enormous amount of data that needs to be provided and compared, low fidelity models are used.

Preliminary design is concerned with very few, typically a single one configuration that is

the conceptual baseline. Upon minor changes, the final system configuration is soon agreed on; and engineers from all contributing disciplines begin their analysis and design work. The level of detail is increased and medium fidelity models are employed.

Detail design is the conclusive phase of design. It is the phase of full scale development, resulting in the first full scale realization of the new system - the prototype. Actual testing of elements and subsystems is preceded by detailed analysis and design. High fidelity models and simulations provide accurate performance estimates[1].

Design is what transforms a societal, industrial, or military need from its sole identification to its physical embodiment and market release. This transformation requires the active involvement of all facets affecting the ultimate design outcome, making design a broad and multidisciplinary effort.

The current climate of globalization, international industrial competition, and the decline of natural resources imposes the need for even broader and more interrelated design practices. The world grows faster and smaller. Communication and transportation become cheaper, quicker, and available worldwide. Customers seek products with superlative performance, quality, robustness, reliability, and cost-effectiveness. As a result, system complexity keeps increasing. At the same time, system requirements change continuously, adding to the intricacy of system engineering efforts [26].

Essentially, design is an organized trial and error approach of finding the optimum solution to a given problem. It demands creativity, engineering experience, a wide set of technical skills, comprehensive knowledge of all involved disciplines, and the ability to integrate that knowledge. The fundamental theme of iterative feedback can be found in two different planes of abstraction, a temporal and a spatial plane.

The temporal plane is described by the phases of design. Even though the simple illustration in Figure 2.1 may not suggest so, the design phases feature feedback loops between each other, and each iteration loop must redefine clear and distinct requirements [60, 28, 184].

The spatial plane is inherent to the system itself. Each system is an entity that can be

[1]Note that every model is subject to assumptions, regardless of the applied level of abstraction or sophistication. Thus, every model is only an approximation of the real world.

broken down into constituent components. Regardless of the decomposition philosophy being disciplinary, functional, or physical; the separated system elements are easier to analyze than the system entity and allow to be studied by engineers specializing in respective fields. However, a successful design requires that the system is viewed as a whole, i.e., it requires the study of component interactions to better understand the system entirety [189, 26, 90].

2.2 Conceptual Design

The decisions made early on in design are of outmost importance. Design freedom progressively diminishes when moving from conceptual to detail design. In other words, once the overall configuration of the new system has been established, there will be no more room for major design changes. While changes in the later phases of design or even the product life cycle are not impossible, they can only be realized at enormous costs [152, 45].

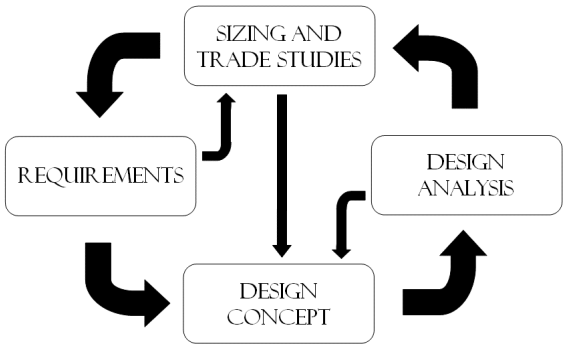

Figure 2.2: The design wheel
Figure 2.1 in Raymer [152]

The large number of possible solutions at the conceptual level results in a large number of sizing and trade studies that need to be performed (Figure 2.2). The design wheel in Figure 2.2 also illustrates the close coupling of design concepts and design requirements. Each possible design alternative will - in one way or another - respond to those requirements. Thus, defining distinct requirements on the basis of a clear understanding of the customer need is imperative to a successful design [58, 49].

An early NASA study on the feasibility of solar powered remotely piloted vehicles (RPV) identified aerodynamic and structural efficiency as the primary enablers of high altitude long

endurance flight. Due to the multitude of configurations potentially satisfying these requirements, a separate study was conducted with the sole purpose of selecting a manageable number of possible solutions.

Initial designs grouped on the left hand side of Figure 2.3 reflect the utilization of multifunctional lifting surfaces by providing a large area for photovoltaics (configurations 1-9) and podded thermal concentrators for solar energy collection (configurations 5-8). With configuration 10 as baseline, the evolution examples on the right hand side document the increased emphasis on simplicity and aerodynamic cleanliness. The final configuration parametrically analyzed is a modified version of configuration 18. The original variable geometry wing was slightly swept and a second set of fixed vertical panels was added [79].

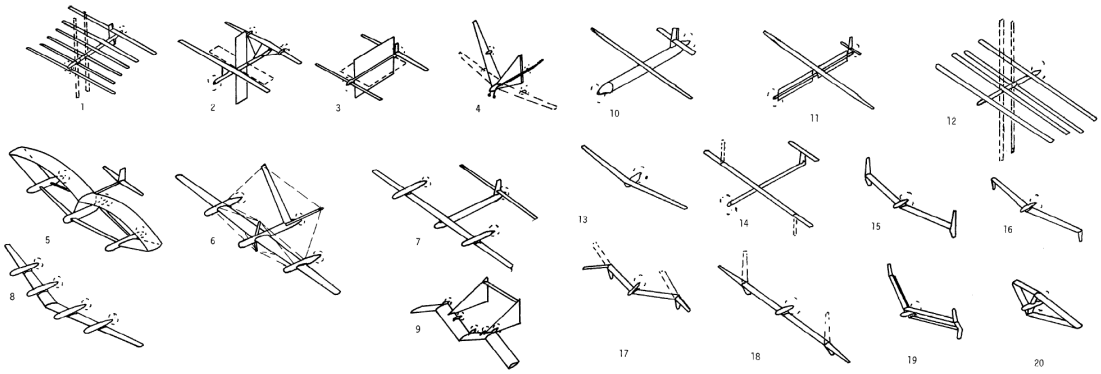

Figure 2.3: Solar powered RPV configurations
Chronological evolution: Configurations 1-9 (1977-1979), Configurations 10-20 (1980-1981) in [79]

The time frame of the above configuration evolution and selection process illustrates not only the imperative and extensive nature of a thorough requirement identification and investigation, but also provides a notion of the voluminous number of possible design solutions at the very outset of the conception of a new aircraft.

Aircraft are complex systems and as such inherently multidisciplinary. The design of such systems is facilitated by the decomposition into contributing disciplines and respective interactions. In traditional conceptual aircraft design, these disciplines are geometry, aerodynamics, propulsion, and structures. To enable the analysis and optimization of the competing configurations, each design alternative is subject to a sizing process. Sizing is

done by iterating on total and required fuel weight while simulating the mission profile (Figure 2.4). Design variables typically include geometric parameters for wing and empennage such as area, aspect ratio, and taper ratio; and airfoil specifications such as thickness to chord ratio at the wing root and tip.

The huge number of combinatorial cases that need to be evaluated at the conceptual level impose stringent restrictions on the execution times of employed analysis and design tools. Quick if not instantaneous results are required. Low fidelity models, table look-ups, and historical databases are used. The ultimate tradeoff between accuracy and efficiency is particularly counterproductive at the conception where the most important decisions are made [60]. It is the conceptual phase that has the most influence on the final design [208, 45]; that unites creativity, ingenuity, and imagination to spawn innovative design solutions; that provides *"the most scope for striking improvements"* [60].

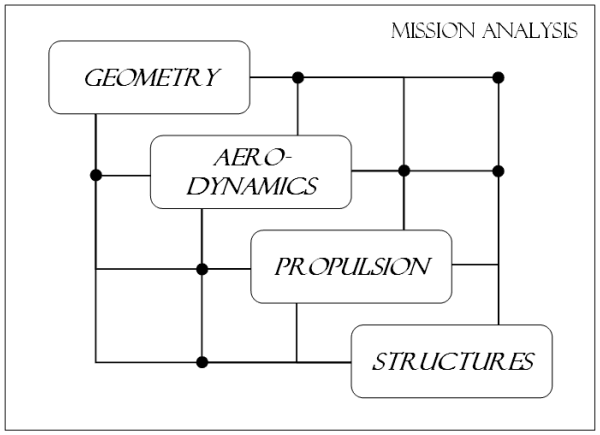

Figure 2.4: Notional conceptual sizing effort

It is also the conceptual phase that has a severe impact on the economic performance in light of the entire system life cycle. The decisions made and actions taken at the conceptual level may not incur major expenditures at the time, but they greatly influence final system costs. In fact, more than half of the projected product life cycle cost is committed during those early stages of design. So even though the majority of product costs are created by the operation, the support, the maintenance, and the retirement (or disposal) of a product, the foundation for these costs is set in conceptual design [55, 47].

2.3 Structures and Aeroelasticity in Conceptual Design

Decisions are a prominent part of design. *"An arbitrary decision represents a wasted opportunity"* because each decision represents a choice; and each choice has the inherent potential to improve the design [60].

The single most important prerequisite for good decisions is knowledge. Knowledge is gained through analysis [183]. At the outset of design, however, there exists an almost infinite number of possible design solutions. Each single one requires evaluation. Associated time constraints impose stern fidelity restrictions on employed analysis tools. Accuracy is traded for swiftness. Resulting shortcomings potentially pave the way for faulty decisions, which will propagate all the way to product release, operation, and maintenance. Testing and fine tuning of the prototype will have marginal effects at best. They cannot rectify an inherent design flaw [183, 184]. *"Quality cannot be built into a product unless it is designed into it"* [47].

The creation of correct knowledge at the conceptual level is no trivial task. Evolutionary configurations benefit from past and current designs. Simple scaling, interpolation, and extrapolation from already existing data provide fast answers. Revolutionary designs, however, do not have the luxury of ancestors. Respective databases are yet to be created. A true perception of their performance can only be enabled through actual analyses.

Traditional conceptual design trades accuracy for speed. The need for fast decisions culminates in the total disregard of certain disciplines. The fields of interest to the present work are weights, structures, and aeroelasticity.

2.3.1 Weights

There is no actual structural analysis in traditional conceptual design. The structures box in Figure 2.4 is a weights model that is based on the regression of historical data, i.e., data from existing aircraft. Figure 2.5 illustrates such regression results.

Empirical weight equations work well for evolutionary designs, but fail for revolutionary designs. The nonexistence of congenerous aircraft and the inherent lack of corresponding data invalidates a statistical regression for nontraditional configurations and new materials.

An example of such an insufficiently comprehensive database is the Unmanned Aerial Vehicle or Uninhabited Air Vehicle (UAV).

Depending on individual definitions, the first UAV may have been the Northrop Observer, a reconnaissance aircraft first flying in 1955. Others may argue in favor of the U.S. Navy TDR-1 drone and its strike mission over Japan in 1944. The introduction and wide spread use of the term UAV itself, however, did not take place until the early 1990s [135].

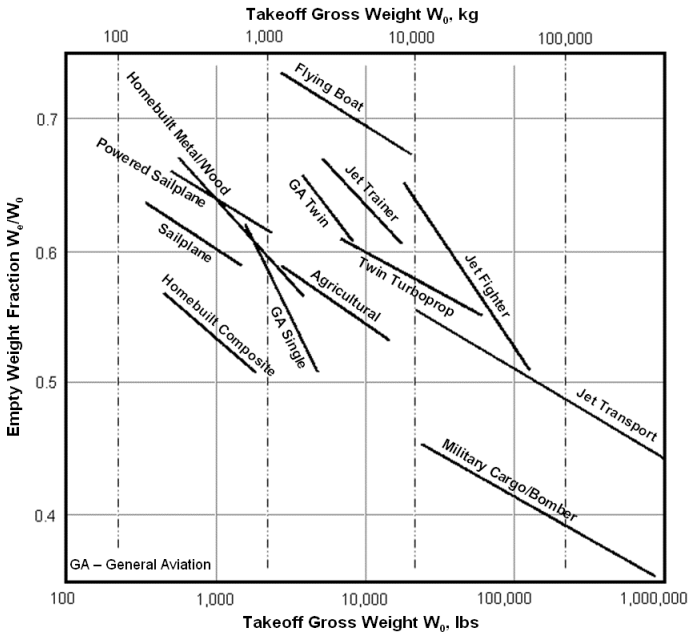

Figure 2.5: Historical weight trends
Figure 3.1 in Raymer [152]

The operational need of UAVs, responding to contemporary needs in atmospheric science and homeland security, originates in the ever increasing demand for information. The notion of autonomously flying agents for military and civilian use spawned a plethora of potential missions. Exemplary assignments are exploration; surveillance; reconnaissance; border control; communication relays; spectral imaging; aerial photography; atmospheric sampling; storm tracking; search and rescue; and traffic and natural resource monitoring.

Recent public interest was aroused by NASA's Environmental Research Aircraft and Sensor Technology (ERAST) program. ERAST was launched in 1993 by the NASA Dryden Flight Research Center and run as joint venture of NASA entities and industry. The

overall goal was the development of environmentally friendly, uninhabited, high altitude long endurance (HALE) aircraft. The ultimate result was a series of four generations of solar powered flying wing aircraft. The evident success of these vehicles is documented by multiple world records in flight altitude and duration [132].

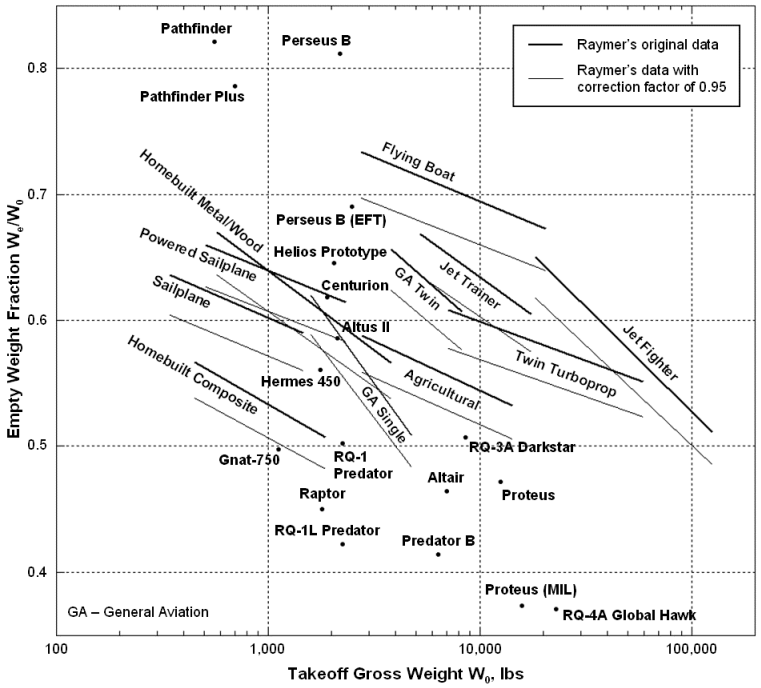

Figure 2.6: UAV data and historical weight trends
UAV weight data in Appendix A

Key enabling technologies for HALE UAVs are advanced composite materials such as Kevlar and Graphite/Epoxy. Raymer alludes to the lack of statistical data for aircraft utilizing those materials and suggests using a correction factor of 0.95 on the empty weight fraction until respective curve fits can be developed [152].

Figure 2.6 shows a collection of UAVs amongst Raymer's historical data. The graph shows both the original empty weight trends and the empty weight trends corrected for advanced composites by using only 95 percent of the empty weight fraction, demonstrating the inadequateness of statistical regressions.

The majority of UAVs shown can be considered conventional. Their design incorporates a fuselage, a main lifting surface in the form of a wing, and some kind of empennage. Figure

2.6 also shows unconventional configurations. Pathfinder, Pathfinder Plus, Centurion, and Helios represent the four generations of the ERAST solar powered flying wing demonstrator. Proteus is a unique combination of tandem wing and twin boom; and Darkstar is a stealthy tailless design with slightly forward swept wings and a payload bearing fuselage.

2.3.2 Structures

In light of the technical feasibility of innovative aircraft, a structural analysis at the conceptual level would greatly contribute to the overall success of the design. An excellent example is the Rutan Voyager (Figure 2.7). The sole mission of this aircraft was to fly around the world non-stop and without refueling. Common industrial practice would have been to entirely omit any structural studies at the conception [152]. But in this case, the resulting imposition of extremely low structural weight (Table 2.1) led to structural sample testing at the outset of the program [159]. The unprecedented design of this aircraft required the determination of its structural adequacy before it could emerge as conceptual baseline.

Figure 2.7: Burt Rutan designs
Left: Rutan Voyager [133]; Right: Global Flyer [132]

The Voyager took off from Edwards Air Force Base in California on December 23, 1986. Nine days, three minutes, and 44 seconds later it returned, making the Voyager the first aircraft to fly around the globe without stopping or refueling. It was the world's longest flight, with an official record range of 24,986 miles [133]. Key to this aviation milestone was the extremely low structural weight. However, this flight would not have been a triumph without also ensuring extremely low drag, accomplished by a small fuselage reducing the parasite drag, and a very high aspect ratio wing reducing the induced drag [159].

Global Flyer by Scaled Composites (Figure 2.7) followed in the footsteps of the Voyager. Perpetuating the success of the ingenious Rutan designs, Global Flyer broke multiple world records. On March 3, 2005 it concluded the fastest global circumnavigation with a flight time of 67 hours and one minute. On February 11, 2006 it established the longest aviation distance with a non-stop, non-refueling flight of 25,766 miles [133].

Global Flyer faced the same design challenges as the Rutan Voyager, i.e., extremely low structural weight, extremely high aerodynamic efficiency, and the ability to carry a fuel weight that is multiple times the empty weight (Table 2.1). Due to these paramount requirements, Global Flyer is made entirely from advanced composite materials [159].

Table 2.1: Burt Rutan design weights

Parameter	Voyager	Global Flyer
Takeoff gross weight	9,697 lbs	22,000 lbs
Empty weight	2,250 lbs	3,350 lbs
Fuel weight	7,011 lbs	18,200 lbs
Structural weight	939 lbs	n/a
Empty weight fraction	0.232	0.152
Structural weight fraction	0.097	n/a

Data from Scaled Composites, LLC and National Air and Space Museum [159, 133]

The combination of highly flexible wings and high aspect ratios results in large deflections during flight. For the Voyager, the wing tip experienced an upward bending between five and nine percent of the wing semi span [133]. For HALE UAVs, the large tip deflections during flight can grow to as much as 25 percent of the wing semi span [144]. Geometry changes of that magnitude have a significant effect on the structural integrity of the aircraft. Providing a means of assessing such characteristics at the early stages of design would reduce the number of costly redesigns downstream of the conceptual phase and eliminate the necessity of ineffectual fixes during the prototype fine-tuning activities.

2.3.3 Aeroelasticity

Aeroelasticity describes the mutual and reciprocal interaction of aerodynamic, elastic, and inertial forces. Appendix B offers a brief introduction to this vast and complex field. The fundamental prerequisite of aeroelasticity is flexibility. Aircraft such as the Rutan Voyager, Global Flyer, and HALE UAVs are very flexible. Respective mission requirements necessitate

ultra light weight structures and aerodynamically efficient wings. The former is accomplished by utilizing advanced composite materials with an extremely high stiffness to weight ratios. The latter is ensured primarily by high aspect ratios. Resulting large deformations during flight affect aircraft dynamics, performance, and reliability [168].

The aeroelastic phenomenon with the arguably most dramatic effects on aircraft design is flutter [25]. Figure 2.8 shows a notional comparison of wing critical speeds. Flutter can be defined as a dynamic instability of oscillatory nature. Depending on the time dependency of the amplitudes, the oscillation can be convergent or divergent. In the first case, the amplitudes decrease over time and the system is stable. In the latter case, the amplitudes increase over time and the system is unstable. The stability boundary in between depicts the wing critical speed for flutter. The amplitudes remain steady, and the system is said to be neutrally stable.

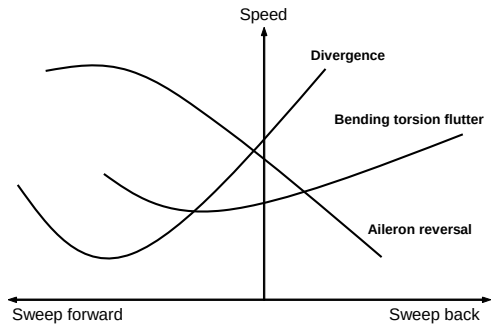

Figure 2.8: Wing critical speeds
Figure 1-8 in Bisplinghoff et al. [25]

Steady or damped oscillations with sufficiently small amplitudes may not accommodate an immediate danger, but the dynamic exposure can greatly contribute to an early structural fatigue. The growth in amplitudes above the flutter speed will quickly result in violent oscillations with devastating consequences [25].

Physical and operational characteristics of highly flexible aircraft stimulate the need for aeroelastic analyses in the design process. The inherent multidisciplinarity of aeroelasticity has far reaching impacts. It affects design criteria in not only aerodynamics and structures; but also performance; stability and control; and propulsion [82]. The need for concurrent

aeroelastic studies in the early design phases is especially fostered in the absence of experience and data as in the case of unconventional and revolutionary configurations.

A precedent of unconventional aviation is the tailless aircraft. Potential performance improvements of up to 10 percent encouraged the development of tailless sailplanes such as the German SB 13 (Figure 2.9) and the English Ricochet in the 1980s [165, 9]. Both aircraft belong to the 15 meter standard class, with 15 meter referring to the wing span (Table 2.2). Either project ran into the mischief of severe aeroelastic instabilities at very low speeds, but only the SB 13 was able to overcome resulting complications.

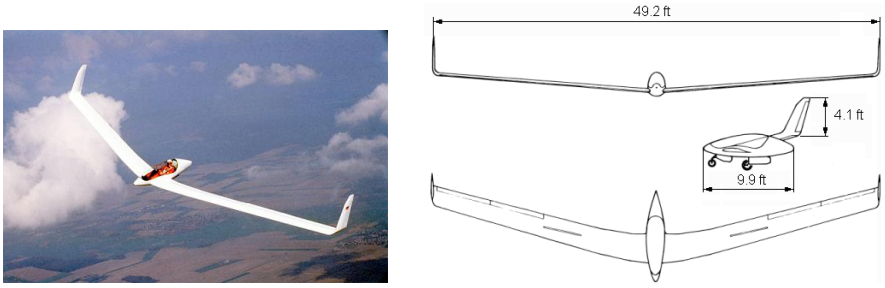

Figure 2.9: The German SB 13
Akaflieg Braunschweig e.V., Technical University Braunschweig, Germany [4]

The flutter problem of the SB 13 was detected during the flight of a downscaled model. Subsequent ground resonance tests provided frequency data and moments of inertia for flutter analyses that revealed a coupling of the rigid body short period mode with the first bending mode. The wing was aeroelastically tailored using numerical optimization. The final structural redesign featured a new main spar and optimized fiber orientations, resulting in a flutter speed increase of over 100 percent at a weight increase of less than 10 percent. The discussion of how to separate the two frequencies of rigid body and bending mode also notes the possibility of a configuration change, but *"because a large effort had already been invested in the aerodynamic lay-out, this solution was not desirable"* [165].

The profound impact of aeroelasticity on aircraft performance and integrity is of critical importance and needs to find proper consideration in the design process [168, 63, 118]. The complexity of corresponding phenomena advocates accurate modeling as early as possible [146, 118]. Aeroelasticity is currently ignored at the outset of aircraft design but needs to

Table 2.2: SB 13 configuration specifications

Parameter	Value
Gross weight	960 lbs
Empty weight	504 lbs
Payload	247 lbs
Aspect ratio	19.4
V_{min}	43 mph
V_{max}	130 mph
L/D	43.5

Akaflieg Braunschweig e.V. [4]

become integral part of the conceptual process in order to allow its effective and economic anticipation, control, and exploitation [168, 208, 118].

2.4 The Helios Prototype

Helios was the flagship of NASA's ERAST program. Its ultimate goal was conducting earth and atmospheric science missions during continuous flight for up to six months at altitudes between 50,000 and 70,000 ft. In order to be an ultra light weight aircraft, it was constructed of mainly composite materials. The main tubular spar of the flying wing was made of carbon fiber and wrapped in Nomex and Kevlar. The carbon fiber wing ribs were fabricated with Graphite/Epoxy. The leading edge was formed by Styrofoam; and the entire wing was covered by a durable plastic skin [132].

Table 2.3: Helios specifications

Parameter	Value
Wing span	247 ft
Wing chord	8 ft
Wing area	1,976 sq ft
Wing thickness	12 percent
Aspect ratio	31
Gross weight	1,600 lbs
Wing loading	0.81 lbs/sq ft
Airspeed	19-27 mph
Propulsion	14 electric motors (2 hp each)

NASA Dryden Flight Research Center [132]

Initial flight tests were conducted with a lithium battery powered aircraft in September 1999. Please refer to Figure 2.10 and Table 2.3 for respective configuration specifications.

Following the installation of more than 62,000 solar cells in 2000, the solar powered prototype achieved a record altitude of 96,863 ft during an almost 17 hour flight on August 13, 2001.

The subsequent development of a fuel cell system promised the achievement of the second milestone: Sustained day and night flight at 50,000 ft. However, both the demonstrator aircraft, a long endurance configuration of the Helios prototype, and the non-regenerative fuel cell system were lost over the Pacific Ocean after a fatal in-flight mishap on June 26, 2003 (Figure 2.11). The aircraft totaled US$ 15 million plus [18].

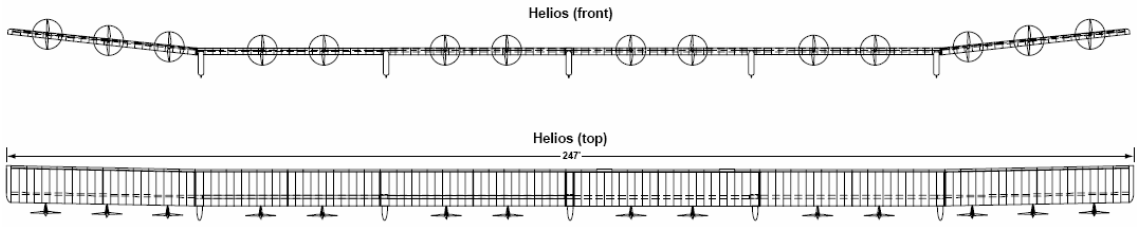

Figure 2.10: Helios high altitude configuration
NASA educational publication [130]

The total elapsed time from takeoff initiation to the impact of the wreckage on the Pacific Ocean was 31 minutes. The time elapsing between the detection of abnormal and potentially dangerous behavior in airspeed, dihedral, and pitch characteristics to the point of airloads starting to tear the vehicle apart was only 91 seconds [137].

The final report investigating the circumstances of the Helios mishap was released on September 3, 2004. The board found that the vehicle could not have been recovered from its unexpected and structurally adverse flight condition. The reason for the structural failure was determined to be a divergent development of pitch oscillations caused by the extreme dihedral. Prior analyses predicted an unstable wing for dihedrals over 30 ft but showed no indication of the increased sensitivity of the aircraft in turbulent air, the unstable nature of the phugoid mode, or the subsequent inability of the Helios prototype to restore itself [137].

The unfortunate loss of the Helios Prototype very vividly illustrates the sudden and violent nature of aeroelastic instabilities. There was no indication of the imminent danger until it was too late. Once the pitching mode grew unstable its amplitude approximately doubled every cycle [137].

Figure 2.11: Helios mishap photographs
Upper left: Normal dihedral during climb; Upper right: Unusually high dihedral prior to structural failure; Lower left and right: Helios remains post structural failure [132]

The mishap substantiates the prominent role of aeroelasticity for highly flexible aircraft. The broad impact of aeroelastic phenomena supports an early inclusion of aeroelasticity in the design process as an early identification of aeroelastic problems is eminent to the finding of effective and appropriate solutions [168, 146, 208, 118].

2.5 Summary

There is an imperative need to increase the fidelity of structural analyses at the conceptual stage of aircraft design. The introduction of new technologies, novel concepts, and unconventional configurations makes traditional statistical approaches such as the historical weights model obsolete and inadequate.

Knowledge drives and guides all design decisions. Conceptual design decisions are particularly prominent. A potential design flaw resulting from a faulty decision based on incomplete or incorrect information will propagate downstream on the design time line. The

later it is detected, the more expensive its remedy or revision. In order to ensure correct design decisions, correct information needs to be provided.

Structures and aeroelasticity lack adequate consideration in conceptual design. Structures enters the design process after a baseline configuration has been committed to. Aeroelasticity, formerly a mere afterthought, now sporadically emerges in preliminary design. Both disciplines need to become integral part of the conceptual design process. Corresponding system parameters are of great importance to vehicle performance and cost. The inability to conduct respective trade studies at the conceptual level disables an adequate assessment of design alternatives, confines the design freedom, and nourishes the development of suboptimal design solutions.

Main incitement of the present work is a contemporary demand for long endurance UAV. Operational needs include but are not limited to surveillance, border control, atmospheric sampling, and storm tracking. Structural and aerodynamic requirements necessitate light weight materials and high aspect ratio wings. Physical and operational characteristics foster the need for structural and aeroelastic studies in the early phases of design; and structural and aeroelastic response characteristics correlate with natural vibration modes.

Paul Davey, Zephyr business development director at QinetiQ, stated that *"The possibilities suggested by unmanned flight are truly exciting"* [24]. While military applications and operations remain the subject of particular interest (and funding), HALE capabilities open a wide range of potentially non-military missions with respect to sensor deployment, data collection, observation, and communication. Expert predictions admit the operation of UAVs in civilian airspace within the next decade [75]. The improvement of reliability, safety, and performance of unmanned aerial vehicles is thus of outmost importance; and the resulting technical challenges start at the outset of design.

Chapter III

PAST RESEARCH EFFORTS

The present work is spured by insufficient design capabilities at the conceptual stage of aircraft design. Focal points of motivation are the fields of structures and aeroelasticity. Both disciplines are of profound significance to the performance and integrity of an aircraft but find inadequate representation in the early phases of design.

This chapter introduces some general considerations regarding structural modeling and simulation. Subsequent sections reflect on past accomplishments and efforts related to the present motivation. The conclusion of this chapter is formed by a review of design challenges and a summarizing statement that will lead into the objective of the present work.

3.1 The Three Axes of Complexity

The complexity of structural optimization presents itself as the combination of three aspects: model complexity, analysis complexity, and optimization complexity (Figure 3.1). Because the evaluation of complexity is manifold and difficult in itself, the present work will inherit the convention by Venkataraman and Haftka and measure complexity in terms of computational cost [191].

Roughly characterized, model complexity is proportional to the number of degrees of freedom; analysis complexity is related to the time dependency of system parameters; and optimization complexity is dependent on the number of analysis runs required. The ultimate goal, that ensures simulation accuracy and a truly optimal design, is to have all three complexity measures at their maximum as denoted by Point P in Figure 3.1. The above introduced surrogate for complexity, i.e. computational cost, inherently implies that there is no practical possibility to implement such a design strategy at the conceptual level. In fact, the three axes of complexity describing structural design suggest the necessity of a fidelity reduction in two directions for any positive movement along one direction [191].

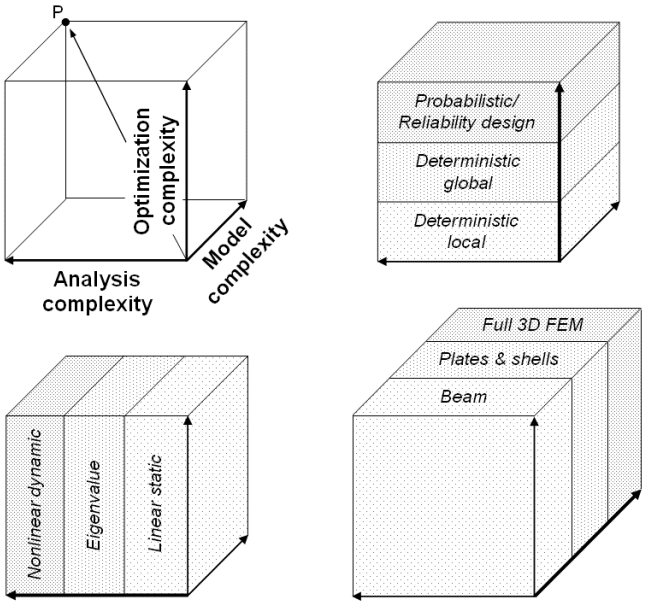

Figure 3.1: The three axes of complexity
Based on Figures 2, 3, 4, and 5 in Venkataraman and Haftka [191]

There is an interesting observation emerging from Figure 3.1 when put in perspective with computerization. In spite of an approximate increase in computing speed and storage capacity of 100 times per decade, a sufficient structural analysis seems to be taking unchangeable several hours [191]. This phenomenon may be ascribed to Parkinson's Law: *"Work expands so as to fill the time available for its completion"* [141]. Similarly, software applications expand to fill the computer resources available. Note that Thimbleby, aphorist of the Computerized Parkinson's Law, argues that complexity in combination with blind faith in computing technology is a hazard, potentially leading to failure. He advocates simplification for managing and designing complex systems [188].

In summary, the practical implementation of structural optimization is facilitated by the appropriate choice of the applied level of model, analysis, and optimization complexity. The constant increase in system intricacy and an ever growing fidelity demand impede the joint maximization of all three complexity measures. The design engineer is forced to not only show, but substantiate a discriminating judgment regarding all three measures.

3.2 Delimitation

By definition, every model and analysis tool is only an approximation of the real world. The ultimate result of using approximate models are inaccuracies in the desired output variables. The inability to predict the exact value of system metrics in design is referred to as uncertainty [124]. It can be met by either increasing the fidelity of employed analysis tools, or by striving for designs that are robust to parametric uncertainties. In conceptual design, the former is considered inappropriate because of the inherent increase in computational cost. However, the creation of robust designs is not inexpensive either. In fact, design for uncertainty stipulates rather great computational demands [8, 147, 67].

Note that parametric uncertainty is twofold. On one side there is the random variation of internal (e.g. material properties) and external (e.g. operational conditions) system parameters pertaining to aleatory[1] uncertainty. On the other side there are potentially inaccurate interdisciplinary coupling variables (e.g. aerodynamic loads) pertaining to epistemic[2] uncertainty. The natural randomness of aleatory parameter variations is amenable to a stochastic depiction. The epistemic uncertainty due to low fidelity analysis codes is not as easily quantified [147], but essentially can also be described in a probabilistic way [207]. That is, input variations are modeled using random variables in combination with random sampling techniques [154]. Both system inputs and outputs will then be given in terms of a distribution rather than a distinct value as illustrated in Figure 3.2. The challenge here lies in the identification of the uncertain variables and the accurate prediction of their variability.

The Monte Carlo Simulation (MCS) is the most accurate sampling technique [102]. MCS attempts to comprise all possible combinations of design variable settings by a large number of analyses. Input settings are determined randomly in accordance with the assigned random variables. An adequate simulation requires some 10,000 analysis runs [8, 207].

The generally large number of trials necessary for an accurate probabilistic representation of the system response prohibits the use of actual analysis tools. The feasibility of conceptual design for uncertainty relies on instantaneous disciplinary evaluations. Conducive data fit

[1] Latin *alea*, dice
[2] Greek *episteme*, knowledge

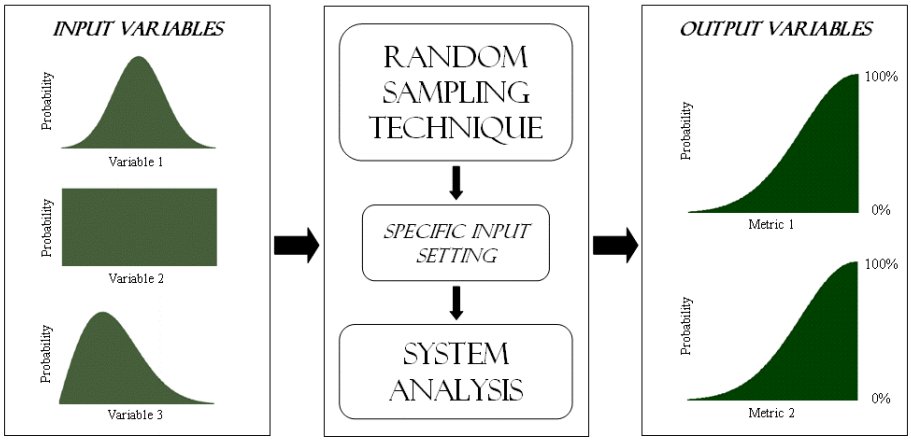

Figure 3.2: Probabilistic Design Schematic

techniques capture the relationship between input and output in an explicit function by regressing sample data from high fidelity analyses. The resulting approximations are referred to as surrogate models.

The choice for a specific surrogate model depends entirely on the type of the system response, which is the very unknown in the first place. For example, the widely used Response Surface Methodology (RSM) works great for quadratic relationships [102]. Radial Basis Functions are conducive to highly nonlinear systems, but lack accuracy for quadratic responses [56]. A faulty choice leads to an erroneous representation. Subsequently, the design space of original and approximate model will diverge and the surrogate based optimization will fail to converge to the optimum of the high fidelity model [5, 54].

Another concern is the complexity of surrogates. The creation of more elaborate models requires not only additional labor and computational time, but also adversely affects optimization characteristics. Neural Networks (NN), powerful nonlinear approximations with an unattainable flexibility in terms of the necessary sample data, require expensive training processes [121, 150]. Kriging, a stochastic extension of RSM and well suited for nonlinear systems, revealed inferior convergence performance when compared to simple second order polynomials because of a significant increase in required function calls [169].

The various implications of probabilistic design can taint an initially appealing implementation at the conceptual level. Improved engineering design relies on the combination of precision and speed; and fast and accurate analyses remain the very foundation of successful design. For that reason, the present work as well as the review of previous work will focus on deterministic design.

3.3 High Fidelity Efforts

The complexity of aeroelastic problems promotes the general necessity of high fidelity analyses. The basic aeroelastic description of a system consists of a structural model and a complementary aerodynamic model. The former is implemented using the Finite Element Method (FEM). The latter can encompass formulations ranging from simple strip theory to elaborate Computational Fluid Dynamics (CFD). For most practical applications, the choice of a specific analysis tool is confined to either a proprietary or a commercial code. An additional option is brought about by Multidisciplinary Design Optimization (MDO).

3.3.1 Commercial Software Packages

Commercially available structural analysis and design tools utilize Finite Element Analysis (FEA). FEA is based on a discrete representation of the system to be studied. Respective modeling capabilities are virtually unlimited, but entail drawbacks considering their application to conceptual design. Note that all software packages mentioned in the following brief discussion are subject to continuous enhancements and improvements.

3.3.1.1 Software Examples

ANSYS and NASTRAN are structural analysis and design tools for general purposes. The Analysis System ANSYS originated in 1970. Its structural simulation and optimization capabilities find wide use in industry and academia [139, 44].

The NASA Structural Analysis System NASTRAN was developed in the late 1960s. Analysis capabilities of the first public release included statics, dynamics, and eigenvalues; with applicability to most linear but only a few nonlinear problems [30]. Today, the NASTRAN source code is utilized in a number of software packages. Some 20 years ago,

MSC/NASTRAN was the supposedly most powerful and most widely used finite element program worldwide [41]. MSC, the MacNeal-Schwendler Corporation, was one of three companies under contract for the original development of NASTRAN [30]. Today, the title of most powerful and widely used FEM package is claimed by MD/NASTRAN, a further advanced version of MSC/NASTRAN [128]. Figure 3.3 shows the practical application of MDO for the design of an environmentally friendly regional jet where MSC/NASTRAN was combined with an external unstructured CFD solver [110].

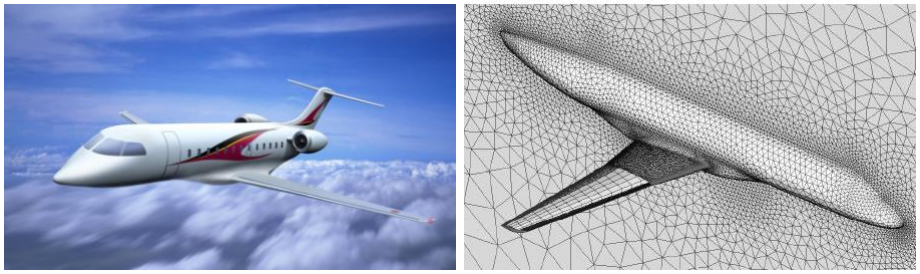

Figure 3.3: Notional regional jet and computational grid
Figures 1 and 11 in Kumano et al. [110]

ASTROS and LAGRANGE were designed for aerospace structures. The Automated Structural Optimization System ASTROS was first developed in 1983. It closely resembles the industry standard set by NASTRAN as to ensure acceptance and compatibility. ASTROS features include statics and dynamics, normal modes, steady and unsteady aerodynamics, as well as static and dynamic aeroelasticity [134]. Its aerodynamic module was greatly improved by the seamless integration of ZAERO. The combined ASTROS/ZAERO package received the name ASTROS* and is capable of analysing wing-body configurations in any Mach number regime [39, 37].

The development of the structural optimization tool LAGRANGE started in 1984. Its finite element model also shows great similarities to NASTRAN. Because it strives for truly multidisciplinary analysis and design, LAGRANGE features an open architecture that enables a high level of flexibility for new implementations and further enhancements [164].

3.3.1.2 Drawbacks

The primary concern of commercial FEM software packages in the light of conceptual analysis and design is the associated computational expense. Computing time is roughly proportional to the cube of the number of degrees of freedom. In most cases, an adequate representation of a system requires many thousand degrees of freedom, causing a single FE analysis to take anywhere from hours to days [44, 70, 191].

FEM software packages originated as structural analysis tools. Their monolithic nature raises two secondary concerns. (1) The weak support of subordinate disciplines disagrees with the industrial practice, where autonomously working specialty groups have control over their domain of expertise. The cohesive nature of monolithic formulations impedes concurrent disciplinary autonomy [46, 177, 187]. (2) Unfavorable scaling properties result in an unmanageable optimization task due to the drastic increase in design variables for complex problems wrapped in a single code [44, 179, 187].

3.3.2 Multidisciplinary Design Optimization

High fidelity analysis tools excel at the accurate modeling of complex problems. The major drawback with respect to the application to design is attributed to the inherent time expenditure. The utilization of surrogate models using RSM, NN, or Kriging alleviates associated computational costs. However, the large number of design variables and the intricacy of complex systems preclude monolithic design solutions [100, 179, 187]. The effective design of complex systems requires the decomposition into more manageable pieces [104, 107].

Multidisciplinary design adheres to a disciplinary decomposition. The contributing disciplines are represented by disciplinary analysis tools. In order to assist the practical solution of MDO problems, various integration strategies have been proposed. Initial formulations directly implemented contributing disciplines at the cost of deficiencies in transparency, maintainability, and data management. Later architectures spured formal integration frameworks for the efficient decomposition, analysis, and optimization of multidisciplinary systems [107].

3.3.2.1 Informal Aeroelastic MDO Solutions

An early development by Roehl was tailored to the preliminary structural design of the wing of a high speed civil transport (HSCT) aircraft. The final result was a hierarchical three level decomposition. Table 3.1 and Figure 3.4 describe the decomposition scheme by summarizing contributing analyses and illustrating respective data flow [155].

Table 3.1: Three-level decomposition analyses

Level	Entity	Tasks	Analysis tool
System	Aircraft	Mission analysis, Performance, Aircraft weight	Flight Optimization System (FLOPS)
Subsystem	Wing	Structural design, Aeroelastic analysis	Automated Structural Optimization System (ASTROS)
Component	Wing skin panel	Maximization of buckling loads	Panel Analysis and Sizing Code (PASCO)

Multilevel decomposition by Roehl [155]

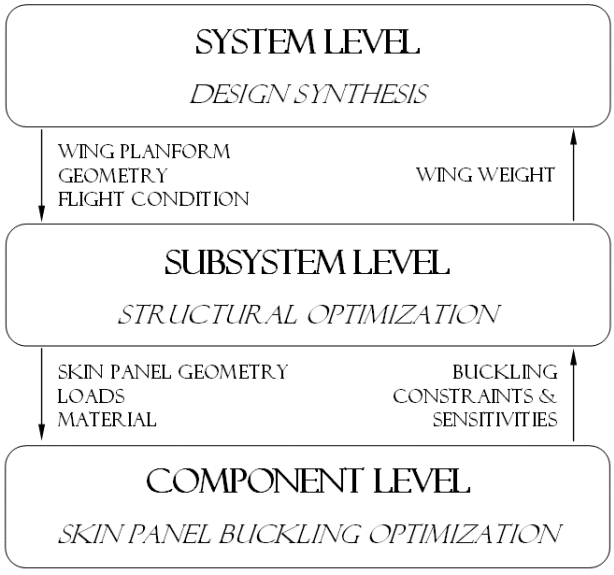

Figure 3.4: Three-level decomposition data flow

Figure 4.1 in Roehl [155]

The system level uses aerodynamic tables provided by WINGDES. At the subsystem and component level, the airload calculation is performed by the aerodynamic module of ASTROS. The objective at the system level is expressed as the weighted sum of individual

targets. The productivity index, the aircraft productivity (payload times speed) normalized by the sum of empty and fuel weight, was introduced as economic metric. The open framework successfully demonstrated multidisciplinary decomposition [155].

Stettner then presented a decomposition based MDO procedure for the airframe aeroelastic modeling and simulation of a civil tiltrotor. His motivation stemed from the need of an organized approach for the investigation of proprotor whirl flutter and its effect on aircraft economic viability. Thus, all disciplinary analyses fed into a single economic objective, the productivity index [182].

Table 3.2: Tiltrotor MDO disciplinary tools

Discipline	Analysis tool
Performance and sizing	V/STOL Aircraft Sizing and Performance Computer Code (VASCOMP)
Airframe structural dynamics	Equivalent Laminated Plate Solution (ELAPS)
Wing unsteady aerodynamics	Coupled airframe wake system based on Peters wake theory (PWAKE)
Rotor aeroelasticity	Proprotor Aeroelastic Stability Analysis (PASTA)
Flutter suppression	Linear Quadratic Regulator Theory (LQR)

Disciplinary analyses / tools for MDO studies by Stettner [182]

Table 3.2 summarizes contributing analyses and tools. Figure 3.5 illustrates their predominantly sequential execution, demonstrating the effective facilitation of multidisciplinary decomposition. The feedback loop between VASCOMP and ELAPS is due to the wing weight, which is calculated in ELAPS based on wing dimensions provided by VASCOMP; and required by VASCOMP for the aircraft sizing [182].

Stettner's non-hierarchic design methodology utilized gradient based optimization by means of the commercial optimization package DOT. In particular, the Modified Method of Feasible Direction (MMFD) moved initially unfeasible designs into the feasible design space. Subsequent Sequential Linear Programming (SLP) then searched for the final optimum design solution [182].

D'Vari and Baker derived motivation from the tacit assumption of fixed loading conditions common in structural optimization. Resulting aeroelastic loads fail to take design variable changes into account. The development of an aeroelastic integrated loads subsystem

(AILS) enabled multidisciplinary optimization for static strength/displacement as well as flutter by providing load sensitivities to structural design variables. FEM and doublet lattice aerodynamics were coupled via a splining matrix that converts deflections from the structural to the aerodynamic coordinate system. The optimization was based on the method of modified feasible direction within DOT. The simultaneous strength and flutter optimization of a subsonic transport showed excellent agreement with MSC/NASTRAN [51].

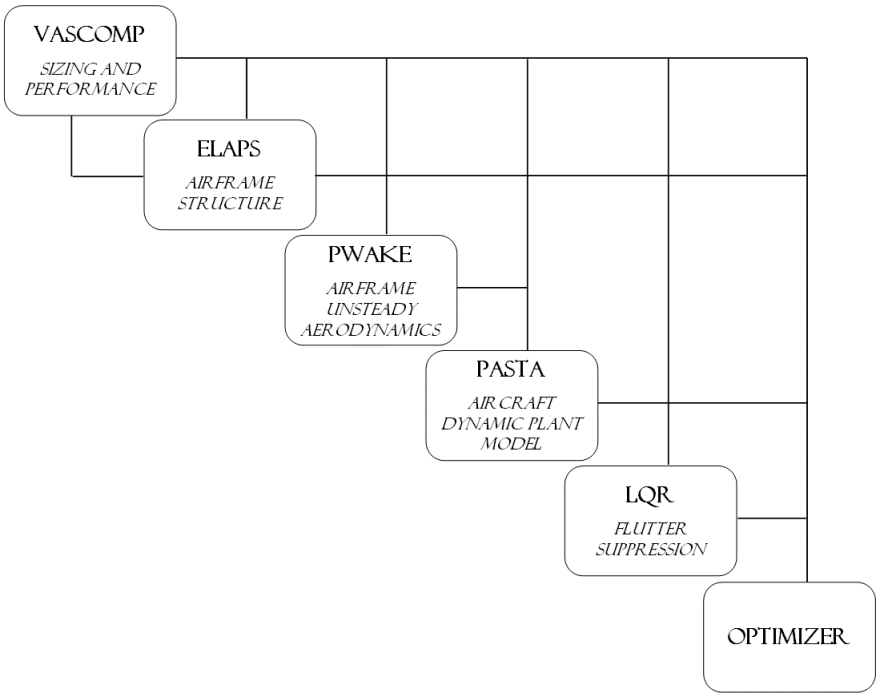

Figure 3.5: Tiltrotor MDO implementation
Figure 4.1 in MDO implementation by Stettner [182]

Results of the coupled aerodynamic and structural sensitivity analysis of a HSCT by Mason and Walsh confirmed the significant effect of coupled loads on stress responses [123]. The detrimental negligence of the dependency of stresses and loads on structural changes was further substantiated by the evaluation of the traditional structural design process at Fairchild Dornier. The documented shortfalls also include the late consideration of aeroelastic requirements detached from and subsequent to all other constraints. It is not uncommon for the resulting suboptimal design solution to entail expensive correctional necessities. The

aeroelastic design of a regional aircraft wing box served as showcase for the efficient application of MDO to a real life aircraft. The design process adheres to a minimum weight objective. Disciplinary analyses are performed by MSC/NASTRAN. The FE model of the aircraft counts some 250,000 degrees of freedom; design variables pertaining to the wing box total more than 2,500. The number of corresponding constraints exceeds 800,000. The modal flutter analysis is based on the *p-k method* [161].

The recognition of the potential benefits of simultaneous aeroelastic analysis and design initiated the Active Aeroelastic Aircraft Structures (3AS) research consortium consisting of 15 European industry, research, and university entities. Proposed application studies of the 3AS project range from long range transport to commuter jet, over high aspect ratio configuration for high altitudes to small RPV. The corresponding multidisciplinary analysis and design tool was designated ARGON. It integrates linear aerodynamics; finite element, plate, and beam structural analysis; and features maneuver loads, eigen analyses, static aeroelasticity, flutter, and aeroservoelasticity [166].

Hunten and Blair engage in improving the design process at the system level by enabling high fidelity studies of new technologies. Corresponding examples are revolutionary concepts such as the blended and joined wing configuration (Figure 3.6). The resulting MISTC framework - MISTC is the signature combination of the subcontractors MSC and TSI - provides a plug and play architecture for physics based modeling tools [89].

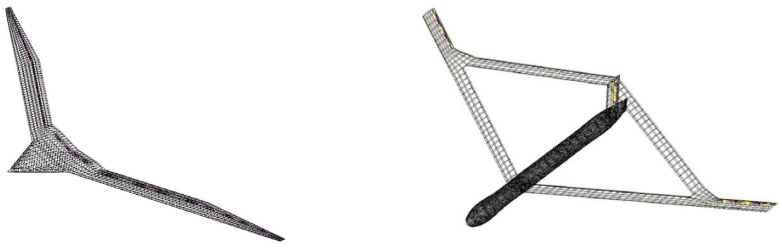

Figure 3.6: Revolutionary wing configurations
Figures 4 and 5 in Hunten and Blair [89]

Goraj et al. implemented an advanced multidisciplinary design process for low cost and high performance of a new HALE aircraft. Reference point for the new surveillance UAV is the Global Hawk. Structural analyses are performed by ANSYS, aerodynamic analyses by

the computer programs VSAERO and MSES. VSAERO is a subsonic potential flow solver. MSES is based on two-dimensional theory. Flutter boundaries of the modal representation are determined using the *V-g method* [75].

The multidisciplinary wing shape design of the small jet aircraft in Figure 3.3 utilizes CFD and NASTRAN for the aerodynamic and structural analyses, respectively. A multi objective Genetic Algorithm (GA) minimizes the cruise drag, the drag divergence for off-cruise conditions, the cruise pitching moment, and the structural wing weight subject to strength and flutter constraints. To reduce the computational expense associated with the objective evaluations, these functions were approximated with Kriging models [110].

3.3.2.2 Formal Aeroelastic MDO Solutions

Formal MDO architectures offer improved efficiency, maintainability, database management, and analysis coordination compared to initial MDO implementations [107]. Examples of formal decomposition solutions are Collaborative Optimization (CO), Concurrent Subspace Optimization (CSSO), and Bi-Level Integrated System Synthesis (BLISS). Respective integration frameworks show both individually distinct properties as well as similarities. Common attributes pertain to the conservation of disciplinary autonomy and interdisciplinary coupling; and go back to the bi-level structure of respective architectures [187].

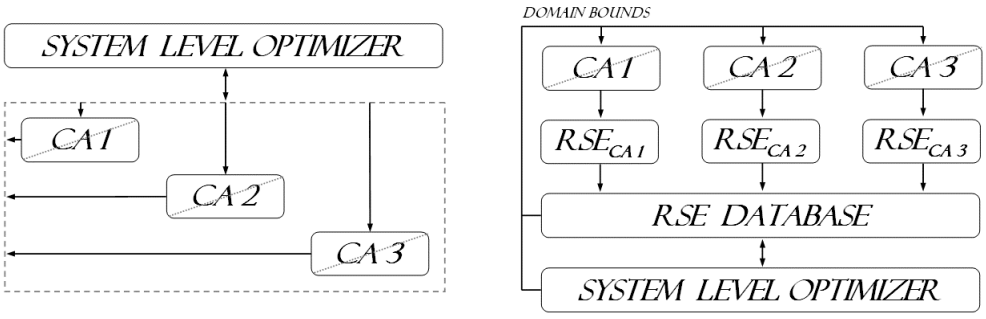

Figure 3.7: MDO architectures
Left: Collaborative Optimization (CO); Right: Bi-Level Integrated System Synthesis (BLISS)

Figure 3.7 illustrates the organization of the two levels for the examples of CO and BLISS. At the subsystem level, disciplinary analyses are employed in the local search of an optimum solution subject to discipline specific objectives and constraints. At the system

level, all contributing analyses (CA) are coordinated by the system level optimizer that ensures compatibility and feasibility while performing a global optimization subject to a global objective and constraints.

Formal decomposition frameworks have been subject to continuous development and investigation. Detailed and comparative elaborations on the various MDO architectures can be found in pertaining literature. A solid starting point is provided within the publications by Balling and Sobieski [7], Sobieski and Haftka [178], DeBaets [44], Kroo [107], Schutte et al. [163], Tedford and Martins [187], and Behdinan et al. [16].

Application examples of CO and BLISS for the design of a supersonic transport are provided by Sobieski et al. [175] and DeBaets [44], respectively. Both implementations utilize disciplinary RSE approximations to support the efficiency of the integrated optimization algorithm by providing inexpensive evaluations of the disciplinary objective functions. The BLISS implementation will be described in more detail in the following section.

3.3.2.3 BLISS Integration Example

The motivation of the MDO solution offered by DeBaets is threefold. (1) Aeroelastic constraint knowledge needs to be conducively mapped onto the conceptual design space; (2) New conceptual design tools continue to play a detached rather than an integrated role; and (3) The integrated environment needs to be flexible enough as to be able to easily exchange the employed high fidelity codes [44]. The integrated framework features three modules in BLISS decomposition format, i.e., structures, aerodynamics, and performance (Figure 3.8).

BLISS is at the heart of contemporary Multidisciplinary Design Optimization. It decomposes a system into its various contributing analyses while retaining disciplinary autonomy and minimizing computational cost. The decomposition into autonomous disciplines resembles the common industrial practice of separate design teams or specialty groups that have full control over their field of expertise. Disciplinary approximations allow almost instantaneous physics based analysis results at the cost of reduced accuracy.

The BLISS flowchart in Figure 3.7 shows domain bounds that are identical to the global

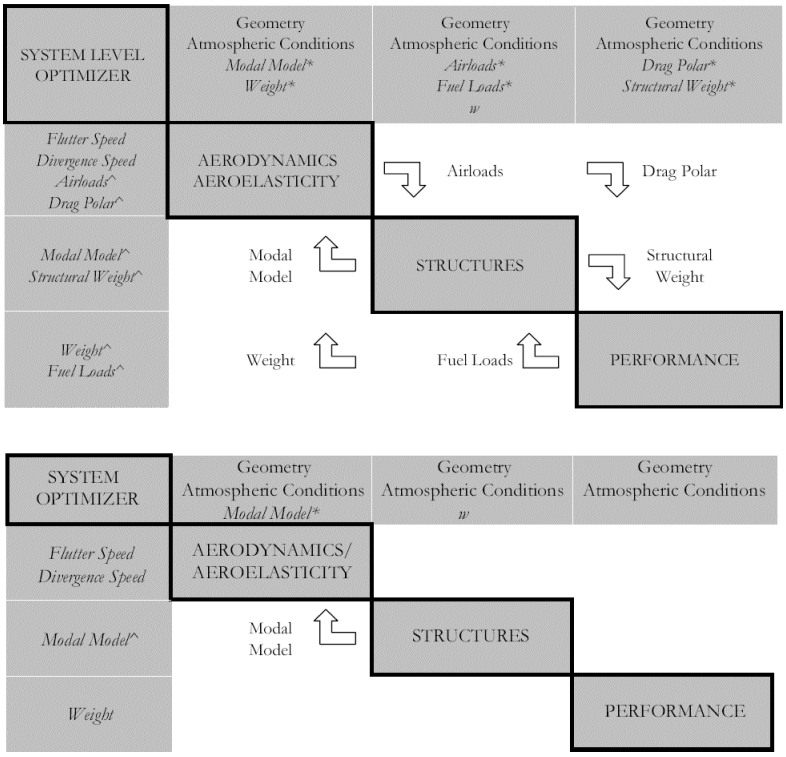

Figure 3.8: Aeroelastic system in BLISS decomposition format

Figures 45 and 40 in DeBaets: System with all interdisciplinary couplings (top) and simplified system (bottom) for BLISS implementation [44]

Nomenclature: *-variables: disciplinary input generated by system level optimizer; ^-variables: disciplinary output; w: weights for subsystem composite objective function

design variable ranges that confine the validity of the created Response Surface (RS) equations. The concurrent subsystem control of BLISS allows for local optimizations performed at the disciplinary level, i.e., minimizing a local objective function subject to local constraints. The disciplinary objective function depends on both local and global input variables; but it also depends on coupling variables, i.e., output variables from other involved disciplines. The RSE database contains approximations of the subsystem optimized results available to the system optimizer. The system level optimizer in turn minimizes a global objective function, subject to global con trains, and ensures feasibility via compatibility constraints linking global and local level.

The disciplinary codes utilized by DeBaets are ANSYS, ZAERO, and FLOPS-ALCCA.

ANSYS provides the modal model for an optimized structural weight. ZAERO provides flutter and divergence speeds for a given modal model [38]. FLOPS-ALCCA provides the takeoff gross weight, which serves as the global objective function to be minimized. Global design variables describe geometry and atmospheric conditions. Global constraints are comprised of modal model compatibility and minimum flutter and divergence speeds.

The implementation consists of four distinct phases. These are initialization, RSE creation, BLISS optimization, and design variable screening. The initialization phase assists the reduction of the overall execution time by providing the system response for a baseline vehicle. Corresponding structural eigenmodes and aerodynamic influence coefficients are held constant during the RS creation phase. The RS creation itself approximates the disciplinary output with a second order polynomial by fitting a quadratic surface through a set of discrete points within the design space. With the RSE database at its disposal, the BLISS optimization can now take advantage of almost instantaneous disciplinary outputs.

Number and arrangement of the discrete points necessary for the RSE generation are determined by techniques pertaining to Design of Experiments (DOE). The corresponding number of required analysis runs for a particular DOE depends on the number of input variables [136]. This dependence turns into an adverse property for an increasing number of inputs as the repeated execution of the high fidelity analysis code becomes prohibitively expensive. To avoid this impracticability, a screening process was performed to find the variables with the greatest impact on the variability of the outputs of interest. In particular, it was determined that only the two lowest eigenmodes need to be kept as distinct inputs for the flutter speed. Similarly, from originally 15 global design variables, nine were found to be important to the aeroelastic speed constraints. On the local level, four out of 11 design variables were found to have a relevant impact on the structural optimization [44].

Table 3.3: Average disciplinary time expenditures

CA	Discipline	Analysis Code	Execution Time
CA 1	Structures	ANSYS	16 hours
CA 2	Aerodynamics	ZAERO	13 hours
CA 3	Performance	FLOPS	Seconds
n/a	Setup	n/a	2 hours

Figure 60 in DeBaets [44]

The successful implementation of BLISS is supported by a quiet supersonic business jet. According to DeBaets, the proof of concept vehicle substantiates the promoted aspects of effective data management; correct representation of tight interdisciplinary coupling; utilization of parallel computing power; and introduction of high fidelity aeroelastic knowledge to the early design [44].

3.3.2.4 MDO Architecture Selection

The right choice of an MDO architecture is prominent to the efficient solution of the multidisciplinary design problem [27, 16]. Pertaining literature seems to agree that loosely coupled systems are better represented by CO, while highly coupled systems benefit from an implementation that adheres to BLISS [16, 104, 105, 187]. Note that industrial applications will typically prefer a loose coupling because of the inherent transparency and flexibility [84].

The categorization of disciplinary coupling depends on the number of interdisciplinary variables. CO has shown to be most effective for subsystem couplings of low dimensionality. Respective systems exhibit more disciplinary than interdisciplinary variables [105].

With regard to the size of the optimization problem at the subsystem level compared to the system level, BLISS has shown to be most effective when the number of local design variables and constraints is relatively large while the number of global design variables and constraints is relatively small [176, 177, 187].

Combining the above information and translating it to the application to the aircraft design process, CO emerges as the better choice for the conceptual phase, while BLISS is more suitable for the preliminary and detail phase [16].

3.3.2.5 Drawbacks

MDO frameworks follow a disciplinary decomposition. The resulting multiple subsystems are represented by existing high fidelity tools. The computational cost associated with respective disciplinary analyses is a drawback that is particularly limiting at the conceptual level of design [174]. Objective function evaluations by means of high fidelity analyses can require an enormous computational time, even in the presence of high performance supercomputer facilities [110, 191].

Time consumption remains a crucial issue for optimization and represents a key detriment for the practical use of high fidelity solvers in conceptual design. Various measures assist the alleviation of time constraints and support the introduction of high fidelity information to early design stages. Foremost, there is the utilization of surrogate models.

Surrogate models have shown great success in enriching the knowledge at the early phases of design by allowing high fidelity analyses and previously ignored information to move upstream on the design timeline as to become part of the early decision making. Their approximate nature allows almost instantaneous physics based analysis results at the cost of reduced accuracy [105, 177, 100]. However, the inherent necessities of setup, preparation, and preprocessing can constitute a rather cumbersome process for the untrained engineer. In addition, in spite of all simplifying efforts, the computational cost associated with high fidelity codes (Table 3.3) poses an insuperable obstacle for conceptual design dedicated to the exploration of numerous design spaces.

The omittance of disciplinary couplings (Figure 3.8) also contributes to overall time savings, but is unfit for the aeroelastic design of highly flexible aircraft. The mutual coupling of participating disciplines in general, and the adherence to resulting structural deformations in particular is imperative for an accurate aeroelastic representation [144]. The lack of an interdisciplinary propagation of design variable changes constitutes a potential weakness of MDO that can invalidate the application to real world design problems [153].

3.4 Reduced Fidelity Efforts

Measures alleviating the computational cost of structural simulation can be taken within the realms of modeling and analysis (Figure 3.1). The former is concerned with reducing dimensionality, the latter with simplifying the physics of the problem.

Mathematical simplification in most cases is not only beneficial but necessary because the numerical implications of the nonlinear equations of motion tend to be insuperable. *"Generally we are forced to linearize in order to reach a practical solution"*, and then it is important to justify the applied assumptions [64].

Reduction in dimensionality requires eligible assumptions if the properties of any real

system ought to be adequately captured in a simplified model. For structures that feature one dimension (thickness) much smaller than the others, two-dimensional surface elements such as plates and shells can be used. Giles applies an equivalent plate model consisting of multiple trapezoidal segments able to represent wing box structures with general planform. He reports analysis results of adequate accuracy obtained up to 60 times faster than FEA [71]. Livne et al. document various references proving the prediction capabilities of equivalent plate models for low aspect ratio wings, showing both feasibility and practicability of multidisciplinary wing design at the early design stages using simplified models [117].

In cases of one dimension (length) being much larger than the other two, the reduction can be taken even further and a one-dimensional beam model is applicable. The high aspect ratios of interest to the present work allow such a one-dimensional treatment. The pertaining literature portraits a vast amount of corresponding research efforts. Only a very brief introduction to analytical and numerical beam theories shall be given here.

3.4.1 Beam Analysis Theories

Beam theories describe a three-dimensional beam as a one-dimensional response problem such that the beam displacement field depends on the spanwise variable, only. The formulation of the governing equations requires three sets of relationships: equilibrium equations that enforce the sum of all body forces to be zero; kinematic relations that connect local strains and displacements; and a constitutive law that relates stresses and strains [14]. The global equilibrium is represented by the equations of motion. The local deformation behavior is described by the kinematic relations. A suitable constitutive law then enables a local sectional analysis separate from the global response analysis [83].

Both local and global analyses are amenable to analytical as well as numerical solutions. Depending on the underlying assumptions, the one-dimensional beam and the two-dimensional sectional analysis can be performed using exact analytical or approximate numerical methods. Respective solutions can be derived in a separate or combined manner.

The literature surrounding beam theories features a vast amount of publications.An excellent comprehensive reference is given by Hodges, the*rightful father of modern composite*

beam theory[81]. Recent reviews of corresponding techniques include Jung et al. [93]; Volovoi et al. [193]; Yu [202]; and Friedmann and Hodges, who admit a section on composite blade modeling in their historical perspective of rotary wing aeroelasticity [61].

3.4.1.1 Analytical Solutions

Analytical beam formulations provide direct and readily attainable solutions in closed form without the need of discretization. The inherent transparency supports the physical understanding of the problem and offers an irreplaceable insight to corresponding cause and effect relationships. Respective implementations produce virtually instantaneous results, but require simplifying assumptions that compromise fidelity and applicability.

Simplifications are typically introduced with respect to cross sectional geometry, material properties, loading conditions, and response characteristics. Resulting restrictions adversely affect the validity of respective theories and constitute a major limitation for the general applicability necessary in design.

3.4.1.2 Numerical Solutions

Approximate solutions based on the powerful method of finite elements offer virtually unlimited modeling and simulation capabilities. The general applicability of FE analyses results in the flexibility and fidelity conducive to conceptual aeroelastic analysis and design.

Computational savings motivate the implementation of beam dimensional reduction in terms of two separate analysis problems in rotary wing aeroelasticity. The study of the three-dimensional rotor blade is decomposed into a local and a global analysis. The local analysis is linear and deals with the two-dimensional cross section. The global analysis is nonlinear and encompasses the investigation of the one-dimensional beam (Figure 3.9). The validity of decoupling local and global level is supported by asymptotic analyses. It can also be shown that the linearity of the local problem complies with the nonlinearity of the global problem [62, 83].

The initiation of the analysis of three-dimensional beams in terms of two separate problems was given by Berdichevsky [17]. The methodology has been refined and extended and is now applicable to beams with cross sections of arbitrary geometry and material [201, 202].

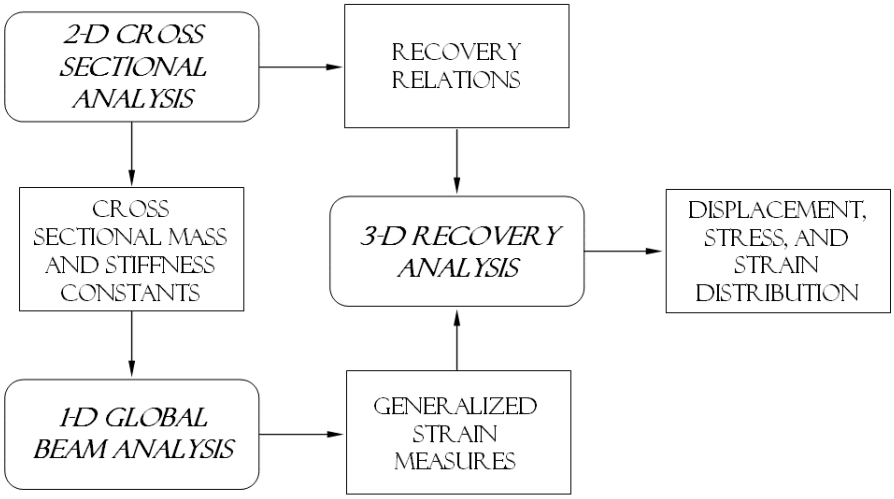

Figure 3.9: Beam analysis methodology
Recreation of Figure 1 in Bauchau and Hodges [15]

Analysis tools developed for dimensional reduction of beam-like structures are VABS and DYMORE. VABS serves the Variational Asymptotic Beam Sectional Analysis in form of a standard two-dimensional FEM program [202, 204]. DYMORE is a finite element based dynamics code for the analysis of flexible, nonlinear multibody systems. It enables the simulation of large displacements and rotations under the assumption of small strains [13]. Combining both tools, an efficient and accurate analysis procedure has been developed that is not restricted to simple cross sectional shapes. It provides tremendous computational savings compared to three-dimensional FEA, making it an efficient and useful integrated approach for realistic engineering applications [15, 200, 194].

3.4.2 Beam Design Applications

Beam theories are solely concerned with the analysis of a given system. The present effort is dedicated to the application of such theories to design. The distinction between analysis and design lies in the autonomy of execution. Analysis is a single-valued problem focused on one system described by a corresponding set of specified input variables. Design on the other hand relies on the exploration of design spaces by analyzing an innumerable amount of systems. Thus, analysis is a primary part of design; but design faces additional challenges with respect to the evaluation, processing, presentation, and utilization of analysis results.

3.4.2.1 CALFUNOPT

A widely and successfully used optimization package is the program CALFUNOPT. Its name stems from the calculation of the flutter speed using normal modes. The wing is modeled as a series of composite box beam elements, with constant cross sectional properties for each element. The contributing disciplines of structures and aerodynamics are represented by the Dynamic Stiffness Method (DSM) and an unsteady aerodynamic strip theory, respectively. The aeroelastic equation of motion is solved using the *V-g method* [112].

The DSM implementation is validated against FE analysis. The high AR wing model consists of 10 box beam elements. In contrast, the FE mesh has a total of 6,075 nodal points. The natural frequencies show reasonable agreement. Flutter and divergence speeds deviate a little, but are reported to be within acceptable margins [112]. An extended work compares the same wing with an ANSYS model of 2,070 eight-noded elements. DSM obtains satisfactory results in significantly less time, i.e., the modal analysis in ANSYS took 22 minutes, the one using DSM only 2 seconds [113].

Butler et al. document a comparison study using NASTRAN. The initial design shows good agreement in displacement, stresses, and vibration results. The CALFUNOPT optimized design for minimum structural weight, however, satisfies the stress and displacement constraints with a 20 percent heavier wing. The explanation for this discrepancy lies in the inability of the DSM model to adjust the local torsional center of the wing box along the span. The details of the three-dimensional FE model allow for a chordwise variation of skin thickness which in turn minimizes the effective torque [29].

The one aspect of DSM supporting its greatest advantage is also responsible for its greatest drawback. The simplicity of the structural elements allows the exact solution of the governing differential equations of motion [185, 186]. Results are provided with a swiftness unobtainable by FEA. The primary limitation of DSM is spawned by the very same simplicity. The exclusive use of box beam elements with constant elemental properties confines both flexibility and fidelity.

3.4.2.2 Multi Level Optimization

Beam dimensional reduction as described earlier gives rise to two separate analysis problems. This two level decomposition can be taken advantage of in respective design studies. At the upper level, global analyses of the beam yield the requirements for the equivalent beam properties. At the lower level, local analyses find the cross sectional design that provides the required properties. The so formulated two level optimization problem holds great computational savings because the upper level design variables in terms of cross sectional stiffness and couplings are much fewer than the lower level design variables describing geometry and material distribution [138, 66].

Great success in multi level optimization was recently achieved with the implementation of a respective scheme for the optimization of composite rotor blades [109, 108]. The integrated approach is shown in Figure 3.10. Analysis tools for global and local level are DYMORE and VABS, respectively. Note that the global optimization is preceded by local analyses. VABS is executed to (a) provide initial input values for DYMORE, and (b) to run a DOE necessary for the construction of a surrogate model of the local design space.

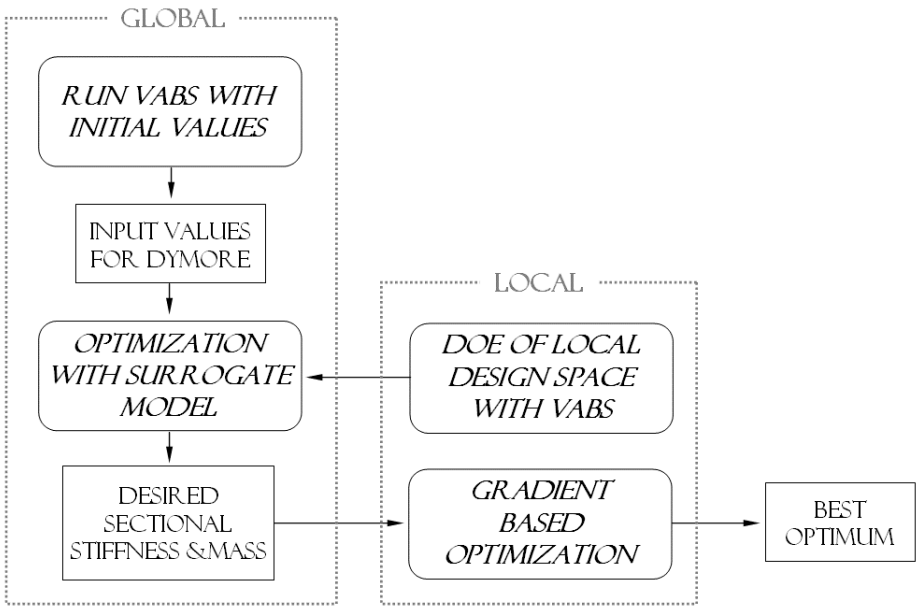

Figure 3.10: Flow chart of multi level optimization
Recreation of Figure 43 in Ku [108]

The surrogate model ensures communication between levels. It guaranties that the design variables at the global level stay within the feasible region of the local design space. It also increases the efficiency of the global optimization because of the virtually instant availability of VABS outputs. An information summary of both optimization levels can be found in Table 3.4. The blade cross section of the implemented showcase is shown in Figure 3.11. The local design space exploration takes advantage of a hybrid two phase optimization scheme in which a Genetic Algorithm scans the cross sectional design space for the most promising local minima prior to the actual gradient based optimization [108].

Table 3.4: Two level composite rotor blade optimization

	Global level	Local level*
Objective	Minimize blade structural weight	(1) Minimize difference between required and calculated sectional mass (2) Minimize combined difference in sectional mass and stiffnesses subject to equal weighting factors
Design variables	Sectional mass; tip mass; torsional, lead lag, & flapping stiffness	Outer and inner ply angle; flexure width and height
Constraints	Autorotation index; natural blade frequencies	(1) Stiffnesses (2) n/a

* Two different formulations with same results, but second one with faster convergence [108]

The upper level is tailored towards the design of rotary wings. The global constraints in Table 3.4 represent crucial safety considerations for rotary wing aircraft. The autorotation index ensures sufficient lift generation and a safe landing after engine failure. The placement of blade natural frequencies ensures resonance avoidance with the rotor rotational speed.

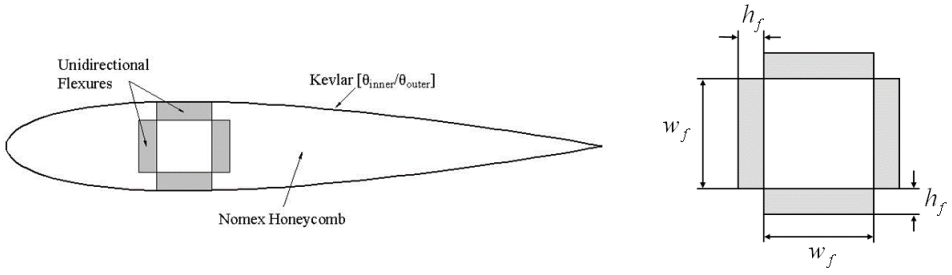

Figure 3.11: GTGH Blade cross section

Recreation of Figure 44 in Ku [108]

The development of the two level scheme is well documented. The biggest challenge was the ensurance of design space compatibility of global and local level [138, 196, 195, 194]. The solution was found in a surrogate model of the local design space. A minor drawback of surrogates are potential labor and time requirements necessary for their creation. Ku et al. decided in favor of a Kriging model [109]. For the simple testcase illustrated in Figure 3.11, the choice of a seven level Full Factorial DOE for the four design variables resulted in 2401 experiments.

3.4.2.3 Other Research Efforts

Chattopadhyay et al. introduced a hybrid optimization technique for the aeroelastic design of composite wings. The optimization objective is minimum wing weight subject to constraints on flutter and divergence speed, as well as wing root stresses due to static loading. Design variables are root chord, ply orientation, and wall thickness. The structural model of the composite wing is reduced to a box beam representation (Figure 3.12). Aerodynamic loads are obtained using a panel method. Aeroelastic speeds are calculated with the widely used *V-g method* [35]. A hybrid optimization scheme combines Simulated Annealing (SA) with a gradient based search algorithm to improve overall optimization efficiency and to allow both continuous and discrete design variables [167].

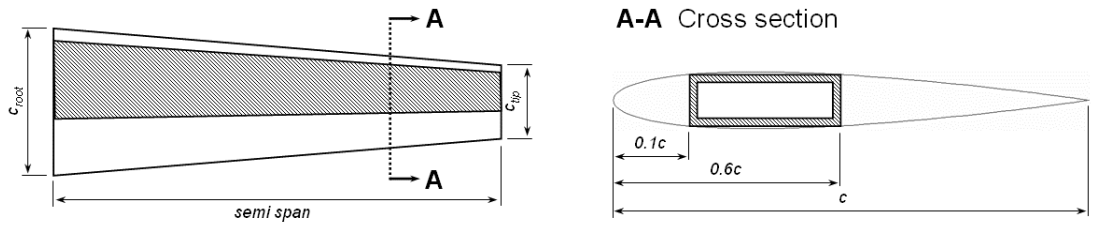

Figure 3.12: Box beam wing model
Figure 1 in Chattopadhyay et al.: Top view (left) and side view (right) of wing geometry [35]

The limiting choice of the exclusive use of rectangular box beams is justified by the close resemblance of real wing structures and by the accurate capture of elastic couplings. The implemented constitutive law, however, neglects couplings. Published comparisons of global bending and twist distribution show very good agreement with experimental data

and VABS, but are limited to a single testcase of a thin-walled composite beam under a tip bending load [35].

The multi level approach by Visser incorporates a reduced structural model by means of panels. The two level optimization strategy exhibits ideas similar to the above two level optimization of rotor blades. It is applied to the composite wing of a 130 passenger jet aircraft subject to aeroelastic and strength constraints. Design variables are reduced by moving the stacking sequence optimization to a lower level (Table 3.5). At the upper level, static and aeroelastic analyses are performed by MSC/NASTRAN. Aerodynamic loads are provided by a panel method. At the lower level, non-dimensionalized flexural lamination parameters accounting for four ply orientation angles are introduced as design variables. Fiber orientation angles are limited to 0, 45, -45, and 90 degree to account for practical constraints. The optimization algorithm is based on sequential convex programming [43].

Table 3.5: Two level composite wing optimization

	Upper level	Lower level
Model	FE wing model	Stiffened skin panels
Objective	Minimize wing weight	Maximize buckling safety margin
Design variables	In-plane panel stiffnesses	Stiffener geometry and stacking sequence
Constraints	Strength, elastic stability, aeroelastic constraints	In-plane panel stiffnesses

Aeroelastic and strength optimization by Visser [43]

Similarly, Liu et al. divide the optimization problem of a composite wing into a global wing level and a local panel level. At the panel level, a cubic response surface is introduced to have available to the upper level a smooth representation of the lower level optimum solution. The use of the response surface was motivated by a review of existing two level approaches with the same implementation difficulties as identified above [114, 115].

3.5 Inverse Perturbation Redesign

Direct methods for analysis and design calculate system characteristics based on a given shape or geometry. In contrast, inverse methods specify the desired characteristics at the outset, and then find the shape or the geometry satisfying these specifications. Success with

inverse solution techniques in the area of structural design subject to frequency and mode shape constraints was achieved with the method of Inverse Perturbation Redesign (IPR).

3.5.1 Theory

Given a baseline structure with unsatisfactory natural mode characteristics, the idea is to determine the stiffness and mass matrices that result in a desired set of normal modes and frequencies without additional FE analyses. Starting point is the eigenvalue problem of the known baseline structure.

$$\left[[k] - \omega^2 [m]\right] \{\psi\} = \{0\} \tag{3.1}$$

The matrices $[m]$ and $[k]$ represent the nxn system mass and stiffness matrices, respectively. For a non-trivial solution, the determinant of Equation 3.1 must vanish. The resulting characteristic polynomial has n roots with corresponding eigenvectors, defining n natural frequencies ω_i^2 with corresponding mode shape $\{\psi_i\}$.

$$\left[\omega^2\right] = \begin{bmatrix} \omega_1^2 & & 0 \\ & \ddots & \\ 0 & & \omega_n^2 \end{bmatrix} \tag{3.2}$$

$$[\phi] = [\{\psi_1\}, \{\psi_2\}, ..., \{\psi_n\}] \tag{3.3}$$

The uncoupled equations of motion take advantage of generalized mass and generalized stiffness matrix.

$$[K] = [M] \left[\omega^2\right] \tag{3.4}$$

$$[M] = [\phi]^T [m] [\phi] \tag{3.5}$$

$$[K] = [\phi]^T [k] [\phi] \tag{3.6}$$

Structural redesign is applied when any of the modal characteristics expressed in Equations 3.2 and 3.3 fail to meet the specified response criteria. The traditional approach would

employ many costly FE analyses in an iterative fashion. The inverse method of redesign avoids comparable expenses by defining the objective system in terms of perturbations from the baseline system.

$$[\hat{m}] = [m] + [\triangle m] \tag{3.7}$$

$$\left[\hat{k}\right] = [k] + [\triangle k] \tag{3.8}$$

$$\left[\hat{\omega}^2\right] = \left[\omega^2\right] + \left[\triangle \omega^2\right] \tag{3.9}$$

$$\left[\hat{\phi}\right] = [\phi] + [\triangle \phi] \tag{3.10}$$

The redesign objective is to determine the structural changes $[\triangle m]$ and $[\triangle k]$ that will result in a system with the desired modal characteristics. The goal is to devise a system of equations that relates structural and modal changes. Structural changes are expressed as linear combination of σ element changes, with each element change being a fractional change from the baseline system.

$$[\triangle m] = \sum_{e=1}^{\sigma} [\triangle m_e] = \sum_{e=1}^{\sigma} [m_e]\, \alpha_e^m \tag{3.11}$$

$$[\triangle k] = \sum_{e=1}^{\sigma} [\triangle k_e] = \sum_{e=1}^{\sigma} [k_e]\, \alpha_e^k \tag{3.12}$$

Modal changes are expressed as linear combination of the baseline mode shapes. Small admixture coefficients with $C_{ii} = 0$ are introduced, such that C_{ij} quantifies the influence of the jth mode to the change in the ith mode.

$$[\triangle \phi] = [\phi]\, [C]^T \tag{3.13}$$

Expansion of the hatted eigenvector matrix in Equation 3.10 using Equation 3.13 makes an understanding of the objective mode shapes in terms of baseline mode shape participation easier.

$$\begin{aligned}\left\{\hat{\psi}_1\right\} &= \{\psi_1\} + C_{12}\{\psi_2\} + ... + C_{1n}\{\psi_n\} \\ &\vdots \\ \left\{\hat{\psi}_n\right\} &= C_{n1}\{\psi_1\} + C_{n2}\{\psi_2\} + ... + \{\psi_n\}\end{aligned} \tag{3.14}$$

Manipulation of the objective eigenvalue problem, carried out in Appendix C, leads to the first order perturbation equation.

$$[\phi]^T [\triangle k][\phi] - [\phi]^T [\triangle m][\phi]\left[\omega^2\right] = [\triangle] \tag{3.15}$$

Expansion yields n^2 scalar equations,

$$\{\psi_i\}^T [\Delta k]\{\psi_j\} - \omega_j^2 \{\psi_i\}^T [\Delta m]\{\psi_j\} = \begin{cases} M_j \triangle \omega_j^2 & \forall i = j \\ M_i C_{ji}\left(\omega_j^2 - \omega_i^2\right) & \forall i \neq j \end{cases} \tag{3.16}$$

that include all structural changes on the left hand side, separated from all modal changes on the right hand side. Alternatively, Equation 3.16 can be devised in compact matrix form,

$$\left\{P^k\right\}^T \left\{\alpha^k\right\} + \{P^m\}^T \{\alpha^m\} = \Delta_{ij}$$

with

$$P_e^k = \{\psi_i\}^T [k_e]\{\psi_j\}, \qquad P_e^m = -\omega_j^2 \{\psi_i\}^T [m_e]\{\psi_j\}$$

such that

$$\left[P^k\right]_{Sx\sigma}\left\{\alpha^k\right\}_{\sigma x1} + [P^m]_{Sx\sigma}\{\alpha^m\}_{\sigma x1} = \{\triangle\}_{Sx1} \tag{3.17}$$

$$[P]_{Sx2\sigma}\{\alpha\}_{2\sigma x1} = \{\Delta\}_{Sx1} \tag{3.18}$$

Equation 3.17 is a linear system of algebraic equations. The choice of solution algorithm depends on the number of modal objectives S, and the number of structural element changes σ. If $S < 2\sigma$, there are more design variables than objectives. The system is underdetermined and requires an optimization routine to be solved. If $S > 2\sigma$, there are more objectives than design variables. The system is overdetermined and requires a minimum error procedure.

If $S = 2\sigma$ and $[P]$ is nonsingular, any available linear solver can be applied to determine the unique solution for the 2σ unknown structural changes.

3.5.2 Redesign Methods

IPR takes advantage of first order perturbations, inverts respective calculations, and determines the structural changes that will shift the baseline modes and frequencies to their desired values. The fundamentals go back to Stetson [181]. A first extension by Sandstrom provided substantial computational savings and relief from the intransparent admixture coefficients by affording direct mode shape specification [157, 158].

Because Equations 3.16 and 3.17 are based on the assumption of small changes, Sandstrom suggested an incremental approach of reanalysis and inverse perturbation in order to enable large changes (Figure 3.13).

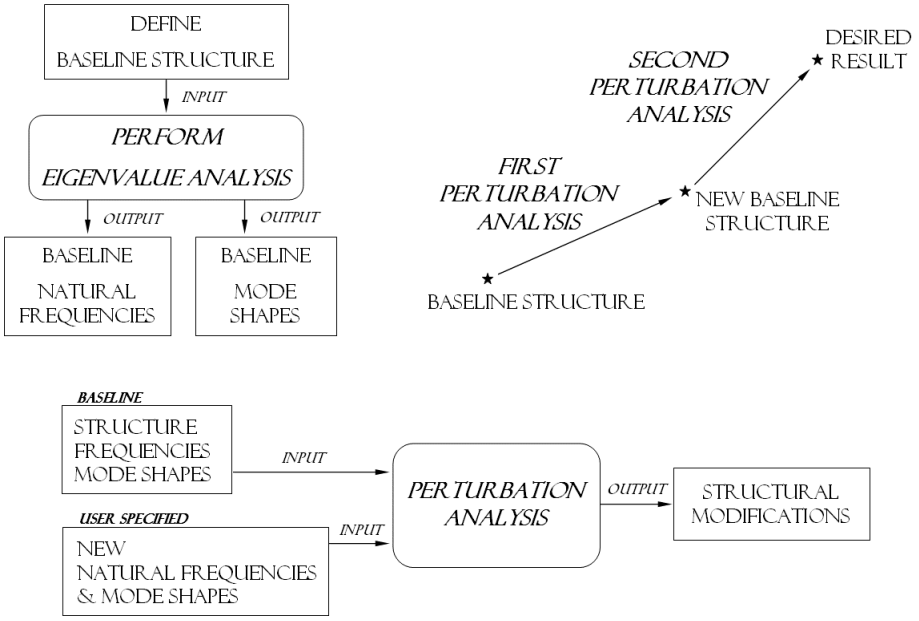

Figure 3.13: Incremental inverse perturbation solution
Upper left: Forward solution of baseline structure; Upper right: Incremental solution using small changes; Bottom: Inverse solution producing modified structure [158]

An alternative was proposed by Hoff et al. An incremental predictor-corrector technique first uses the linear perturbation equations to provide an estimate of the structural changes,

then calculates resulting approximate eigenvectors, and lastly uses these eigenvectors to correct the elemental changes, thus allowing large modal changes based on a single FEA of the baseline [85, 87]. However, the repeated use of approximated mode shapes in the corrector phase can easily lead to substantial error accumulation [86].

Kim et al. found that the second order term $\triangle k \triangle \phi$, discarded as higher order term in the derivation of the first order perturbation equation (Equation 3.16), can take values of the same order as first order terms. To avoid the associated introduction of substantial error, Kim et al. kept all terms in the perturbation equation development. The resulting nonlinear method was shown to be superior over the linear method for large mode shape changes. However, large changes benefit from an approximate starting point. Structural changes remain a linear combination of σ element changes [101].

The incremental predictor-corrector approach for large changes was further developed by Bernitsas et al. The new algorithm was called the method of Large Admissible Perturbations (LEAP); and it was implemented in the computer program RESTRUCT. LEAP is capable of handling static displacement objectives [20, 23], as well as systems with forced response and proportional damping [19].

3.5.3 Redesign Applications

The perturbation equations provide a meaningful relationship between modal and structural changes. They have been utilized in structural redesign subject to small changes in vibratory characteristics. Particular significance of the method stems from the substantially reduced cost compared to traditional trial and error approaches [158].

The most common and recurring examples of inverse redesign found in the literature are a cantilever beam, an offshore light tower, and an aluminum disk drive. The beam is typically used to illustrate the method and its accuracy. The latter two are shown in Figure 3.14. They are presented in literature as large scale complex systems.

The light tower is used for model correlation studies. That is, the three-dimensional numerical representation of the tower is adjusted in its structural properties to match full scale measurements of the natural frequencies. The FE model consists of 442 elements

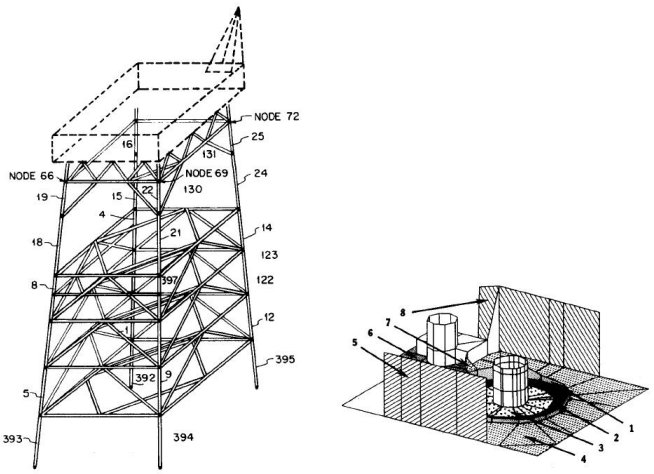

Figure 3.14: IPR applications
Left: Computer model of the offshore light tower [158]; Right: Aluminum disk drive [87]

resulting in 810 dof. Out of the total of 397 beam and 45 plate elements, only a subset of the beam elements is allowed to change. Computational effort is further reduced by linking design variables of similar elements. An additional check of the strain energy determines the modal influence of each element group, yielding a final set of 5 design variables, which relate the change of inner and outer diameter of the tubular beams. Deformation is limited to twist and elongation [86].

The FE model of the disk drive features 312 elements with a total of 1254 dof. The application of design variable linking to the 160 plate elements results in 16 element sets. Beam and spring elements are not allowed to change. The strain energy test confirms a total of 8 design variables, each linked to the thickness of the grouped plates. The redesign objective is to increase the first natural frequency by 30 percent [87].

3.5.4 Limitations

IPR provides a meaningful way to find small structural changes that satisfy a set of specified vibratory response criteria without additional FE analyses. Efficiency and accuracy of IPR have been documented for a small number of redesign examples. The incremental utilization within optimization and design has been suggested but potential design methodological implementation problems have not yet found consideration.

Relevant application examples are restricted to isotropic bending beams. Performance

requirements of military assignments resulted in composite materials contributing up to 70 percent to modern airframe weights [6]. Composite wings inherently defy an isotropic treatment within an Euler-Bernoulli beam model.

Structural changes are defined as linear deviations by means of multipliers α to the baseline stiffness and mass matrices. Mass matrix changes are typically omitted or its multiplier α^m assumed to be the same as the stiffness multiplier α^k. The elemental change α_e defined in Equation 3.12 results in the same relative change of all stiffness coefficients as each and every matrix entry is multiplied with the same parameter. The final solution of the redesign problem in terms of the aforementioned matrices disengages actual physical design variables.

3.6 Review of Design Challenges

The present work evolves around the development of a structural optimization approach suitable for frequency placement and conceptual design of high aspect ratio wings. Design in general is faced with challenges in the realms of analysis, optimization, and automation. The successful resolution of these crucial points will enable the formulation and implementation of desired capabilities.

3.6.1 Analysis

The single most important barrier for conceptual design studies is the computational cost of associated analyses. Detailed FE models can simulate the structural response with a high level of accuracy, but entail computational expenses that make them impractical for conceptual design and trade studies. Economic practicality is achieved by transforming a complete three-dimensional FEA to a reduced analysis of the important dimensions [35, 202].

The standard approach for structural optimization consists of a modal treatment for dynamic response problems and a discrete treatment for static problems and stress recovery [97, 98]. The modal approach can reduce the size of the problem by many orders of magnitude, but presupposes that the structural response can be described as linear combination of a set of baseline modes. These modes are the normal eigenmodes that correspond to the natural frequencies of the system.

The modal approach also has a natural conduciveness to aeroelasticity because the flutter stability boundary corresponds to a coupling of natural modes with the lowest frequency (Appendix B). The analysis of an entire aircraft typically requires in the order of 50 natural vibration modes. For the flutter analysis of an aircraft wing, only 10 of the lowest frequency modes typically suffice [209]. Experience for large aspect ratio wings has shown, that either the first bending or the first torsion mode leads to flutter [25].

The beam like geometry of high aspect ratio wings allows dimensional reduction. The literature review identified the advantages of the decomposition of such a three-dimensional structure into a local and a global analysis problem. VABS and DYMORE have been established to successfully implement respective analyses by providing fast yet sufficiently accurate results [15, 200]. An integrated approach for the design of rotor blades has been implemented by tailoring local and global analyses to capture dynamic characteristics of rotary wings [196, 195, 108].

3.6.2 Optimization

Optimization is the process of strategic and comparative evaluation of a design space. The constitutive goal is to find the design variable settings that result in the optimal satisfaction of both objective function and constraints. The choice for an appropriate optimization algorithm depends on the size and the character of the problem. Two distinctly different approaches exist. These are gradient based and stochastic optimization.

Gradient based techniques attempt a well informed decision about the most promising direction in the design space by evaluating local derivatives. This gradient evaluation has two major drawbacks. (1) Because of the general inavailability of analytical formulations, the determination of the search direction relies on Finite Differences (FD) by evaluating adjacent design points. The inherent necessity of multiple executions of the analysis can result in great computational costs. (2) The utilization of local information in terms of gradients implies a dependence on the starting point and thus, the possible convergence to a local minimum [190, 119].

Stochastic methods are essentially random, but have significantly improved chances of

converging to the global optimum. Their most attractive attribute stems from design space independence, i.e., they are only marginal susceptible to nonsmooth design spaces that feature discontinuities and/or nonconvexities. Unlike gradient based techniques, stochastic schemes can handle discrete design variables; they do not rely on a feasible starting point; and they do not depend on FD. Stochastic methods only need the objective function value itself. However, the large number of function calls can inflict an impractical computational cost. Also, not all solutions will be a global minimum as there is no formal proof of consistent convergence for stochastic optimization schemes [190, 77, 119].

The economy of structural and aeroelastic optimizers relies on the minimization of repetitive mode calculation [78]. Recent publications document improvements in computational efficiency using hybrid optimization. A hybrid optimizer combines two search techniques by taking advantage of their best features in either a sequential or a symbiotic fashion. A sequential implementation applies a stochastic method to find the deepest valley and then uses a directed algorithm to climb down [31]. A symbiosis is realized by enhancing certain sequences of a non-gradient method with gradient based information [167, 192].

In summary, the performance of an MDO environment depends on the efficiency of the optimization algorithm [16]; and the greatest handicap of optimization algorithms is the associated number of function calls.

3.6.3 Automation

A survey within the Daimler-Benz Aerospace AG Military Aircraft Division (DASA-M) about industrial needs in aeroelastic structural design in particular and MDO in general identified five major barriers for the use of disciplinary analyses in design [84]. Table 3.6 summarizes respective findings and presents automation as one of the grand challenges.

Design is a human centered process that relies on experience, creativity, intervention, and deliberation [106, 116, 119]. Utter automation of the design process is neither desirable nor attainable [52]. In contrast, the economy of a design tool greatly depends on its efficiency; and automation greatly contributes to overall run time reductions.

Fully automated disciplinary data transfer optimizes the overall information flow by

Table 3.6: Major barriers for multidisciplinary design

Barrier	Description
1	Tool robustness
2	Automation level
3	Ease of use and checking
4	Lack of expert control
5	Lack of disciplinary interfaces

Barriers identified in DASA-M survey by Hoenlinger et al. [84]

removing subsequent input requirements. It also eliminates the need of a comprehensive knowledge of the applied disciplinary analyses, which alleviates user restrictions from specialists to untrained engineers. Parametric input capabilities spur further time reductions by minimizing the set of required input variables as well as by simplifying geometric model and grid generation.

3.7 Summary

In spite of many research efforts and amazing accomplishments in the area of aeroelastic analysis and design, there is a remaining need for aeroelastic design capabilities in the early phases of the design process. The present work will not attempt to provide a comprehensive aeroelastic design environment. It merely derives its motivation from the significance of structural and aeroelastic response characteristics to aircraft performance and integrity, and from the corresponding physical significance of natural vibration modes.

The current state of insufficient consideration counteracting the disciplinary importance of structures and aeroelasticity stems from prevalent handicaps in analysis as well as optimization. Both processes face serious fidelity and efficiency detriments.

The NASA Langley Research Center summarizes general deficiencies in a statement of requested work for a design and analysis tool in the Remotely Operated Aircraft (ROA) sector. It is clearly stated that the capabilities needed are precluded by the substantial time requirements associated with existing tools. Emphasis is placed on the need for a physics-based modeling and simulation environment that enables rapid and efficient decision making. Desired capabilities require improved measures of breadth and depth in order to treat the diversity of vehicles proposed [131].

The goal of the present work is the composition of an efficient and effective optimization scheme for high aspect ratio wings subject to natural frequency constraints. The next chapter will reiterate on the corresponding motivation, present a concise definition of the research objective, and introduce both the intended application and potential benefits of the new optimizer.

Chapter IV

PRESENT RESEARCH EFFORT

This chapter briefly reflects on some salient points made in preceding sections before presentingthe present research objective. It affirms the motivation, illustrates the contribution, and presents a preliminary framework of the notional methodology based on the review of past and current efforts. Research questions will illuminate emerging challenges related to the implementation of this notional framework. Hypotheses will provide answers to the posed questions, but will remain without proof until evidentiary results from the implemented methodology are available.

4.1 Research Objective

Design relies on the integral elements of analysis and optimization. Analysis determines the response of a given system in a specified environment. Optimization determines the system with the presumably best response characteristics. Both are vital to the performance of design and the quality of the solution. The present work is attributed to optimization but obliterates the distinct borderline to analysis.

Two different optimization techniques exist in the form of gradient based and stochastic methods. The former make informed decisions about usability and feasibility of local search directions. The latter are essentially random but greatly increase the chances of finding a global optimum. Common handicap to both is a potentially large number of function calls.

Directed optimization algorithms typically identify the most promising search direction first and then find the step size along this direction. Figure 4.1 illustrates the identification of the search direction by means of local gradients. Because of the general unavailability of analytical expressions for objective function and constraints, gradients are evaluated numerically on the basis of finite differences. For structural design problems that translates to a large number of FEA making a respective optimization extremely time consuming.

Research Objective of the present work is the development of an optimization approach for high aspect ratio wings subject to natural frequency constraints. Goal is the composition of a directed search algorithm free of gradient evaluations. Founding idea is the incremental application of small modal perturbations combined with sequential reanalysis to enable a swift local exploration of the design space without compromising accuracy.

Motivation for the current research is derived from insufficient structural and aeroelastic design capabilities at the conceptual stage of design. Beam dimensional reduction and small perturbation theory are used to provide potential remedy. The former serves efficient analyses by decomposing the structural response of a high aspect ratio wing into a local and a global analysis problem. The latter shows great promise for an efficient optimization scheme subject to modal constraints. The combination of computational efficiency and fidelity inherent to both theories is key to the efficiency and effectiveness of the proposed optimization algorithm.

The envisioned optimizer builds on an extension of Inverse Perturbation Redesign. Figure 4.1 illustrates the computational savings inherent to an incremental application of small modal perturbations. The sequential solution promises a directed exploration of the design space at reduced computing costs. Unlike gradient based algorithms, each iteration or increment of the envisioned algorithm performs a single FEA to find the small changes necessary to move closer to the optimum solution.

Motivational rationale for natural frequency placement is their physical significance. The dynamic response of a structure depends on exciting forces and modal eigen characteristics. The danger of resonance stipulates comprehensive care with regards to range and location of respective frequencies. The deformation of a structure can be expressed in terms of natural modes and frequencies. Critical aeroelastic modes correspond to free vibration modes.

The one-to-one correspondence of aeroelastic and natural modes allows the placement of natural frequencies with a particular conduciveness for aeroelastic design. The aeroelastic phenomenon with the arguably most dramatic effects on aircraft design is flutter. For high

Minimize:

$$F(X) \qquad \text{Objective function}$$

Subject to:

$$g(X) \leq 0 \qquad \text{Inequality constraint}$$

and

$$X^L \leq X \leq X^U \qquad \text{Side constraints}$$

where

$$X = \{\ X_1 \quad X_2\ \}^T \qquad \text{Design variables}$$

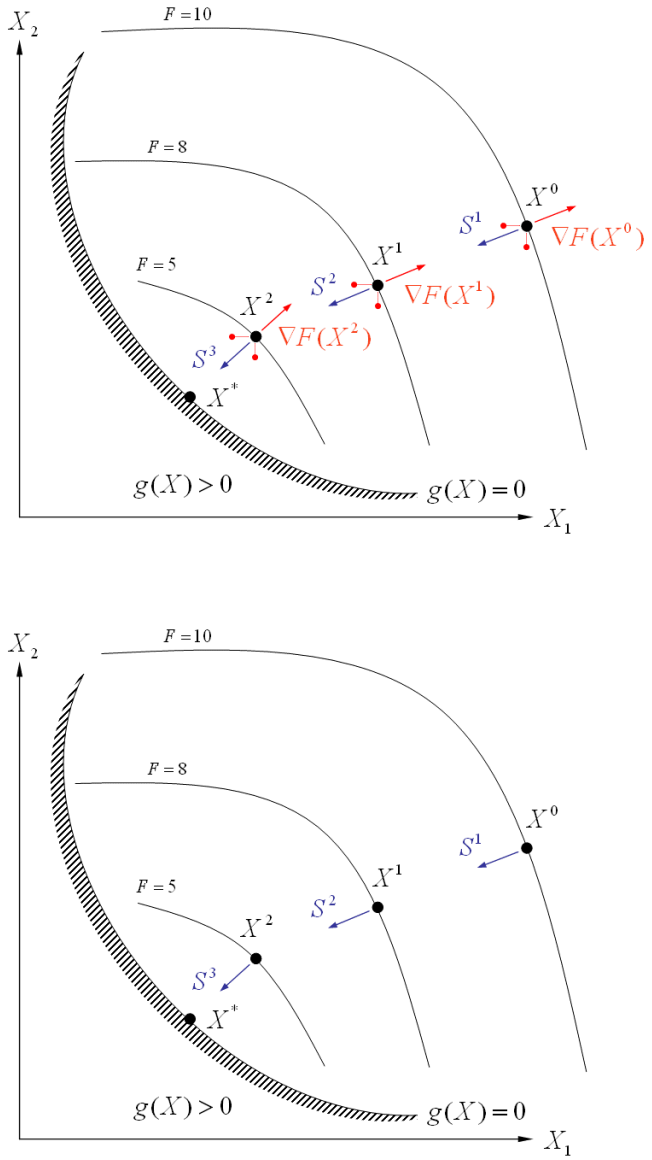

Figure 4.1: Directed search optimization

Top: Traditional gradient based algorithm; Bottom: Envisioned small perturbation based algorithm

aspect ratio wings either the fundamental bending or the fundamental torsion mode will lead to the classic manifestation of this dynamic instability [25].

Analytical and experimental investigations by Hollowell and Dugundji confirm a wide aeroelastic response spectrum based on the coupling of bending and torsion modes [88]. Weisshaar and Frost discuss stiffness effects of bending and torsion and illustrate their impact on aeroelastic characteristics [198]. Meirovitch and Seitz even examined the optimization of natural frequencies for the aeroelastic tailoring of low aspect ratio wings [126].

4.2 Ultimate Design Goal

Knowledge drives and guides all design decisions. The broad impact of structures and aeroelasticity necessitates an early inclusion of both disciplines in the design process. The finding of an effective design solution especially for unconventional configurations requires an early identification of corresponding problems.

This ultimate design goal of conceptual structural and aeroelastic analyses can be established on two counts. New and improved system metrics augment quantity and quality of information available to the conceptual designer; and new constraint lines contribute to better mapping capabilities and design space visualization.

4.2.1 New and Improved System Metrics

Wing parameters such as aspect ratio, sweep, and dihedral transcend disciplinary borders and have a significant impact on the overall aircraft design [53, 153]. The experienced designer may be able to a-priori confine these parameters to avoid critical designs; but the availability of flutter and divergence speeds would enable actual trade capabilities.

The flexibility of high aspect ratio wings greatly impacts the lift distribution [40]. Respective analyses are traditionally ignored at the conceptual stage and an unloaded configuration is considered. The analysis framework of the current implementation provides wing deformations that would improve the fidelity of aerodynamic calculations. Structural deflections could also be used to satisfy additional constraints such as maximum wing bending.

Aircraft weights are traditionally based on empirical equations. Empirical weights work

very well for conventional configurations but are destined to fail for unconventional or revolutionary configurations due to nonexistence of corresponding aircraft. The current implementation provides an improved estimate of the wing weight by integrating the cross sectional mass output over the wing span.

4.2.2 New Constraint Lines

Key to a successful presentation of the vast amount of data in design is a conducive visualization. The format most valuable to the conceptual designer is the thrust loading vs. wing loading plot. It reflects segments of the mission profile and maps a number of constraints and performance parameters onto a concise description of the conceptual design space. Figure 4.2 illustrates the location and reach of feasible and infeasible regions that enable thorough engineering judgment and design decisions.

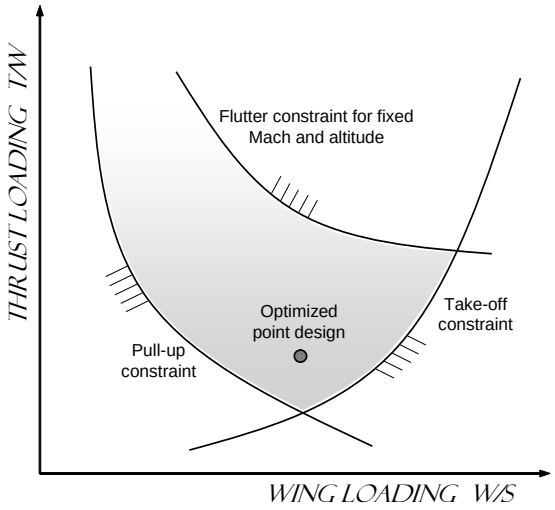

Figure 4.2: The conceptual design space
Based on Figure 46 by DeBaets [44]

Thrust and wing loading are scalable parameters that allow an invaluable comparison of different aircraft. They affect basic performance criteria and reflect the requirements that drive the design process. *"If the chosen suite of design constraints is incomplete, incorrect, or poorly analyzed, the apparent best aircraft may not in fact be usable, or a better aircraft may be missed"* [153]. Figure 4.2 illustrates how the addition of the notional flutter constraint affects potential design solutions by further confining the design space.

A conducive visualization to the structural optimization expert is the V-n diagram. It depicts the aircraft maneuver loads by plotting the limit load factor as function of airspeed. The addition of the notional flutter constraint in Figure 4.3 shows that this particular configuration is not adversely affected as the dive speed V_{max} takes effect prior to the critical flutter speed. Limit load is equivalent to plastic deformation, while ultimate load denotes structural failure. The crossing point of limit load and dive speed in the upper right corner of the V-n diagram is crucial to structural sizing. It represents the combination of maximum dynamic pressure and maximum load factor, which the aircraft is designed to withstand.

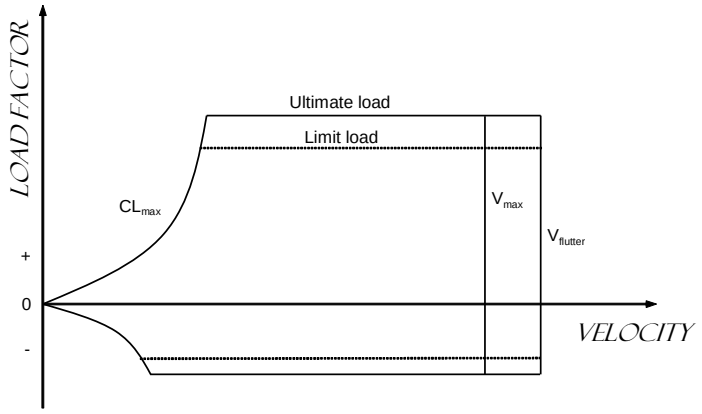

Figure 4.3: The V-n diagram

Another comprehensive means of visualization is found in the flight envelope. Flight conditions can be evaluated in dependency of altitude and Mach number. Plotting the flutter constraint to the flight envelope typically reveals increased flutter susceptibility for low altitudes and transonic flows [82].

4.3 Scope of Work

Past design efforts show one commonality. Respective implementations strive for a comprehensive MDO environment by utilizing a combination of existing high and moderate fidelity analysis codes. Each code represents a modular building block spawned by a disciplinary system decomposition. The design environment is completed by a system level optimizer that coordinates disciplinary metrics and ensures satisfaction of objectives and constraints.

The present research departs from the creation of an all-embracing MDO environment. It abandons the idea of an optimizer wrapped around an assortment of disciplinary analysis codes. Instead, it goes beyond a black box employment of analysis tools by merging the formerly distinctively separated disciplines of analysis and optimization.

The idea of using perturbations in structural design is not a new one. A brief tribute paid to past perturbation based design efforts will precede the reasoning behind and the application of the present research effort. Some of the perturbation methods have already been introduced in the review of past research efforts but shall be repeated here in favor of a self contained brief history of perturbation methods in structural design.

4.3.1 Perturbation Methods in Structural Design

Stetson was the first to present the mathematical basis of first order perturbation theory. His motivation was derived from the inverse problem of structural design for stiffness and mass properties resulting in a set of desired eigen characteristics [180, 181]. Sandstrom manipulated the first order equations for greatly improved transparency and substantial computational savings [157, 158].

Kim et al. extended the method for the inclusion of all nonlinear terms by introducing an optimization penalty for residual forces [101]. Hoff et al. realized the structural redesign using nonlinear perturbation equations by means of a predictor corrector technique [85, 87].

Bernitsas et al. further extended the method for modal and static displacement constraints based on the idea of large admissible perturbations [20, 23]. The method of large admissible perturbations was further refined to account for forced response, proportional damping, and static stresses [19, 21]. It was also applied to the redesign of plates [22].

Gans and Anderson incorporated centrifugal and coriolis effects. The nonlinear perturbation scheme was applied to two rotating beams with satisfactory results [68].

4.3.2 Present Perturbation Based Design Effort

Conceptual design is concerned with finding the basic configuration arrangement. It performs numerous trade studies using initial estimates of size, weight, and performance parameters.

The conceptual sizing effort is dominated by aerodynamic efficiency considerations in terms of the lift to drag ratio (L/D) that in turn strongly depends on the configuration arrangement. Key drivers of the wing geometry are wing span and total surface area. The former indicates the induced portion of drag related to lift generation. The latter indicates the parasite portion of drag caused mainly by skin friction [152].

The traditional measure of total wing efficiency is the aspect ratio. The geometry of the conceptual baseline is thus driven by L/D and aspect ratio. Once the conceptual baseline enters the preliminary phase of design there is no more room for major changes. Engineers from all contributing disciplines begin their analysis and design work on the basic configuration arrangement given to them.

The vehicle class of interest to the present study features unconventional configurations able to comply with operational needs created by contemporary concerns in atmospheric science and homeland security. Potential mission reach from storm tracking to surveillance and require long endurance flight at moderate to high altitudes. Structural and aerodynamic requirements necessitate light weight materials and high aspect ratio wings. Traditional conceptual analysis tools become obsolete and inadequate and can result in the violation of constraint lines associated with aeroelastic instabilities (Figure 4.2).

Recall that the rectification of design flaws becomes increasingly difficult and expensive when moving down on the design time line. However, the initial design of a wing commonly experiences a flutter problem due to the lack of aeroelastic studies at the conceptual stage [112, 161]. Unconventional configurations are particularly and adversely affected by the lack of corresponding experience and data. The tailless aircraft was introduced earlier as a precedent of unconventional aviation. Many carefully thought out tailless gliders faced aeroelastic instabilities in first flight tests necessitating extensive redesign, a complete design overhaul, or the discontinuation of the project [165]. Note that the redesign of a sailplane that belongs to a standard competition class faces additional restrictions as the wing planform provides very limited room for changes [9].

Scope of the Present Work is the development of an optimization algorithm that allows the effective redesign of a conceptual baseline or existing prototype with stability problems as determined by preliminary analyses or first flight tests, respectively. The corresponding design methodology enables the optimization of high aspect ratio wings when there is little or no room to change the driving planform parameters such as aspect ratio, wing chord, and taper ratio. It provides an efficient and accurate way to find a solution for a stability problem that can be specified in terms of natural frequency objectives.

Recall that the current work is solely concerned with the optimization of the wing. On one hand, the methodology under development is new and the restriction to the wing represents a simplification necessary for a fundamental feasibility study. On the other hand, the aircraft wing is a key element for overall vehicle performance and structural integrity. Chapter 2 showcased the particular prominence of high aspect ratio wings to the vehicle class of interest.

4.4 Notional Methodology

This section presents a notional introduction of the proposed optimization algorithm. It is based on the research objective and provides a visualization of the stated goal. The preliminary description in Figure 4.4 presents a two level analysis, two level design methodology.

The incentive for multi level optimization stems from potentially enormous computational savings. These savings are enabled by a split of the design variables that are fewer in number at the global level than they are at the local level [66, 194].

Independent input and design variables of the local level are the physical parameters that describe geometry and material of the cross sections along the span. Output variables are local stiffness coefficients and mass properties. They serve as the design variables of the response analysis at the global level.

The baseline structure is the reference design of the optimization. It is analyzed, and the results are used as starting point for the global optimization. Once global objective

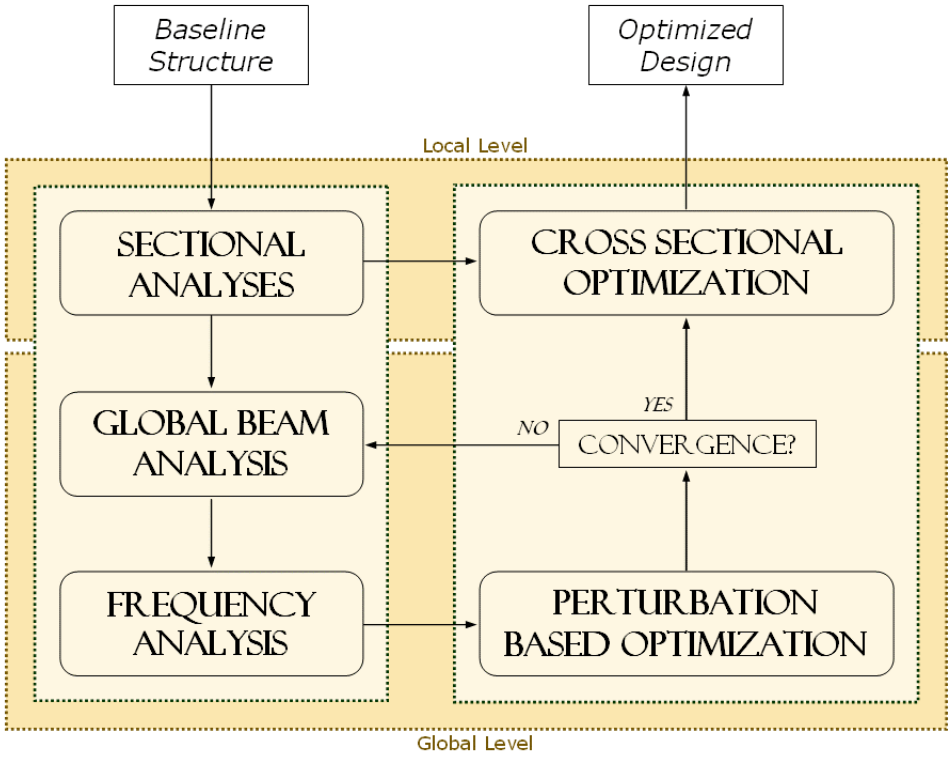

Figure 4.4: Notional design methodology

and constraints are satisfied, a local optimization is performed to find the cross sectional geometry that results in the stiffness and mass properties obtained by the global optimizer.

4.4.1 Global Level Optimization

Global analyses and optimization begin after initial analyses at the local level are completed. The global beam analysis determines the discrete stiffness and mass matrices of the wing model along with natural modes and frequencies. A subsequent frequency analysis identifies critical modes, upon which frequency objectives can be determined. The consequent solution of the small perturbation equation provides local stiffness and mass property changes that result in the specified frequency objective.

Inverse Perturbation Redesign is based on the assumption of small changes. The global optimizer thus applies small incremental changes to the specified frequencies until both optimization objective and constraints are satisfied. Figure 4.5 illustrates this incremental approach. The repetition of global analyses is terminated upon convergence. Cross sectional

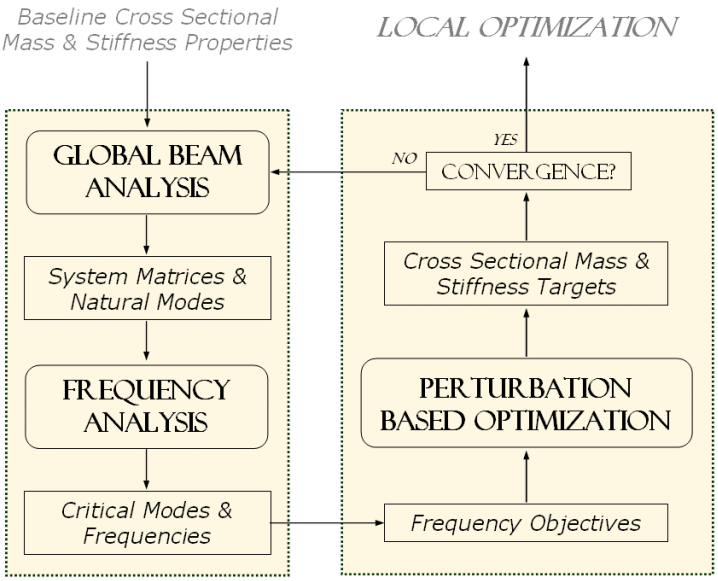

Figure 4.5: Notional global level

stiffness and mass properties from the last increment correspond to the optimal settings that are passed to the local level optimizer.

4.4.2 Local Level Optimization

Once the global optimizer has found the optimum values for the global design variables, the local optimizer is faced with the challenge of finding the physical parameters that correspond to the cross sectional properties.

Figure 4.6 shows that the initial analyses at the local level provide a set of surrogate models. Surrogate models of cross sectional properties were introduced by Ku et al. as inter level communicator to ensure that the global optimization remains within the feasible domain of the physical design space [109, 108]. The surrogates encapsulate the relationship between cross sectional beam properties and physical design variables. The local optimizer thus has at its disposal almost instantaneous functional responses. Objective of the optimization is a minimum discrepancy between the desired equivalent beam properties and the ones *producable* by a specific set of physical input variables.

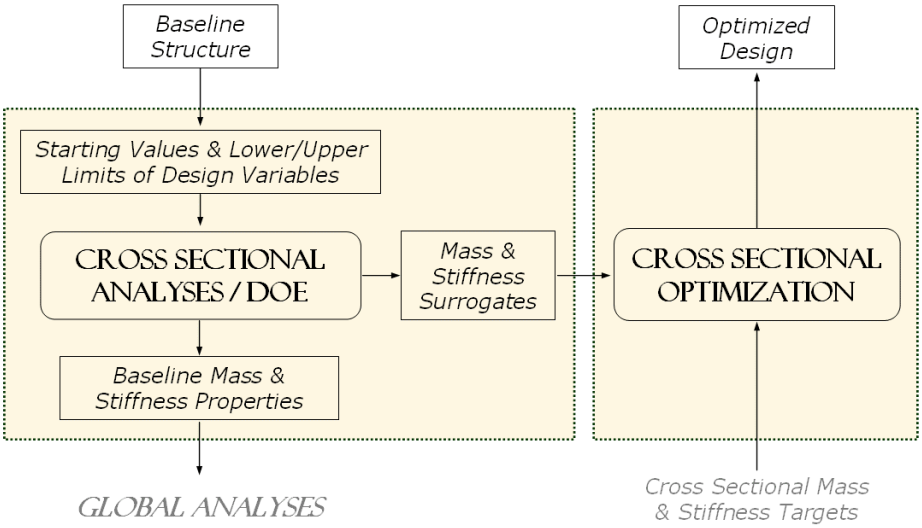

Figure 4.6: Notional local level

4.5 Research Questions

The successful composition of the proposed methodology affords a set of very specific research questions. Answers will be given in terms of hypotheses that will be revisited upon availability of implementation results.

> **Research Question 1** Can the theory of beam dimensional reduction be made an integral part of inverse perturbation redesign?

Inverse perturbation redesign introduces small perturbations to the equations of motion. After cancellation of all higher order terms, a linear system of equations relates structural changes on one side to modal changes on the other side. Structural changes are defined as linear deviations by means of multipliers to the baseline stiffness and mass matrices.

Stiffness and mass matrices are the discrete representation of structural properties. These matrices stem from a finite element discretization of the continuous system within the Finite Element Methodology. The global problem is reconstructed by assembling elemental matrices into system matrices according to corresponding degrees of freedom.

Beam dimensional reduction decomposes the three-dimensional beam into a two-dimensional problem of the cross section and a one-dimensional problem of the global beam. The linear analysis of the cross section provides local properties in terms of stiffness effects and mass that are used in the global assemblage of system matrices. The linear summation of individual contributions leads to the following hypothesis.

> **Hypothesis 1** Structural changes in the small perturbation equation can be expressed as a linear combination of local mass and stiffness effects in accordance with the cross sectional model of the dimensionally reduced beam.

As before, each individual change constitutes a fractional change from respective baselines values, and the first order perturbation equation is solved for the structural changes that correspond to a specified modal objective.

> **Research Question 2** Can the incremental solution of the first order perturbation equation guide the optimizer to a local optimum?

The first order perturbation equation is derived from the governing equations of motion. The cancellation of higher order terms in this derivation gives rise to a negligible error that should not affect the validity of the equation as long as the underlying assumption of small perturbations is not violated. An accumulation of the aforementioned error is avoided by performing a reanalysis at the beginning of each increment.

> **Hypothesis 2** The solution of the small perturbation equation adheres to the governing equations of motion. Defining the modal objectives on the right hand side according to overall design goals will dictate magnitude and direction of resulting structural changes.

The objective of this research was stated as the development of an optimization approach for high aspect ratio wings subject to natural frequency constraints. These constraints are the modal objectives of the small perturbation equation mentioned above.

> **Research Question 3** Can the incremental application of a small perturbation solution yield computational savings compared to a gradient based optimization?

The solution of the small perturbation equation can be unique, overdetermined, or underdetermined; requiring a linear solver, a minimum error, or an optimization routine, respectively. Regardless of the nature of the linear system of equations, the solution procedure only deals with algebraic equations as opposed to FEA that are necessary to find the change in the system response due to the isolated change of each individual design variable.

> **Hypothesis 3** Solving the small perturbation equation is faster than finding FEA based gradients because it requires the execution of algebraic equations with virtually instantaneous responses.

The above considerations assume that an increment of the envisioned algorithm is equivalent to an iteration of a traditional optimization approach. Note that the underdetermined case of the small perturbation equation is most suitable for the present study because it entails the specification of an optimization criterion that can be used to further specify the overall design goal.

Chapter V

PRELIMINARY DEVELOPMENT

Foundational corner stones of the search algorithm under development are beam dimensional reduction and small perturbation theory. This chapter performs a preliminary feasibility investigation. Starting point is the simulation of the recurring simple bending beam. A series of subsequent testcases will focus on the implementation of mass and stiffness changes as well as the specification of frequency objectives.

5.1 Beam Model Refinement

IPR as put forward by application examples in pertaining literature is limited to proportional stiffness changes applied to classic bending beams. Upcoming challenges are the extension to the Timoshenko beam model, and the comprehensive consideration of both mass and stiffness characteristics. Prerequisites of the successful implementation of the new Timoshenko refined IPR (TIPR) scheme are the dissection of the discrete global representation and an appropriate stiffness effect separation.

5.1.1 Classic Bending Beam

The cantilever beam in Figure 5.1 was used by Sandstrom and Anderson to illustrate the application details and accuracy of IPR [158]. The model consists of two beam elements with $E = 1.0$, $I_1 = 1.0$, and $I_2 = 1.6$. Two lumped masses with $m_1 = 0.5$ and $m_2 = 0.25$ are located at $x = 0.5$ and $x = 1.0$, respectively.

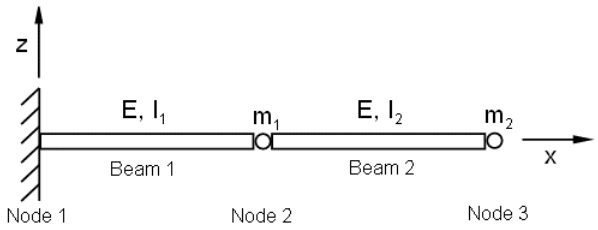

Figure 5.1: Cantilever bending beam

The beam is allowed to undergo pure lateral bending, only. The nodal degrees of freedom are thus restricted to deflection and rotation within the xz-plane. Beam element stiffness matrices (Figure 5.1) are obtained with a displacement based Finite Element Method using cubic shape functions. The system stiffness matrix is then derived by direct summation of the elemental matrices using the Direct Stiffness Method.

$$k_e = \frac{EI}{L^3} \begin{bmatrix} 12 & 6L & -12 & 6L \\ & 4L^2 & -6L & 2L^2 \\ & & 12 & -6L \\ sym & & & 4L^2 \end{bmatrix}$$

Starting point of the illustration is the *exact* analysis of two structures, the baseline above and a modified structure with $I_1 = 0.9$. The results of these two *exact* analyses will serve as IPR input and validation data. Note that *exact* refers to an FEA based on the aforementioned assumptions.

Table 5.1: Cantilever beam analysis results

	Baseline Structure				Modified Structure			
	Sandstrom		DYMORE		Sandstrom		DYMORE	
	Mode 1	Mode 2	Mode 1	Mode 2	Mode 1	Mode 2	Mode 1	Mode 2
Frequency, rad/sec	3.208	18.047	3.208	18.047	3.051	17.477	3.051	17.477
Node 1 deflection	0	0	0	0	0	0	0	0
Node 1 rotation	0	0	0	0	0	0	0	0
Node 2 deflection	0.6144	-1.2738	0.6144	-1.2738	0.6178	-1.2721	0.6178	-1.2721
Node 2 rotation	2.1327	0.6005	2.1327	0.6004	2.1443	0.8168	2.1443	0.8168
Node 3 deflection	1.8014	0.8689	1.8014	0.8689	1.7990	0.8738	1.7990	0.8737
Node 3 rotation	2.4947	6.1279	2.4947	6.1277	2.4715	6.0292	2.4715	6.0292

Rotations of modified structure not published by Sandstrom and Anderson [158] and thus reproduced; DYMORE results based on quadratic finite elements

The baseline is fully known in terms of its structural and vibrational characteristics. The modified structure represents the unknown objective of the redesign process. The analysis results in Table 5.1 are used to determine the modal objectives. The goal is to apply IPR to the baseline and to find the structural changes that will result in the modal characteristics of the modified structure.

The development of the IPR equation is documented in Appendix C. For the present example, the modal objectives are limited to the frequency and the tip displacement of the first natural mode. Furthermore, structural changes are limited to changes in the moment of inertia I. Thus, the IPR equation (Equation C.14) for the problem at hand simplifies to a well posed system of two linear equations.

$$\begin{bmatrix} P_{11} & P_{12} \\ P_{21} & P_{22} \end{bmatrix} \begin{Bmatrix} \alpha_1 \\ \alpha_2 \end{Bmatrix} = \begin{Bmatrix} \triangle\omega_1^2 \\ \Delta\psi_{1,Tip} \end{Bmatrix} \tag{5.1}$$

$$\triangle\omega_1^2 = \hat{\omega}_1^2 - \omega_1^2$$

$$\Delta\psi_{1,Tip} = \hat{\psi}_{1,Tip} - \psi_{1,Tip}$$

$$P_{11} = \{\psi_{1,Beam1}\}^T [k_{Beam1}] \{\psi_{1,Beam1}\}$$

$$P_{12} = \{\psi_{1,Beam2}\}^T [k_{Beam2}] \{\psi_{1,Beam2}\}$$

$$P_{21} = \frac{\psi_{2,Tip}}{\omega_1^2 - \omega_2^2} \cdot \{\psi_{2,Beam1}\}^T [k_{Beam1}] \{\psi_{1,Beam1}\}$$

$$P_{22} = \frac{\psi_{2,Tip}}{\omega_1^2 - \omega_2^2} \cdot \{\psi_{2,Beam2}\}^T [k_{Beam2}] \{\psi_{1,Beam2}\}$$

Recall that the right hand side of Equation 5.2 identifies the desired modal properties of the objective system, and that the perturbation coefficients on the left hand side depend solely on the known baseline characteristics (Table 5.1). Mode shapes are normalized for unit generalized mass.

Equation 5.1 is solved for α_1 and α_2. These two unknowns are representative for the necessary change in the bending stiffness of Beam 1 and Beam 2, respectively. Based on Equations 3.8 and 3.12, stiffness matrices and moments of inertia of the objective structure can now be evaluated.

$$\hat{k_e} = k_e + \Delta k_e = k_e(1 + \alpha_e), \qquad e = 1, 2 \tag{5.2}$$

$$\hat{I_e} = I_e + \Delta I_e = I_e(1 + \alpha_e), \qquad e = 1, 2 \tag{5.3}$$

The results on the left hand side in Table 5.2 confirm that the IPR results for the projected 10 percent change in bending stiffness closely match the exact values. The error margin is smaller than one percent.

Table 5.2: Cantilever beam IPR results

	Sandstrom	DYMORE		
	Ref. [158]	Linear	Quadratic	Cubic
$\Delta\omega_1^2$	-0.9827	-1.0660	-0.9784	-0.9784
$\Delta\psi_{1,Tip}$	-0.0024	-0.0017	-0.0024	-0.0024
α_1	-0.1009	-0.1005	-0.1006	-0.1006
α_2	-0.0009	0.0001	0.0002	0.0002
I_1	0.90	0.90	0.90	0.90
I_2	1.60	1.60	1.60	1.60

5.1.2 Timoshenko Beam

The Euler-Bernoulli beam in Figure 5.1 exclusively accounts for bending moment effects and only requires the specification the bending stiffness EI. The discrete representation falls back on beam elements that are comprised of two nodes, resulting in a total of 4 elemental degrees of freedom.

Modern aircraft are made of composite materials that constitute up to 70 percent of the airframe weight [6]. The simple isotropic beam model for the wing no longer suffices because composite materials require the consideration of all possible deformations [202].

The generalized Timoshenko beam accounts for extension, shear, torsion, and bending effects. The corresponding constitutive relation is provided in Equation 5.4. The cross sectional stiffness properties are expressed by means of 21 coefficients to fully populate a symmetric stiffness matrix that relates sectional strains and stress resultants.

$$\begin{Bmatrix} F_1 \\ F_2 \\ F_3 \\ M_1 \\ M_2 \\ M_3 \end{Bmatrix} = \begin{bmatrix} S_{11} & S_{12} & S_{13} & S_{14} & S_{15} & S_{16} \\ & S_{22} & S_{23} & S_{24} & S_{25} & S_{26} \\ & & S_{33} & S_{34} & S_{35} & S_{36} \\ & & & S_{44} & S_{45} & S_{46} \\ & sym & & & S_{55} & S_{56} \\ & & & & & S_{66} \end{bmatrix} \begin{Bmatrix} \varepsilon_1 \\ \gamma_{12} \\ \gamma_{13} \\ \kappa_1 \\ \kappa_2 \\ \kappa_3 \end{Bmatrix} \tag{5.4}$$

Diagonal coefficients for prismatic beams made of isotropic material are functions of the Young's modulus of elasticity E, the shear modulus G, the cross sectional area A, the torsion constant J, and two area moments of inertia I.

$$S_{11} = EA, \quad S_{22} = k_2 GA, \quad S_{33} = k_3 GA, \quad S_{44} = GJ, \quad S_{55} = EI_2, \quad S_{66} = EI_3$$

The structural analysis code used in the present work is DYMORE, a finite element based analysis tool for nonlinear elastic multibody systems. The beam representation in DYMORE uses the above generalized Timoshenko model for the cross section and an isoparametric finite element discretization. Element matrices stem from a weighted residual formulation and are evaluated using reduced Gaussian integration [13]. Number and order of finite elements determine the total number of nodes per beam. Each node has six degrees of freedom accounting for translation and rotation along the three body axes. Beam stiffness properties are specified in terms of the 21 coefficients.

5.1.3 Bending Beam Simulation

For the DYMORE analysis of the illustration example, only the fundamental stiffnesses are considered. Coupling is eliminated by setting all off-diagonal coefficients to zero. The stiffness coefficient $S_{55} = EI$ is set according to the values of $I_1 = 1.0$ and $I_2 = 1.6$. The remaining diagonal entries of the cross sectional stiffness matrix are virtually infinite to prevent respective motion. Table 5.1 shows analysis results in excellent agreement. It also suggests that linear finite elements show inferior analysis accuracy, and quadratic elements will be used from now on unless stated otherwise.

The application of IPR required additional considerations. The derivation of the DYMORE finite element matrices is shown by Bauchau [13]. For the implementation of the illustration example, each beam was discretized using a single finite element. The beam element stiffness matrices depend on the order of the finite element. The size of the resulting square matrices depends on the elemental number of degrees of freedom (Table 5.3).

Table 5.3: Finite element DOF

Order	Shape	N	DOF
1	Linear	2	12
2	Parabolic	3	18
3	Cubic	4	24

N - Number of beam element nodes

In order to reproduce the IPR results of the illustration example provided by Sandstrom, it is noted that the moment of inertia enters the global FEA through the stiffness term $S_{55} = EI$. However, S_{55} only enters the calculation of stiffness coefficients that are associated with the global lateral bending degree of freedom; and an exclusive impact of the bending stiffness EI on the entire stiffness matrix as in Figure 5.1 is nonfactual. For linear finite elements for example, S_{55} contributes to the calculation of four global stiffnesses.

$$k_{5,5} = \frac{L}{4} S_{33} + \frac{1}{L} S_{55} \tag{5.5}$$

$$k_{11,5} = \frac{L}{4} S_{33} - \frac{1}{L} S_{55} \tag{5.6}$$

$$k_{11,11} = \frac{L}{4} S_{33} + \frac{1}{L} S_{55} \tag{5.7}$$

The change in I is no longer uniformly propagated throughout the stiffness matrix. The previously assumed relationship $[\Delta k_e] = [k_e]\,\alpha_e$ is redundant. Global stiffness coefficients affected by I need to be regarded separately.

$$\hat{k}_e = k_e + \triangle k_e^I = k_e + \left[k_{e,ij}^I\right] \alpha_e \tag{5.8}$$

$$i, j = 6n - 1, \qquad n = 1, ..., N$$

The determination of bending specific global changes depends on the order of the shape function. For a linear element with three nodal points, the bending stiffness $EI = S_{55}$ influences the global stiffness matrix at four locations.

$$\triangle k_e^I = \Delta k_{5,5} + \triangle k_{5,11} + \Delta k_{11,5} + \Delta k_{11,11} \tag{5.9}$$

$$\Delta k_{5,5} = \frac{E}{L}\Delta I_e = \frac{EI_e}{L}\alpha_e$$

$$\Delta k_{11,5} = -\frac{E}{L}\Delta I_e = -\frac{EI_e}{L}\alpha_e$$

$$\Delta k_{11,11} = \frac{E}{L}\Delta I_e = \frac{EI_e}{L}\alpha_e$$

The individual stiffness changes in Equation 5.9 can now be developed. The example below illustrates the derivation of the change in the global stiffness coefficient $k_{5,5}$ associated with local changes in moment of inertia.

$$\hat{k}_{5,5} = k_{5,5} + \Delta k_{5,5} \tag{5.10}$$

$$\frac{L}{4}S_{33} + \frac{1}{L}\hat{S}_{55} = \frac{L}{4}S_{33} + \frac{1}{L}S_{55} + \Delta k_{5,5}$$

$$\Delta k_{5,5} = \frac{E}{L}\Delta I_e = \frac{EI_e}{L}\alpha_e$$

Equation 5.1 can now be solved for α_1 and α_2. Elemental stiffness matrices of the objective system are determined using Equation 5.8. Corresponding moments of inertia can be found using either Equation 5.3, or Equations 5.5 - 5.6. Table 5.2 shows respective results in excellent agreement.

5.1.4 Basic Stiffness Effect Separation

Stiffness properties of importance can be identified from Equation 5.4 as the cross sectional area A, the torsional moment of inertia J, and the two area moments of inertia I_{22} and I_{33}. To facilitate a performance investigation of the envisioned TIPR scheme with respect to

those four variables, the DYMORE finite element stiffness matrices were reproduced. Recall that the DYMORE discretization is based on isoparametric finite elements and reduced Gaussian integration. Elemental stiffness coefficients at the global level are a function of finite element length and contributing local stiffness coefficients. They furthermore depend on the order of the FE shape function.

The decomposition of the discrete system representation enabled the isolation of four sparse matrices that correspond to the impact of the individual stiffness property. This basic stiffness effect separation is expressed by Equations 5.11 and 5.12. Its application to the new TIPR scheme is demonstrated by Equations 5.13 - 5.15.

$$k = k_A + k_J + k_{I_{22}} + k_{I_{33}} \tag{5.11}$$

$$k_A = k_{S_{11}} + k_{S_{22}} + k_{S_{33}} \tag{5.12}$$

$$\hat{k} = k + \Delta k \tag{5.13}$$

$$\Delta k = \Delta k_A + \Delta k_J + \Delta k_{I_{22}} + \Delta k_{I_{33}} \tag{5.14}$$

$$\Delta k = k_A \alpha_A + k_J \alpha_J + k_{I_{22}} \alpha_{I_{22}} + k_{I_{33}} \alpha_{I_{33}} \tag{5.15}$$

5.2 Unique Solution

The testbeam for the following applicability studies is shown in Figure 5.2. It is a simple cross-ply beam that exhibits no coupling effects. Main diagonal stiffnesses are defined as follows.

$$S_{11} = 9e^5,\ S_{22} = 4e^4,\ S_{33} = 2e^4,\ S_{44} = 8e^3,\ S_{55} = 4e^4,\ S_{66} = 1e^5$$

The discrete global representation relies on two second order finite elements. The beam models a uniform wing. Both elements are assumed to have identical properties.

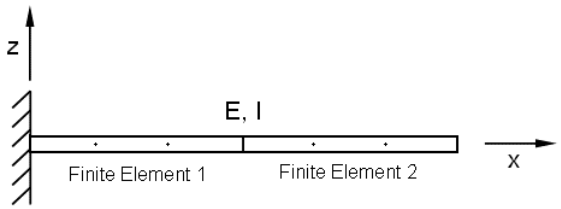

Figure 5.2: Cantilever Timoshenko beam
Beam model with parabolic finite elements and cross sectional stiffness without couplings

To assess the accuracy of the TIPR scheme, the baseline system is analyzed first. Upon application of a prescribed stiffness change α_{exact} to respective cross sectional coefficients, the system is analyzed again. From the second analysis one can identify a natural frequency change that will serve as TIPR objective. The TIPR equation is then solved for α. The accuracy of this result is measured by a relative percentage error.

$$\alpha_{error} = 100\% \cdot \frac{\alpha - \alpha_{exact}}{\alpha_{exact}} \tag{5.16}$$

Recall that classic IPR gives practical meaning to the structural changes $[\triangle k]$ and $[\triangle m]$ by decomposing the system change into σ element changes. The consideration of all finite elements results in a multitude of potential design variables. Conceptional design requires simple parametric geometries. For the following applicability studies it will be assumed that the baseline represents the spanwise mass and stiffness distribution. Changes in structural properties will have the same relative effect along the span. This assumption allows a minimum of design variables at the cost of limited design freedom.

5.2.1 Exclusive Stiffness Change

The TIPR scheme can now be applied to the baseline to find the stiffness change that will result in a specified frequency change. For a proportional global stiffness change, the system of perturbation equations simplifies to a single equation with a single unknown. Equations 5.17 - 5.21 represent the isolated impact of each of the four stiffness effects.

$$\{\psi_i\}^T [k_{I_{22}}] \{\psi_i\} \alpha_{I_{22}} = \triangle\omega_i^2 \tag{5.17}$$

$$\{\psi_i\}^T [k_{I_{33}}] \{\psi_i\} \alpha_{I_{33}} = \triangle\omega_i^2 \tag{5.18}$$

$$\{\psi_i\}^T [k_J] \{\psi_i\} \alpha_J = \triangle\omega_i^2 \tag{5.19}$$

$$\{\psi_i\}^T [k_A] \{\psi_i\} \alpha_A = \triangle\omega_i^2 \tag{5.20}$$

$$\triangle\omega_i^2 = \hat{\omega}_i^2 - \omega_i^2 \tag{5.21}$$

Table 5.4 shows the TIPR results for a stiffness reduction of 10 percent. It is evident that the mode choice in the TIPR solution for the stiffness change is important. The first four modes are bending modes. Inherently, a change in the torsional moment of inertia J will not have any affect.

Recall that a second FE analysis was performed prior to finding the TIPR solution only to find the exact values of corresponding stiffness and frequency perturbations. TIPR itself requires no additional FEA. That is, Equations 5.17 - 5.20 are solved for the unknown α using natural modes and frequencies of the known baseline. For a combined change in I_{22}, I_{33}, and J using modes 1, 2, and 3, the perturbation Equation 5.22 is composed as linear system of equations with results shown in Table 5.5.

$$\begin{bmatrix} \psi_1^T k_{I_{22}} \psi_1 & \psi_1^T k_{I_{33}} \psi_1 & \psi_1^T k_J \psi_1 \\ \psi_2^T k_{I_{22}} \psi_2 & \psi_2^T k_{I_{33}} \psi_2 & \psi_2^T k_J \psi_2 \\ \psi_3^T k_{I_{22}} \psi_3 & \psi_3^T k_{I_{33}} \psi_3 & \psi_3^T k_J \psi_3 \end{bmatrix} \begin{Bmatrix} \alpha_{I_{22}} \\ \alpha_{I_{33}} \\ \alpha_J \end{Bmatrix} = \begin{Bmatrix} \triangle\omega_1 \\ \triangle\omega_2 \\ \triangle\omega_3 \end{Bmatrix} \tag{5.22}$$

In summary, the successful application of stiffness effect separation to the perturbation equations relies on the correct allocation of cross sectional stiffnesses and natural modes. A stiffness effect paired with a mode that it has no impact on will result in a zero perturbation coefficient and no solution can be found. In turn, the purer the mode in terms of the corresponding stiffness effects, the better the solution.

Table 5.4: TIPR results for isolated stiffness changes

Mode	$\triangle\omega_i$	$\psi_i^T k_\alpha \psi_i$	α	Error, %
I_{22}				
1	-0.7070	7.06317	-0.1001	0.10
2	0	0	nan	n/a
3	-27.753	275.485	-0.1007	0.74
4	0	0	nan	n/a
5	0	0	nan	n/a
I_{33}				
1	0	0	nan	n/a
2	-1.7584	17.5613	-0.1001	0.13
3	0	0	nan	n/a
4	-66.859	662.552	-0.1009	0.91
5	0	0	nan	n/a
J				
1	0	0	nan	n/a
2	0	0	nan	n/a
3	0	0	nan	n/a
4	0	0	nan	n/a
5	-156.82	1568.20	-0.1000	0
A				
1	-0.0081	0.07336	-0.1110	11.0
2	-0.0253	0.22792	-0.1110	11.0
5	0	0	nan	n/a
7	-294.59	2738.79	-0.1076	7.56
9	-2905.8	29057.9	-0.1000	0

5.2.2 Exclusive Mass Change

Preventive measures for clearing a wing from flutter for example not only rely on adjusting the stiffness properties, but also on optimizing the mass distribution [25]. Distributive mass optimization can be performed on a local as well as on a global level. An example of cross sectional mass optimization is moving the center of gravity closer to the center of twist to decrease the coupling between bending and torsion. Examples of global mass optimization are nacelle location along the wing or tip mass placement on rotor blades. For the conceptual designer, the vehicle gross weight is of outmost importance, and conceptual synthesis and sizing operates under the objective of a minimum gross weight.

Finite element mass matrices are a function of mass and mass moments of inertia per unit span. Due to proportionality, a single multiplier suffices in representing mass changes.

Table 5.5: TIPR results for combined stiffness changes

	α	Error, %
Modes 1, 2, 3		
I_{22}	-0.1001	0.07
I_{33}	-0.0500	0.05
J	nan	n/a
Modes 1, 2, 5		
I_{22}	-0.1001	0.10
I_{33}	-0.0500	0.06
J	-0.1500	0.00

	α	Error, %
Modes 1, 2, 3		
I_{22}	-0.1001	0.07
I_{33}	-0.0500	0.05
J	nan	n/a
Modes 1, 2, 5		
I_{22}	-0.1001	0.10
I_{33}	-0.0500	0.06
J	0.0500	0.00

Left: 10% reduction in I_{22}, 5% reduction in I_{33}, and 15% reduction in J

Right: 10% reduction in I_{22}, 5% reduction in I_{33}, and 5% increase in J

$$\triangle m = [m]\,\alpha_m \tag{5.23}$$

$$-\omega_i^2 \{\psi_i\}^T [m] \{\psi_i\} \alpha_m = \triangle\omega_i^2 \tag{5.24}$$

The accuracy illustration uses the same beam that was used for the stiffness demonstration. After the baseline analysis, the mass properties were reduced by 10 percent, and the new system analyzed to provide the frequency change that will serve as redesign objective. Table 5.6 shows somewhat unsatisfactory results, but confirms a performance independence from the natural mode utilized in the IPR equation.

Table 5.6: TIPR results for isolated mass change

			Linear IPR		Nonlinear IPR	
Mode	$\triangle\omega_i$	$-\omega_i^2\psi_i^T m\psi_i$	α	Error, %	α	Error, %
1	0.7929	-7.1365	-0.1111	11.11	-0.1000	0.00
2	1.9766	-17.789	-0.1111	11.11	-0.1000	0.00
3	33.045	-297.41	-0.1111	11.11	-0.1000	0.00

Nonlinear IPR: Linear first order IPR w/ second order term $\triangle\omega^2\phi^T\triangle m\phi$

Recall the derivation of the general first order perturbation equation via cancellation of all higher order terms. If one were to keep the second order term including $\triangle\omega^2$ and $\triangle m$, the perturbation Equation 5.24 would become nonlinear in the desired frequency change. Also recall that the elements of the testbeam are assumed to undergo identical change, allowing Equation 5.25 to be simplified by taking advantage of the mode shape normalization.

$$-\omega_i^2 \{\psi_i\}^T [m] \{\psi_i\} \alpha_m = \triangle\omega_i^2 + \triangle\omega_i^2 \{\psi_i\}^T [m] \{\psi_i\} \alpha_m \tag{5.25}$$

$$-\left(\omega_i^2 + \triangle\omega_i^2\right) \alpha_m = \triangle\omega_i^2 \tag{5.26}$$

The solution of Equation 5.26 will generate an α identical to the exact value, which can be explained by manipulating the uncoupled equations of motion of the objective system. Given that only the system mass matrix is subject to change, an explicit expression for α can be derived. Manipulation of Equation 5.26 will lead to the same expression.

$$K = \hat{M}\hat{\omega}^2 = M\left(1 + \alpha\right)\hat{\omega}^2 \tag{5.27}$$

$$\omega^2 = \hat{\omega}^2(1 + \alpha) \tag{5.28}$$

$$\alpha = \frac{\omega^2}{\hat{\omega}^2} - 1 \tag{5.29}$$

In summary, mass changes impact all natural modes. The solution of the perturbation equations representing an exclusive mass change are independent of the allocated mode shape. Respective perturbation coefficients evaluate to the negative product of unit generalized mass and the square of the natural frequency of the baseline system. For exclusive and uniform changes in system mass, an exact solution to the perturbation equation can be found. This exact solution is arrived at when deriving the first order perturbation equation and retaining the second order term $\triangle\omega^2\phi^T\triangle m\phi$.

5.2.3 Combined Mass and Stiffness Change

The cross sectional optimization of stiffness and mass is generally bound by a dependent relationship that accounts for a simultaneous change in both properties. However, local stiffness and mass optimization can also fall back on finding the material best suited for a given area and/or shape resulting in the decoupling of mass and stiffness properties.

5.2.3.1 Dependent Mass and Stiffness Changes

Equations 5.30 state the general relationships for the area moments of inertia with respect to the center of mass. Since area and density amount to mass per unit span, a stiffness increase for a cross section of the same material will always also result in a mass increase.

$$I_{22} = I_y = \int_A z^2 dA, \quad I_{33} = I_z = \int_A y^2 dA, \quad I_{23} = I_{yz} = \int_A yz dA \tag{5.30}$$

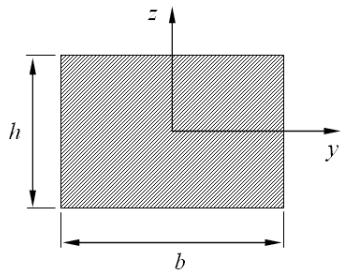

Figure 5.3: Solid rectangular cross section

Consider the example of the solid rectangle in Figure 5.3. Changing the height of this rectangular cross section will result in an identical relative change in both mass per unit span and moment of inertia. Changing the base of the same rectangle, however, will result in a stiffness change that is cubic to that of the involved mass change. For instance, reducing the base by 10% will reduce area and mass by 10%, and area moment of inertia by 27.1%.

$$I_{22} = \frac{hb^3}{12}, \qquad A = hb, \qquad m = \rho A \tag{5.31}$$

$$I_{22} = \frac{hb^3}{12}, \qquad \hat{I}_{22} = \frac{h\,(0.9b)^3}{12} \tag{5.32}$$

$$\hat{I}_{22} = I_{22}(1 + \alpha_{I_{22}}), \qquad \alpha_{I_{22}} = 0.9^3 - 1 \tag{5.33}$$

$$\alpha_A = -0.1, \qquad \alpha_{I_{22}} = -0.271 \tag{5.34}$$

Above considerations are tested using a linear system of corresponding first order perturbation equations. Equation 5.35 shows the implemented separation of related effects.

That is, $\alpha_{I_{22}}$ is used to represent the change in bending stiffness; and α_A is used to represent both mass and stiffness changes. The latter involves changes in the first three diagonals of the cross sectional stiffness matrix (Equation 5.36). The indices i and j denote the natural modes used in the formulation of the linear system of perturbation equations. Equation 5.37 shows the perturbation coefficients corresponding to the first three natural modes.

$$\begin{bmatrix} \psi_i^T k_{I_{22}} \psi_i & \psi_i^T k_A \psi_i - \omega_i^2 \psi_i^T m \psi_i \\ \psi_j^T k_{I_{22}} \psi_j & \psi_j^T k_A \psi_j - \omega_j^2 \psi_j^T m \psi_j \end{bmatrix} \begin{Bmatrix} \alpha_{I_{22}} \\ \alpha_A \end{Bmatrix} = \begin{Bmatrix} \triangle\omega_i^2 \\ \triangle\omega_j^2 \end{Bmatrix} \tag{5.35}$$

$$\Delta k_A = k_A \alpha_A = (k_{S_{11}} + k_{S_{22}} + k_{S_{33}})\alpha_A \tag{5.36}$$

$$\psi_1^T k_{I_{22}} \psi_1 = 7.0632, \quad \psi_1^T k_A \psi_1 - \omega_1^2 \psi_1^T m \psi_1 = -7.0632, \quad \Delta\omega_1^2 = -1.3446 \tag{5.37}$$

$$\psi_2^T k_{I_{22}} \psi_2 = 0, \quad \psi_2^T k_A \psi_2 - \omega_2^2 \psi_2^T m \psi_2 = -17.561, \quad \Delta\omega_2^2 = 1.9485 \tag{5.38}$$

$$\psi_3^T k_{I_{22}} \psi_3 = 275.49, \quad \psi_3^T k_A \psi_3 - \omega_3^2 \psi_3^T m \psi_3 = -275.49, \quad \Delta\omega_2^2 = -53.086 \tag{5.39}$$

Composing Equation 5.35 using $i = 1$ and $j = 2$ has a rather unsatisfactory solution. Table 5.7 reveals the results of the corresponding linear system of perturbation equations. Utilizing the second order term including $\triangle\omega^2$ and $\triangle m$ as introduced previously shows significant improvement. Corresponding results feature negligible error. Table 5.8 compares corresponding values of the actual frequency objectives.

Table 5.7: TIPR results for dependent mass and stiffness change 1

		Linear IPR		Nonlinear IPR	
	α_{exact}	α	Error, %	α	Error, %
Modes 1 and 2					
I_{22}	-0.271	-0.3013	11.19	-0.2712	0.09
m, A	-0.1	-0.1110	10.95	-0.0999	-0.13
Modes 1 and 3					
I_{22}	-0.271	n/a	n/a	-1.000	269
m, A	-0.1	n/a	n/a	-1.000	900

Composing Equation 5.35 with modes 1 and 3 produces an ill-conditioned system of equations. The perturbation coefficients P_{11} and P_{12}, as well as P_{21} and P_{22} evaluate to

Table 5.8: Frequency results for dependent mass and stiffness change

		Linear IPR		Nonlinear IPR	
Frequency	Target	IPR	Error, %	IPR	Error, %
ω_1^2	5.7919	5.6208	-2.95	5.7893	-0.05
ω_2^2	19.738	19.977	1.21	19.735	-0.01

Percentage reduction: 10% in area and 27.1% in area moment of inertia

identical magnitude of opposite sign. The determinant of the coefficient matrix is zero because of the linearly dependent columns in the coefficient matrix. Combined with the non-zero frequency objectives on the right hand side, a solution for this particular problem is nonexistent.

The singular coefficient matrix can be explained when decomposing the generalized stiffness matrix into its main diagonal stiffness effects at the local level. This decomposition is expressed by Equation 5.40. The resulting six generalized stiffness effects reflect the relative impact of the local stiffness properties associated with S_{ii} on the j^{th} global mode.

$$K_j = \sum_{i=1}^{6} K_{ii} = \sum_{i=1}^{6} \{\psi_j\}^T [k_{S_{ii}}] \{\psi_j\} \tag{5.40}$$

Table 5.9 shows the generalized stiffness effect separation for the test beam in Figure 5.2. It is evident that modes 1 and 3 are bending modes composed completely and solely of local level stiffness contributions from A and I_{22}. The perturbation coefficients thus represent the uncoupled equations of motion. The coefficient associated with the stiffness change is equal and opposite in sign to the coefficient associated with the mass change. Combined with the non-zero frequency objectives on the right hand side, no solution can be found for this particular problem.

Utilizing modes 1 and 3 in the newly devised nonlinear perturbation equations will add to the second column of the coefficient matrix. The unit generalized mass normalization will result in this addition being identical to the corresponding frequency objectives on the right hand side. The solution evaluates to negative unity and is of no use.

Equations 5.35 - 5.39 are now used to capture a uniform ten percent reduction in A and I_{22} by simply adjusting the frequency objectives as given by Equations 5.41 - 5.43.

Table 5.9: Generalized stiffness effect separation

Effect	S_{ii}	Mode 1	Mode 2	Mode 3	Mode 4	Mode 5
Extension	S_{11}	0	0	0	0	0
Shear	S_{22}	0	0.2279	0	65.712	0
Shear	S_{33}	0.0734	0	21.923	0	0
Torsion	S_{44}	0	0	0	0	1568.2
Bending	S_{55}	7.0632	0	275.49	0	0
Bending	S_{66}	0	17.561	0	662.55	0
Total	ω_j^2	7.1365	17.789	297.41	728.26	1568.2

$$\psi_1^T k_{I_{22}} \psi_1 = 7.0632, \quad \psi_1^T k_A \psi_1 - \omega_1^2 \psi_1^T m \psi_1 = -7.0632, \quad \Delta\omega_1^2 = 0 \tag{5.41}$$

$$\psi_2^T k_{I_{22}} \psi_2 = 0, \quad \psi_2^T k_A \psi_2 - \omega_2^2 \psi_2^T m \psi_2 = -17.561, \quad \Delta\omega_2^2 = 1.9485 \tag{5.42}$$

$$\psi_3^T k_{I_{22}} \psi_3 = 275.49, \quad \psi_3^T k_A \psi_3 - \omega_3^2 \psi_3^T m \psi_3 = -275.49, \quad \Delta\omega_3^2 = 0 \tag{5.43}$$

Table 5.10 confirms a significant improvement when using modes 1 and 2 in combination with the nonlinear perturbation equations. Corresponding results feature negligible error. Using modes 1 and 3 results in zero frequency objectives because both modes are completely described by the stiffness effects associated with A and I_{22}. This is a rather obvious and expected result. Given the uncoupled equations of motion, $K = \omega^2 M$, one can extract the generalized relationship for each mode (Equations 5.44 and 5.45). A mutual and uniform change in mass and stiffness matrices leaves the frequency unchanged.

$$K_i = \omega_i^2 M_i \tag{5.44}$$

$$K_i = \{\psi_i\}^T [k] \{\psi_i\}, \; M_i = \{\psi_i\}^T [m] \{\psi_i\} \tag{5.45}$$

A last study uses a linear system of three perturbation equations to solve for the combined change of A, J, and I_{22}. Table 5.11 summarizes the TIPR performance. The utilization of modes 1, 2, and 3 fails to produce a suitable result because the torsional moment of inertia has no effect on either mode. The perturbation coefficients associated with α_J evaluate to zero and no solution can be found.

Table 5.10: TIPR results for dependent mass and stiffness change 2

		Linear IPR		Nonlinear IPR	
	α_{exact}	α	Error, %	α	Error, %
Modes 1 and 2					
I_{22}	-0.1	-0.1110	10.95	-0.0999	-0.13
m, A	-0.1	-0.1110	10.95	-0.0999	-0.13
Modes 1 and 3					
I_{22}	-0.1	0	-100	0	-100
m, A	-0.1	0	-100	0	-100

Table 5.11: TIPR results for dependent mass and stiffness change 3

		Linear IPR		Nonlinear IPR	
	α_{exact}	α	Error, %	α	Error, %
Modes 1, 2, 3					
m, A	-0.10	-0.1110	10.95	-0.0999	-0.13
J	-0.05	n/a	n/a	n/a	n/a
I_{22}	-0.15	-0.1665	11.02	-0.1499	-0.07
Modes 1, 2, 5					
m, A	-0.10	-0.1110	10.95	-0.0999	-0.13
J	-0.05	-0.0554	10.79	-0.0499	-0.27
I_{22}	-0.15	-0.1665	11.03	-0.1499	-0.06

In summary, there exist any number of solutions in terms of multipliers α capable of changing mass and stiffness to obtain a specified frequency. The successful implementation of dependent mass and stiffness changes strongly depends on the modal choice. If all of the employed modes are fully described by the selected stiffness effects, then the perturbation coefficients mimic the uncoupled equations of motion. The columns of the coefficient matrix are linearly dependent, and the system of equations has no unique or no solution. At the same time, an equal relative change in system mass and stiffness will have no effect on the natural frequency of modes that are composed solely of the stiffness properties subject to change. Finally, if a stiffness effect lacks contribution to all of the modes used in the formulation of the perturbation equations, no solution can be found for this particular effect.

5.2.3.2 Independent Mass and Stiffness Changes

Table 5.12 contains materials that highlight how stiffness can be increased while mass is decreased. Two testcases of decoupled mass and stiffness changes will be presented.

Table 5.12: Tensile modulus and density

	E, GPa	ρ, g/cm^3	E/ρ
Steel	210	7.8	26.9
Aluminum 2024-T4	73	2.7	27.0
Aluminum 6061-T6	69	2.7	25.5
E-glass epoxy	22	1.97	10.9
Kevlar epoxy	40	1.40	29.0
Carbon fiber epoxy	83	1.54	53.5
Boron epoxy	106	2.00	53.0

Conventional materials and cross-ply fiber composites from Agarwal and Broutman [3]

Equation 5.46 shows the first order perturbation equation. The indices i and j denote the natural modes used in the formulation of the linear system of perturbation equations. Perturbation coefficients and frequency objectives correspond to a 10% reduction in both bending stiffness EI_{22} and system mass.

$$\begin{bmatrix} \psi_i^T k_{I_{22}} \psi_i & -\omega_i^2 \psi_i^T m \psi_i \\ \psi_j^T k_{I_{22}} \psi_j & -\omega_j^2 \psi_j^T m \psi_j \end{bmatrix} \begin{Bmatrix} \alpha_{I_{22}} \\ \alpha_m \end{Bmatrix} = \begin{Bmatrix} \triangle\omega_i^2 \\ \triangle\omega_j^2 \end{Bmatrix} \tag{5.46}$$

$$\psi_1^T k_{I_{22}} \psi_1 = 7.0632, \quad \omega_1^2 \psi_1^T m \psi_1 = 7.1365, \quad \Delta\omega_1^2 = 0.0073 \tag{5.47}$$

$$\psi_2^T k_{I_{22}} \psi_2 = 0.0000, \quad \omega_2^2 \psi_2^T m \psi_2 = 17.789, \quad \Delta\omega_2^2 = 1.9766 \tag{5.48}$$

$$\psi_3^T k_{I_{22}} \psi_3 = 275.49, \quad \omega_3^2 \psi_3^T m \psi_3 = 297.41, \quad \Delta\omega_3^2 = 2.2083 \tag{5.49}$$

Table 5.13 compares the results of linear and nonlinear perturbation redesign for uniform and non-uniform changes in mass and stiffness properties. The nonlinear extension produces improved results when posing the system of perturbation equations with modes 1 and 2. It results in an deterioration when utilizing modes 1 and 3. This observation is in full agreement with Equation 5.27 and previous deductions.

Table 5.14 provides a comparison of resulting natural frequencies using the linear perturbation equations with modes 1 and 3. It shows that the deterioration portrayed in Table 5.13 refers only to the anticipated structural change. Using the solution obtained from Equation

Table 5.13: TIPR results for independent mass and stiffness change

		Linear IPR		Nonlinear IPR	
	α_{exact}	α	Error, %	α	Error, %
Modes 1 and 2					
I_{22}	-0.1	-0.1112	11.23	-0.1001	0.10
m	-0.1	-0.1111	11.11	-0.1000	0.00
Modes 1 and 3					
I_{22}	-0.1	-0.1008	0.83	-0.0916	-8.40
m	-0.1	-0.1008	0.83	-0.0916	-8.41

		Linear IPR		Nonlinear IPR	
	α_{exact}	α	Error, %	α	Error, %
Modes 1 and 2					
I_{22}	-0.1	-0.0953	-4.66	-0.1001	0.10
m	0.05	0.0476	-4.76	0.0500	0.00
Modes 1 and 3					
I_{22}	-0.1	-0.0864	-13.57	-0.0916	-8.4
m	0.05	0.0564	12.87	0.0598	19.62

Top: Uniform mass and stiffness change; Bottom: Non-uniform change

Table 5.14: Frequency results for independent mass and stiffness change

Frequency	Target	IPR	Error, %
ω_1^2	7.1439	7.1439	0.00
ω_3^2	299.62	299.63	0.01

Frequency	Target	IPR	Error, %
ω_1^2	6.1233	6.1769	0.88
ω_3^2	256.81	258.84	0.79

Left: Uniform mass and stiffness change; Right: Non-uniform change

5.46, the baseline properties are changed accordingly, and the objective system is analyzed. The results show that the error in the frequency objectives remains within one percent.

In summary, the successful implementation of the nonlinear extension for combined mass and stiffness changes depends on the modal choice. Respective improvements are possible only if one of the equations in the system of perturbation equations utilizes a mode that is unaffected by the stiffness effects subject to change.

5.3 Frequency Shifting

IPR strives to determine structural changes that, applied to a given baseline, will result in a desired set of eigen modes. The modal objectives, however, can not be of arbitrary nature. Any structural change of the baseline system will not only modify a particular frequency or mode shape, but will shift the entire frequency spectrum. For illustration, the eigen problem

of baseline and objective system are reformulated below.

$$[k]\{\psi\} = \omega^2 [m]\{\psi\} \tag{5.50}$$

$$\left[\hat{k}\right]\left\{\hat{\psi}\right\} = \hat{\omega}^2 [\hat{m}]\left\{\hat{\psi}\right\} \tag{5.51}$$

Mass and stiffness matrices of the objective system are defined by Equations 3.7 and 3.8. The objective mode shapes, given by Equations 3.10 and 3.13, are further developed.

$$\left[\hat{\phi}\right] = [\phi]\left([I] + [C]^T\right) = [\phi]\begin{bmatrix} 1 & C_{21} & \cdots & C_{n1} \\ C_{12} & 1 & & \\ \vdots & & \ddots & \\ C_{1n} & & & 1 \end{bmatrix} \tag{5.52}$$

The mode shape associated with the jth natural frequency of the objective system can thus be expressed as a linear combination of the baseline modes.

$$\left\{\hat{\psi}_j\right\} = [\phi]\{c_j\} \tag{5.53}$$

$$\{c_j\} = [C_{ji}]^T, \qquad i = 1, ..., n, \quad i \neq j, \quad c_j = 1$$

For convenience of subsequent developments, let $\left\{\hat{\psi}\right\}$ denote any arbitrary eigen vector of the objective structure.

$$\left\{\hat{\psi}\right\} = [\phi]\{c\} \tag{5.54}$$

Substitution of the above expressions into the objective eigen problem, premultiplication with $[\phi]^T$and recalling that the eigen vectors of the baseline have been normalized for unit generalized mass then yields a linear system of equations.

$$\left[diag(\omega^2 - \hat{\omega}^2) + [\phi]^T [\Delta k][\phi] - \hat{\omega}^2 [\phi]^T [\Delta m][\phi]\right]\{c\} = 0 \tag{5.55}$$

Application of fractional system mass and stiffness changes in the style of Equations 3.11 and 3.12 enables further simplification.

$$\triangle m = [m]\,\alpha_m, \qquad \triangle k = [k]\,\alpha_k \tag{5.56}$$

$$\left[diag(\omega^2)\,(1+\alpha_k) - diag(\hat{\omega}^2)\,(1+\alpha_m)\right]\{c\} = 0 \tag{5.57}$$

The admixture coefficients $C_{ij} \neq 0$. Thus, the determinant of the matrix in Equation 5.57 must vanish. Figure 5.4 shows the roots of the corresponding polynomial, and a joint increase of all natural frequencies. This uni-directional shift can be better described by taking advantage of the diagonal structure of Equation 5.57, and arriving at an independent equation for each natural mode.

$$\hat{\omega}_i^2 = \frac{1+\alpha_k}{1+\alpha_m}\omega_i^2 \tag{5.58}$$

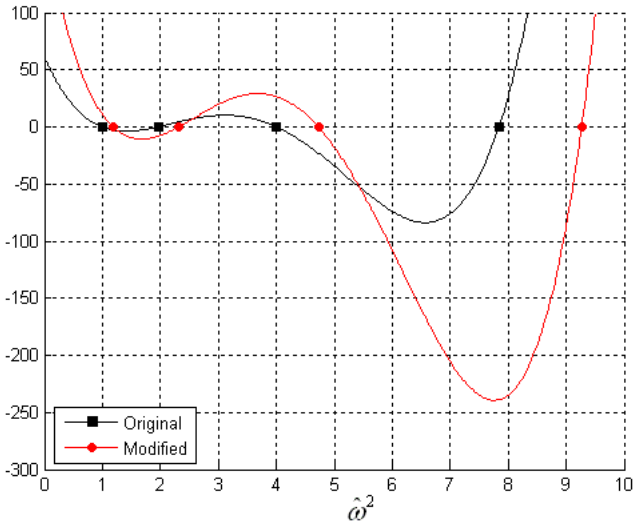

Figure 5.4: Characteristic polynomial for uniform change

The uniform frequency shift defined by Equation 5.58 is an immediate result of the simplifying assumptions of IPR. Considering the eigen problem in Equation 5.50, the natural frequency ω^2 represents the factor of proportionality between mass and stiffness matrix. The linear fractional changes restated in Equations 5.56 impose a uniform change in both mass and stiffness. Thus, the change in natural frequencies is consistent with that uniform change.

The adoption of the terminology and derivations of Bauchau allow a more general formulation [12]. Structural changes are redefined by means of a localization array h.

$$\triangle m = \mu \{h\} \{h\}^T, \qquad \triangle k = \gamma \{h\} \{h\}^T \tag{5.59}$$

The length of the vector h depends on the number of discrete system nodes. It is a zero vector with ones at the nodal degrees of freedom that reflect the mass and stiffness change of magnitude μ and γ, respectively. Substitution of Equations 5.59 into Equation 5.55, and introducing $\theta^2 = \frac{\gamma}{\mu}$ yields another determinant.

$$\left[diag(\omega^2 - \hat{\omega}^2) + \mu \left(\theta^2 - \hat{\omega}^2\right) [\phi]^T \{h\} \{h\}^T [\phi] \right] \{c\} = 0 \tag{5.60}$$

Again, the determinant is a polynomial, and its roots are the natural frequencies of the objective system. Figure 5.5 shows both baseline and objective natural frequencies corresponding to Equation 5.60. Note that the modal movement is no longer uni-directional.

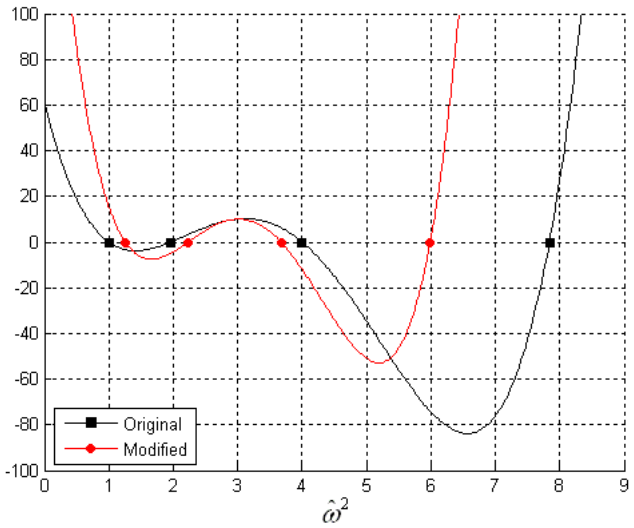

Figure 5.5: Characteristic polynomial for localized change

To increase transparency, Equation 5.60 can be premultiplied by Equation 5.61, further manipulated, and divided by $\{h\}^T [\phi] \{c\}$ to yield the scalar function Φ.

$$\frac{\{h\}^T [\phi]}{\mu \left(\theta^2 - \hat{\omega}^2\right)} diag \left(\frac{1}{\omega^2 - \hat{\omega}^2} \right) \tag{5.61}$$

$$\Phi\left(\hat{\omega}^2\right) = \frac{1}{\mu\left(\theta^2 - \hat{\omega}^2\right)} + \{h\}^T [\phi]\, diag\left(\frac{1}{\omega^2 - \hat{\omega}^2}\right) [\phi]^T \{h\} = 0 \tag{5.62}$$

Equation 5.62 is a scalar function illustrated in Figure 5.6. The characteristic parameter θ^2 drives and controls modal changes across the entire frequency spectrum. θ^2 acts like a sink. All eigen frequencies shift towards it. For cases of pure mass or pure stiffness changes, the frequency shift returns to a uni-directional movement [12].

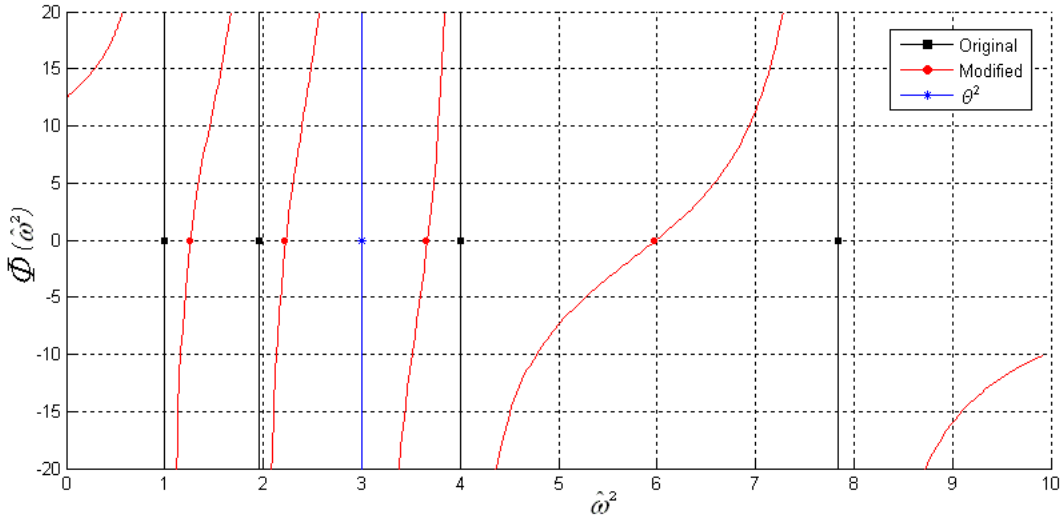

Figure 5.6: Natural frequency shift
All objective frequencies "*shift towards the frequency introduced by the structural modification*" [12].

In summary, the small changes inherent to perturbation theory ensure a resemblance of the objective system to the baseline system. Thus, the desired modal characteristics of the objective system can not be of arbitrary nature. As the natural frequencies of the baseline system are very particular properties innate to the system, the modified frequencies will show a well organized resemblance of the baseline frequencies. The specification of the modal objectives on the right hand side of the system of perturbation equations needs to rely on a minimum number of natural frequencies and resort to inequality rather than equality constraints.

5.4 Underdetermined Solution

Above investigations allow the conclusion that the perturbation equations of TIPR feature more design variables than frequency objectives. The system of equations is underdetermined. No unique solution exists. The identification of the best solution relies on optimization criteria such as objective function and constraints.

5.4.1 Objective Function

Classic redesign is usually applied to an already existing structure. Equation 5.63 captures the desired minimum departure from the baseline system in an objective of minimum change.

$$F = \sum_{e=1}^{\sigma} \alpha_e^2 \tag{5.63}$$

An alternative objective proposed by Bernitsas et al. attempts to minimize both the absolute change and the difference between adjacent element changes. The additional term in Equation 5.64 is augmented with a penalty coefficient [19].

$$F = \sum_{e=1}^{\sigma} \alpha_e^2 + \gamma \sum_{e=1}^{\sigma-1} (\alpha_e - \alpha_{e+1})^2 \tag{5.64}$$

Smith and Hutton build a functional objective as shown in Equation 5.65. It accounts for minimum change and residual force errors [173]. Kim et al. also append a summation of residual force errors to account for the violation of the dynamic equilibrium when redesigning for large structural changes [101]. The idea of residual forces was renewed by Chen who introduced an acceleration factor based on the norm of residual forces to improve the convergence of his nonlinear method [36].

$$F = \sum_{e=1}^{\sigma} \alpha_e^2 + \mu \delta^T \delta \tag{5.65}$$

The most frequently used objective function for perturbation redesign applications is the minimum change criterion. It provides sound solutions by seeking a minimum departure from the existing baseline. It also ensures the validity of the small perturbation equations by avoiding large structural differences between the baseline and its redesigned counterpart.

Structural design typically seeks a solution in terms of minimum weight. Equation 5.66 shows the corresponding objective function for the simple bending beam subject to classic IPR. Its utilization, however, was shown to produce pathological optimization results by simply driving all thickness variables to their lower limits [68].

$$F = \sum_{e=1}^{\sigma} \alpha_e \tag{5.66}$$

The TIPR performance of different objective functions is investigated using a uniform cantilever beam. Cross section and material properties are found in Figure 5.7 and Table 7.3. The six plies with layup angle θ adhere to a stacking sequence identical to the CAS beam in Table 7.5 used in a later section for validation purposes. The discrete representation of the cross section relies on 15 finite elements along the width, 10 along the height, and six along the wall thickness. The global beam model uses four second order finite elements.

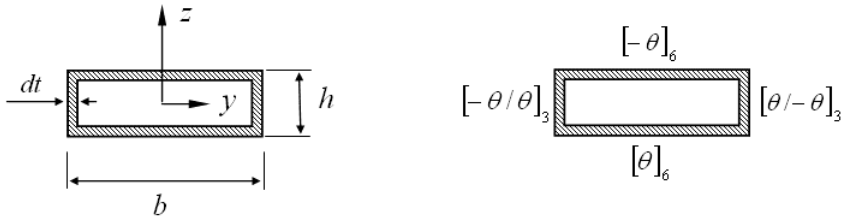

Figure 5.7: Box beam cross section

In accordance with the TIPR stiffness effect separation derived in Equation 5.15, there are four stiffness properties of particular interest at the global level. Their individual impact is reflected by four design variables. Equation 5.67 shows the TIPR stiffness effect separated small perturbation equation for a desired frequency change in the i^{th} natural mode. The size of the TIPR system of equations depends on the number of frequency objectives. The following applicability study will use a single equation to solve for the four unknowns. The frequency objective on the right hand side of Equation 5.67 will account for a five percent increase in the natural frequency of the first mode.

$$\begin{bmatrix} P_A & P_J & P_{I_{22}} & P_{I_{33}} \end{bmatrix} \begin{Bmatrix} \alpha_A & \alpha_J & \alpha_{I_{22}} & \alpha_{I_{33}} \end{Bmatrix}^T = \triangle\omega_i^2 \tag{5.67}$$

$$P_A = \{\psi_i\}^T [k_A] \{\psi_i\} - \omega_i^2 \{\psi_i\}^T [m] \{\psi_i\} \tag{5.68}$$

$$P_J = \{\psi_i\}^T [k_J] \{\psi_i\} \tag{5.69}$$

$$P_{I_{22}} = \{\psi_i\}^T [k_{I_{22}}] \{\psi_i\} \tag{5.70}$$

$$P_{I_{33}} = \{\psi_i\}^T [k_{I_{33}}] \{\psi_i\} \tag{5.71}$$

The global optimizer relies on upper and lower bounds for global design variables to ensure a feasible design. These bounds are provided by local level analyses in terms of cross sectional stiffness limits. Equations 5.72 to 5.74 present the stiffness effect manipulation to find the upper limit of the design variable representing the bending stiffness S_{55} of a linear finite element.

$$k_{5,5}^{base} = \frac{L}{4} S_{33}^{base} + \frac{1}{L} S_{55}^{base}, \qquad k_{5,5}^{upper} = \frac{L}{4} S_{33}^{base} + \frac{1}{L} S_{55}^{upper} \tag{5.72}$$

$$\Delta k_{5,5}^{upper} = \frac{S_{55}^{upper} - S_{55}^{base}}{L} = \frac{S_{55}^{base} \alpha_{I_{22}}^{upper}}{L} \tag{5.73}$$

$$\alpha_{I_{22}}^{upper} = \frac{S_{55}^{upper}}{S_{55}^{base}} - 1 \tag{5.74}$$

Wall thickness is the only variable allowed to change for the testbeam in Figure 5.7. The Layup angle θ is zero. Physical limits of the local level design variable and corresponding limits of the global design variables are provided in Table 5.15.

Table 5.15: Box beam design variable limits

	Lower limit	Baseline	Upper limit
dt	0.02 in	0.03 in	0.04 in
α_A	-0.3240	0	0.3146
α_J	-0.3052	0	0.2797
$\alpha_{I_{22}}$	-0.2990	0	0.2677
$\alpha_{I_{33}}$	-0.3081	0	0.2846

Objective functions are investigated using the optimizer *fmincon* from the optimization toolbox in Matlab. The optimization problem is subject to the single equality constraint given by Equation 5.67 and the upper and lower limits in Table 5.15.

Table 5.16: TIPR results using equality constraint

	$\{\alpha\}^T\{\alpha\}$	α_A	$\alpha_A - \sum_{i=2}^{4}\alpha_i$	$\alpha_A - \alpha_{I_{22}}$
α_A	-0.0524	-0.3240	-0.0524	-0.0524
α_J	0	0	0.2797	0
$\alpha_{I_{22}}$	0.0524	-0.2191	0.0524	0.0524
$\alpha_{I_{33}}$	0	0	0.2846	0
$\omega_1 = 3.8389$, $\hat{\omega}_1 = 4.0308$				
Ω_1	4.0407	4.1187	4.0407	4.0407
Error, %	0.24	2.18	0.24	0.24

Frequencies: ω - Baseline, $\hat{\omega}$ - Desired, Ω - Reanalysis post α application

The first two objective functions in Table 5.16 represent minimum change and minimum weight, respectively. The results confirm an inferior performance of minimum weight. The optimizer goes straight to the lower limit without violating the equality constraint of Equation 5.67. The modified system, however, after application of stiffness changes and reanalysis, shows a dissatisfactory error in the natural frequency. Third and forth objective function in Table 5.16 represent the desire to simultaneously minimize weight and maximize stiffness. The two implementations differ in the number of stiffness effects considered. Using torsional as well as both bending stiffnesses shows a pathological behavior similar to that of minimum mass. The optimizer activates the upper bounds of the two design variables that correspond to a zero perturbation coefficient.

Using the ratio of mass and stiffness related design variables to minimize weight while maximizing stiffness causes division by zero because of the design variable baseline values. Other objective functions are derivatives of the ones presented and based on the idea of weighting factors. Their solution shows great dependence on the weights as these are indicative of the relative importance of the individual objectives. Weighting factors cause unpredictable results and should not be used [190].

5.4.2 Constitutive Laws

The objective functions in Table 5.16 feature an independent change of individual properties. The design variable associated with area and mass is driven towards the negative limit. Remaining design variables are driven towards the positive limit. The equality constraint of Equation 5.67 is satisfied but the solution for $\{\alpha\}$ violates constitutive laws. Figure 5.8 illustrates the behavior of equivalent beam properties as a function of wall thickness and attests to their simultaneous increase or decrease.

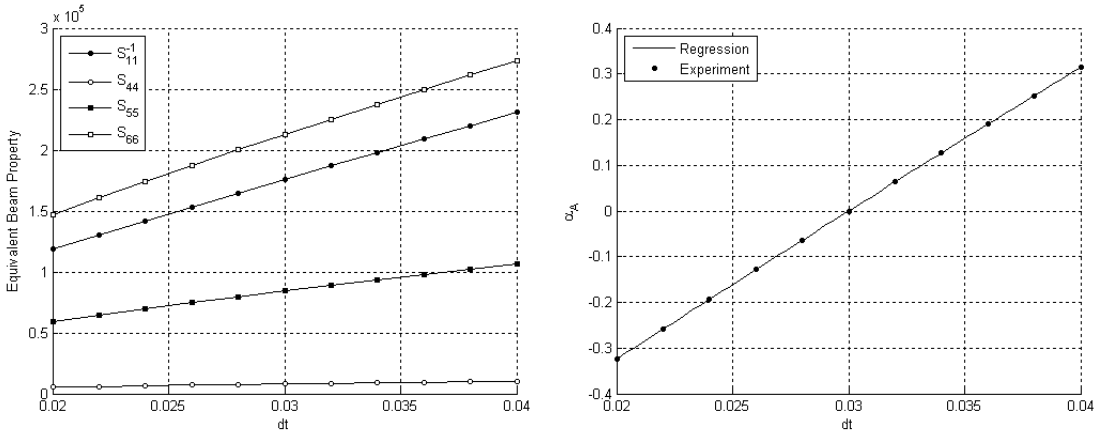

Figure 5.8: Cross sectional stiffness dependence 1
Left: Exclusive change of wall thickness for $\theta = 0$; Right: Global design variable regression

Recall the notional methodology introduced earlier. Local level analyses provide not only the starting point for the global optimization, but also surrogate models of the cross sectional properties in dependence of the design variables at the local level. The primary purpose of the surrogate models is to ensure that the global optimizer stays within the feasible domain of the physical design space. A secondary advantage is derived from the virtually instantaneous responses that allow for a rapid optimization at the local level.

Why not capitalize on these already existing surrogate models in the global optimization. They are fast approximations that capture the fundamental physical relationship between local and global level design variables. Instead of just keeping the global optimizer within bounds, they could be used as viability constraints that ensure instantaneous feasibility of the global level solution. Moreover, local level design variables introduced at the global level

eliminate the need of a local level optimization altogether.

The relationship between stiffness and wall thickness is representative of the relationship between global and local level design variable. If the stiffness coefficient is a function of the local level design variable, then the corresponding α can also be expressed as a function of the local level design variable. Figure 5.8 visualizes this dependence using the example of axial stiffness. The second order polynomial regression was performed using experimental design points based on Equation 5.76.

$$\hat{S}_{11} = S_{11} + \Delta S_{11} = S_{11} + S_{11}\alpha_A \tag{5.75}$$

$$\alpha_A = \frac{\Delta S_{11}}{S_{11}} = \frac{\hat{S}_{11}}{S_{11}} - 1 \tag{5.76}$$

The formulation of the optimization problem is modified as follows. Wall thickness becomes the global design variable subject to lower and upper limits. The problem remains constrained by Equation 5.67 but is now imposed as inequality constraint. In addition, it features so called viability constraints in form of polynomial approximations for α that enforce constitutive laws.

$$\left[\begin{array}{cccc} P_A & P_J & P_{I_{22}} & P_{I_{33}} \end{array} \right] \left\{ \begin{array}{cccc} \alpha_A & \alpha_J & \alpha_{I_{22}} & \alpha_{I_{33}} \end{array} \right\}^T \leq \triangle\omega_i^2 \tag{5.77}$$

The inequality of Equation 5.67 relaxes the problem. The combination of both TIPR and polynomial equality constraints for the present example bears no solution. Posing the TIPR objective as inequality constraint gives the optimizer more leeway while at the same time ensuring the validity of TIPR by limiting structural changes to small perturbations.

The relative percentage error in Table 5.17 compares the first natural frequency predicted by the small perturbation equation using the optimized values for α with the first natural frequency obtained from the reanalysis of the modified system. The results confirm the necessity of an appropriate choice for both objective function and TIPR equation. The modal inequality constraint above combined with a minimum change objective naturally results in no change.

Table 5.17: TIPR results using inequality constraint

	$\{\alpha\}^T\{\alpha\}$	α_A	$\alpha_A - \sum_{i=2}^{4}\alpha_i$	$\alpha_A - \alpha_{I_{22}}$
dt	0.03	0.02	0.04	0.02
α_A	0	-0.3240	0.3146	-0.3240
α_J	0	-0.3051	0.2796	-0.3051
$\alpha_{I_{22}}$	0	-0.2989	0.2676	-0.2989
$\alpha_{I_{33}}$	0	-0.3081	0.2845	-0.3081
$\omega_1 = 3.8389$, $\hat{\omega}_1 \leq 4.0308$				
$\hat{\Omega}_1$	3.8389	3.8855	3.7498	3.8855
Ω_1	3.8389	3.9077	3.7712	3.9077
Error, %	0.00	0.57	0.57	0.57

Frequencies: ω - Baseline, $\hat{\omega}$ - Desired, $\hat{\Omega}$ - TIPR equation, Ω - Reanalysis post α application

Note that global design variables are no longer defined as a set of multipliers. The global optimizer now solves directly for the physical parameter dt and the multipliers α act as intermediate design variables. However, creating the intermediate design variable surrogates at the outset of the global optimization compromises their incremental application. The fractional change exemplified in Figure 5.8 is valid only with reference to the initial baseline. The proposed TIPR optimization scheme relies on an incremental update such that the modified system of the last increment serves as the baseline system for the new increment.

Equation 5.78 illustrates the solution to this problem by simply creating a surrogate model for the cross sectional stiffness. The fractional change is now expressed as function of the respective stiffness effect surrogate relative to the current baseline.

$$\alpha_S = \frac{\hat{S}}{S_{base}} - 1 = \frac{f_S(dt)}{S_{base}} - 1 \tag{5.78}$$

5.4.3 Extended Stiffness Effect Separation

Advanced composite materials are a key technology for contemporary aircraft. Ply angles and stacking sequences have been shown to have a great impact on design objectives and critical aeroelastic speeds [63, 35, 77]. The introduction and wide application of composites gave rise to aeroelastic tailoring, a discipline solely dedicated to taking advantage of directional stiffness properties.

Recall the basic stiffness effect separation demonstrated in Equations 5.11 - 5.15. Axial

and shear stiffnesses have been assumed to be exclusively dependent on area. A single intermediate design variable α_A was introduced to represent changes in all three stiffness coefficients. The strong influence of ply angle and stacking sequence on effective material properties of composites advocates the individual treatment of stiffness effects. Figure 5.9 illustrates layup effects for the simple testbeam at hand.

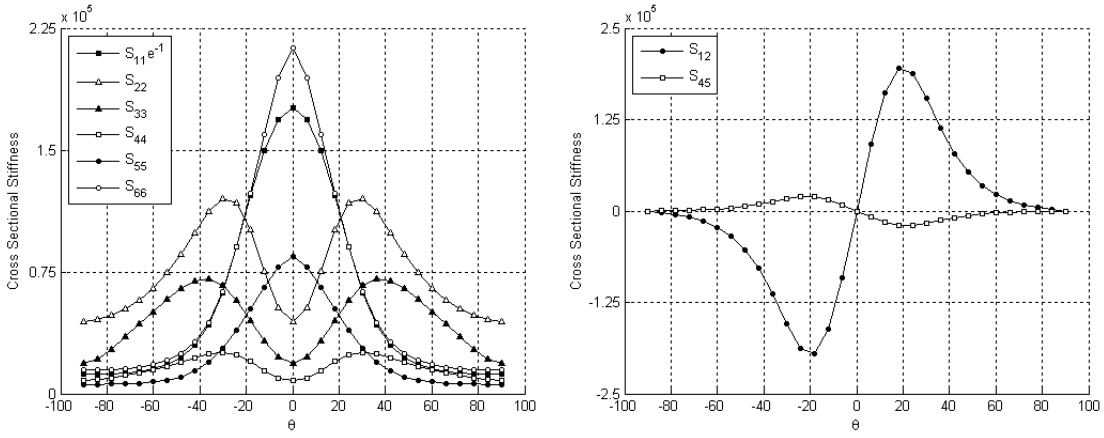

Figure 5.9: Cross sectional stiffness dependence 2
Exclusive change of layup angle for $dt = 0.03$ inch

Equation 5.79 showcases a Timoshenko stiffness effect separation that accounts for all 21 coefficients in the cross sectional stiffness matrix. Equation 5.80 introduces six intermediate design variables for all main stiffness effects along with an additional term that captures cross coupling effects. Equation 5.81 introduces a single intermediate design variable for system mass as necessary for a minimum weight solution conducive to the conceptual design space.

$$k = \sum_{i=1}^{6} \sum_{j=i}^{6} k_{S_{ij}} \tag{5.79}$$

$$\Delta k = \sum_{i=1}^{6} \sum_{j=i}^{6} \Delta k_{S_{ij}} = \sum_{i=1}^{6} k_{S_{ii}} \alpha_{ii} + \Delta k_{CC} \tag{5.80}$$

$$\Delta m = m \alpha_m \tag{5.81}$$

The cross coupling term Δk_{CC} is explained upon observation of Figure 5.9. The baseline

of the current increment may be free of coupling effects. Equation 5.78 then evaluates to not a number. Because there is no remedy for the division by zero, corresponding effects need to be carried along without intermediate design variables.

5.5 Frequency Sensitivities

A previous section emphasized the very particular nature of the eigen spectrum innate to every system. The characteristics of natural frequencies shall now be further examined.

Equation 5.83 captures the dependency of the natural frequency on the length L, the mass per unit span m, and the bending stiffness EI of a cantilevered beam [14]. It allows two deductions.

$$\omega \propto \frac{1}{L^2}\sqrt{\frac{EI}{m}} \tag{5.82}$$

First, the natural frequencies of beam-like structures such as the high aspect ratio wings of interest to the present study are predominantly determined by the wing span. The optimization algorithm under development is intended to solve stability problems of an existing configuration with limited authority to change the driving wing planform parameters. It is important to realize that the primary driver of the frequency is in fact a parameter that is not under the control of the present scope of work.

Second, the sensitivity of the natural frequency with respect to the stiffness is greatly mitigated by the square root effect. That is, if the wing experiences flutter at a speed below the design speed then the stiffness of the wing must be maximized while at the same time minimizing the weight penalty. Equation 5.83 very distinctly shows that a 100 percent increase in the stiffness will inflict an increase in the corresponding frequency of only 40 percent.

The structural engineer in pursuit of an improved stiffness design for a wing with predetermined span thus has very little latitude to solve a potential stability problem. Material selection becomes an important last resort.

For a weight sensitive design such as a high altitude long endurance aircraft the wing will be a thin walled structure, and Equation 5.83 can be further reduced [14].

$$\omega \propto \frac{h}{L^2}\sqrt{\frac{E}{\rho}} \tag{5.83}$$

Bauchau uses Equation 5.83 to introduce $\sqrt{E/\rho}$ as material performance index for stiffness designs [14]. Using this performance index on an isotropic metallic material such as aluminum it is evident that the structural engineer has almost no chance to succeed. The stiffness to weight ratios of modern composite materials on the other hand unlock the design space, and the highly directional nature of composite fibers creates additional degrees of freedom.

To fully exploit the advantages brought about by these additional degrees of freedom the design engineer must refrain from using composite materials in the same way as metallic materials. The design solution should go beyond the simple weight savings offered by modern composites. Instead, layup angles and stacking sequences for a given cross section are optimized for a truly aeroelastically tailored design.

5.6 Summary

The preceding chapter extended classic IPR to a more refined beam model by introducing the Timoshenko stiffness effect separation. TIPR confirmed an outstanding efficiency as it requires a single one finite element analysis to redesign a structural system for small changes. Swiftness and accuracy suggest great promise for design applications.

Above development studies also disclosed potential deficits and design methodological considerations so far disregarded. For example, critical mode identification along with stiffness effect separation and selection are crucial to the efficient and comprehensive consideration of mass and stiffness changes. The well organized nature of the eigen spectrum of natural frequencies prohibits arbitrary frequency changes in multiple modes. The independent global level optimization of stiffness effects causes the violation of underlying dependencies. The consequential enforcement of constitutive laws relieves of an optimization at the local level altogether.

Chapter VI

PROPOSED METHODOLOGY

The present work evolves around the development of a gradient-free optimization algorithm for high aspect ratio wings subject to frequency constraints. Founding idea is the incremental application of small modal perturbations and sequential reanalysis to enable a swift and accurate local design space exploration. The novelty of the proposed methodology will present itself on three counts.

ONE The combined application of dimensional reduction and perturbation theory is unique. Both methods will be utilized in the composition of an efficient optimization scheme that enables conceptual design capabilities.

TWO The innovative heart of the proposed methodology lies in the perturbation based optimization algorithm. The driving idea is the realization of a directed search without gradient evaluations. The associated reduction in necessary FE analyses will result in computational savings that greatly contribute to the efficiency of the proposed design methodology.

THREE Viability constraints in terms of surrogate models will enforce the constitutive laws. Making direct use of the physical design variables at the global level ensures instantaneous feasibility of the solution and eliminates the need for a concluding local level optimization.

6.1 Basic Structure

The methodological framework in Figure 6.1 proposes a two level analysis, one level optimization approach. It features one primary difference to the initially envisioned methodology presented in Figure 4.4. This distinction is established by the successful elimination of the local level optimization. The new design process is complete upon convergence of the

global level optimizer. The corresponding solution is given in terms of actual physical design variables; and is feasible at both levels.

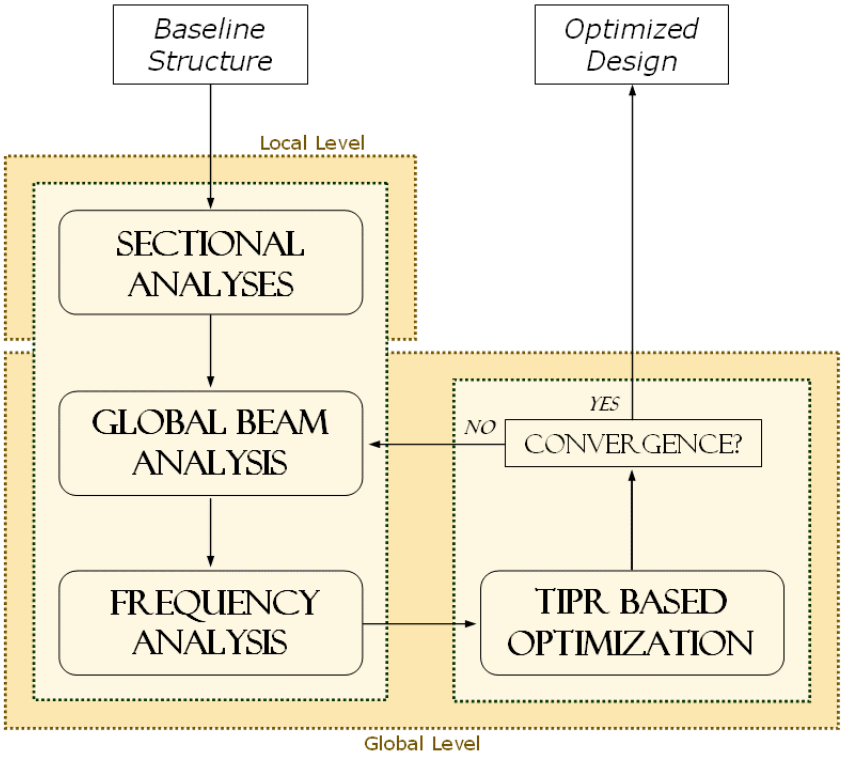

Figure 6.1: Proposed Methodology

Key enabler of this major improvement are surrogate models. As before, local level analyses determine equivalent beam properties. Figure 6.2 depicts two basic outcomes of the local level. Baseline values that serve as starting point for the optimization at the global level, and surrogate models that provide approximate relationships between physical and intermediate design variables. Recall that the latter are TIPR enablers that reflect the changes in cross sectional beam properties. Previously, surrogate models were used solely to guaranty that the global optimizer stays within the feasible domain of the physical design space. The new methodology greatly expands their role and responsibility by adding them as constitutive laws to the global level. This addition ensures local level feasibility and eliminates the need for a respective optimization.

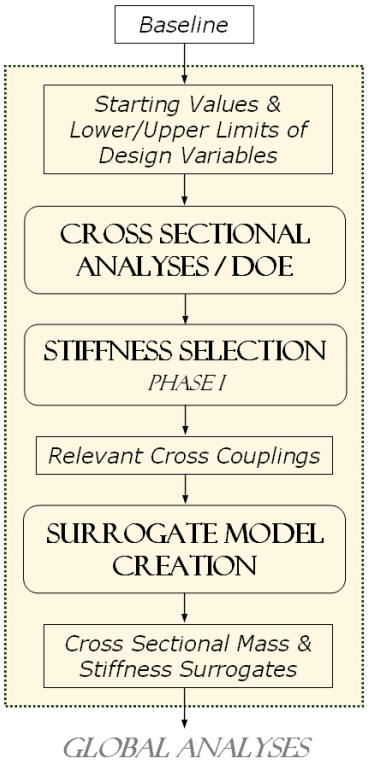

Figure 6.2: Proposed local level

Global analyses and optimization begin after initial analyses at the local level are completed. The global beam analysis determines system mass and stiffness matrices of the wing model along with natural modes and frequencies. A subsequent frequency analysis identifies critical modes, upon which the frequency objectives for the TIPR equations are determined. The consequent solution will provide incremental changes to local stiffness and mass properties that ultimately result in the specified natural frequency change.

The present approach is very different from traditional implementations. On the one hand it employs global and local level analyses to capitalize from potentially enormous computational savings. On the other hand it takes advantage of surrogate models that eliminate the need for multiple optimization levels. The split of the design variables, that are fewer at the global level than at the local level, is preserved for analyses, but revoked for optimization purposes. The developed stiffness effect separated TIPR equations allow a

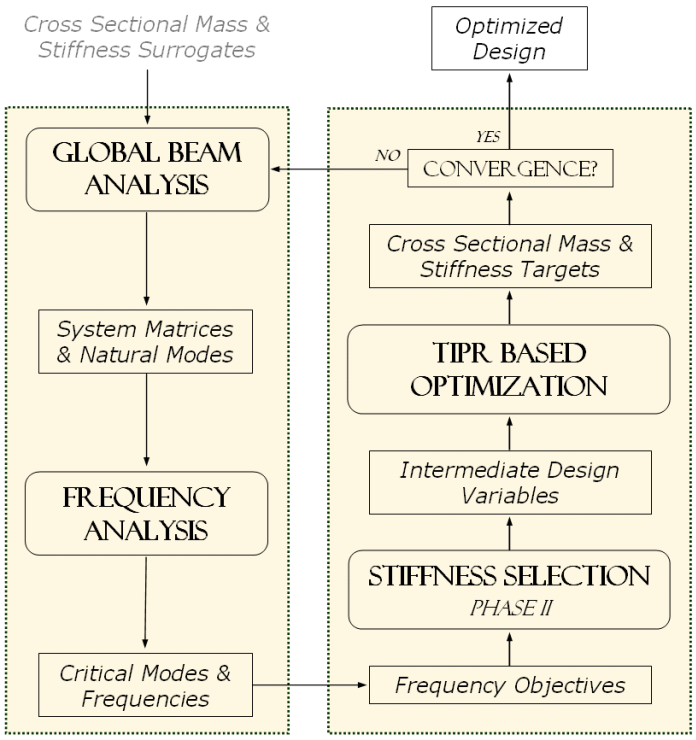

Figure 6.3: Proposed global level

complete exploitation of surrogates. The propagation of these readily available approximations through the small perturbation equations enables great performance and effectiveness enhancements. It capacitates a methodology consisting of multi level analyses feeding into a single level optimization.

6.2 Wing Model

Conceptual design studies typically fall back on box beam models that represent the load carrying structure of the wing. Figures 6.4 and 6.5 show different examples of corresponding wing models. The specific details depend on a variety of assumptions based on engineering judgment and the disciplinary integration of structures in the overall design process.

Chattopadhyay et al. fixed aspect ratio, taper ratio, and box height to width ratio; and made root chord, wall thickness, and ply orientation angles subject to change [35]. Isogai ignored front and rear spar and exclusively focused on upper and lower skin by allowing membrane thickness and fiber orientation at a specified number of spanwise locations to

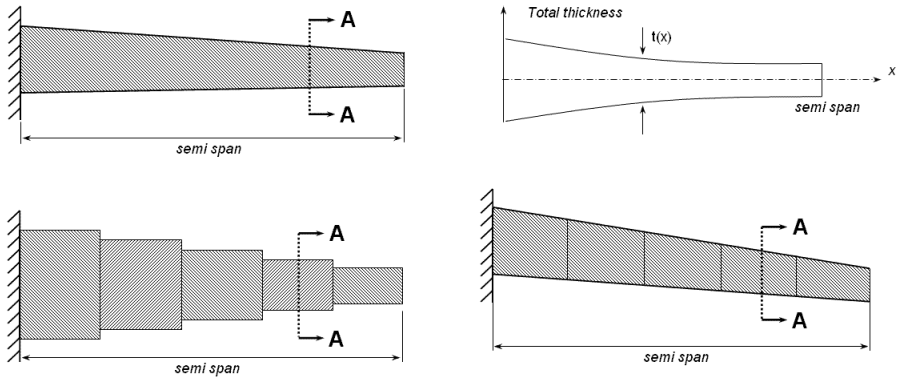

Figure 6.4: Box beam wing model examples
Upper left: Chattopadhyay et al. [35]; Upper right: Isogai [91]
Lower left: Lillico et al. [112]; Lower right: Gua et al. [77]

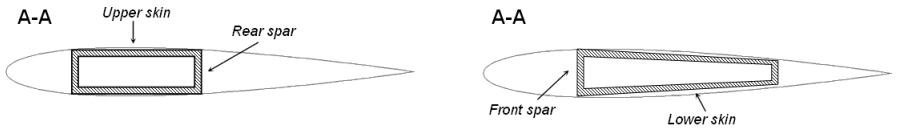

Figure 6.5: Box beam cross section examples

change [91]. Lillico et al. represented the wing by a series of box beams. Thickness and laminate orientation of both skin and spar were allowed to change [112]. Guo et al. divided the wing into five sections. Each section in turn is divided into four panels representing upper and lower skin and front and rear spar. The cross sectional model features a wing box height that varies across the chord (Figure 6.5). The variation is linear and fixed for each optimization. The only variables allowed to change are the fiber orientation angles. Each panel consists of eight layers, amounting to a total of 16 design variables per section [77].

A parametric description is an essential prerequisite for numerical optimization. The choice of disciplinary parameters depends on the phase of the design process. Prevalent design variables for the detailed structural design engineer are finite element thicknesses. Design model techniques such as element grouping or variable linking may be applied to reduce the design variable count. An important practical consideration is regarding design manufacturability. That is, the final design must feature continuous surfaces and distributions to be suitable to go into production [103].

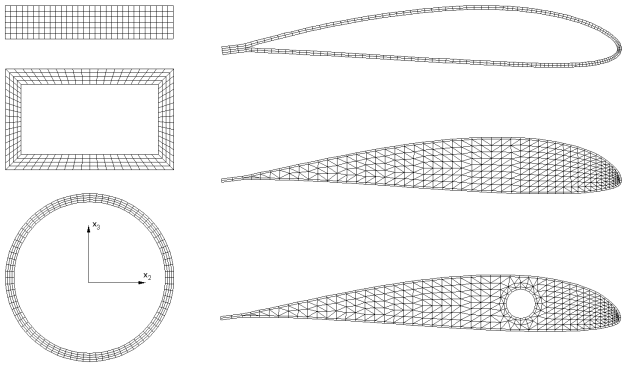

Figure 6.6: Library of cross sectional designs

Conceptional design requirements in terms of low cost analyses, easy disciplinary linkage, and efficient trade capabilities entail simple parametric geometries. The design of a new regional jet at Fairchild Dornier for example may lead to a detailed aircraft model with thousands of design variables and over 800,000 constraints. Its conceptual representation, however, is a simplified beam model representing global stiffness and mass distribution [161].

The conceptual design engineer is looking for a concise set of design variables that ensures flexible concept generation as well as convenient manipulation. The corresponding goal of the proposed methodology is the optimization of the wing structure in terms of continuous geometric and structural property distributions along the span. Airfoil shape and global wing parameters such as span, root chord, and taper ratio are typically assumed to be aerodynamic requirements that are held fixed during structural optimization [111]. The specification of the internal wing geometry relies on a Cross Sectional Design (CSD) library. Geometries from the CSD library are assigned along the span at as many locations as necessary to represent the spanwise mass and stiffness distribution. Local analyses provide resulting cross sectional properties. The global computational structural dynamics code linearly interpolates these properties between adjacent spanwise locations.

Figure 6.6 depicts currently available geometries from the CSD library. Each CSD has a set of physical parameters describing dimensional and material properties. The wing baseline model requires initial values for each CSD inherent parameter at each spanwise location. The resulting cross sectional properties are representative of the spanwise distribution.

6.3 Analysis Framework

In accordance with the proposed methodology in Figure 6.1, the analysis framework consists of two levels. Figure 6.7 shows the execution sequence and respective analysis tools. The framework is fully automated and implemented in Matlab. It is operated without GUI. Input is derived from text files. Output is provided in text and graphical form.

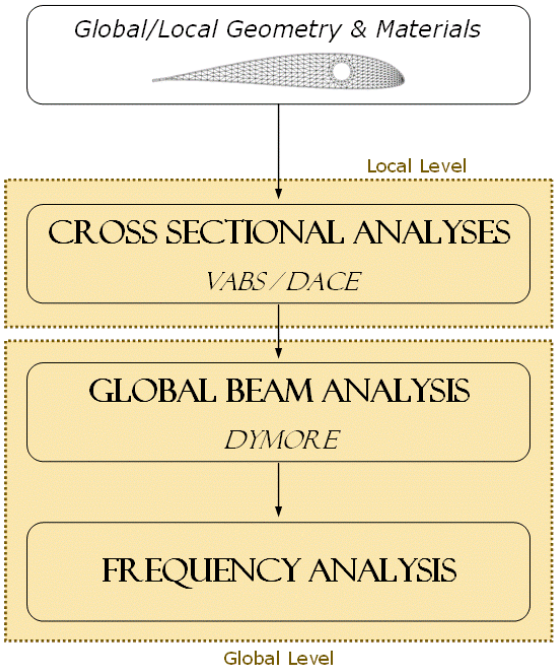

Figure 6.7: Analysis framework

The preparation of the optimization process involves the configuration of the wing model, the assignment of geometry descriptors, and the specification of respective baseline values and validity bounds. The optimization process is initiated upon the analysis of the reference design and the establishment of surrogate models. Local level surrogates are created using DACE, a toolbox that is discussed in a subsequent section dedicated to local level surrogates. DACE provides functional approximations that capture the dependence of cross sectional mass and stiffness properties on physical design variables.

Cross sectional analyses are performed by VABS version 2.1.1 released June 14, 2005. VABS is a comprehensive analysis code based on Variational Asymptotic Beam Sectional

Analysis and standard two-dimensional FEM. Results are efficient and accurate, and not restricted to simple cross sectional shapes. VABS provides cross sectional properties required by the global beam analysis tool. These properties are 21 stiffness coefficients, mass per unit span, three mass moments of inertia per unit span, and the center of mass location [202, 204].

The global response analysis is performed by DYMORE version 2.0. DYMORE is a finite element based dynamics code for the analysis of flexible, nonlinear multibody systems. It accepts the VABS output to define a linear variation of beam properties along the span [11].

Frequency analysis in Figure 6.1 refers to the determination of the natural frequencies that become TIPR modal constraints. The identification of critical aeroelastic modes usually falls back on the lowest natural frequencies. Fundamental bending and torsion are of predominant interest. At the current time there are no actual such analyses incorporated. Critical modes and frequency objectives are provided by the user to allow elaborate performance investigations of the incremental TIPR optimization algorithm.

6.4 Stiffness Selection

The generalized Timoshenko beam model features 21 stiffness coefficients that translate to six intermediate design variables α plus 15 potential cross coupling effects Δk_{CC} to be considered in the TIPR Equation 5.80. The aspired efficiency of the proposed optimization algorithm requires the reduction to a minimum set of relevant stiffness effects.

6.4.1 Provisional Screening

The primary challenge in fixed wing aeroelastic design is the coupling of torsion and bending modes [63, 76, 50]. This identifies the torsional stiffness GJ and the bending stiffnesses EI_{22} and EI_{33} as the significant players that also were made exclusive use of in a multi level rotor blade optimization subject to dynamic stability constraints [109, 108].

A provisional screening of individual stiffness effects on the five lowest natural frequencies is used to verify the validity of the exclusive use of these three stiffness parameters. By definition, screening refers to the experimental process of finding a ranked list of the few factors with significant effect on the outcome; and screening designs identify the experimental plan necessary to economically conduct respective analyses [1]. The present stiffness

screening forgoes such an experimental plan. The objective is to assess if the negligence of 18 stiffness coefficients is in general legitimate.

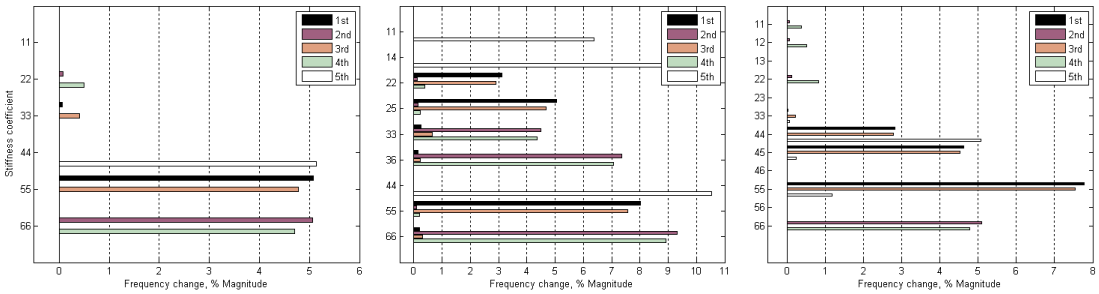

Figure 6.8: Provisional stiffness screening
Left: Cross-ply; Middle: Antisymmetric layup; Right: Symmetric layup

Three testcases representing three beam categories by means of their composite layer orientation are investigated. Please refer to Section 7.1 for a discussion of layup conventions. Figure 6.8 shows relevant stiffness coefficients for a cross-ply, an antisymmetric, and a symmetric beam. It also shows the isolated effect of a 10 percent reduction in each one of the coefficients on the five lowest natural frequencies. These sporadic screening results are sufficient to conclude that the exclusive consideration of torsion and bending is not generally justified.

Pertaining literature offers sparse remedy for the limited validity of the exclusive consideration of torsion and bending stiffnesses. A popular solution is the confinement of stacking sequences to very specific layup types. A multitude of implementations exclusively focus on symmetrical layups [91, 112, 35, 77]. Volovoi et. al improve the presence of relevant stiffness effects by extending the range of global design variables to include the axial stiffness EA [194]. Another measure by Volovoi et al. is to ensure negligibility of cross couplings by enforcing extension-torsion and torsion-bending couplings to be smaller than one percent of corresponding main stiffnesses and adding respective constraints at the local level [195].

6.4.2 Selection Process

The present implementation refrains from excluding stiffness effects per se. Alleviation from potentially irrelevant perturbation coefficients in the stiffness effect separated TIPR equation

comes from a two phase selection process.

The first phase takes place at the local level. It determines the relative importance of coupling effects upon completion of the local level DOE. The results for cross sectional coupling coefficients from all experiments are checked for a minimum of five percent significance. That is, they are added to the set of relevant stiffness effects if and only if Equation 6.1 is satisfied for any DOE.

$$100\frac{S_{ij}^2}{S_{ii}S_{jj}} > 5, \qquad i = 1, ..., 6, \quad j = i + 1, ..., 6 \tag{6.1}$$

The second phase of the selection process takes place at the global level. It starts upon identification of the critical mode j subject to change and is repeated at the beginning of each TIPR increment. Focal points are the six main diagonal entries in the stiffness matrix. Selection is based on a generalized stiffness effect separation with respect to the critical mode. The generalized main stiffness effect K_i in Equation 6.2 is identical to the potential TIPR perturbation coefficient that evaluates to a non-zero quantity if and only if it has an impact on the critical mode.

$$\sum_{i=1}^{6} K_i = \sum_{i=1}^{6} \{\psi_j\}^T [k_{S_{ii}}] \{\psi_j\} \tag{6.2}$$

The above selection process identifies all relevant stiffness effects. The first phase determines the total number of surrogate models to be created. It is a one time evaluation that takes place after the completion of the local level DOE. The second phase determines the number of intermediate design variables α for each new increment of the TIPR based optimization as well as the corresponding perturbation coefficients.

Surrogate models are created for mass per unit span, all diagonal cross sectional stiffness coefficients, and all cross sectional couplings identified in the first phase of the selection process. These surrogates provide a normalized functional approximation of the cross sectional mass and stiffness dependence on physical design variables.

Equations 6.1 and 6.2 represent a generalized approach to the selection process. Materials often feature planes of symmetry that result in the vanishing of terms in the stiffness matrix. In those cases the number of coefficients to be considered inherently reduces. Isotropic

materials constitute an extreme. Identical response characteristics in all directions leave only two elastic constants that populate nine of the 21 general locations in the stiffness matrix. The remains are zero.

6.5 Local Level Surrogates

The proposed methodology incorporates two effective enablers. Matrix multipliers α in the stiffness effect separated TIPR equation and cross sectional surrogate models. The former embody the essence of small perturbation theory by enabling linear fractional changes to local stiffness and mass properties. The latter provide an approximate functional relationship between physical design variables and equivalent beam properties. The symbiotic utilization of these two enablers is a fundamental prerequisite for the efficient TIPR solution.

Surrogate models fall into two categories. Parametric models assume a specific form of the response prior to applying the modeling technique. Non-parametric models refrain from such a priori assumptions and instead use a collection of functions associated with individual design sites. Response Surfaces, for example, are parametric because they assume that the underlying relationship can be described by a (quadratic) polynomial. The Gaussian Process (GP) on the other hand is stochastic and utilizes random variables to fit a smooth surface through all experimental data points.

Numerous modeling techniques exist. Their successful application depends on the complexity and dimensionality of the problem. Respective considerations include both accuracy and efficiency of the model. Non-parametric techniques generally show significant advantages over parametric techniques for highly nonlinear design spaces [129, 197].

The present work decided in favor of Kriging. Kriging is a special case of GP that realizes a deterministic response as a parametric regression combined with a stochastic extension. The latter is a random function that essentially represents the approximation error of the regression model with respect to the true value of the response. The underlying assumption is that the error is in fact random, i.e., experimental deviations from the regression model have a mean of zero.

The choice for Kriging originates from a suitable balance of accurate modeling capacity and ready availability of a corresponding software package called DACE. Theoretical background and implementation details are given in a technical report that also serves as manual. DACE is free and written in Matlab, which make it an expedient and convenient accessory to the completion of the present research [120].

6.6 Global Level Optimization

The global optimization begins once the initial local level analyses are concluded. The global beam analysis determines system mass and stiffness matrices along with eigen characteristics of the wing model. Frequency objectives for the perturbation equation are determined upon specification of the critical modes subject to change. The consequent solution of the perturbation equation provides incremental changes to local stiffness and mass properties that ultimately result in the specified natural frequency change.

Recall the notional methodology initially proposed. It was composed of two optimization levels, one at the global and one at the local level. Inherent problem to such multi level schemes is the communication between levels. A potential methodological flaw is the determination of a global level solution that is infeasible at the local level. The stiffness effect separated TIPR equation of the present approach overcome this problem by utilizing local level surrogates to ensure local constitutive laws at the global level. This enhancement holds great improvements for both accuracy and efficiency. It allows the global optimizer to immediately find the design variables of interest to the design engineer while at the same time eliminating the need of a concluding optimization at the local level.

Equation 6.3 extends the generalized global stiffness effect separation to all cross sectional stiffnesses including both main and off diagonal coefficients. Local level surrogates are created for mass per unit span, main stiffness coefficients, and all cross sectional couplings identified in the first phase of the selection process. Intermediate design variables α are assigned to mass and main stiffness effects, only (Equation 6.4). Cross coupling effects, if present, will be added to the TIPR equation as generalized change. Equation 6.5 defines this generalized change for the general case of 15 cross couplings.

$$K = \sum_{i=1}^{6}\sum_{j=i}^{6} K_{ij} = \sum_{i=1}^{6}\sum_{j=i}^{6} \{\psi\}^T \left[k_{S_{ij}}\right] \{\psi\} \tag{6.3}$$

$$\Delta K = \sum_{i=1}^{6}\sum_{j=i}^{6} \Delta K_{ij} = \sum_{i=1}^{6} K_{ii}\alpha_{ii} + \Delta K_{CC} \tag{6.4}$$

$$\Delta K_{CC} = \{\psi\}^T \Delta k_{CC} \{\psi\}, \quad \Delta k_{CC} = \sum_{i=1}^{6}\sum_{j=i+1}^{6} \Delta k_{S_{ij}} \tag{6.5}$$

The size of the perturbation coefficient matrix in the final TIPR Equation 6.6 depends on the number of frequency objectives S and the number of intermediate design variables N_{total}. The very organized nature of the eigen frequency spectrum advocates a minimum number of modal objectives that should rely on inequality rather than equality formulations. The maximum number of intermediate design variables N_{total} is seven, one for mass as denoted by the index m and six stiffness related ones as denoted by the index n.

$$\begin{bmatrix} P_{sn} & P_{sm} \end{bmatrix} \begin{Bmatrix} \alpha_n \\ \alpha_m \end{Bmatrix} + \Delta K_{CC} \gtreqless \triangle\omega_s^2 \tag{6.6}$$

$$P_{sn} = \{\psi_s\}^T [k_n] \{\psi_s\}, \qquad P_{sm} = -\omega_s^2 \{\psi_s\}^T [m] \{\psi_s\} \tag{6.7}$$

$$s = 1, ..., S, \qquad n = 1, ..., N$$

The second phase of the stiffness selection process determines which intermediate design variables are active. Each α in the above equation is expressed by means of the corresponding local level surrogate model as depicted in Equations 6.8 and 6.9. These so called viability constraints enable the global optimizer to directly solve for the physical design variables x. They ensure feasibility of the design solution by enforcing local constitutive laws and thus eliminate the need for a concluding optimization at the local level.

$$\alpha_m = \frac{\hat{m}}{m} - 1 = \frac{f_m(x)}{m} - 1 \tag{6.8}$$

$$\alpha_n = \frac{\hat{S}}{S} - 1 = \frac{f_S(x)}{S} - 1 \tag{6.9}$$

Equations 6.8 and 6.9 represent the linear fractional change from the incrementally updated baseline. The hatted quantities denote the unknown objective value for each new increment of the TIPR based optimization.

Equation 6.6 has multiple solutions and an optimization routine is needed. The identification of the best solution depends on an optimization criterion. Equation 6.10 expresses a minimum weight objective conducive to the conceptual design space. Equation 6.11 states the minimum change criterion as desired for an existing baseline configuration with stability problems.

$$F = \alpha_m \tag{6.10}$$

$$F = \{\alpha\}^T \{\alpha\} \tag{6.11}$$

6.7 Summary

A new and unique optimization methodology for the frequency placement of high aspect ratio wings applicable in the early stages of design has been proposed. It is rooted in the symbiotic utilization of beam dimensional reduction and small perturbation theory. The innovative heart is an incremental perturbation based optimization algorithm that enables a directed search without the need for gradient evaluations. The resulting reduction in necessary FE analyses promises great computational savings.

The high aspect ratio wing is modeled as a one-dimensional beam structure with cross sections specified along the span. Analysis is initiated at the cross sectional level. Results from a design of experiments are used in the creation of surrogate models. Local level outputs in terms of cross sectional stiffness and mass properties of the baseline are fed into a global beam analysis that determines system matrices and eigen characteristics. Outputs from both levels are then submitted to the global optimizer.

The perturbation based optimization algorithm is derived from the generalized eigenvalue problem of a baseline and an objective structure. The objective structure is defined by unknown structural properties that correspond to a set of desired natural frequencies.

$$[K] = [M]\left[\omega^2\right]$$

$$\left[\hat{K}\right] = \left[\hat{M}\right]\left[\hat{\omega}^2\right]$$

$$[M] = [\phi]^T [m] [\phi], \qquad [K] = [\phi]^T [k] [\phi]$$

The traditional design approach would employ many costly FE analyses in an iterative fashion. The inverse method of redesign avoids comparable expenses by defining the objective system in terms of small perturbations from the baseline system. Structural changes are expressed in terms of multipliers α to the baseline matrices that are referred to as intermediate design variables at the global level.

$$[\hat{m}] = [m] + [\triangle m] = [m] + [m]\,\alpha_m$$

$$\left[\hat{k}\right] = [k] + [\triangle k] = [k] + [k]\,\alpha_k$$

Using above relations in the generalized equation of motion of the objective system, expanding and cancelling all higher order terms yields a linear system of equations that relates structural and modal changes. The redesign objective is to determine the structural changes $[\triangle m]$ and $[\triangle k]$ that will result in the desired modal characteristics.

$$\{\psi_i\}^T [\Delta k] \{\psi_i\} - \omega_i^2 \{\psi_i\}^T [\Delta m] \{\psi_i\} = \triangle\omega_i^2$$

This is where the proposed TIPR based optimization starts diverging from the classic IPR scheme. The matrix defining the stiffness change is decomposed in accordance with dimensional reduction. The decomposition stems from a stiffness effect separation innate to the generalized Timoshenko beam model. It is based on a system stiffness that is a linear combination of at most 21 stiffness effects. Intermediate design variables defining a linear fractional change from the baseline are assigned to main effects, only.

$$\Delta k = \sum_{i=1}^{6} \sum_{j=i}^{6} \Delta k_{S_{ij}} = \sum_{i=1}^{6} k_{S_{ii}} \alpha_i + \Delta k_{CC}$$

Not all 21 stiffness effects will generally be considered in the newly devised TIPR equation. A two phase stiffness selection process determines the stiffness effects of interest to the modal redesign objective. The first phase concentrates on cross couplings and takes place at the local level. It is a one time evaluation performed upon completion of the local level DOE. The second phase focuses on main effects. It determines the number of intermediate design variables α for each new increment of the TIPR based optimization.

$$100 \frac{S_{ij}^2}{S_{ii} S_{jj}} > 5, \qquad i = 1, ..., 6, \quad j = i + 1, ..., 6$$

$$K_i = \{\psi\} [k_{S_{ii}}] \{\psi\}, \qquad i = 1, ..., 6$$

Surrogate models are available for mass per unit span, the six main stiffness coefficients, and all cross sectional couplings identified in the first phase of the selection process. Intermediate design variables α are expressed as function of corresponding local level surrogates and added to the optimization as viability constraints.

$$\hat{S}_{ii} = S_{ii} + \Delta S_{ii} = S_{ii} + S_{ii} \alpha_i = S_{ii} (1 + \alpha_i)$$

$$\alpha_i = \frac{\hat{S}_{ii}}{S_{ii}} - 1 = \frac{f_{S_{ii}}(x)}{S_{ii}} - 1$$

The term *viability constraints* was chosen because respective constraints turned into the single most important relationship with respect to the realizability and practicability of the proposed optimization methodology.

Based on the identification of critical modes and corresponding frequency objectives S and the number of relevant stiffness effects N, the final optimization problem poses itself as follows.

Minimize:

$$F(x) \qquad \text{Objective function}$$

Subject to:

$$\left[\begin{array}{cc} P_{sn} & P_{sm} \end{array} \right] \left\{ \begin{array}{c} \alpha_n \\ \\ \alpha_m \end{array} \right\} + \Delta K_{CC} \lessgtr \triangle \omega_s^2 \qquad \text{Modal constraints}$$

with

$$\alpha_n = \frac{f_S(x)}{S} - 1, \quad \alpha_m = \frac{f_m(x)}{m} - 1 \qquad \text{Viability constraints}$$

and

$$x_d^L \leq x_d \leq x_d^U \qquad \text{Side constraints}$$

where

$$x = \left\{ \begin{array}{c} x_1 \\ \vdots \\ x_D \end{array} \right\} \qquad \text{Physical design variables}$$

and

$$s = 1, ..., S \qquad \text{Number of frequency objectives}$$

$$d = 1, ..., D \qquad \text{Number of design variables}$$

$$m \qquad \text{Index for mass related } \alpha$$

$$n = 1, ..., N \qquad \text{Indices for stiffness related } \alpha$$

The present implementation uses *fmincon* from the Matlab optimization toolbox to solve the problem above. The enforcement of constitutive laws by means of local level surrogates is a key enabler of the new TIPR algorithm. It instantly ensures the feasibility of the global level solution at both levels and thus eliminates the need for a concluding optimization at the local level.

Chapter VII

RESULTS

Prior to examining the performance of the proposed design methodology, the correct implementation and accuracy of the automated analysis framework is established. Test data is derived from a variety of theoretical and experimental beam studies. The relative percentage error in Equation 7.1 defines the figure of merit used henceforth in the performance investigation of the proposed TIPR design methodology.

$$error,\ \% = 100 \cdot \frac{k_{present} - k_{benchmark}}{k_{benchmark}} \tag{7.1}$$

The thorough validation of the analysis framework is a direct result of the very same framework being used in the performance assessment of the TIPR algorithm. Optimization examples include uniform composite beams as well as a wing model of a real world remotely piloted aircraft.

7.1 Analysis Framework Validation

The validation of the automated analyses starts with a brief introduction to composite layup terminology. Subsequent validation studies address both cross sectional and global analyses.

7.1.1 Layup Conventions

Composite layer input conventions are adopted from VABS [203]. VABS obeys two right hand rotations between three coordinate systems. Figure 7.1 illustrates these conventions on two box beam examples. First, the global system (x_1, x_2, x_3) is rotated about x_1 by the amount $0 \leq \theta_1 \leq 360$ to form the intermediate ply system (y_1, y_2, y_3), which is then rotated about y_3 by the amount $-90 \leq \theta_3 \leq 90$ to form the material property system (e_1, e_2, e_3).

Composite box beams can be categorized by the orientation of their composite layers as cross-ply, symmetric, and antisymmetric. Cross-ply layups feature alternating plies of 0

and 90. Ply stacking sequences on opposite walls of symmetric box beams are mirror images of each other with respect to the mid axes. Ply stacking sequences on opposite walls of antisymmetric box beams on the other hand are of reversed nature [34].

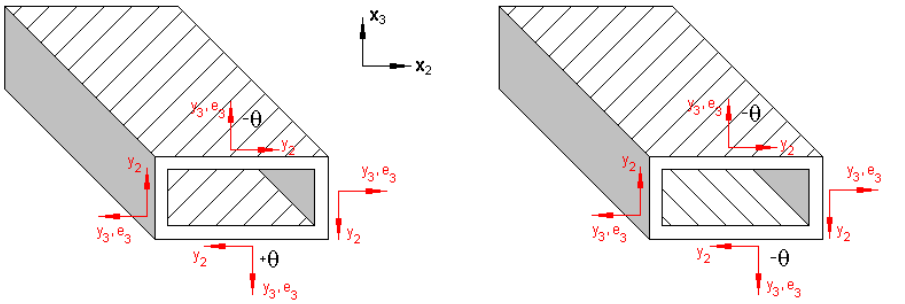

Symmetric layup (CAS)
Bending - Torsion; Extension - Shear

Antisymmetric layup (CUS)
Bending - Shear; Extension - Torsion

Figure 7.1: Layup conventions and elastic couplings

Symmetric layups result in a circumferentially asymmetric stiffness (CAS). Antisymmetric layups result in a circumferentially uniform stiffness (CUS). Their stacking sequence is defined by the layup angle θ_3. It is expressed from the innermost layer to the outermost layer. For the example beams in Figure 7.1, the same layup angle θ is assigned to each wall.

7.1.2 Cross Sectional Stiffnesses

A first validation of the correct implementation of the automated cross sectional analysis is performed using the classical 4x4 model. The constitutive relation handles extension, torsion, and bending. Corresponding axial, torsional, and two bending stiffnesses for an isotropic material are given by Equation 7.2. E denotes the Young's modulus of elasticity, G the shear modulus, A the cross sectional area, J the Saint Venant torsion constant, and I the second area moment of inertia.

$$S_{11} = EA, \qquad S_{22} = GJ, \qquad S_{33} = EI_2, \qquad S_{44} = EI_3, \tag{7.2}$$

Two closed cross sections are used. Geometric properties of the hollow rectangular cross section are listed in Table 7.5. Radius and wall thickness of the hollow circular cross section are identical to the outer width and wall thickness of the hollow rectangular section.

Corresponding moments of inertia and torsion constants can be found in standard tables [48]. The isotropic material has an elastic modulus E of 30e6 psi and a Poisson ratio $\nu = 0.3$. The stiffnesses in Tables 7.1 and 7.2 show excellent agreement with analytical results.

Table 7.1: Stiffnesses of isotropic hollow rectangular cross section

Stiffness	Analytical	VABS			Relative error, %		
		4 nodes	8 nodes	9 nodes	4 nodes	8 nodes	9 nodes
S_{11}	2.5740e6	2.5740e6	2.5740e6	2.5740e6	0	0	0
S_{22}	1.0602e5	1.1290e5	1.0926e5	1.0926e5	6.49	3.06	2.98
S_{33}	1.2664e5	1.2685e5	1.2664e5	1.2664e5	0.16	0.00	0.00
S_{44}	3.1276e5	3.1299e5	3.1276e5	3.1276e5	0.08	-0.00	-0.00

Coarse grid: IM = 10, JM = 5, KM = 1; Total number of FE: 30

Stiffness	Analytical	VABS			Relative error, %		
		4 nodes	8 nodes	9 nodes	4 nodes	8 nodes	9 nodes
S_{11}	2.5740e6	2.5740e6	2.5740e6	2.5740e6	0	0	0
S_{22}	1.0602e5	1.0862e5	1.0826e5	1.0822e5	2.46	2.11	2.08
S_{33}	1.2664e5	1.2665e5	1.2664e5	1.2664e5	0.01	0.00	0.00
S_{44}	3.1276e5	3.1277e5	3.1276e5	3.1276e5	0.00	-0.00	-0.00

Fine grid: IM = 50, JM = 25, KM = 5; Total number of FE: 750

Table 7.2: Stiffnesses of isotropic hollow circular cross section

Stiffness	Analytical	VABS			Relative error, %		
		4 nodes	8 nodes	9 nodes	4 nodes	8 nodes	9 nodes
S_{11}	5.3043e6	5.2765e6	5.2658e6	5.2658e6	-0.52	-0.73	-0.73
S_{22}	1.7954e6	1.7693e6	1.7694e6	1.7694e6	-1.46	-1.45	-1.45
S_{33}	2.3341e6	2.3113e6	2.3001e6	2.3001e6	-0.98	-1.45	-1.45
S_{44}	2.3341e6	2.3016e6	2.3004e6	2.3004e6	-1.39	-1.44	-1.44

Coarse grid: IM = 30, JM = 1; Total number of FE: 30

Stiffness	Analytical	VABS			Relative error, %		
		4 nodes	8 nodes	9 nodes	4 nodes	8 nodes	9 nodes
S_{11}	5.3043e6	5.3032e6	5.3027e6	5.3027e6	-0.02	-0.03	-0.03
S_{22}	1.7954e6	1.7943e6	1.7943e6	1.7943e6	-0.06	-0.06	-0.06
S_{33}	2.3341e6	2.3331e6	2.3327e6	2.3327e6	-0.04	-0.06	-0.06
S_{44}	2.3341e6	2.3327e6	2.3327e6	2.3327e6	-0.06	-0.06	-0.06

Fine grid: IM = 150, JM = 5; Total number of FE: 750

A solid Graphite/Epoxy beam first investigated by Abarcar and Cunniff [2] serves as validation case for a solid rectangular cross section. Width, height, and length of the beam are given as 0.5 inch, 0.125 inch, and 7.5 inch, respectively. Table 7.3 lists corresponding material properties. Table 7.4 shows the Timoshenko stiffness matrix by Yu fully reproduced

[200]. Stiffness coefficients are subject to the following index convention: 1 - extension; 2, 3 - shear; 4 - torsion; and 5, 6 - bending.

Table 7.3: Mechanical properties

Parameter	Value
E_{11}	$18.73e^6$ psi
$E_{22} = E_{33}$	$1.364e^6$ psi
G_{12}	$0.7479e^6$ psi
G_{13}	$0.6242e^6$ psi
G_{23}	$0.3686e^6$ psi
ν	0.3
ρ	$1.45e^{-4}$ $lb \cdot s^2/in^4$

Parameter	Value
E_{11}	$20.59e^6$ psi
$E_{22} = E_{33}$	$1.42e^6$ psi
$G_{12} = G_{13}$	$8.70e^5$ psi
G_{23}	$6.96e^5$ psi
$\nu_{12} = \nu_{13} = \nu_{23}$	0.42 (CAS)
$\nu_{12} = \nu_{13}$	0.30 (CUS)
ν_{23}	0.34 (CUS)

Left: Solid rectangular beam; Right: CAS/CUS box beam

Table 7.4: Solid rectangular stiffness coefficients

Stiffness	Unit	VABS	Present	Relative error, %
S_{11}	lb	0.3566e6	0.3566e6	0
S_{12}	lb	0.1274e6	0.1274e6	0
S_{22}	lb	0.1005e6	0.1005e6	0
S_{33}	lb	0.8634e4	0.8634e4	0
S_{44}	$lb.in^2$	0.5069e3	0.5069e3	0
S_{45}	$lb.in^2$	-0.3215e3	-0.3215e3	0
S_{55}	$lb.in^2$	0.4578e3	0.4578e3	0
S_{66}	$lb.in^2$	0.4062e4	0.4062e4	0

VABS results by Wenbin Yu for 30° layup orientation [200]

Further validation is performed using hollow rectangular cross sections. A cross-ply box beam with the CAS properties in Table 7.3 and stacking sequence $[0/90]_3$ for each wall confirmed no elastic couplings. The diagonal stiffness terms range from $k_{44} = 0.08e^5$ to $k_{11} = 9.43e^5$. The largest off-diagonal zero stiffness coefficient is 1.6e-8. Symmetric and antisymmetric box beam data is shown in Figure 7.2 and Table 7.7. Present results are compared to original VABS results as well as NABSA results used in the original validation of VABS itself. Details for both testbeams can be found in Tables 7.3 and 7.5.

Grid points of original and current VABS implementation coincide. In both cases, 15 elements were used along the width, 10 elements along the height, and six elements along the thickness for a total of 300 elements. The six elements along the thickness represent six composite plies.

Table 7.5: CAS/CUS beam properties

Parameter	Value
Outer width	0.953 in
Outer height	0.53 in
Wall thickness	0.03 in
Ply thickness	0.005 in

Wall	CAS	CUS
Upper	$[-15]_6$	$[-15]_6$
Lower	$[15]_6$	$[-15]_6$
Left	$[-15/15]_3$	$[-15]_6$
Right	$[15/-15]_3$	$[-15]_6$

Left: Geometry; Right: Stacking sequence

Table 7.6: Total number of elements and nodes

	Elements	Nodes
VABS original	300	700
Present 4 nodes	300	350
Present 8 nodes	300	1000
Present 9 nodes	300	1300

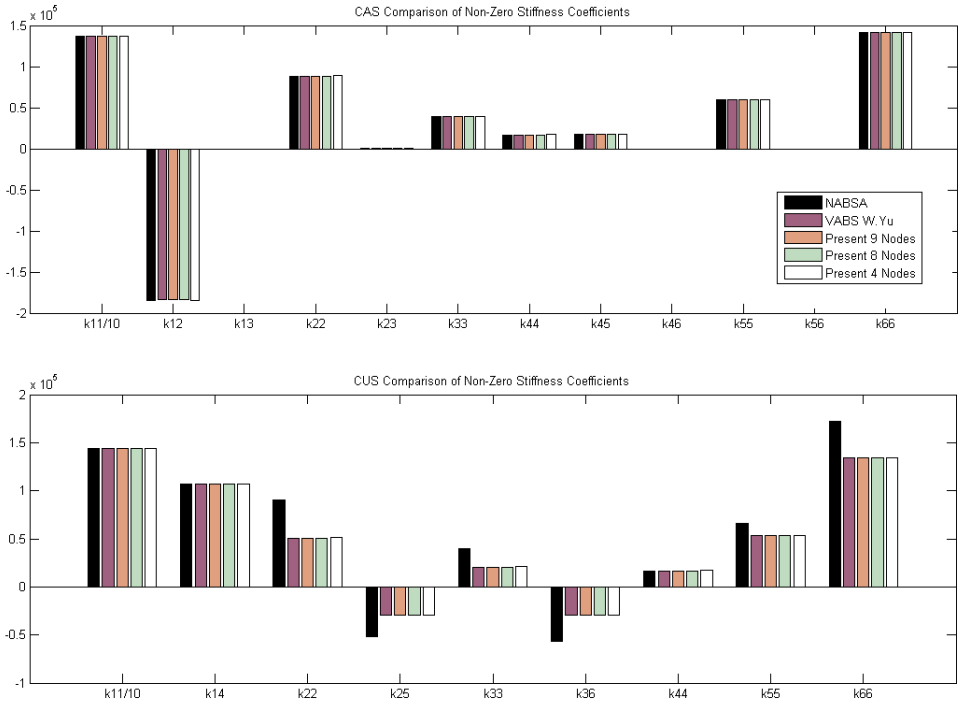

Figure 7.2: CAS/CUS stiffness results

Note that the original VABS implementation by Yu uses 6-noded elements. The present implementation allows 4-, 8- or 9-noded elements (Table 7.6). Figure 7.2 illustrates that the original VABS results by W. Yu are very well reproduced. The relative percentage error with

respect to the original VABS results in Table 7.7 shows excellent agreement for quadratic elements (8 and 9 nodes). For linear elements (4 nodes), the discrepancies can be as high as 16 percent for the CAS, and 2.6 percent for the CUS beam. The absolute value of zero coefficients remains less than 1e-7. All subsequent studies, unless specified otherwise, will use quadratic 8-noded elements in the cross sectional analysis.

Table 7.7: CAS non-zero stiffness coefficients

	NABSA	VABS W.Yu	VABS present			Relative error, %		
	9 nodes	6 nodes	4 nodes	8 nodes	9 nodes	4 nodes	8 nodes	9 nodes
S_{11}	0.137e7	1.3673e6	1.3691e6	1.3671e6	1.3670e6	0.1300	-0.0119	-0.0253
S_{12}	-0.184e6	-1.8378e5	-1.8462e5	-1.8376e5	-1.8374e5	0.4619	-0.0093	-0.0178
S_{13}	-0.150e3	-1.3256e2	-1.1031e2	-1.3460e2	-1.3448e2	-16.7818	1.5437	1.4495
S_{22}	0.885e5	8.8362e4	8.9132e4	8.8353e4	8.8341e4	0.8719	-0.0102	-0.0236
S_{23}	0.803e2	7.3025e1	6.1597e1	7.4017e1	7.4080e1	-15.6485	1.3595	1.4456
S_{33}	0.387e5	3.8778e4	3.9210e4	3.8772e4	3.8763e4	1.1150	-0.0159	-0.0385
S_{44}	0.170e5	1.6959e4	1.7097e4	1.6958e4	1.6957e4	0.8107	-0.0065	-0.0142
S_{45}	0.176e5	1.7612e4	1.7655e4	1.7611e4	1.7611e4	0.2421	-0.0051	-0.0076
S_{46}	-0.349e3	-3.5060e2	-3.4327e2	-3.5037e2	-3.5046e2	-2.0922	-0.0655	-0.0420
S_{55}	0.591e5	5.9125e4	5.9175e4	5.9116e4	5.9106e4	0.0858	-0.0151	-0.0318
S_{56}	-0.371e3	-3.7045e2	-3.6493e2	-3.7037e2	-3.7053e2	-1.4899	-0.0234	0.0198
S_{66}	0.141e6	1.4147e5	1.4193e5	1.4144e5	1.4141e5	0.3257	-0.0195	-0.0449

NABSA - Original VABS validation [202]; VABS W. Yu - Original VABS results [203]

7.1.3 Box Beam Deformations

Chandra et al. conducted experimental box beam studies that are used throughout the field for the validation of analytical and numerical box beam theories [34]. Slight differences, however, exist in the referenced box beam properties. Materials, geometry, and stacking sequences used in the validation of the current analysis framework can be found in Tables 7.8, 7.5, and 7.9, respectively. Unless specified otherwise, the global beam model uses four cubic finite elements.

The antisymmetric box beam B1 is known to show significant differences [205]. Figure 7.3 illustrates the validation of two stacking sequences. The lower plot shows the present implementation fully reproducing published VABS results. The upper plot illustrates the mentioned discrepancies. Note that the $[15]_6$ layup documented by Popescu and Jung et al. [148, 94] is incorrect. Both used a $[-15]_6$ stacking sequence [200].

Table 7.8: Mechanical properties of AS4/3501-6

Parameter	Value
E_{11}	$20.59e^6\ psi$
E_{22}	$1.42e^6\ psi$
G_{12}	$8.90e^5\ psi$
ν_{12}	0.42
ρ	$1.35e^{-4}\ lb \cdot s^2/in^4$

Hercules AS4/3501-6 Graphite/Epoxy used by Chandra et al. [34]

Table 7.9: Stacking sequence of box beams B1-B5

Wall	B1	B2	B3	B4	B5
Upper	$[15]_6$	$[-30]_6$	$[-15]_6$	$[0/45]_3$	$[-45]_6$
Lower	$[15]_6$	$[30]_6$	$[15]_6$	$[0/45]_3$	$[45]_6$
Left	$[15]_6$	$[-30/30]_3$	$[-15/15]_3$	$[0/45]_3$	$[-45/45]_3$
Right	$[15]_6$	$[30/-30]_3$	$[15/-15]_3$	$[0/45]_3$	$[45/-45]_3$

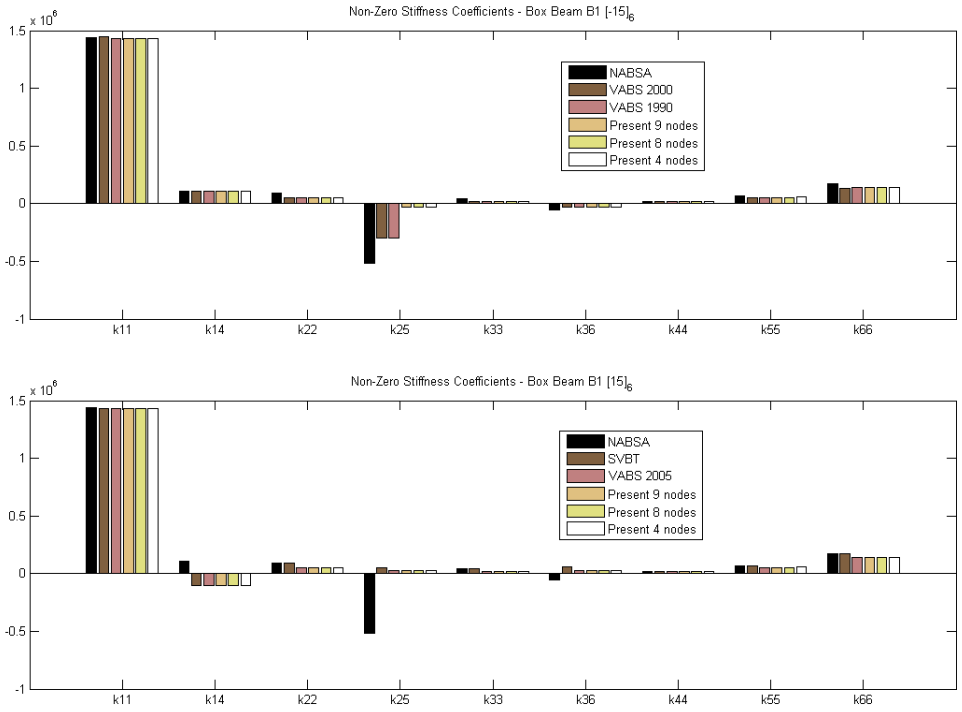

Figure 7.3: B1 stiffness results

References: NABSA, VABS 2000, VABS 1990 [94]; SVBT, VABS 2005 [200]

Yu finds that the Chandra box beam B1 is the only case to have noteworthy discrepancies compared to the Saint-Venant approach (SVBT) and NABSA [200]. Shear and bending-shear stiffnesses, however, are of less importance for slender beams [94]. The excellent

agreement with experimental and analytical results shown in Figures 7.4 and 7.5 confirm the negligibility of corresponding structural effects.

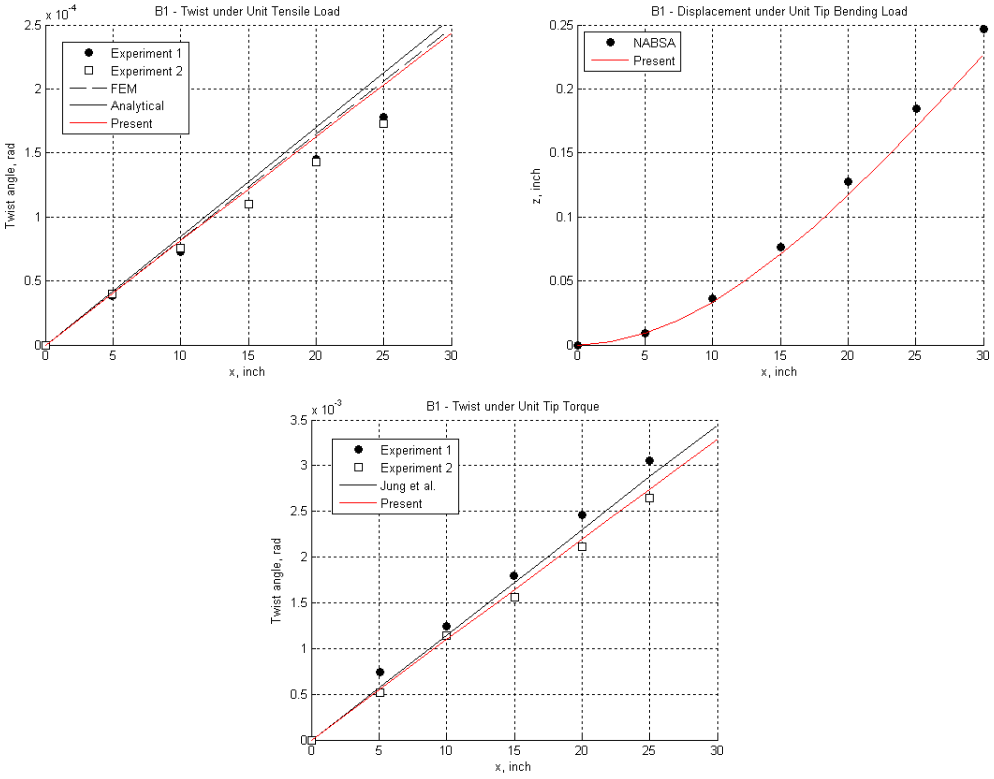

Figure 7.4: Antisymmetric box beam B1 deformation under unit tip load
References: Experiment 1, Experiment 2, FEM, Analytical [34]; NABSA [94]

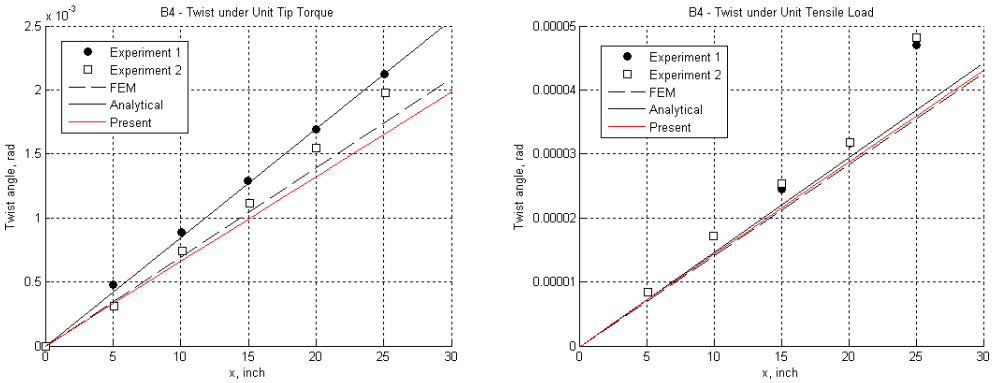

Figure 7.5: Antisymmetric box beam B4 deformation under unit tip load
Figures 19 and 20 in Chandra et al. [34]

The symmetric box beams B2, B3, and B5 produce very good results for bending induced twist but lack fidelity for torsional tip loading. Figures 7.6, 7.7, and 7.8 show qualitative and quantitative discrepancies. Cross sectional properties reveal no abnormalities. The stiffness matrices are properly populated. Maximum non-zero coefficients are 1e-7.

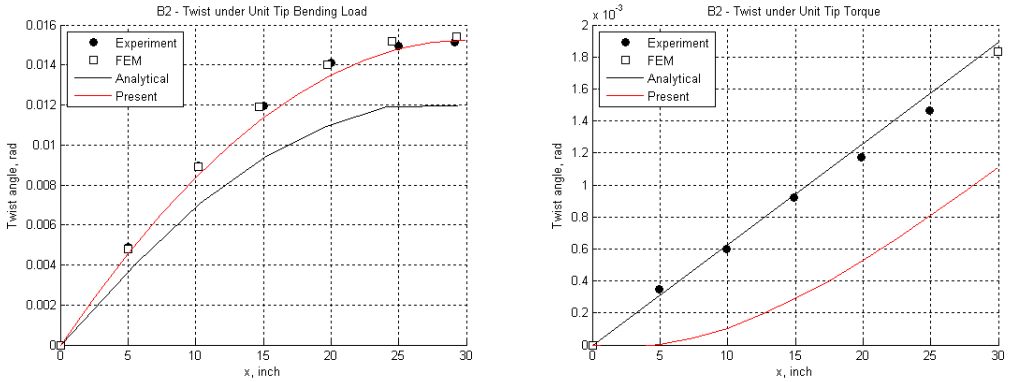

Figure 7.6: Symmetric box beam B2 deformation under unit tip load
Figures 6 and 11 in Chandra et al. [34]

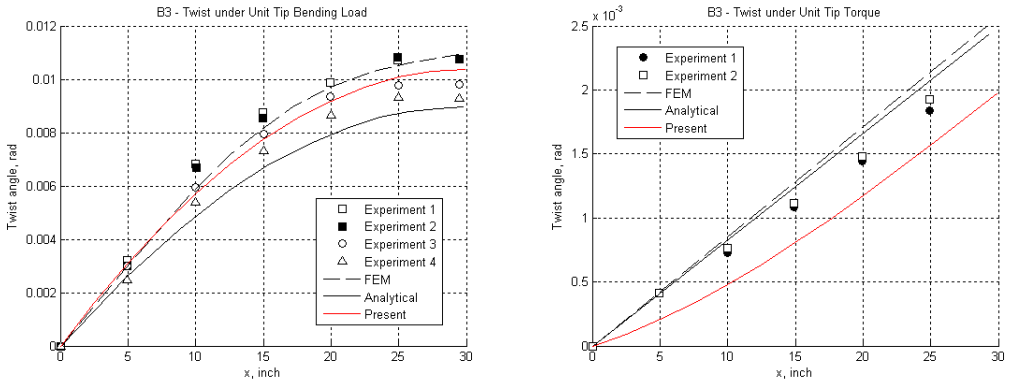

Figure 7.7: Symmetric box beam B3 deformation under unit tip load
Figures 4 and 9 in Chandra et al. [34]

Further investigations of the twist angle in dependence of the ply angle $\theta_3 = \theta$ are shown in Figure 7.9. Antisymmetric box beams adhere to a stacking sequence of $[0/\theta]_3$. Symmetric box beams adhere to $[\theta]_6$ and $[-\theta]_6$ for top and bottom, and $[\theta/-\theta]_3$ and $[-\theta/\theta]_3$ for side walls. Present results compare well to theoretical and experimental data. Note that the extension induced twist angle published by Smith and Chopra (lower right in Figure 7.9)

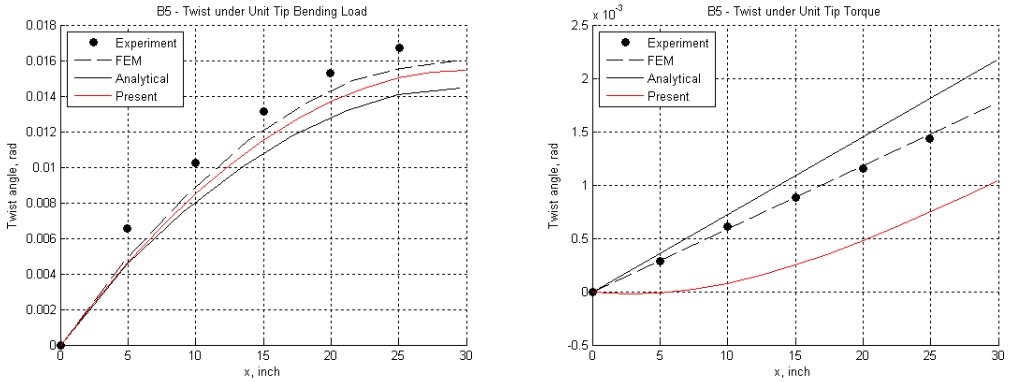

Figure 7.8: Symmetric box beam B5 deformation under unit tip load

Figures 8 and 13 in Chandra et al. [34]

was reduced by one order of magnitude to be consistent with respective results published by Chandra et al. [34], Kim et al. [99], and Qin and Librescu [149].

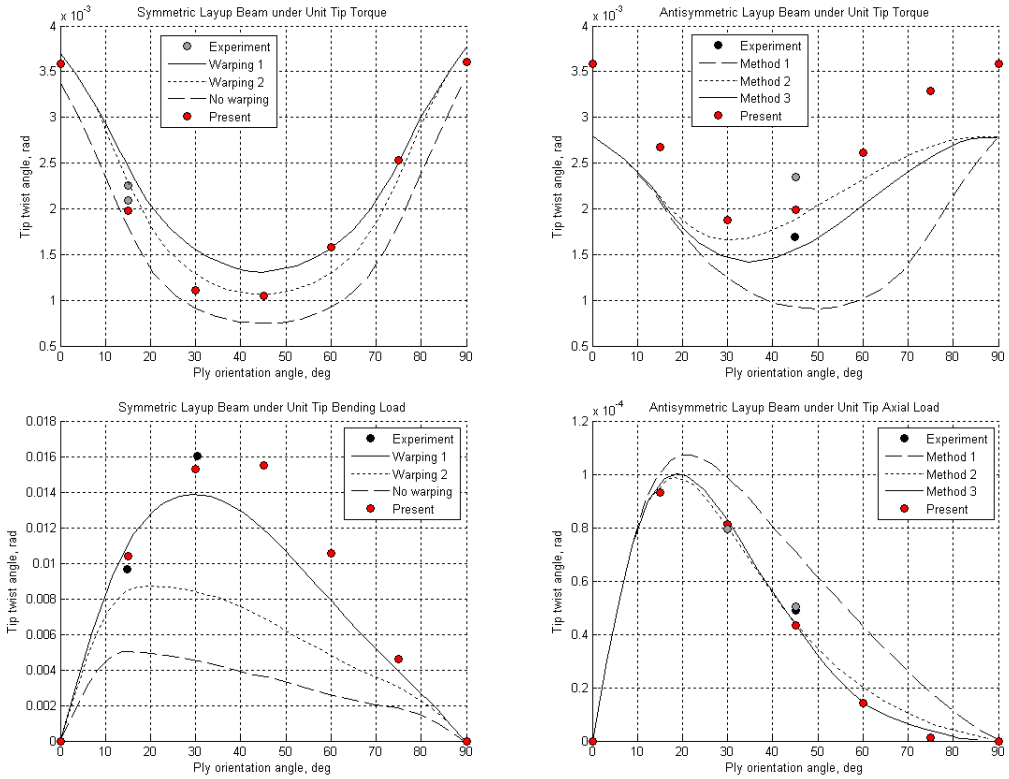

Figure 7.9: Effect of ply orientation on tip twist

Figures 7a & 7b (left) and Figures 9a & 9b (right) in Smith et al. [171]

Experiments: Smith et al. [171] published (black), Chandra et al. [34] extrapolation (gray)

The box beam B5 also served the validation of a higher-order laminate plate formulation. Geometric and material properties are published in McCarthy and Chattopadhyay [125]. Figure 7.10 shows the present implementation as good as reproducing the correlation studies by Chattopadhyay et al. [35].

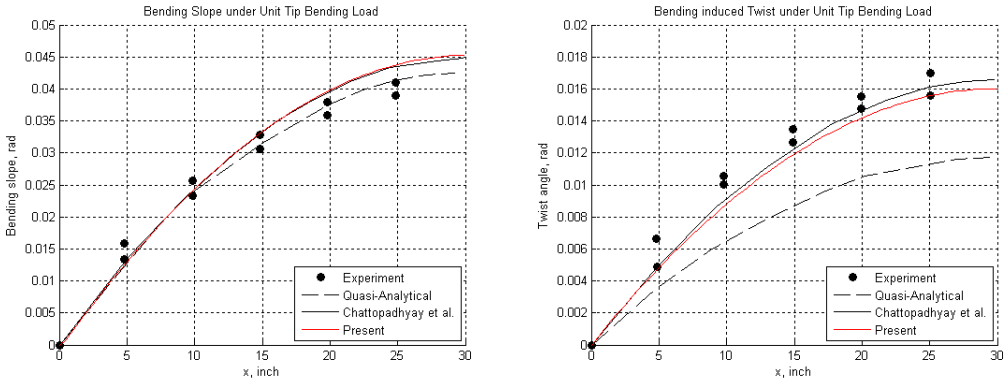

Figure 7.10: Static box beam results
Figures 5 and 6 in Chattopadhyay et al. [35]

7.1.4 Circular Beam Deformations

The composite hollow circular beams with thin and thick walls used for the validation of the present analysis framework were investigated by Kim and White [99]. Mechanical and geometrical properties are summarized in Tables 7.10 and 7.11, respectively. Figures 7.11 and 7.12 show the present implementation in excellent agreement with published results. Stacking sequences correspond to an antisymmetric layup.

Table 7.10: Mechanical properties of T300/5208

Parameter	Value
E_{11}	146.85 GPa
$E_{22} = E_{33}$	11.03 GPa
$G_{12} = G_{13}$	6.21 GPa
G_{23}	3.86 GPa
$\nu_{12} = \nu_{13}$	0.28
ν_{23}	0.50

T300/5208 Graphite/Epoxy [99]

Table 7.11: Circular beam geometry

	Thin wall		Thick wall	
	SI, mm	US, inch	SI, mm	US, inch
Length	356.0	14.02	1524.0	60.0
Outer radius	21.0	0.83	50.8	2.0
Wall thickness	1.0	0.04	15.2	0.60
Ply thickness	0.127	0.005	0.127	0.005

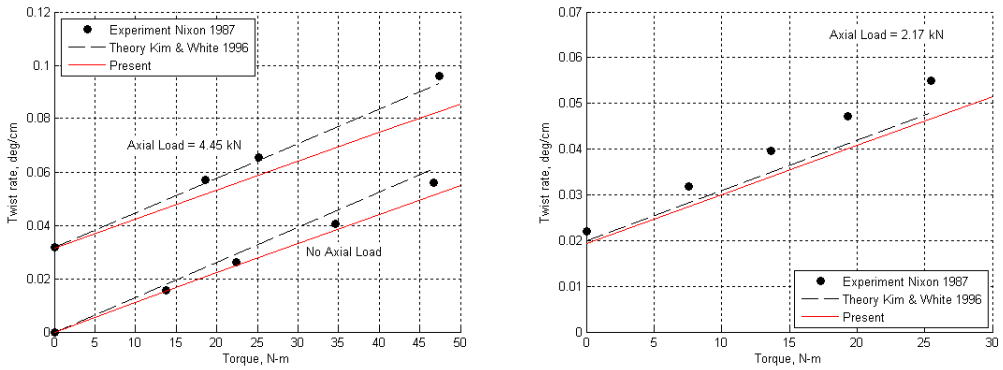

Figure 7.11: Twist rate as function of tip torque
Figures 3 and 4 for $[20°/-70°]_4$ (left) and $[40°/50°]_4$ (right) thin-walled circular beam in Kim and White [99]

7.1.5 Natural Frequencies

Natural frequencies show reasonable agreement to experimental and theoretical vibration studies by Chandra and Chopra [33]. Figure 7.13 reveals the relative percentage error of present results with respect to experimental data to not be fully satisfactory. However, the present implementation compares very well to other theories.

A second validation study is performed using a series of symmetric Graphite/Epoxy box beams (Table 7.8). Inner dimensions are stated in Table 7.5. The beam length is 33.25 inch. The stacking sequence denotes $[\theta]_6$ for horizontal, and $[\theta/-\theta]_3$ for vertical walls. The natural frequencies of the first eigenmode show excellent agreement for both nonrotating and rotating operating condition.

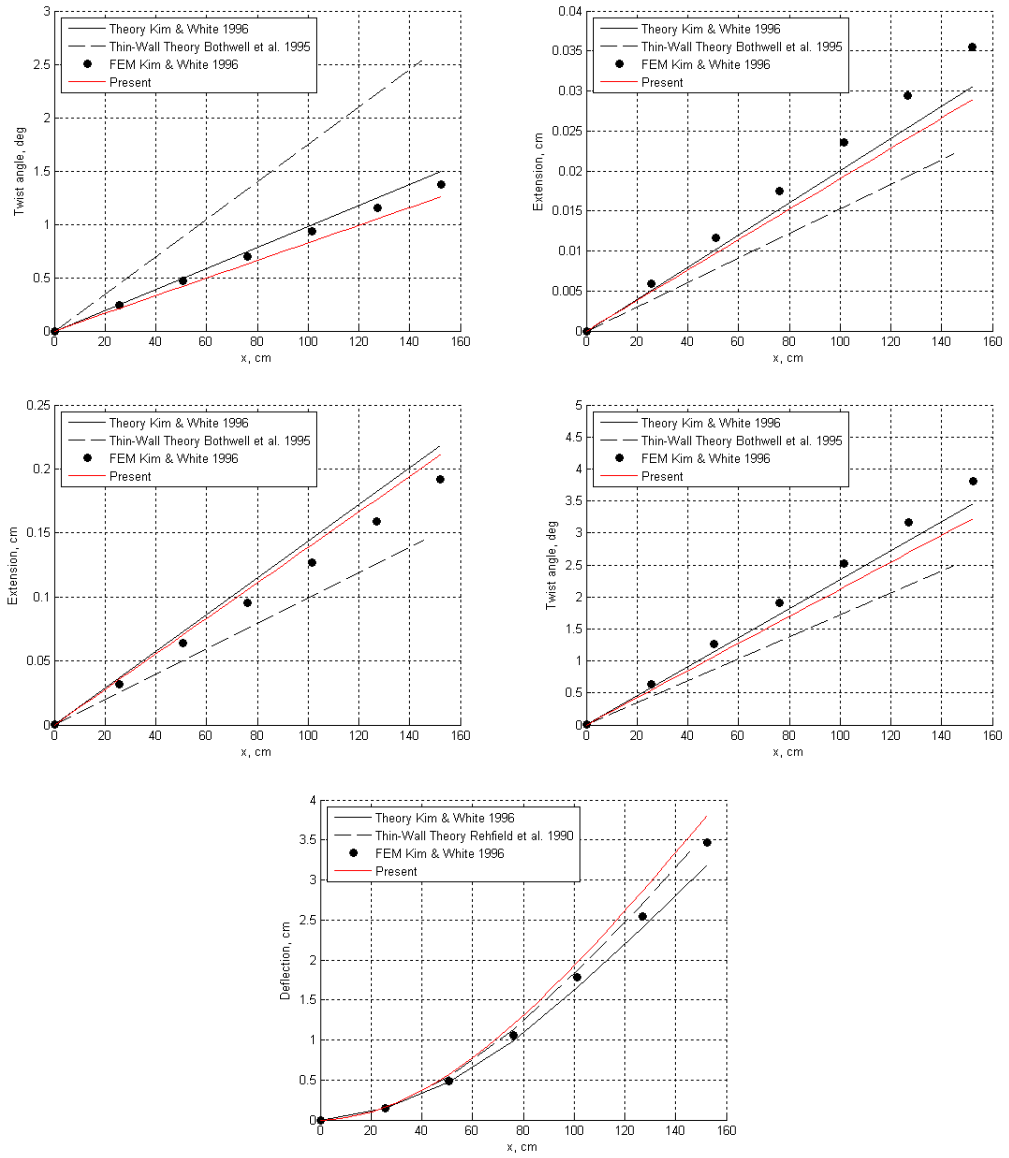

Figure 7.12: Thick-walled circular beam deformations

Figures 5 - 9 for composite layup of $[20^{\circ}_{30}/70^{\circ}_{30}]_2$ in Kim and White [99]

Load cases: 1.13 kN-m tip torque (top), 222.5 kN tip axial load (middle), 4.45 kN tip shear load (bottom)

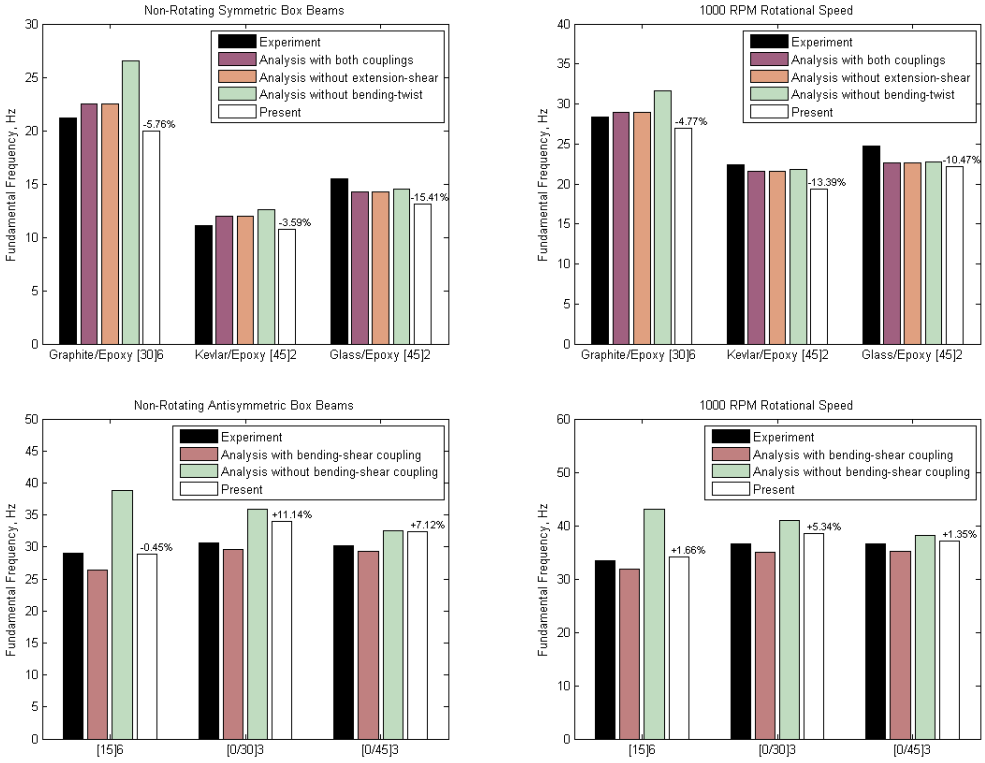

Figure 7.13: Box beam natural frequencies

Symmetric (top) and antisymmetric (bottom) box beam natural frequencies

Top: Figures 4 and 5, Bottom: Figures 11 and 12 in Chandra and Chopra [33]

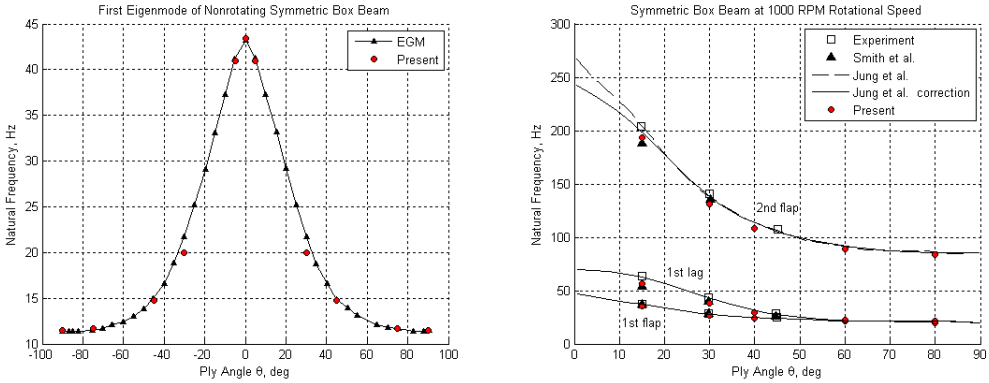

Figure 7.14: Symmetric box beam natural frequencies

Nonrotating (left) and rotating (right) natural frequencies

Left: Figure 8 in Qin and Librescu [149], EGM - Extended Galerkin's Method; Right: Figure 2 in Jung et al. [92] with experiments by Chandra et al. [32], and Smith et al. [172]

The vibration analysis of the solid rectangular beam described in Tables 7.3 and 7.4 fully reproduces the results by Yu [200]. Tables 7.12 and 7.13 show the lowest frequencies comparing very well to published data. Agreement deteriorates with increasing mode number but remains within an acceptable margin of scattered results. The relative percentage error in Tables 7.12 and 7.13 is computed using the presented results from the experiment.

Table 7.12: Solid rectangular beam frequencies

Mode	Experiment	SCBE	ANSYS	BDR	Present	Relative error, %
1	52.7	52.8	54.4	52.6	52.6	-0.19
2	n/a	210.0	214.3	209.8	209.8	n/a
3	331.8	329.5	339.7	326.3	326.3	-1.66
4	924.7	916.1	947.1	899.8	899.8	-2.69
5	n/a	1263.9	1317.4	1284.9	1284.9	n/a
6	1766.9	1756.0	1685.5	1661.3	1661.3	-5.98
7	1827.4	1858.0	1857.5	1744.8	1744.8	-4.52
8	2984.0	2909.6	3038.5	2782.9	2782.9	-6.74

Solid rectangular beam with 30° symmetric layup

Experiment by Abarcar et al. [2]; Super Convergent Beam Element (SCBE) by Mitra et al. [127]; Beam Dimensional Reduction (BDR) by Yu [200]

Table 7.13: Solid rectangular beam frequencies

Mode	Experiment	Analysis	RSDM	Present	Relative error, %
1	82.5	80.8	82.2	82.0	-0.65
2	n/a	n/a	329.2	325.7	n/a
3	511.3	501.5	511.8	502.7	-1.69
4	1423.4	1376.0	1415.4	1356.2	-4.72
5	1526.9	1579.3	1742.9	1499.3	-1.81
6	n/a	n/a	2062.9	1926.0	n/a
7	2783.6	2648.7	2747.6	2565.4	-7.84
8	4364.6	4189.0	4413.7	3983.5	-8.73

Solid rectangular beam with 15° symmetric layup

Experiment and Analysis by Abarcar et al. [2]; Refined Structural Dynamics Model (RSDM) by Jung et al. [95]

7.1.6 Structural Weight

The weight calculation of the present implementation utilizes the mass per unit span output by VABS in a linear weight summation. Nonlinear cross sectional geometries with will thus exhibit a dependence on the cross sectional finite element grid. Grid refinement will improve the shape representation. Table 7.14 contains weight results for the hollow circular tube in

very good agreement to the exact solution even for coarse grids.

Chattopadhyay et al. implemented an optimization scheme for the weight minimization of the box beam in Figure 3.12. The documented approach for corresponding calculations, however, reveals a small deficiency. The box beam weight is computed by determining the surface areas; and multiplying those by wall thickness, density, and gravitational acceleration. As a result, the box beam volume contains the overlapping areas in the corners of the box beam cross section twice. Figure 7.15 shows the structural weight results of baseline and optimized solution. Present results bear close resemblance to the analytical solution of an obelisk with identical footprints.

Table 7.14: Hollow circular tube weight

Grid	Weight, lbs	Relative error, %
20 x 6	0.835358	-1.63
40 x 12	0.845720	-0.41
60 x 18	0.847695	-0.18
80 x 24	0.848350	-0.10
100 x 30	0.848667	-0.07
200 x 60	0.849088	-0.02
Analytical	0.849225	0

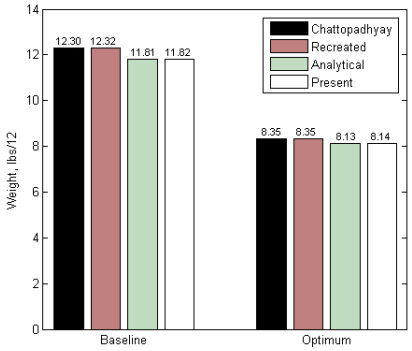

Figure 7.15: Wing box weights

7.2 Box Beam TIPR

The cross section of the uniform box beam used is shown in Figure 7.16. The two-dimensional design space consists of wall thickness dt and ply angle θ. Baseline values are $dt = 0.03$ and $\theta = 45°$. Lower and upper bounds are [0.02 0.04] and [0 90], respectively.

The six plies along the box beam walls have identical thickness. DOE settings have three equidistant design sites along dt and 21 equidistant design sites along θ. The discrete representation of the cross section relies on 15 finite elements along the width, 10 along the height, and six along the wall thickness. The global beam model uses four second order finite elements.

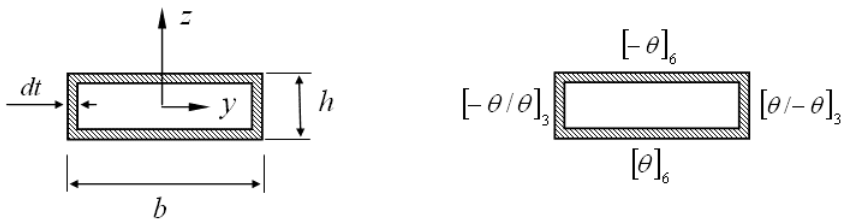

Figure 7.16: Box beam cross section

The first phase of the stiffness selection process screens for potential cross couplings using the DOE cross sectional stiffness results. As expected, the CAS beam reveals extension-shear (1,2) and bending-torsion (4,5) coupling. Surrogate models are created for mass per unit span, all main stiffness coefficients, and the two potential cross couplings. Figure 7.17 shows normalized examples of respective surrogates. The second phase of the stiffness selection process employs generalized main stiffness effects to find the intermediate design variables.

The implementation results of the box beam example are presented in two consecutive parts. A first study investigates the relative error for a single TIPR increment using varying TIPR parameters. A second study adheres to an overall design goal that is achieved by incrementally applying the TIPR algorithm.

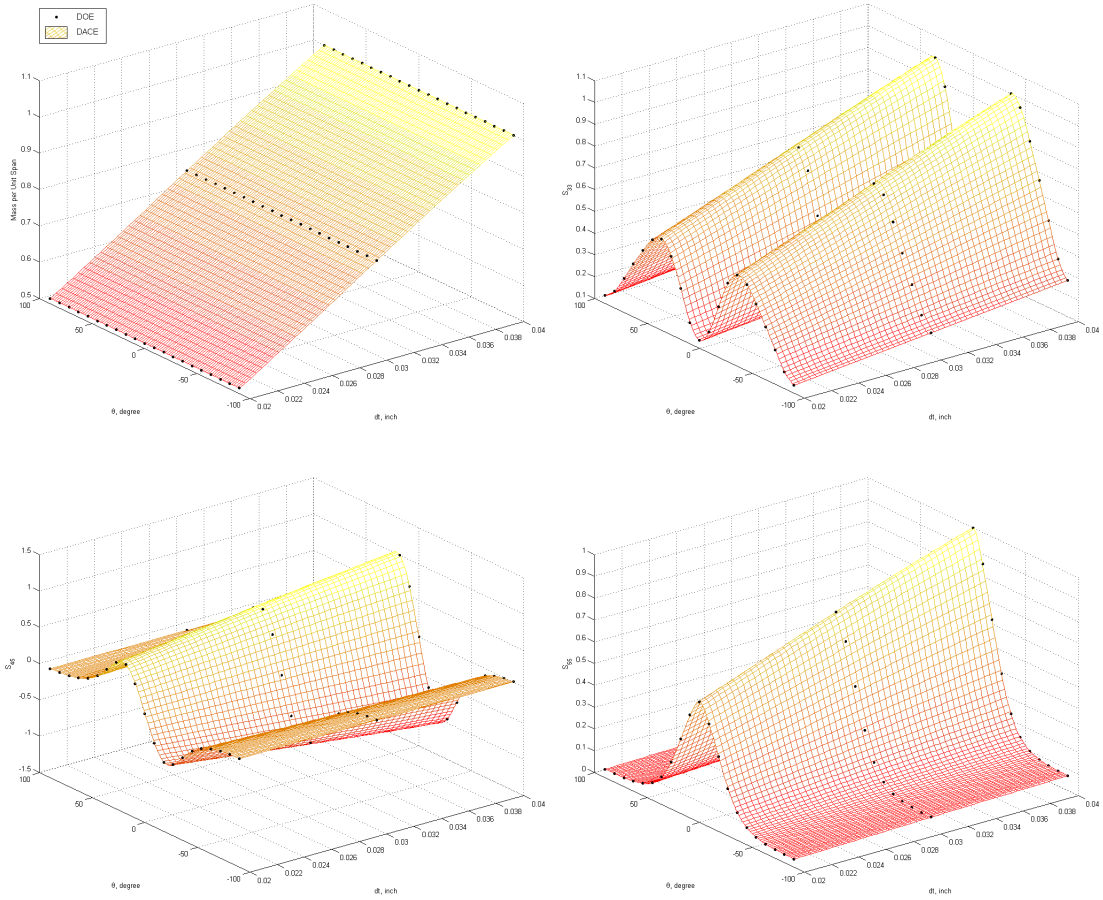

Figure 7.17: Box beam surrogate models

Kriging model using DACE and zero order polynomial along with cubic spline correlation function

Mean Square Error: $m = 0.0000,\ S_{33} = 0.0010,\ S_{45} = 0.0030,\ S_{55} = 0.0007$

7.2.1 Relative Error Study

The objective function of the relative error study is a minimum change from the baseline. The frequency objective is to increase the first natural frequency. The corresponding modal inequality constraint specifies the first natural frequency of the objective system to be greater or equal that of the baseline system.

The redesign problem for the box beam relative error study reads as follows.

Minimize:

$$F(x) = \{\alpha\}^T \{\alpha\} \qquad \text{Objective function}$$

with

$$\{\alpha\}^T = \left\{ \begin{array}{cccc} \alpha_3 & \alpha_4 & \alpha_5 & \alpha_m \end{array} \right\}$$

Subject to:

$$[P]\{\alpha\} + \Delta K_{CC} \geqq \triangle\omega_1^2 \qquad \text{Modal constraint}$$

with

$$\alpha_n = \frac{f_S(x)}{S_{base}} - 1, \quad \alpha_m = \frac{f_m(x)}{m_{base}} - 1 \qquad \text{Viability constraints}$$

$$n = 3, 4, 5$$

and

$$x = \left\{ \begin{array}{c} dt \\ \theta \end{array} \right\} \qquad \text{Design variables}$$

with

$$\left\{ \begin{array}{c} 0.02 \\ 0 \end{array} \right\} \leq x \leq \left\{ \begin{array}{c} 0.04 \\ 90 \end{array} \right\} \qquad \text{Side constraints}$$

Figure 7.18 shows the TIPR performance for an increasing frequency objective. The relative percentage error is calculated using $\hat{\Omega}$, the frequency determined by the TIPR equation; and Ω, the frequency determined by a DYMORE reanalysis after application of the TIPR determined stiffness changes. The TIPR frequency $\hat{\Omega}$ is arrived at by rearranging the modal constraint in the above optimization problem.

$$error = 100 \cdot \frac{\hat{\Omega}_1 - \Omega_1}{\Omega_1}$$

$$\hat{\Omega}_1 = \sqrt{[P]\{\alpha\} + \Delta K_{CC} + \omega_1^2}$$

The minimum change redesign objective results in an equality satisfaction of the modal constraint. Small and moderate frequency objectives result in negligible errors.

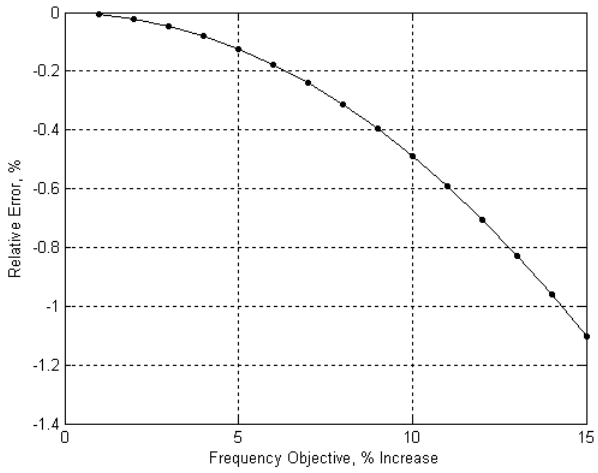

Figure 7.18: Box beam minimum change relative error
$F(x) = \{\alpha\}^T \{\alpha\}, \quad [P]\{\alpha\} + \Delta K_{CC} \geqq \triangle\omega_1^2$

Figure 7.19 presents two more redesign studies of the CAS beam. The difference to the previous redesign problem is that the new objective function in terms of minimum mass requires additional constraints in form of lower and upper limits on the constitutive variables. The results in Figure 7.19 plot the relative error in the natural frequency over an increasing magnitude of α bounds. A white face color for data points indicates that the optimizer was unable to find a feasible solution to the posed redesign problem.

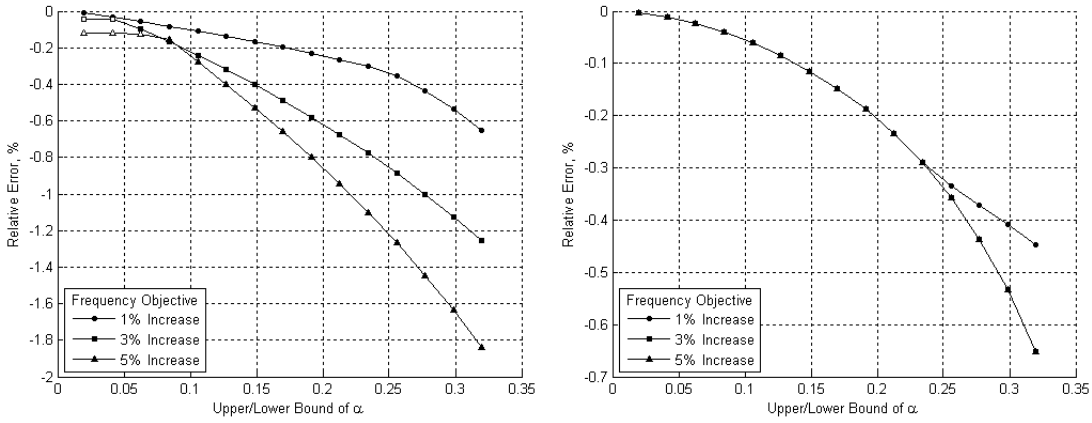

Figure 7.19: Box beam minimum mass relative error

$F(x) = \alpha_m,\ \alpha^L \leqq \alpha \leqq \alpha^U,$ Left: $[P]\{\alpha\} + \Delta K_{CC} \geqq \triangle\omega_1^2,$ Right: $[P]\{\alpha\} + \Delta K_{CC} \leqq \triangle\omega_1^2$

Minimum mass is the objective desired by the conceptual design engineer. For the CAS beam at hand, increasing the first natural frequency to or above the modal objective while at the same time minimizing mass is constrained by the lower bound on α_m. The results on the right in Figure 7.19 show a range of identical errors for all three frequency objectives. That is because the optimizer arrives at the same frequency that is below the one specified, and the optimum solution is then bound and characterized by the same lower limit on α_m.

The trends in Figures 7.18 and 7.19 clearly indicate a TIPR performance deterioration for increasing magnitude in changes. Both frequency objective and structural changes in terms of alpha need to reflect the small perturbation assumption to maintain validity of the TIPR equation.

7.2.2 Optimization Study

Because the flutter speed increases with the frequency of the underlying natural mode, the CAS beam from the above redesign study is subjected to a 30 percent total increase in the first natural frequency. TIPR is applied in increments. After each increment, the structural system is updated using the structural changes determined by TIPR. A reanalysis of the global problem then provides the baseline for the new increment and enables an incremental progression towards the specified objective system.

Figure 7.20 shows the relative frequency error for different incremental size over the duration of the TIPR based optimization. It confirms a superior performance of smaller changes. Corresponding design variable changes are presented in Figure 7.21.

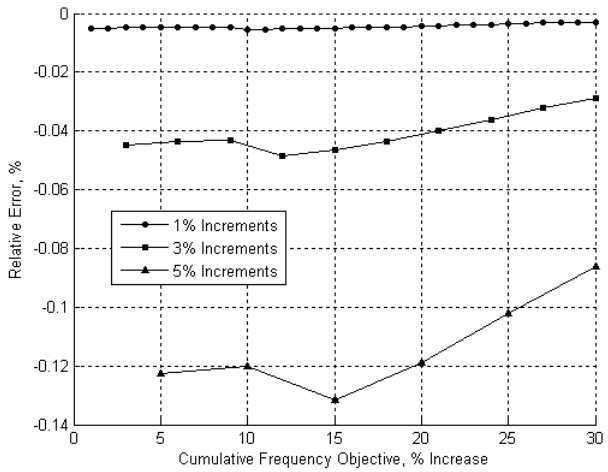

Figure 7.20: Box beam minimum change incremental error
$F(x) = \{\alpha\}^T \{\alpha\}, \quad [P]\{\alpha\} + \Delta K_{CC} \geqq \triangle\omega_1^2$

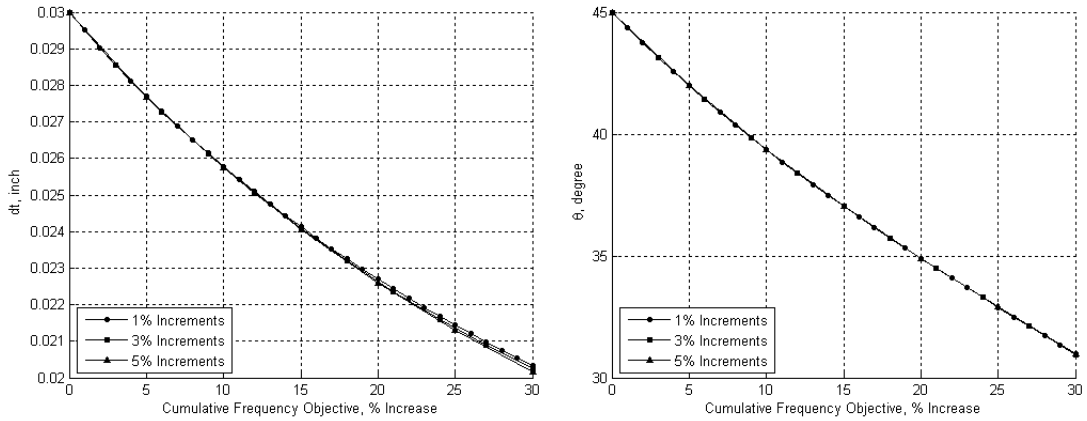

Figure 7.21: Box beam minimum change design variables
$F(x) = \{\alpha\}^T \{\alpha\}, \quad [P]\{\alpha\} + \Delta K_{CC} \geqq \triangle\omega_1^2$

Figure 7.22 corresponds to Figure 7.19. The relative error measures the performance of the TIPR based optimization using a minimum mass objective function. Structural changes have an incremental limit of five percent. Data points with white face color indicate an infeasible solution.

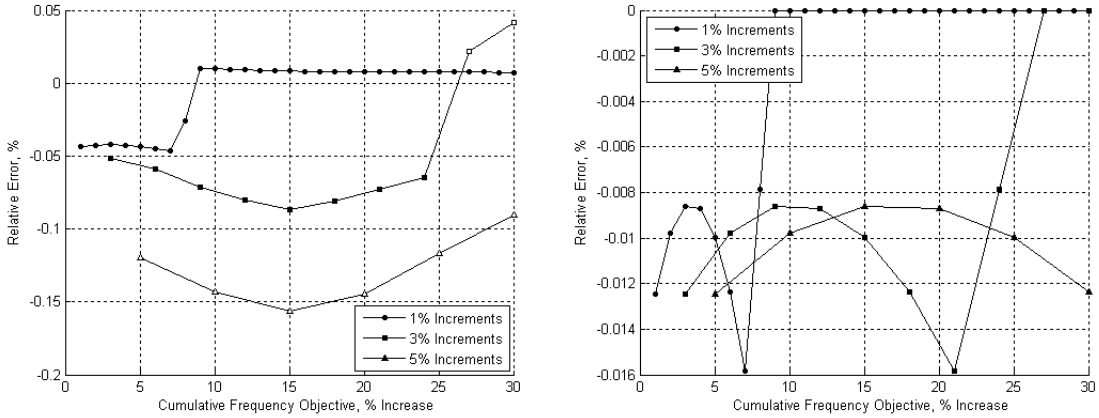

Figure 7.22: Box beam minimum mass incremental error

$F(x) = \alpha_m,\ \alpha^L \leqq \alpha \leqq \alpha^U,$ Left: $[P]\{\alpha\} + \Delta K_{CC} \geqq \triangle\omega_1^2,$ Right: $[P]\{\alpha\} + \Delta K_{CC} \leqq \triangle\omega_1^2$

The behavior of the relative error shows some distinctive traits. Looking at the problem on the left hand side: The optimization with one percent incremental change arrives at the lower limit of wall thickness at the end of the eighth increment. From there on only the layup angle is changed to satisfy the frequency constraint. The last two increments of the optimization sequence using a three percent frequency increase need to violate the lower bound on wall thickness to produce a solution compliant with objective and modal constraint. The optimization with five percent frequency increments is infeasible given the bounds on structural changes.

The optimization problem on the right hand side seeks a minimum mass solution with a frequency constraint that specifies an upper limit on the change. It thus requires no frequency increase and all three optimizations only change wall thickness. Once the the lower limit of wall thickness is reached, no more changes are applied. Note that the abscissa designates the cumulative frequency increase, not the increment number. Counting the individual increment points on respective plots, one can easily determine that the size of the incremental frequency change has no influence here. All three optimizations arrive at the lower limit of wall thickness at the eighth increment by changing the mass properties according to the alpha limit.

The performance of the TIPR based optimization is compared to a gradient based optimization algorithm. The latter is implemented as a Sequential Quadratic Programming (SQP) problem via *fmincon* in the Matlab optimization toolbox. The objective function for the comparison study is minimum mass. The modal constraint is specified as a minimum increase of 30 percent in the first natural frequency. Starting point is the CAS beam above with a wall thickness of $dt = 0.03$ inch and a ply angle of $\theta = 45°$.

The TIPR formulation of the problem reads as follows.

Minimize:

$$F(x) = \alpha_m \qquad \text{Objective function}$$

Subject to:

$$[P]\{\alpha\} + \Delta K_{CC} \geqq \triangle\omega_1^2 \qquad \text{Modal constraint}$$

with

$$\{\alpha\}^T = \left\{ \begin{array}{cccc} \alpha_3 & \alpha_4 & \alpha_5 & \alpha_m \end{array} \right\}$$

and

$$\alpha_n = \frac{f_S(x)}{S} - 1, \quad \alpha_m = \frac{f_m(x)}{m} - 1 \qquad \text{Viability constraints}$$

$$-0.03 \leqq \alpha_{n,m} \leqq 0.03,\ n = 3, 4, 5$$

where

$$x = \left\{ \begin{array}{c} dt \\ \theta \end{array} \right\} \qquad \text{Design variables}$$

with

$$\left\{ \begin{array}{c} 0.02 \\ 0 \end{array} \right\} \leqq x \leqq \left\{ \begin{array}{c} 0.04 \\ 90 \end{array} \right\} \qquad \text{Side constraints}$$

The corresponding SQP formulation is presented below.

Minimize:

$$F(x) = mass \qquad \text{Objective function}$$

Subject to:

$$g = 1.3 \cdot \omega_1^{base} - \omega_1 \leqq 0 \qquad \text{Modal constraint}$$

with

$$x = \left\{ \begin{array}{c} dt \\ \theta \end{array} \right\} \qquad \text{Design variables}$$

and

$$\left\{ \begin{array}{c} 0.02 \\ 0 \end{array} \right\} \leqq x \leqq \left\{ \begin{array}{c} 0.04 \\ 90 \end{array} \right\} \qquad \text{Side constraints}$$

SQP solves a quadratic subproblem at each iteration. That is, the search problem is solved using a quadratic approximation of the objective function subject to linear approximations of the constraints. Gradient information is based on (first order) finite differences [190]. The Matlab implementation of SQP relies on formulae presented in references [57, 74].

Figure 7.24 shows the optimization progress for SQP and TIPR. Design variables are normalized due to magnitude differences. To allow a valid comparison and to yield design space movements of similar size, TIPR uses two percent frequency increments. The results in Figure 7.24 show an approximate design variable change of three percent per iteration or increment. Figure 7.23 presents corresponding changes in the objective frequency of an average two percent per iteration or increment.

The similarities in Figures 7.24 and 7.23 confirm that an iteration in SQP is equivalent to an increment in the TIPR based optimization algorithm. For the minimum mass example presented, the TIPR alpha limits are equivalent to the SQP step size. Both methods march

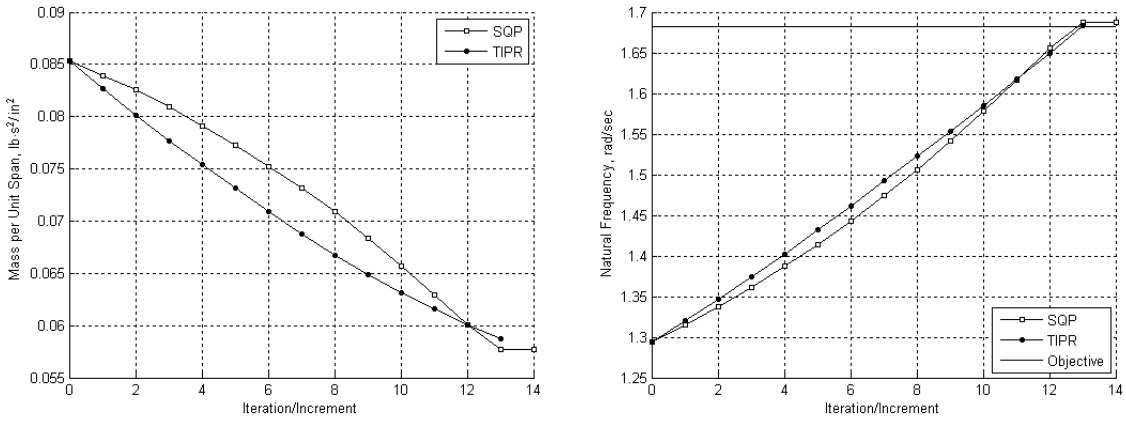

Figure 7.23: Box beam objective and constraint

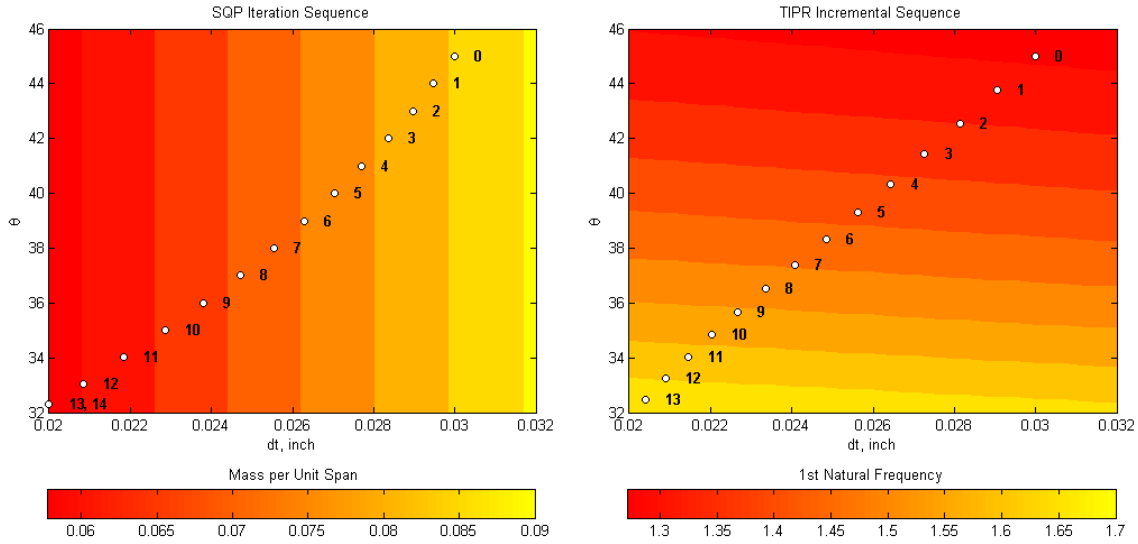

Figure 7.24: Box beam design space comparison

Contours based on VABS/DYMORE results on 11x11 analysis grid

in the same direction and arrive at the essentially same solution. The major difference lies in the efficiency of getting to this solution.

Table 7.16 shows what Figure 7.24 fails to disclose. SQP requires two additional function calls per iteration for the gradient evaluation that serves the determination of the search direction. These additional function calls consist of running both VABS at the local and DYMORE at the global level.

Iteration zero in Figure 7.24 designates the baseline. It requires three FEA to initiate

the first iteration. One for the baseline itself, and one additional FEA per design variable for the gradient evaluation. The total number of function calls for SQP thus evaluates to 45. In contrast, TIPR evaluates the baseline system by running a global FEA. It then performs the small perturbation analysis to redesign for the incremental change, updates structural properties by applying the changes that the TIPR calculated, and has at its disposal the baseline of the new increment without any additional FEA.

Table 7.15 validates the TIPR natural frequency of the first mode. *Baseline* corresponds to the initial starting point of the optimization, *Objective* to the minimum desired increase of 30 percent. *Final TIPR* shows the converged TIPR solution. The convergence criterion equals satisfaction of the modal objective. The last entry in Table 7.15 uses the design variable values determined in the last TIPR increment in a complete two level reanalysis. Table 7.15 confirms the accuracy of both TIPR optimization and DACE model.

Table 7.15: Box beam TIPR frequency validation

	Frequency, rad/sec
Baseline	1.2943
Objective	1.6825
Final TIPR	1.6832
VABS/DYMORE	1.6804

Table 7.16 compares computing time. The two TIPR listings differ in the execution of local level analyses. The first TIPR in Table 7.16 runs VABS 63 times to provide local level results necessary to create the surrogate models shown in Figure 7.17. The second TIPR avoids local level DOE runs by using the DOE results from the first TIPR.

The absolute times necessary for each optimization confirm the incremental TIPR based optimization to be more efficient than the gradient based optimization. SQP is computationally more expensive. TIPR requires less FEA regardless of the necessity of local level DOE analyses. It is particularly attractive when local level surrogate models are already in place.

The question of using a surrogate model for both local and global analyses inherently poses itself. Why not approximate the relationship between design variables and system metrics without the two level decomposition. The question exhibits undeniable validity.

Table 7.16: Box beam computational expenses

Number of	SQP	TIPR*	TIPR**
Local function calls	45	63	0
Global function calls	45	14	14
Iterations/Increments	14	13	13
Total Time, sec	199	99	58
Total Time, min	3.3	1.7	1.0

* 63 DOE runs of VABS to create local level surrogates; ** Using saved DOE data to omit VABS runs

Respective approaches are promising indeed and numerous successful implementations exist in the literature. The quest of the current research, however, was to find a way to utilize the advantages of beam dimensional reduction and small perturbation theory. The presented approach achieved exactly that. Running the same DOE of 63 experiments for the present example at both local and global level took 266 seconds (4.4 minutes).

7.3 Flat Beam TIPR

The second TIPR testcase is a uniform cantilever flat beam of 0.4 meter length. The symmetric cross section and the composite material properties are identical to those used by Tailor and Butler [185]. Figure 7.25 shows the balanced stacking sequence of the initial design with each layer having identical thickness.

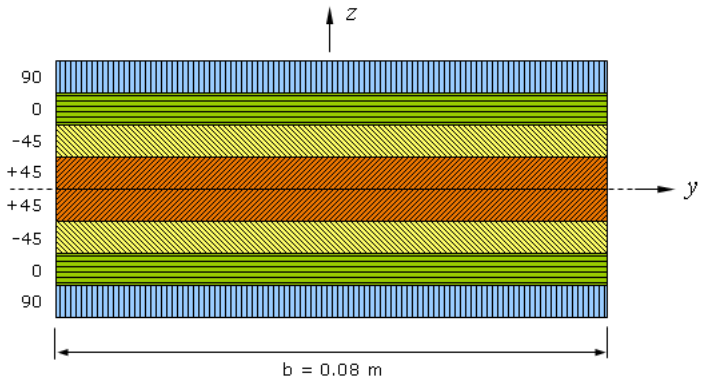

Figure 7.25: Flat beam cross section

The implementation results of the flat beam example are presented in three sections. The first section investigates the relative error for a single TIPR increment using varying TIPR parameters and a reduced set of design variables. The second and third section show

the pursuit of an overall design goal by incrementally applying the TIPR algorithm with a reduced and the full set of design variables, respectively.

7.3.1 Relative Error Study

The relative error investigation uses a reduced set of two design variables. These two design variables are defined as layer thicknesses according to Table 7.17. The cross sectional DOE features six equidistant design sites between and including lower and upper design variable bounds. Figure 7.27 shows four of the normalized surrogate models.

Table 7.17: Flat beam design variable ranges

	Layer	Lower limit	Baseline	Upper limit
dt_{90}	90 and 0	0.125 mm	0.5 mm	2 mm
dt_{45}	45 and -45	0.125 mm	0.5 mm	2 mm

The relative error study investigates the TIPR performance for an isolated frequency change in dependence on the mode number. Figure 7.26 illustrates that for small changes, the accuracy of TIPR is unaffected by the mode number. The results also project a potentially drastic performance degradation for structural and modal changes beyond the small perturbation assumption. Five percent frequency increments or 10 percent move limits on alpha sketch the severity of associated errors.

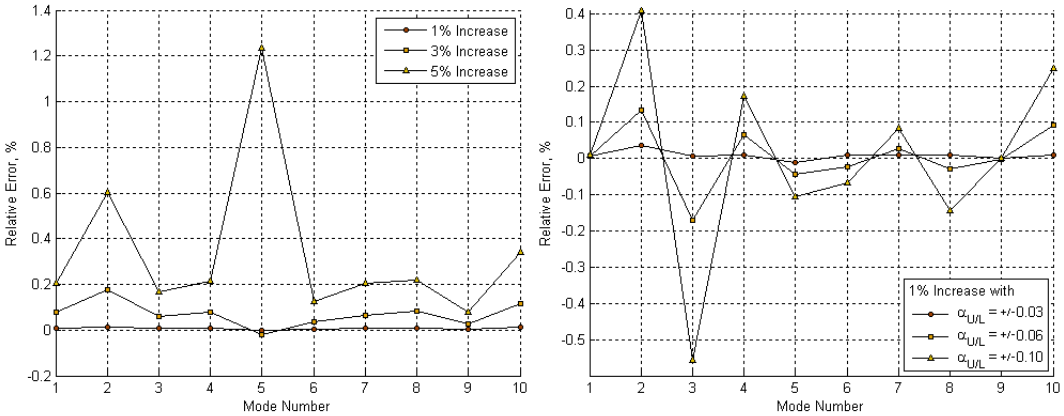

Figure 7.26: Flat beam relative error

$[P]\{\alpha\} + \Delta K_{CC} \geqq \triangle\omega_1^2$, Left: $F(x) = \alpha^T\alpha$, Right: $F(x) = \alpha_m$, $\alpha^L \leqq \alpha \leqq \alpha^U$

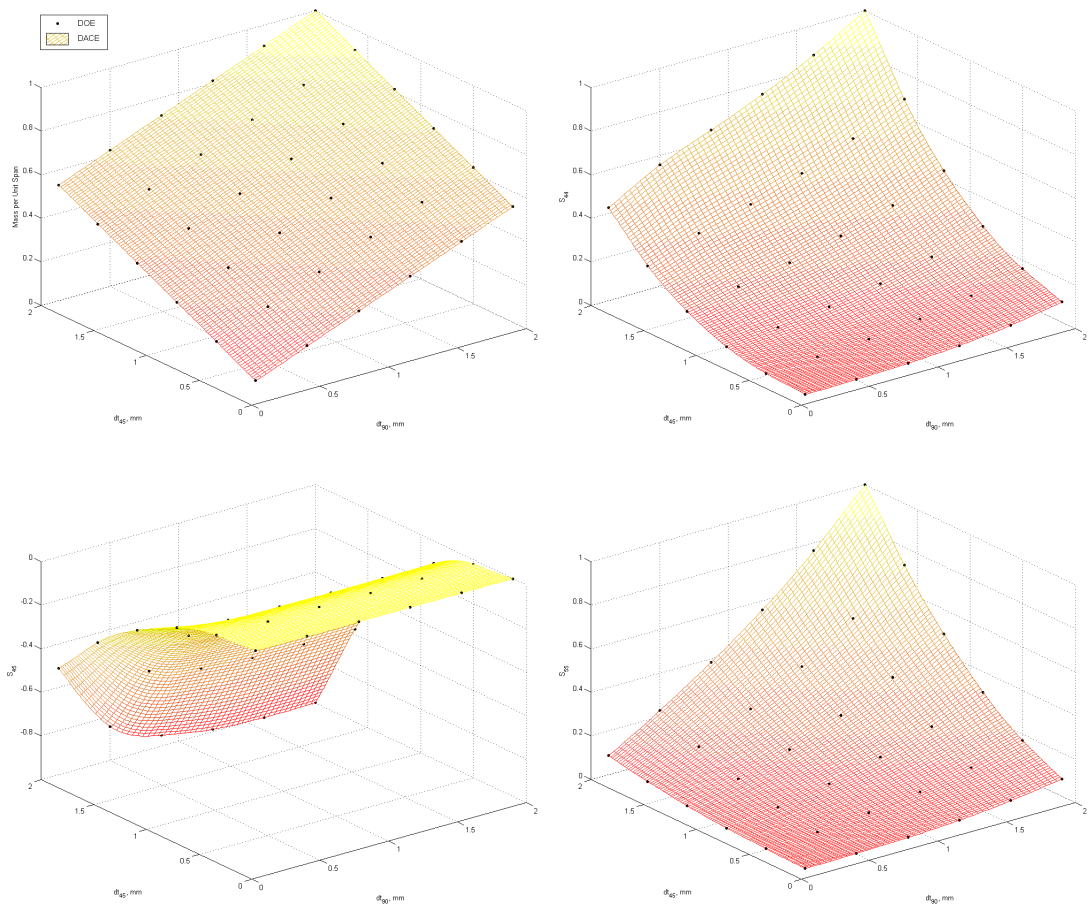

Figure 7.27: Flat beam surrogate models

Kriging model using DACE and zero order polynomial along with cubic spline correlation function

Mean Square Error: $m = 0.0000,\ S_{33} = 0.0002,\ S_{45} = 0.0000,\ S_{55} = 0.0000$

7.3.2 Optimization Study 1

The first optimization study uses the flat composite beam with reduced set of two design variables in an optimization subject to a 10 percent increase in the first natural frequency. TIPR is applied in 10 one percent increments. After each increment, the structural system is updated using the structural changes determined by TIPR. A reanalysis of the global problem then provides the baseline for the new increment.

TIPR is implemented using two different objective functions, i.e., minimum change and minimum mass. Upper and lower α bounds for the latter are set to 0.05.

The upper right plot in Figure 7.28 shows a virtually identical frequency evolution. Naturally, the mass per unit span for the minimum mass objective remains below that of the minimum change objective. The lower left of Figure 7.28 shows the corresponding development of design variables. It gives a formidable testimony to the compliance with the two different objective functions.

Similarly, the design space in Figure 7.29 illustrates how the minimum change objective takes the quick way to get to the specified frequency target. The minimum mass optimization on the other hand takes a wide detour in order to ensure that the involved mass increase is kept to a minimum.

‘

The design variables in Figure 7.28 show a diverse behavior, but also exhibit a common trend. Both optimization problems decrease the cross ply thickness and increase the diagonal ply thickness. The reason for this behavior can be found in the bending nature of the first mode. A beam in bending creates both curvature and displacement fields. Induced axial stresses are of particular interest to the current optimization study.

Physical properties of composite materials are highly directional. The stiffness in the direction of the fibers can exceed the stiffness in the direction transverse to the fibers by a factor of 20 [122]. The plies with 0 degree layup angle are thus aligned in the direction where the stiffness is needed. Their wall thickness, however, is bound to that of the 90 degree plies. As a result, the impact of increasing the wall thickness of the 0 plies depreciates in light of the combined impact of the diagonal plies.

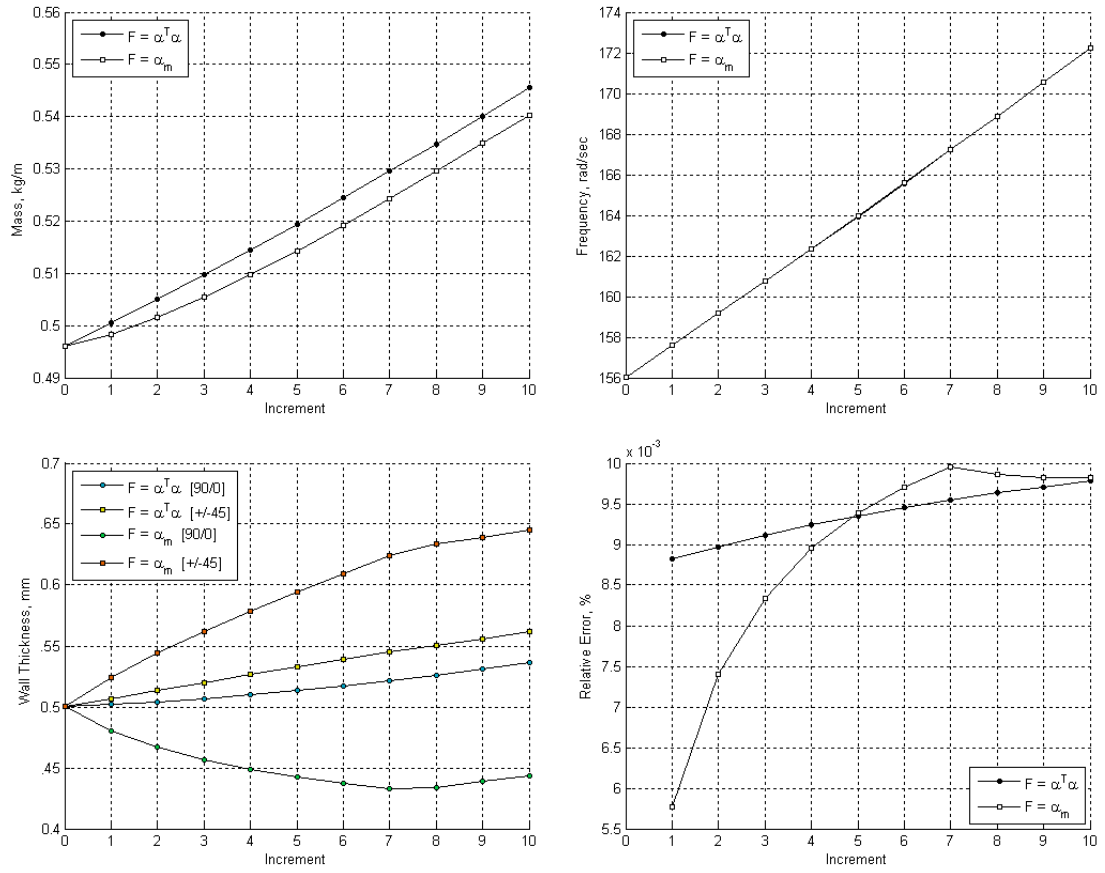

Figure 7.28: Flat beam output comparison

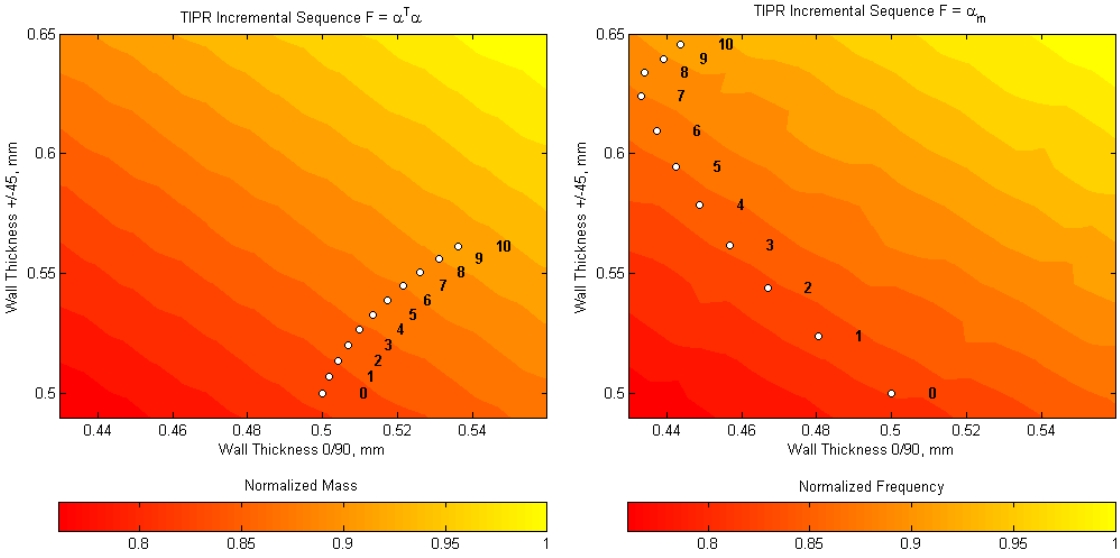

Figure 7.29: Flat beam design space comparison

Contours based on VABS/DYMORE results on 21x21 analysis grid

The TIPR optimized design variable settings are used in a reanalysis at both local and global level. The frequency results in Table 7.18 confirm the accuracy of the TIPR optimization as well as the accuracy of the surrogate models created by DACE.

Table 7.18: Flat beam TIPR frequency results

Frequency, rad/sec	$F = \alpha^T \alpha$	$F = \alpha_m$
Baseline	156.05	
Objective	171.65	
Final TIPR	172.24	172.25
VABS/DYMORE	172.00	171.32

7.3.3 Optimization Study 2

Because classical flutter can be traced back to a coalescence of bending and torsion modes, putting a lower bound on the separation between corresponding natural frequencies is considered *good design practice* [185]. The second optimization study simulates such design practice by minimizing the mass of the flat composite beam subject to a single frequency separation constraint. The constraint is specified by means of a minimum value ω_{diff} for the difference between the two frequencies.

Optimization study 2 compares the TIPR based algorithm to the gradient based SQP algorithm. For a fair comparison, local level analyses are substituted by local level surrogates for both TIPR and SQP implementations. The excellent performance of the DOE in the previous redesign studies (Figure 7.27) led to the adoption of corresponding settings. The current DOE thus features six equidistant design sites along all four design variables. The full factorial execution of 1296 VABS analyses took about 38 minutes.

The SQP problem presents itself in the standard formulation below.

Minimize:

$$F(x) = \frac{m}{m_{base}} \qquad \text{Objective function}$$

Subject to:

$$g = 1 - \frac{\omega_2 - \omega_1}{\omega_{diff}} \leqq 0 \qquad \text{Modal constraint}$$

with

$$x = \left\{ \begin{array}{c} x_{90} \\ x_0 \\ x_{-45} \\ x_{+45} \end{array} \right\} \qquad \text{Design variables}$$

and

$$\left\{ \begin{array}{c} 0.125 \\ 0.125 \\ 0.125 \\ 0.125 \end{array} \right\} \leqq x \leqq \left\{ \begin{array}{c} 2.0 \\ 2.0 \\ 2.0 \\ 2.0 \end{array} \right\} \qquad \text{Side constraints}$$

Two respective TIPR based optimizations are realized. TIPR 1 allows the first frequency to decrease while at the same time making sure it stays above a lower limit specified as 95 percent of the corresponding baseline frequency. TIPR 2 simultaneously enforces a decrease in the first and an increase in the second frequency. The former of which is again defined with respect to the baseline frequency. Both implementations subject the second frequency to an incremental increase until the modal separation constraint is satisfied. Once the specified frequency separation is reached, the optimizer further attempts to minimize mass without violating the modal separation constraint. The system is updated at the end of each TIPR increment using the determined structural changes. A reanalysis of the global problem provides the baseline for the new increment until convergence is reached.

The TIPR 1 formulation of the problem reads as follows.

Minimize:

$$F(x) = \alpha_m \qquad \text{Objective function}$$

Subject to:

$$\triangle\omega_1^2 - [P_1]\{\alpha\} - \Delta K_{CC,1} \leqq 0 \qquad \text{Modal constraint 1}$$

$$\triangle\omega_2^2 - [P_2]\{\alpha\} - \Delta K_{CC,2} \leqq 0 \qquad \text{Modal constraint 2}$$

with

$$\hat{\omega}_1 = 0.95 \cdot \omega_1^{base}$$

$$\hat{\omega}_2 = \min\left(\omega_{diff} + \omega_1,\ \omega_2 + \Delta\omega_2\right)$$

The TIPR 2 formulation of the problem reads as follows.

Minimize:

$$F(x) = \alpha_m \qquad \text{Objective function}$$

Subject to:

$$[P_1]\{\alpha\} + \Delta K_{CC,1} - \triangle\omega_1^2 \leqq 0 \qquad \text{Modal constraint 1}$$

$$\triangle\omega_2^2 - [P_2]\{\alpha\} - \Delta K_{CC,2} \leqq 0 \qquad \text{Modal constraint 2}$$

with

$$\hat{\omega}_1 = \omega_1^{base}$$

$$\hat{\omega}_2 = \min\left(\omega_{diff} + \omega_1,\ \omega_2 + \Delta\omega_2\right)$$

The minimum separation between first bending and first torsion frequency is specified to be greater than or equal to ω_{diff} = 800 rad/sec. Convergence is defined by a relative change in the objective function with respect to the baseline that is less than 0.1 percent for two consecutive iterations. That translates to a termination of the optimization if for two consecutive iterations the change in the normalized mass is less than 0.0001.

Table 7.19: Flat beam solution comparison

	SQP 1	SQP 2	TIPR 1	TIPR 2	TIPR 1	TIPR 2
			$\alpha_{U/L} = \pm 0.01$		$\alpha_{U/L} = \pm 0.03$	
Objective function						
	0.8211	0.8212	0.8215	0.8220	0.8198	0.8210
Optimized mass, kg/m						
	0.4072	0.4073	0.4075	0.4077	0.4066	0.4072
Optimized frequencies, rad/sec						
1	156.9	157.0	156.1	156.0	155.1	156.0
2	963.3	963.4	956.2	956.0	953.1	956.0
Difference	806.4	806.4	800.1	800.0	798.0	800.0

Baseline frequencies: ω_1 = 156.05 rad/sec, ω_2 = 935.89 rad/sec

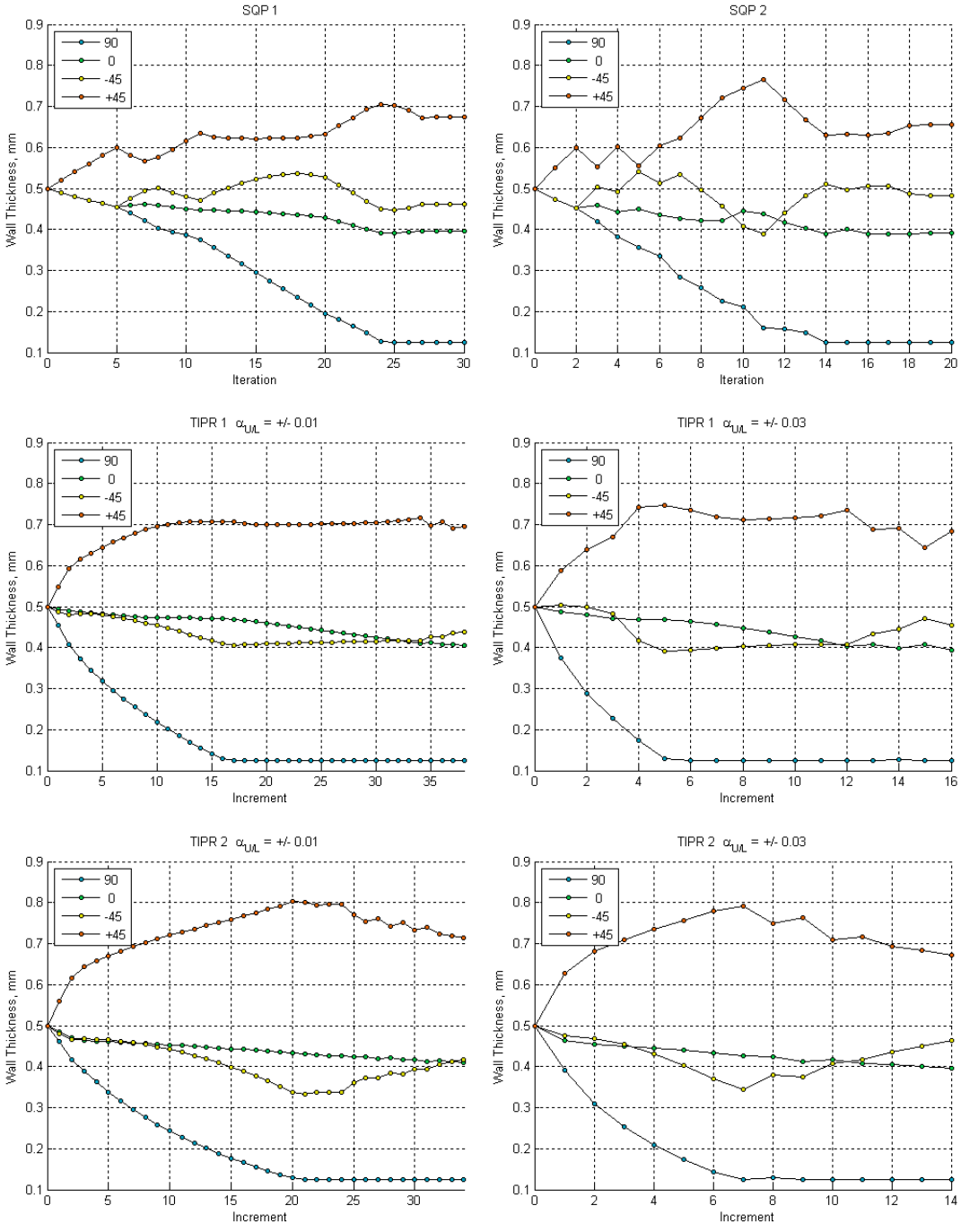

Figure 7.30: Flat beam design variables

SQP 1: Relative step size bound $2e^{-5}$, SQP 2: Relative step size bound $5e^{-5}$

TIPR: $\Delta\omega_2 = 1\%$ for $\alpha_{U/L} = \pm 0.01$, and 3% for $\alpha_{U/L} = \pm 0.03$

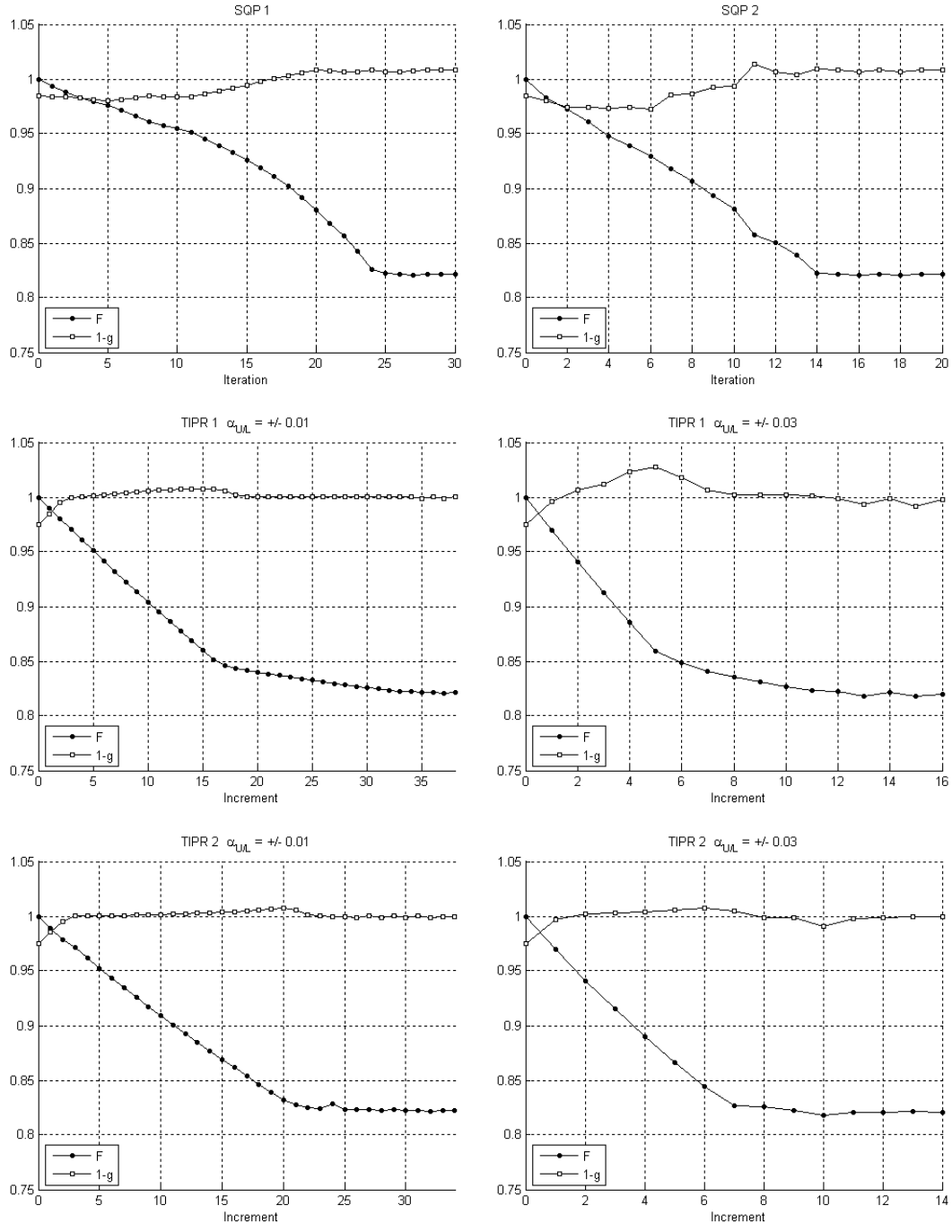

Figure 7.31: Flat beam objective and constraint

SQP 1: Relative step size bound $2e^{-5}$, SQP 2: Relative step size bound $5e^{-5}$

TIPR: $\Delta\omega_2 = 1\%$ for $\alpha_{U/L} = \pm 0.01$, and 3% for $\alpha_{U/L} = \pm 0.03$

The design variables in Figure 7.30 show the same overall trends, but also reveal differences in the solution for their optimized values. Table 7.19 and Figure 7.31, however, attest to an essentially mutual and uniform satisfaction of both objective and constraint.

Figure 7.32 shows the TIPR development beyond that of Figures 7.30 and 7.31. The corresponding implementation simply disables the convergence criterion and allows continuation of the optimization process for a specified number of increments. Figure 7.32 shows that the TIPR optimizer eventually reaches the same design variable settings as SQP, but based on the current objective and constraint specification there is no need to carry the solution forward.

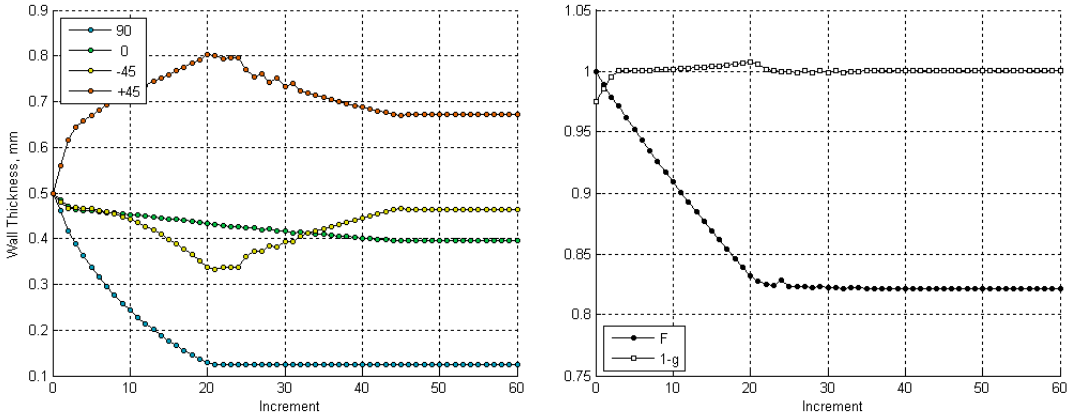

Figure 7.32: Flat beam maximum iteration TIPR

Recall the previously mentioned *good design practice* of encountering classical flutter by enforcing a minimum frequency difference between corresponding natural modes [185]. The modal constraint of the current optimization study specifies a minimum separation between two natural frequencies. The first corresponds to the fundamental bending, the second to the fundamental torsion mode of the baseline configuration.

From the aspect of avoiding a coalescence of these two modes, it has been observed that an increase in the torsional mode is preferred to a change in the bending mode [111]. The results in Table 7.19 agree with this observation. Compliance to the modal separation constraint is predominantly effectuated by an increase in the second frequency. The frequency of the first bending mode barely changes.

The optimized design variables reflect the very same circumstance. The wall thickness of the 90 degree plies is driven to their lower limit due to their negligible influence on either mode and in compliance with the minimum mass objective. The 0 degree layers experience some decline to complement the combined impact of the diagonal plies.

It should be noted that during the course of the optimization a mode switching took place. The second mode of the optimized design exhibits predominantly bending effects. It is no longer the fundamental torsion mode that was established by the baseline design. An implementation that accounts for mode switching would require frequency constraints on variable mode numbers but is not part of this research effort.

The present study also enables an unbalanced laminate. Laminate balance manifests itself in behavioral characteristics. Balanced designs exhibit no coupling between extension and shear nor between extension and bending. A tensile load produces pure extension. For an unbalanced design the corresponding coupling coefficients are non-zero resulting in the display of nonclassical behavior.

The baseline configuration is comprised of an equal number of 45 and -45 degree plies along with an equal number of 0 and 90 degree plies that are all of the same thickness. The baseline composite is balanced and symmetric. The laminae of the optimized configuration on the other hand, due to the set up of the optimization problem, are unequal in their thicknesses. The final design is symmetric but unbalanced.

Table 7.20 compares the execution times of the six different implementations. In a computer age of FEA and CFD runs that take days or even weeks to complete, none of the optimization problems presented here takes particularly long. However, TIPR showcases tremendous computational savings on a relative scale.

Table 7.20: Flat beam computational expenses

	SQP 1	SQP 2	TIPR 1	TIPR 2	TIPR 1	TIPR 2
Number of			$\alpha_{U/L} = \pm 0.01$		$\alpha_{U/L} = \pm 0.03$	
Local function calls	-	-	-	-	-	-
Global function calls	182	106	39	35	17	15
Iterations/Increments	30	20	38	34	16	14
Total Time, sec	878	530	207	191	113	104
Total Time, min	14.6	8.8	3.5	3.2	1.9	1.7

7.4 Generic Wing TIPR

The final TIPR application study uses a generic uniform composite wing to illustrate the ties between TIPR and flutter and to touch on some additional practical considerations. The wing model is derived from the wing section of a typical glider shown in Figure 7.33 originally published in the aeroelastic redesign study of the tailless SB 13 [165].

Figure 7.33: Typical sailplane wing section
Figure 14 by Schweiger et al. [165]

The wing structure for the present study has been simplified to a single cell box beam as illustrated in Figure 6.5. The representative wing box width and height are 0.3 and 0.1 meter, respectively with a semi span of 7.5 meter. The composite laminates adhere to a symmetric layup with $[0/\theta_{skin}]_2$ for upper and lower wall, and $[\theta_{spar}/-\theta_{spar}]_2$ for the side walls. Both skin and spar are made of high tension carbon fibers and feature two design variables each, i.e. thickness and layup angle, amounting to a total of four design variables. The corresponding baseline values and design variable ranges in Table 7.21 lack realism and were chosen merely to suit the present illustrative purpose. Material properties can be found in Table 5 of the SB 13 redesign study [165].

Table 7.21: Generic wing design variable ranges

Design variable	Unit	Lower limit	Baseline	Upper limit
θ_{skin}	degree	0	90	90
θ_{spar}	degree	0	45	90
dt_{skin}	m	0.001	0.002	0.003
dt_{spar}	m	0.001	0.006	0.011

The DOE uses seven equidistant design sites along both layup angles and three equidistant design sites along both wall thicknesses. The execution of the resulting 441 VABS analyses took a little under 11 minutes. Figure 7.34 shows the surrogate models of selected equivalent beam properties with θ_{spar} and dt_{skin} at their baseline values. The normalization was performed using the maximum value of the equivalent beam property DOE.

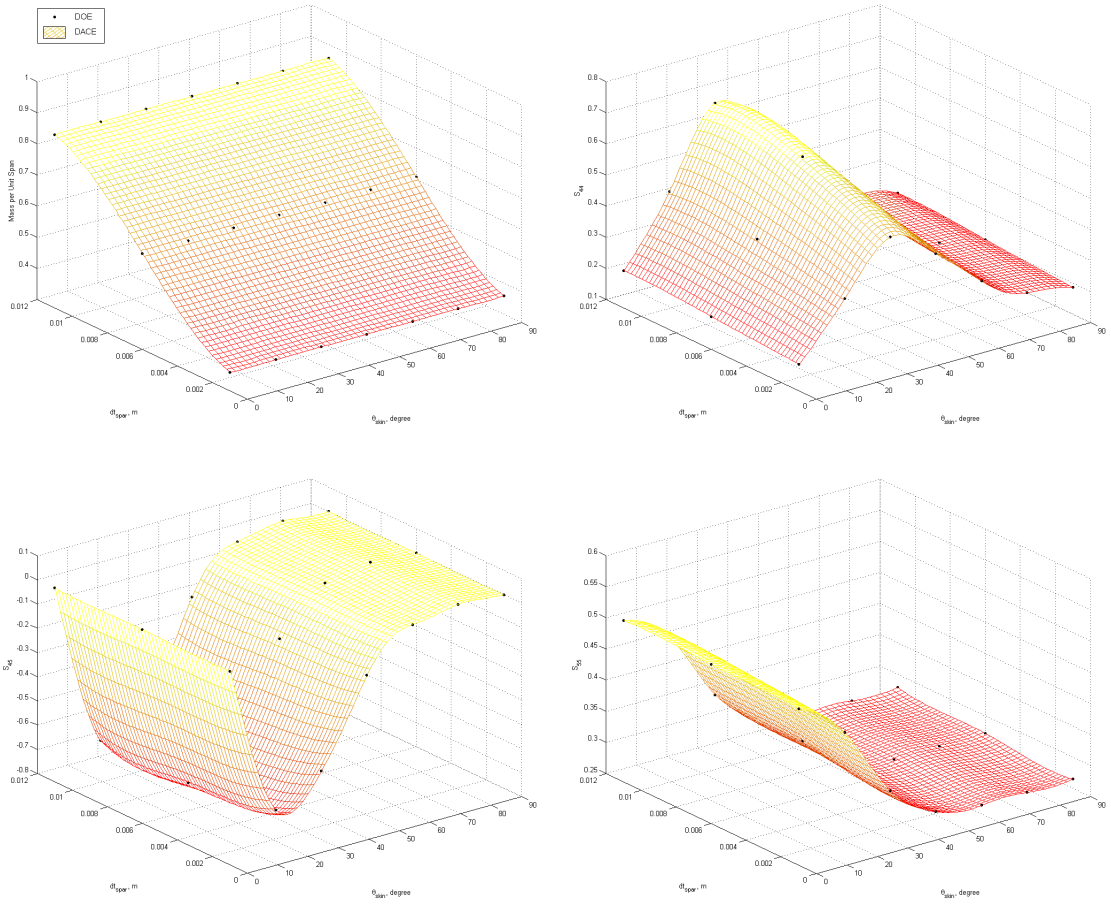

Figure 7.34: Generic wing surrogate models

Kriging model using DACE and zero order polynomial along with cubic spline correlation function

$\theta_{spar} = 45^{\circ}$, $dt_{skin} = 0.002m$

Mean Square Error: $m = 0.0001,\ S_{44} = 0.0003,\ S_{45} = 0.0052,\ S_{55} = 0.0004$

7.4.1 Simplified Flutter Analyses and Optimization

Flutter is a manifold and complex phenomenon. The aeroelastic instabilities of the swept back tailless SB 13 and Ricochet were traced back to the coupling of the first wing bending and the short period rigid body mode of the aircraft. The latter was identified as the immediate cause of the instability mainly due to an extremely low aircraft pitching moment of inertia [9, 165].

Straight wings on the other hand commonly experience the classical coupling of fundamental bending and torsion modes. An example is the English Kestrel with a flutter speed of 70 m/s [9, 10]. Appendix B gives a brief taste of the wide and fascinating field of aeroelasticity and describes simplified models and analyses for the investigation of flutter. One such simplified model is the typical section that *"for purposes of flutter prediction ... can be made to represent fairly well a straight wing of large span"* [25]. A corresponding simplified flutter analysis is the p-k method.

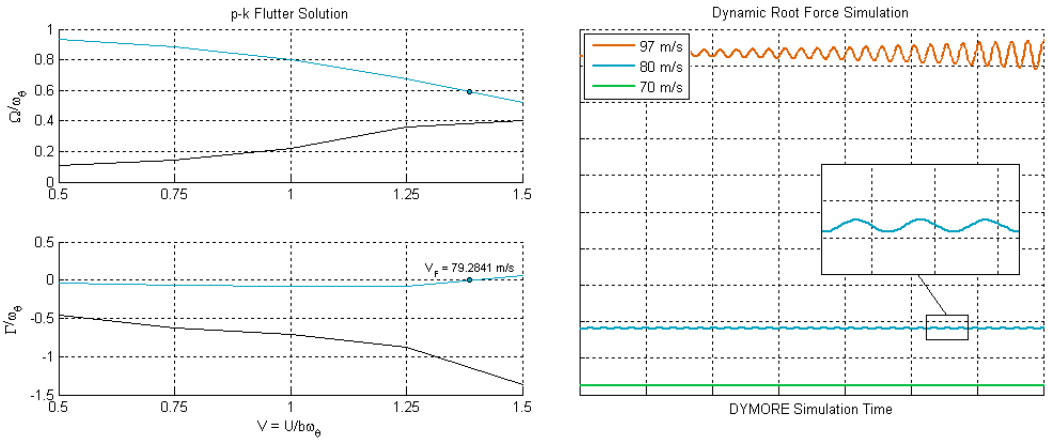

Figure 7.35: Generic wing baseline flutter analyses

Left: Frequency Ω and damping Γ of fundamental bending (black) and fundamental torsion (blue) mode

The representative section of the generic wing example has a bending and a torsion degree of freedom as illustrated in Figure B.5. Figure 7.35 presents the corresponding results of a p-k flutter analysis of the baseline configuration. The damping of the torsion mode initially increases but eventually reverses and crosses the abscissa at 79 m/s freestream velocity. This

is the critical speed for flutter that also brings about a frequency coalescence of the involved fundamental bending and torsion mode. Note that the p-k flutter plots are normalized with respect to the airfoil semi chord b and the fundamental torsion frequency.

An increase in the frequency of the unstable torsion mode promises an increase of the flutter speed. Figure 7.36 presents the simplified flutter analyses of an optimized wing with a critical speed of 95 m/s. The optimized wing is the result of a TIPR optimization that specified a 60 percent increase in torsional frequency.

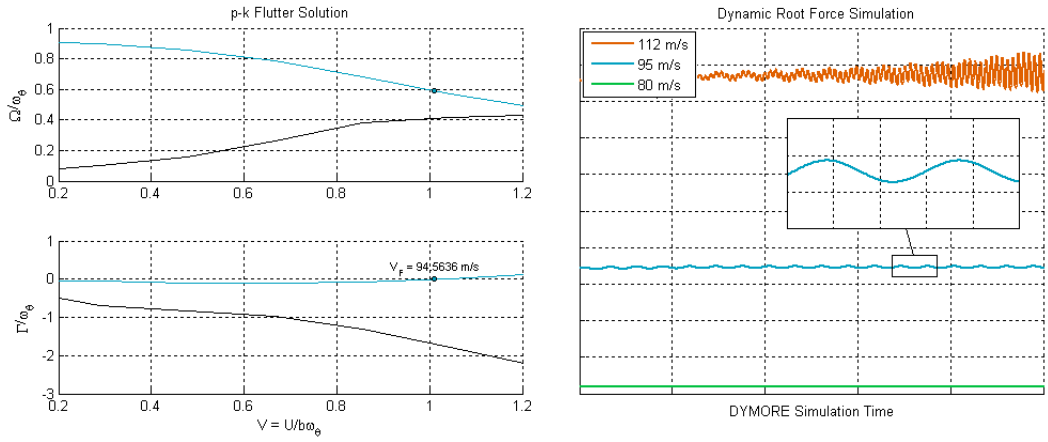

Figure 7.36: Generic wing optimum flutter analyses

Left: Frequency Ω and damping Γ of fundamental bending (black) and fundamental torsion (blue) mode

The simplified flutter analyses of baseline and optimized generic wing configuration above are supported by the global response characteristics derived from a dynamic DYMORE simulation. Recall the definition of flutter provided in Appendix B. Flutter is a dynamic instability with the critical speed being the lowest airspeed that results in sustained simple harmonic oscillations of the structure. Figures 7.35 and 7.36 thus confirm the simplified analysis results of the typical section. The global wing response shows no oscillations below the flutter speed and growing oscillation amplitudes above the flutter speed.

The aerodynamic parameters required by DYMORE are based on a NACA0012 airfoil at a one degree initial angle of attack. The two-dimensional airfoil properties in terms of lift, drag and pitching moment coefficients are provided in airtables. The wing is assigned a uniform chord of 0.64 meter and a 0.99 tip loss factor [11].

The frequency objective of the current optimization study is identical to the aforementioned 60 percent increase in the natural torsional frequency. The modal spectrum of the baseline configuration allows the identification of the fourth mode as the fundamental torsion mode. The corresponding modal constraint is expressed in Equation 7.4. The optimization criterion is defined as minimum wing mass. The corresponding objective function is expressed in Equation 7.3. The optimization is terminated as soon as the frequency objective is satisfied. Note that the difference in the order of magnitude required the normalization of the design variables for the SQP implementation.

$$F = \frac{m}{m_{base}} \tag{7.3}$$

$$G = \frac{1.6 \cdot \omega_{4,base}}{\omega_4} - 1 \leqq 0 \tag{7.4}$$

Figure 7.37 shows similar trends for the design variables with slight differences in the final results. It also gives testimony to the simultaneous satisfaction of objective and constraint by either implementation. The major advantage of TIPR is the efficiency of the optimization. Table 7.22 quantifies the function calls required by SQP for the gradient evaluation and responsible for the considerable increase in computational cost compared to TIPR.

Table 7.22: Generic wing computational expenses

Number of	SQP	TIPR
Local function calls	-	-
Global function calls	85	19
Iterations/Increments	16	19
Total Time, sec	444	102
Total Time, min	7.4	1.7

Recall that the current optimization exclusively considers the torsion mode by means of a single frequency objective. The resulting increase of the torsion frequency is accompanied by an increase in the bending frequency. Table 7.23 shows the frequency results of both modes for the baseline configuration, the optimized solution that uses equivalent beam property surrogate models, and the final results of a full VABS/DYMORE reanalysis. The increase of the bending frequency amounts to approximately 25 percent.

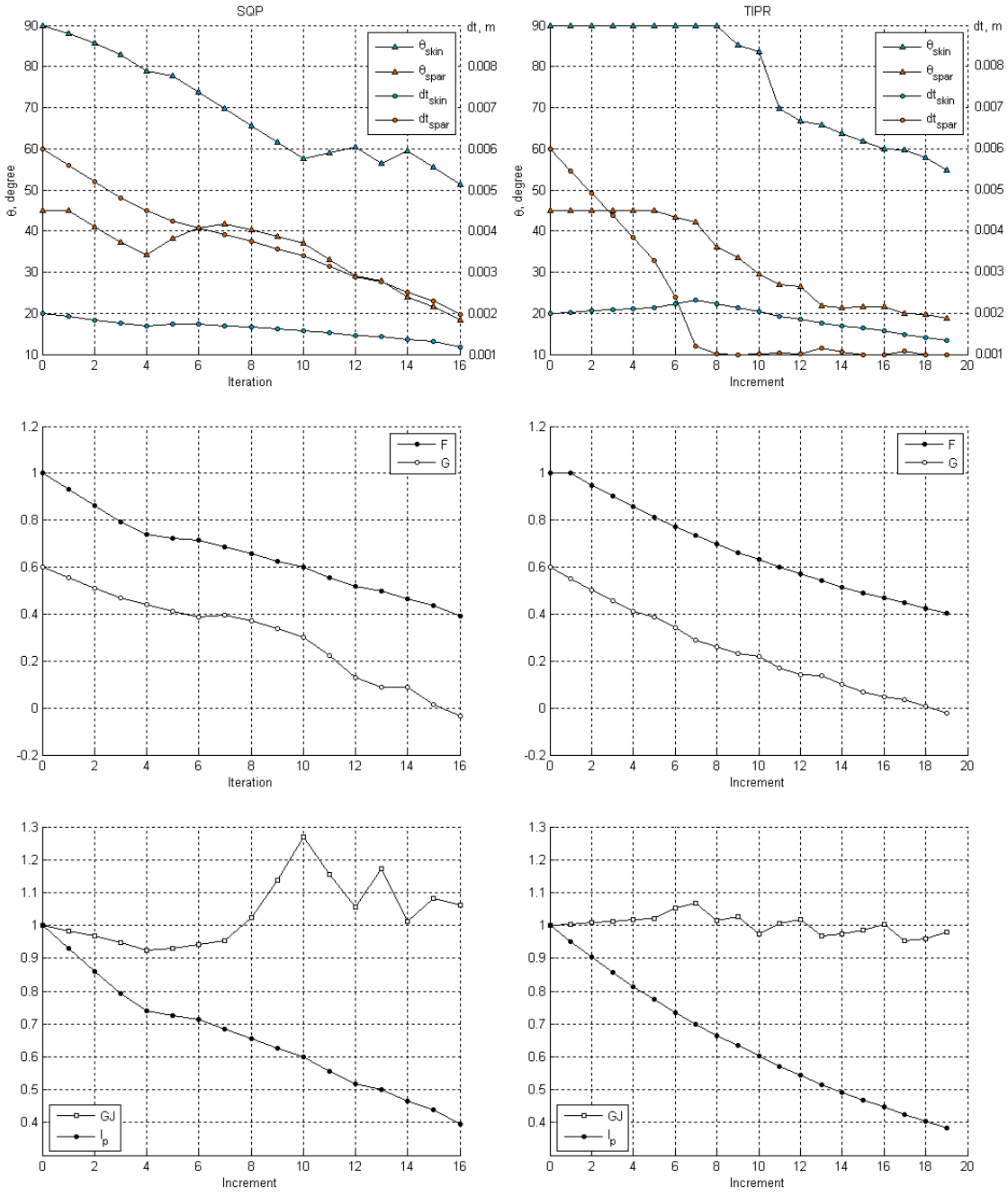

Figure 7.37: Generic wing optimization results

SQP: Relative step size bound $4e^{-4}$, TIPR: $\Delta\omega_4 = 3\%$ and $\alpha_{U/L} = \pm 0.05$

Table 7.23: Generic wing frequency results

	Bending Mode		Torsion Mode	
Frequency, rad/sec	SQP	TIPR	SQP	TIPR
Baseline	14.97		168.27	
Objective	n/a		269.23	
Optimized	18.80	19.51	278.32	275.09
VABS/DYMORE	18.66	19.57	280.13	272.05

Figure 7.37 also shows the two main drivers of the torsional frequency as captured by Equation 7.5. These are the sectional polar moment of inertia per unit span I_p and the torsional stiffness coefficient S_{44} that will simply be referred to as torsional stiffness GJ.

$$\omega \propto \frac{1}{L}\sqrt{\frac{GJ}{I_p}} \tag{7.5}$$

The graphical representation of GJ and I_p in Figure 7.37 is normalized with respect to the corresponding baseline value and allows the following observation. The final solution of both SQP and TIPR is mainly due to the change of the inertial properties. This change is accomplished by driving the wall thicknesses and thus the sectional mass per unit span along with the sectional polar moment of inertia to their minimum values.

The torsional stiffness for the current problem depends on the layup angles but experiences only a small impact on the final solution. Equation 7.5 states that an increase of GJ would further contribute to the current frequency objective. The SQP results are in agreement with this expectation. The TIPR results show a slight decrease of the final torsional stiffness compared to its baseline value that is compensated by a slightly lower value for the polar moment of inertia.

TIPR satisfies both the optimization objective and the frequency constraint as provided by the optimization formulation. A performance improvement in terms of more realistic design variable values can only be brought about by an improved formulation of the optimization problem itself. The results of the current optimization study confirm that additional constraints and/or analyses are necessary in order to capture other important requirements of structural integrity. The thin walls of the final generic wing design clearly disregard stress and buckling constraints.

7.4.2 Localized Reinforcement

The flutter problem of the SB 13 was caused by a coupling of the aircraft rigid body short period mode with the first wing bending mode. The discussion of how to separate the two frequencies and thus increase the flutter speed abandoned all possible solutions but one. This finally selected approach combined the application of high modulus carbon fibers with aeroelastic tailoring to increase the frequency of the wing bending mode. The documentation of solution possibilities also noted a configuration change, but *"because a large effort had already been invested in the aerodynamic lay-out, this solution was not desirable"* [165].

The redesign of the SB 13 as described above captures the essence of a practical aspect of great importance. Time and effort already invested in an existing aircraft entail the desire for a minimum departure from the already existing configuration; and the rectification of potential stability problems is sought to require minimum change from the baseline. Also, the additional costs associated with the realization of necessary changes increase dramatically with the significance and the extent of the change. The proposed TIPR optimization methodology is naturally conducive to the minimum change criterion.

The truly least amount of change needs to factor in the spanwise significance of a structural modification to the mode of interest. The first order perturbation equation as utilized in classic IPR makes use of elemental structural changes. Both the linearized equation of motion and the elemental stiffness and mass changes are repeated below.

$$\{\psi\}^T [\Delta k] \{\psi\} - \omega^2 \{\psi\}^T [\Delta m] \{\psi\} = \Delta\omega^2$$

$$[\triangle m] = \sum_{e=1}^{\sigma} [\triangle m_e] = \sum_{e=1}^{\sigma} [m_e] \alpha_e^m$$

$$[\triangle k] = \sum_{e=1}^{\sigma} [\triangle k_e] = \sum_{e=1}^{\sigma} [k_e] \alpha_e^k$$

A corresponding extension of the TIPR scheme is straightforward. The discrete system matrices are further decomposed to not only capture individual stiffness effects but also the global contribution of individual finite elements. The generalized stiffness effects introduced

in Equations 6.2 to 6.5 are redefined to account for elemental contributions. Generalized elemental mass effects are derived accordingly.

$$\Delta K = \sum_{e=1}^{\sigma} \Delta K_e \tag{7.6}$$

$$\Delta K_e = \sum_{i=1}^{6} \sum_{j=i}^{6} \Delta K_{e,\,ij} = \sum_{i=1}^{6} K_{e,\,ii} \alpha_{e,\,ii} + \Delta K_{e,\,CC} \tag{7.7}$$

$$K_{e,\,ij} = \{\psi\}^T \left[k_{e,\,S_{ij}}\right] \{\psi\} \tag{7.8}$$

$$M_e = \{\psi\}^T \left[m_e\right] \{\psi\} \tag{7.9}$$

Recall that the above generalized effects not only serve as the perturbation coefficients in the TIPR modal constraint equation but also indicate the relative significance of the corresponding structural change to the specified natural frequency. Figure 7.38 shows the mode shapes of the first two lateral bending modes of the generic wing baseline configuration. The elemental contributions that stem from the application of Equations 7.8 and 7.9 are visualized in Figure 7.39.

Looking at the more pronounced shape of the bending mode on the right hand side. Figure 7.39 illustrates that a stiffness increase will be most effective when applied to the location of zero bending slope half between root chord and wing tip. A mass change will have a similar effect with zero influence at the location where the mode shape crosses the abscissa. This location is identical to the stationary point of the corresponding natural vibration.

Figure 7.39 shows that the *Where* of a structural modification is just as important as the *How*. Returning to the elemental stiffness effects on the right hand side and adding the contributions of finite elements 7, 8, 9, and 10 one arrives at a combined modal contribution that makes up 46 percent of the total generalized stiffness.

The localized TIPR implementation thus only applies changes to the finite elements 7, 8, 9, and 10. In contrast, the global TIPR applies the same change to all 15 finite elements for a uniform change of the entire wing. The frequency objective of the current study is a ten

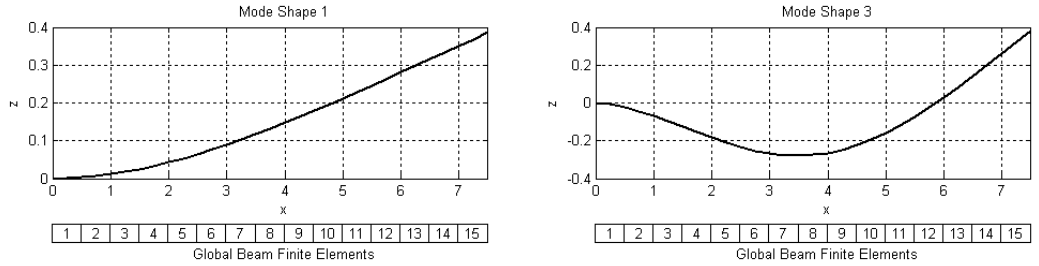

Figure 7.38: Generic wing bending mode shapes

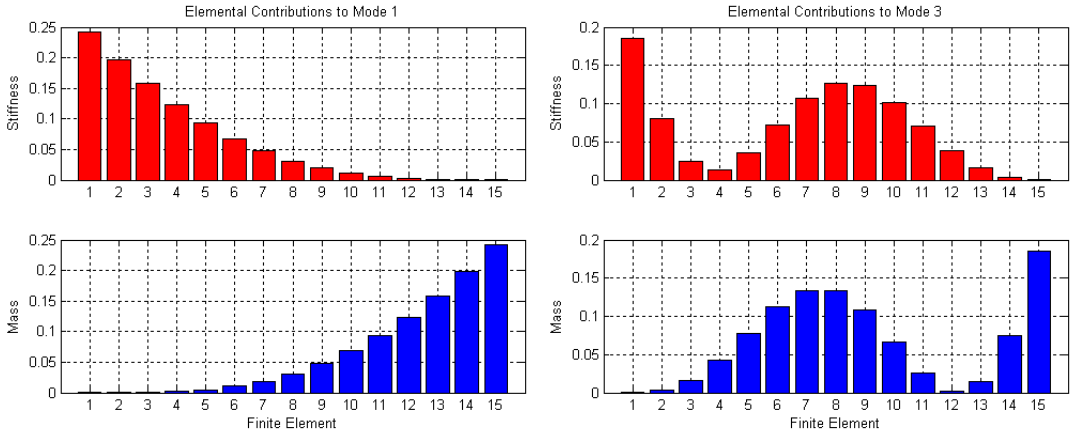

Figure 7.39: Generic wing elemental modal contributions

percent increase in the natural frequency of the second lateral bending mode that translates to an absolute frequency of 99.72 rad/sec. Both TIPR implementations use an incremental frequency increase of one percent and an incremental alpha limit of three percent resulting in a total of ten increments.

The results in Table 7.24 show that both global and localized TIPR arrive at the essentially same frequency objective. However, the idea of localized stiffness reinforcement represents a more practicable way of structural redesign. The global scheme entails more drastic changes as evidenced by the final wall thicknesses of the representative wing structure. Not only are these wall thicknesses a greater departure from the corresponding baseline value but also do they have to be applied to the entire wing. The final wall thickness values of the localized TIPR scheme represent smaller absolute changes and only find application at a finite location along the span.

Table 7.24: Generic wing TIPR result comparison

	Baseline	Global TIPR	Localized TIPR
Frequency, rad/sec	90.71	100.27	100.65
Wing mass, kg	26.64	23.93	24.83
Skin layup angle, degree	90	90	90
Spar layup angle, degree	45	45	46
Skin thickness, m	0.002	0.0022	0.0021
Spar thickness, m	0.006	0.0043	0.0056

The results of the generic wing studies above provide grounds for an important TIPR limitation. Structural analysis and design has to account for numerous loading conditions and failure modes. The proposed TIPR scheme exclusively considers stiffness and mass effects on modal characteristics. It disregards other central disciplinary problems of equal importance. Immediate examples that suggest itself based on the generic wing results are failure due to exceedance of allowable stresses or the collapse due to the buckling.

7.5 Summary

The TIPR algorithm performs an optimization in accordance with the problem statement. The smaller the modal and structural changes, the better the TIPR results. The relative error, caused by the negligence of higher order terms in the first order perturbation equation, shows no other pattern for the presented redesign and optimization studies.

The minimum change criterion performs slightly better than the minimum mass criterion due to its natural representation of the small perturbation assumption. The latter greatly benefits from move limits on the intermediate design variables. Corresponding incremental limits on respective structural changes prevent pathological solutions caused by mass related design variables driven to their lower limit.

Perturbations of less than ten percent are generally accompanied by acceptable errors. The dependency study on the mode number revealed isolated discrepancies without transparent explanation. Keeping modal and structural changes as low as three percent consistently showed negligible errors in the TIPR solution.

The surrogate models used in the present implementation are appropriate for the relatively simple design spaces at hand. TIPR results compare very well with results from a

full VABS/DYMORE reanalysis using the final design variable settings determined by the TIPR based optimizer.

Optimization comparison studies show that the SQP implementation is outperformed by the TIPR based algorithm. Both optimizers arrive at the essentially same solution given corresponding problem statements. However, the gradient liberation of TIPR entails computational savings making TIPR up to five times faster than SQP.

An important practical redesign aspect is a minimum departure from the existing baseline configuration. The proposed TIPR optimization scheme is naturally conducive to this practical aspect by using a minimum change optimization criterion. An elemental formulation of the TIPR modal equation further contributes to a minimum change solution. In fact, taking the spanwise significance of a structural modification to the mode of interest into consideration greatly benefits the practical realization of modal redesign objectives.

Chapter VIII

DISCUSSION

This chapter completes the present research effort by offering a critical discussion of the implemented methodology. A brief review summarizes the documented journey from motivation to end result. A reiteration on research questions and hypotheses will lead to conclusions that highlight individual accomplishments. Secondary application possibilities are followed by current limitations and suggestions for future work. A final remark will bring this work to a close.

8.1 Review

Motivation for the present research was derived from an operational need of unconventional aircraft that comply with contemporary concerns in atmospheric science and homeland security. The prominent role of the conceptual phase in designing respective vehicles currently faces an incidental deficit of corresponding analysis and design capabilities.

Objective of the present research was the composition of a methodology for the accurate and efficient optimization of high aspect ratio wings subject to natural frequency constraints. The spectrum of eigen modes innate to every system is particularly important to the vehicle class of interest due to distinct structural and aeroelastic response characteristics. The careful placement of natural frequencies in the light of future service loads can eliminate potential instabilities.

The proposed optimization algorithm allows the specification of natural frequencies. It incrementally approaches these modal objectives by solving a small perturbation equation. The solution is brought about by an optimization routine that finds structural changes based on a criterion such as minimum mass or minimum change. Each increment is concluded by a reanalyses using the small structural change solution and providing the baseline values for the subsequent increment.

The avoidance of costly FEA gradient evaluations showed great computational promise. TIPR implementation results confirm accuracy as well as economic superiority compared to a standard SQP algorithm. Efficiency and fidelity make the new TIPR algorithm a very attractive optimization tool for the redesign of high aspect ratio wings with aeroelastic instabilities.

8.2 Research Questions and Hypotheses

The conclusions to follow will start with a validity assessment of posed hypotheses based on the results of the implemented methodology. Below is a recapitulation of both hypotheses and underlying research questions.

Research Question 1 Can the theory of beam dimensional reduction be made an integral part of inverse perturbation redesign?

Hypothesis 1 Structural changes in the small perturbation equation can be expressed as a linear combination of local mass and stiffness effects in accordance with the cross sectional model of the dimensionally reduced beam.

Research Question 2 Can the incremental solution of the first order perturbation equation guide the optimizer to a local optimum?

Hypothesis 2 The solution of the small perturbation equation adheres to the governing equations of motion. Defining the modal objectives on the right hand side according to overall design goals will dictate magnitude and direction of resulting structural changes.

Research Question 3 Can the incremental application of a small perturbation solution yield computational savings compared to a gradient based optimization?

Hypothesis 3 Solving the small perturbation equation is faster than finding FEA based gradients because it requires the execution of algebraic equations with virtually instantaneous responses.

8.3 Conclusions and Recommendation

The preceding chapter gave testimony to both the successful development and implementation of the proposed methodology. The results presented in the above redesign and optimization studies allow the following statements.

1. The optimization algorithm developed in the present research effort stems from the unique combination of beam dimensional reduction and small modal perturbation theory. Compatibility of both methods was achieved by the introduction of a generalized Timoshenko stiffness effect separation that propagates into system stiffness matrices.

2. The solution of the TIPR perturbation equation provides incremental guidance to the optimizer. The comparison of optimization results provided by TIPR and a gradient based method showed that both optimizers arrive at the essentially same solution given corresponding problem statements in terms of objective and constraints.

3. The incremental solution of the TIPR perturbation equation allows the omittance of costly FEA gradient evaluations resulting in an efficient optimization. Because the numerical evaluation of a gradient requires at least one additional function call per design variable, the computational savings of the present algorithm depend on the dimensionality of the design space.

4. The two levels of the dimensionally reduced beam analysis suggest corresponding levels of local and global optimization. Past implementations adhere to this suggestion. The present approach is different. It introduces local level surrogate models that capacitate a methodology consisting of two level analyses feeding into a single level optimization. The successful reduction of optimization levels contributes to both efficiency and accuracy. Previously, the global optimizer was merely kept within the validity bounds of the physical design space. A concluding optimization at the local level then had to minimize the discrepancy between desired and feasible design variables. The present algorithm uses local level surrogates as integral part to ensure constitutive laws and to yield a global level solution in terms of physical design variables.

5. Surrogate models are a key enabler of the developed methodology. In addition to reducing the number of optimization levels, surrogates gave practicality to modal perturbation redesign. The redesign solution is facilitated by matrix multipliers that represent linear changes to stiffness and mass properties. These multipliers bear no connection to physical design variables. The new approach employs surrogate models to express the linear fractional change as direct function of physical design variables.

6. The extension of the algorithm for point masses appears unproblematic and seamless. Each concentrated mass populates very specific locations in the discrete representation of the system mass conducive to an inertial effect separation. The decomposition of respective matrices would be similar to that performed on the stiffness matrix using stiffness effect separation. Each point mass, if subject to change, is then assigned a fractional multiplier and added to the set of active intermediate design variables.

8.4 Applicability

The primary application of the developed algorithm corresponds to the motivation and the objective of the present research to provide a methodological optimization approach for the effective redesign of high aspect ratio wings subject to aeroelastic instabilities. Efficiency and accuracy also suggest secondary application opportunities.

Structural Redesign The motivation of the present research was derived from the late and detached consideration of aeroelastic response characteristics in traditional design processes. The associated shortfalls documented in the motivation of the present work often yield design solutions that entail aeroelastic stability problems.

The rectification of corresponding design flaws in detail design and beyond can only be realized at enormous correctional costs. The TIPR algorithm provides an efficient and accurate way to keep associated expenses low. It offers a minimum change solution to a redesign problem that is specified in terms of natural frequency objectives.

An additional aspect of practicability for the structural redesign of an existing aircraft is brought about by localized stiffness reinforcements. The perturbation coefficients indicate

the discrete modal importance of individual finite elements. Only elements at locations along the span crucial to the mode of interest will have significance in a respective redesign and/or optimization solution. The larger the coefficient, the greater the elemental effect on the mode, the smaller the necessary structural change associated with the specified frequency perturbation. These considerations were taken advantage of in an elemental TIPR routine that makes local reinforcement adjustments to a given structure.

MDO Integration The design of an aircraft responds to an identified need expressed in a set of corresponding requirements. For the final design to be the in fact best solution, the design process must consider all contributing disciplines along with their interactions. Figure 8.1 illustrates how the TIPR algorithm could be used as disciplinary optimizer within a comprehensive MDO environment.

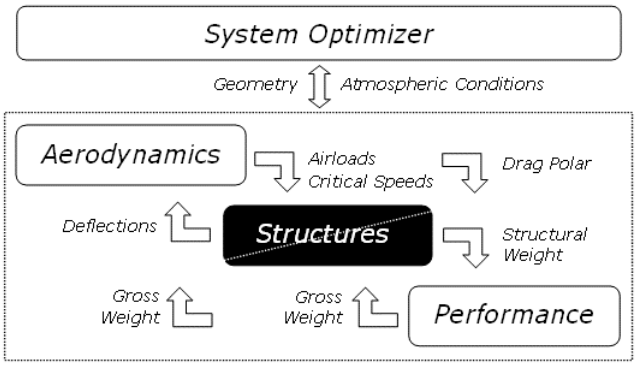

Figure 8.1: TIPR MDO integration

TIPR optimizer

The efficiency of the TIPR optimizer could also be taken advantage of at the conceptual stage of aircraft design. Combined with simplified aeroelastic analyses it could be used in the creation of a flutter constraint line as depicted in the conceptual design space in Figure 4.2. The conceptual designer is not interested in a vast amount of details but the conducive mapping of performance requirements and constraints by means of thrust loading and wing loading requires basic wing dimensions. These dimensions could be made design variables in the TIPR perturbation equation.

FEM Correlation Analyses on existing structures are often performed by numerical experiments using FEA. To ensure accurate response predictions, the discrete model needs to be in accordance with the real system that it is representing. TIPR allows the adjustment of FE structural properties to match full scale measurements of the natural frequencies. The redesign is then simply performed by using the measured frequency results as the modal objectives on the right hand side of the perturbation equation.

Failure Analysis Structural damage often results in a loss of stiffness that is accompanied by a decrease in natural frequencies. The elemental TIPR perturbation coefficients are indicative of the effectiveness of structural changes with respect to a specified modal objective. The simulation of a decrease in natural frequencies could be used to identify locations that are most prone to stiffness loss. These locations could then be subjected to shorter observation/maintenance intervals to ensure their structural integrity.

TIPR can also be applied as direct method with a forward solution that allows the fast determination of modal characteristics given structural changes. The simulation of various scenarios of structural degradation could give insight to resulting modal alterations.

Another application that suggests itself is damage detection. Given the indicative nature of the elemental perturbation coefficients it is intuitive to assume that the TIPR solution for a decreased natural frequency could be used to indicate the location of the damage that caused the frequency decrease. However, damage detection based on natural frequencies and mode shapes entails unresolved problems and faces manifold practical limitations [156, 65].

Stiffness sensitivities with respect to the frequencies are very low. The prevention of damage propagation and failure requires an early detection. The initial phase of a defect, however, is typically a very local and minor phenomenon that will have an insignificant effect on the dynamic properties. Long structures such as high aspect ratio wings show a particularly low sensitivity to local damage because the wing span is the key driver of the global vibratory response and a local defect will not result in measurable changes.

Mode shapes have been identified to be more meaningful diagnostic parameters than natural frequencies. Their utilization showed very satisfactory results but can not defy a

strong dependence on the size of the damage [140, 151]. Performance further deteriorates in the presence of noise as inherent to experimental measurements.

8.5 Limitations

The proposed algorithm showed an impressive performance in terms of accuracy and efficiency. It also entails a series of limitations that shall not remain disregarded.

Problem Setup The formulation of redesign and optimization problems subject to a minimum change criterion are straight forward and only require the specification of reasonably sized frequency increments that comply with the small perturbation assumption. The minimum mass criterion, however, should always be accompanied by move limits on the intermediate design variables. Choosing an adequate combination of incremental frequency changes and incremental limits on fractional structural changes can be difficult. A TIPR increment has no feasible solution if the incremental frequency change is too big for the structural move limits.

Move limits exist to enhance the accuracy of the optimization. The present study showed that, as long as the TIPR parameters represent small perturbations, a solution for the incremental modal objective will typically be found, only it violates the structural move limits. The TIPR based optimization then simply continues using the *infeasible* solution from the last increment as baseline for the new increment. Error accumulation is avoided by the reanalysis at the end of each increment.

Structural Breadth A comprehensive structural optimization requires the consideration of numerous factors. To improve the quality of initial designs, the conceptual designer should include static and dynamic constraints such as stresses, deflections, and flutter and/or divergence speed. Focal point of the TIPR based algorithm is the placement of natural frequencies. The present research thus makes only a small contribution to the ultimate goal of comprehensive conceptual design capabilities.

Optimal stiffness is designed into a system. If the absence of corresponding analyses

results in a conceptual baseline or an already existing aircraft wing with aeroelastic instabilities, TIPR offers an effective solution for design goals expressible in natural frequency objectives by means of a minimum change to the baseline configuration.

Mode Switching A common difficulty in structural optimization subject to frequency constraints is the switching of vibration modes. The implications of mode switching are twofold. On one hand, the optimized solution may not satisfy the frequency constraints because these were imposed on the wrong mode. On the other hand, gradient based optimizers may experience oscillatory convergence difficulties or break down altogether due to discontinuous constraint sensitivities.

There are tools for the identification and tracking of critical modes, but they are formidable and not infallible [162]. Presently, the TIPR optimization places the natural frequencies of specified modes. It is unknown how the incremental application of TIPR performs in the presence of mode switching that requires the consideration of varying frequency objectives and mode numbers.

Manufacturability Good design practice for composite structures requires working experience and/or formal training in composite materials because the design space is constricted by manufacturing limitations and production needs associated with composite materials.

On one hand there are physical aspects that require extended analysis. The curing process of manufacturing a composite laminate induces thermal stresses and can lead to distortion and/or matrix cracking. The response characteristics of composite layers under thermal loads are directional. Deformation differences can introduce residual stresses that require a structural analysis for combined thermal and mechanical loads.

On the other hand there are practical aspects. Discontinuous distributions are unsuitable for the manufacturing process. Commercial composites often come as unidirectional sheets with fixed thickness. Ply orientations are often limited to a finite set of specified angles. These aspects can be taken into account by correcting the wing model, by refining the formulation of the optimization problem, or by restricting possible design variable settings.

The TIPR algorithm currently lacks the consideration of manufacturing aspects. The

problem formulation, however, can easily be extended to account for the latter category of practical manufacturing aspects.

Hygrothermal Effects Composite materials exposed to temperature and moisture variations can develop stresses in the absence of mechanical loads. The consideration of corresponding thermal and hygral effects is important for the prediction of the true mechanical performance during operating life.

Thermal and hygral loads cause expansion of composite materials with different rates for matrix and fiber materials. The latter experience an additional dependency due to the directional nature of their properties. For most applications it may be assumed that the fibers are not prone to hygral effects. The matrix material, however, starts absorbing moisture from the surrounding humid air immediately upon manufacture.

An unconstrained material subject to hygrothermal loads will deform without developing internal stresses. Composite materials are made of layers. Each layer is composed of oriented plies embedded in a matrix material. Because the individual layers are bonded together, the deformation differences associated with the directional properties of each layer constitutes a constraint for adjacent layers, and hygrothermal strains are accompanied by residual stresses.

Deformations and residual stresses due to environmental variations in temperature and moisture are a major concern for shape stability and material degradation and failure. The stacking sequence, for example, has a significant impact on composite deformation characteristics. It is an important aspect of hygrothermal stability with respect to curvature development or warping of the composite material in changing operating conditions.

8.6 Future Work

Above limitations and unaddressed issues inherently enclose additional research and related work conducive to the improvement of the developed algorithm. The following will outline some very specific suggestions for the extension and the enhancement of the presented optimization scheme.

Nonlinear Scheme The derivation of the first order perturbation equation requires cancellation of all higher order terms in the expanded equation of motion. Pertaining literature also offers nonlinear solutions that carry all perturbation terms to enable large changes without increments.

For redesign solutions that require modifications of magnitudes beyond the small perturbation assumption, the TIPR stiffness effect separation and the introduction of surrogate models at the local level could be adopted by the nonlinear scheme or vice versa. A separate study on accuracy and efficiency would have to be performed in order to determine if the nonlinear method is superior to the incremental linear method.

Scaling Law The 6x6 stiffness matrix from VABS can be partitioned into four quadrants as depicted in Figure 8.2. Coefficients in the upper left are proportional to the cross sectional area. Coefficients in the upper right are proportional to the square root of the cubed area; and coefficients in the lower right are proportional to the square of the area. Global beam properties rely on the linear interpolation of cross sectional properties along the span; and each cross section along the span requires a VABS analysis.

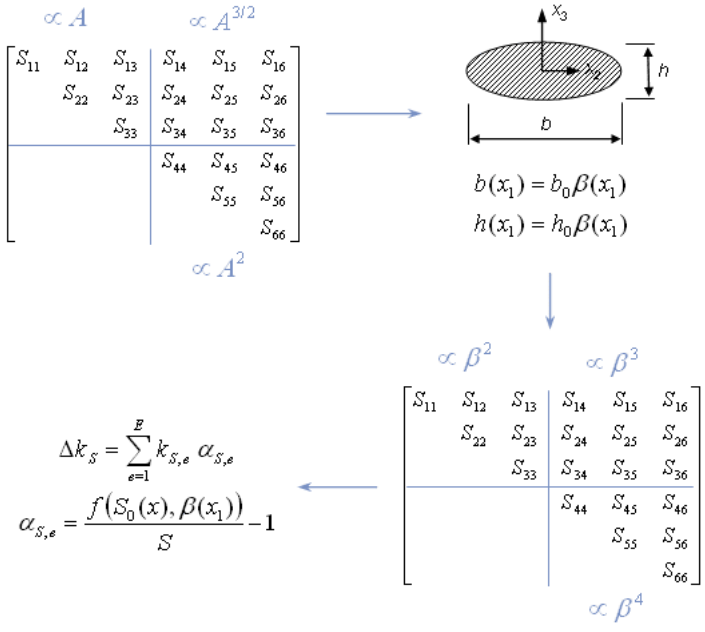

Figure 8.2: Scaling law utilization

VABS III is the latest version and much faster than the VABS release used in the present study [206]. However, if a proven scaling law for cross sectional properties was available, a single VABS run would suffice for all cross sections that are geometric-similar. The result could be taken advantage of in the definition of the intermediate design variables α that represented the Timoshenko separated stiffness effects.

Figure 8.2 illustrates the utilization of the scaling law. The index 0 denotes the baseline analyzed by VABS. The sectional stiffness coefficient S depends on the physical design variables x. The scaling parameter β depends on the spanwise coordinate x_1.

Surrogate Study The choice of a surrogate model depends on the system response of interest. A faulty choice leads to an erroneous representation and the surrogate based optimization converges to a faulty solution. The implementation studies presented above fall back on rather simple design spaces. In general, however, guidance on the nature of specific local design spaces along with a suitable surrogate modeling technique would greatly support the efficiency and the success of related design efforts.

Additional Constraints Traditional conceptual design disregards stress related constraints. The introduction of corresponding analysis capabilities would enable failure analyses as well as conceptual fatigue and maintenance studies.

Literature pertaining to inverse perturbation redesign offers stress objectives in the redesign algorithm [96, 21]. If suitable for application within TIPR, VABS analyses would be expanded to also recover stress fields. VABS III provides respective results in the material coordinate system for subsequent failure analyses.

Another constraint of interest to the aircraft designer relates to the static displacement of the wing. Static displacements are typically expressed as linear superposition of natural vibration modes, giving rise to the intuitive speculation that TIPR can be extended to limit static deflections by introducing respective objectives and/or constraints.

Large Deflections The combination of highly flexible wings and high aspect ratios results in large deflections during flight that can significantly change structural dynamics, natural

frequencies, and aeroelastic behavior [143, 145, 144]. The utilization of prestressed modes would greatly contribute to the validity of aeroelastic response analyses and would require the eigen analysis for the determination of natural frequencies and mode shapes to be performed about the deflected steady state equilibrium of the wing.

Hybrid Optimization Commercial unidirectional sheets with fixed thicknesses and orientation angles limited to a finite set of specified values require discrete programming techniques. The implementation of the developed TIPR optimizer currently solves a continuous optimization problem at each increment. An extension of the TIPR algorithm to account for discrete or integer design variables could simply employ a corresponding optimization routine. Problems arise when the discrete layup settings are widely spaced causing a violation of the TIPR small perturbation assumption.

In that case it might be desirable to use a global optimization technique such as a Genetic Algorithm or Simulated Annealing first to scan for promising location of the design space and then use TIPR as supplied before.

Smart Reanalysis and Incremental Perturbation Size TIPR presently subjects the global beam problem to a reanalysis at the beginning of each increment. The implementation results presented earlier revealed negligible errors for small perturbations. These small errors in the modal objectives indicate the legitimate possibility of running TIPR without a reanalysis at each increment. A corresponding implementation would require an error projection scheme that identifies the current need for reanalysis.

Similarly, one could determine the optimum perturbation size at the beginning of each increment. The realization of either one the smart reanalysis or the smart perturbation size would further reduce computational costs.

8.7 Final Remark

Some of the findings of the present research seem obvious at the conclusion of this work. Hindsight is said to be easier than foresight though and the route documented did not exactly have easy access roads. The toll was usually more than the change available; and long detours along with frustrating stop overs had to be accepted.

In the end, the research presented has marginal significance at best. Its small contribution, however, stems from offering a solution to three pertaining problems. The violation of constitutive laws in multi level optimization schemes. The practical disconnect of the fractional multipliers in modal perturbation redesign; and the computational expense of directed search algorithms for frequency constrained optimization based on gradients.

Appendix A

UAV WEIGHT DATA

Compiling a complete UAV database is challenging. Most data is confidential or proprietary and as such not accessible to the public. Published data for the same vehicle varies with reference. Tables A.1 and A.2 summarize the data utilized in Figure 2.6.

Table A.1: Unconventional UAV weights

UAV	Gross weight, lbs	Empty weight, lbs	Additional information	Reference
Pathfinder	560	*460*	100 lbs payload	NASA [132]
Pathfinder Plus	700	*550*	150 lbs payload	NASA [132]
Centurion	1,900	1,175		NASA [132]
Helios	2,048	1,322		NASA [132]
RQ-3A Darkstar	8,600	4,360		www [72]
Proteus	12,500	5,900		NASA [132]
Proteus (MIL)	15,800	5,900	Military use	NASA [132]

www - world wide web; MIL - military use

Weight entries in italic font were not explicitly disclosed. Respective values were calculated using additional information provided by the reference. That is, $W_{empty} = W_{gross} - W_{payload}$ for the solar powered UAVs in Table A.1, and $W_{empty} = W_{gross} - W_{payload} - W_{fuel}$ for the conventionally configured UAVs in Table A.2. Fuel capacity for Altus II and Perseus B were listed in gallons. Both vehicles are propelled by a piston engine[1]. Fuel weight was determined using general aviation gasoline with a specific weight of 6 lbs/gal.

[1] Altus II: Rotax 912 four-cylinder piston engine rated at 100 hp; Perseus B: Rotax 914 four-cylinder piston engine rated at 105 hp.

Table A.2: Conventional UAV weights

UAV	Gross weight, lbs	Empty weight, lbs	Additional information	Reference
Altair	7,000	*3,250*	750 lbs payload; 3,000 lbs fuel	NASA [132]
Predator B	6,400	*2,650*	750 lbs payload; 3,000 lbs fuel	NASA [132]
YMQ-9A Predator B	10,000	3,050		www [142]
RQ-4A Global Hawk	22,900	8,490		www [72]
RQ-1L Predator	2,250	950		www [142]
RQ-1 Predator	2,249	1,129		www [199]
I-Gnat	1,550	850		www [142]
Gnat-750	1,126	560		www [142]
Altus II	2,130	*1,248*	330 lbs payload; 92 gal fuel capacity, *552 lbs*	NASA [132]
Raptor	1,800	810		www [72]
Perseus B	2,200	*1,785*	175 lbs payload; 40 gal internal fuel capacity, *240 lbs*	NASA [132]
Perseus B (EFT)	2,500	*1,725*	additional 60 gal external fuel tanks, *360 lbs*	NASA [132]
Hermes 450	1,765	990		www [72]

www - world wide web; EFT - external fuel tanks

Appendix B

AN INTRODUCTION TO AEROELASTICITY

Any aeroelastic discussion would be incomplete without Collar's triangle of forces [42]. It concisely depicts both the three types of forces involved and the problems akin to their interaction. The interdependencies cast in Figure B.1 are by no means a self-contained exposition of aeroelasticity. They merely provide a taste of this vast and fascinating field.

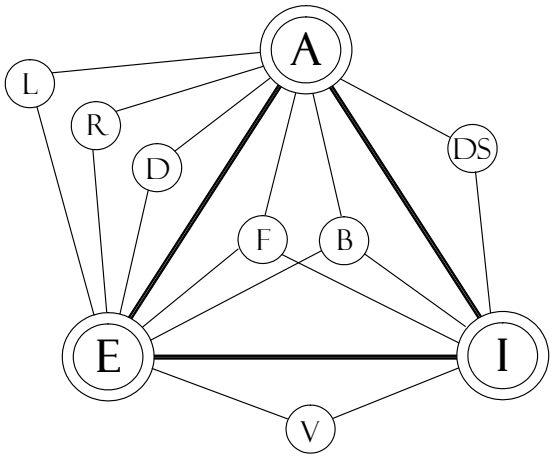

Figure B.1: Aeroelastic triangle of forces
Forces: A - Aerodynamic, E - Elastic, I - Inertial
Static aeroelastic phenomena: D - Divergence, R - Control reversal, L - Load distribution
Dynamic aeroelastic phenomena: F - Flutter, B - Buffeting
Related fields: DS - Rigid body dynamic stability, V - Mechanical vibrations

Many aeroelastic events are attributed to complex nonlinearities such as shocks, stall, flow separation and turbulence. Others can be described within the assumption of potential flow [69, 25]. Aerodynamic load distribution, divergence, and flutter are aeroelastic phenomena of most common interest. They are addressed in the following sections. Simplified models assist a basic understanding of their fundamental nature.

B.1 Load Distribution

The mutual interaction of structures and aerodynamics depicts the primary reciprocative mechanism of aeroelasticity. As aerodynamic forces act on the structure, deformations will be procured. As a result, the aerodynamic load distribution will change and affect the aerodynamic impact on the structure. In a stable system, those interrelated changes will adjust themselves until equilibrium is reached.

Figure B.2 illustrates the effect of torsional compliance on the spanwise lift distribution of a straight wing. As will be seen in Equation B.1, the two-dimensional lift of an elastic wing (compared to a rigid wing) has an additional contribution that results in an outward movement of the spanwise center of pressure. The associated increase in bending moment is of immediate interest to the structural designer.

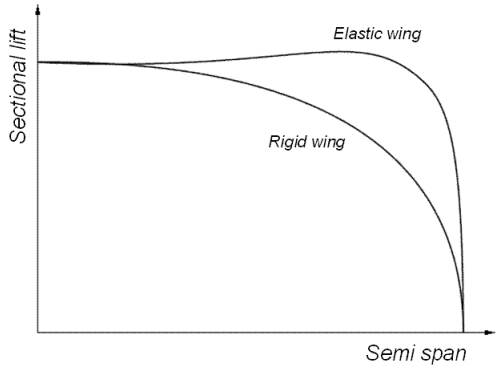

Figure B.2: Change in lift distribution due to wing torsional flexibility
Recreation of Figure 4.14 in Hodges et al. [82]

A dynamic treatment of the above problem requires the consideration of time dependent external loads potentially exciting structural vibrations. The resulting dynamic response problem features inertial forces that cause dynamic overstresses. These stresses are of outmost importance to the structural integrity of the aircraft. For instance, the root bending moment of an elastic wing exposed to a gust can easily be up to 20% greater than that of a rigid wing in the same gust condition [25].

B.2 Divergence

Divergence is a phenomenon of static instability. For illustration, consider a straight wing represented by a rigid airfoil in two-dimensional flow as shown in Figure B.3. The airfoil is pivoted at the elastic axis with a spring representing torsional flexibility. The distance of the aerodynamic center, the center of gravity, and the elastic axis from the leading edge are denoted by x_{ac}, x_{cg}, and x_p, respectively.

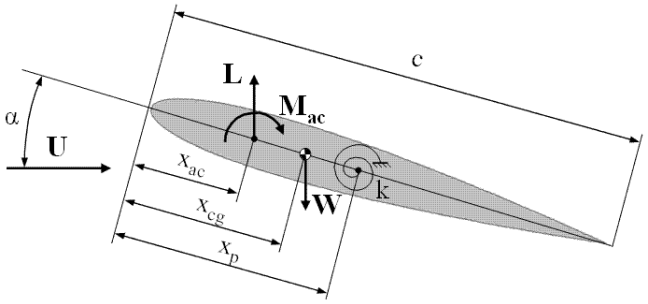

Figure B.3: Rigid airfoil on torsionally flexible support

The assumption of small angular displacements in subsonic flow allows the application of linear aerodynamic theory. The wing of area S and constant chord c is subject to the dynamic pressure $q_\infty = \frac{\rho_\infty}{2} V^2$ The total angle of attack αhas a rigid (initial) contribution α_r and an elastic (twist due to flexible support) contribution θ.

$$C_L = a\alpha = a(\alpha_r + \theta) \tag{B.1}$$

$$L = q_\infty S C_L \tag{B.2}$$

$$M_{ac} = q_\infty S c C_{mac} \tag{B.3}$$

Assuming a linear spring, an expression for the elastic twist can be developed.

$$k\theta = M_{ac} + L(x_p - x_{ac}) - W(x_p - x_{cg}) \tag{B.4}$$

$$\theta = \frac{q_\infty S c C_{mac} + q_\infty S a \alpha_r (x_p - x_{ac}) - W(x_p - x_{cg})}{k - q_\infty S a (x_p - x_{ac})} \tag{B.5}$$

The denominator in Equation B.5 vanishes for $k = q_\infty Sa(x_p - x_{ac})$, producing an infinitely large angle of twist. It is this very condition that is referred to as torsional divergence. Defining the offset between the aerodynamic center and the elastic axis as $e = x_p - x_{ac}$, the divergence dynamic pressure and the corresponding critical speed evaluate to

$$q_D = \frac{k}{Sae}, \qquad V_D = \sqrt{\frac{2}{\rho_\infty}\frac{k}{Sae}}. \tag{B.6}$$

In order to avoid catastrophic failure, operating conditions must be well below the critical values. Equation B.6 suggests two structural design variables eligible to manipulate the divergence dynamic pressure. However, increasing the torsional stiffness k is not only expensive but also holds additional weight penalties. Thus, the decrease in e by moving the elastic axis forward constitutes a preferred design solution [25].

B.3 Flutter

Flutter is an oscillatory instability. The flutter speed denotes the air speed at which the oscillation is able to maintain a constant amplitude. This critical speed represents the stability boundary. At speeds below the flutter speed, damping effectuates decreasing amplitudes over time. At speeds above the flutter speed, the decay of damping admits the growth of amplitudes over time, quickly leading to violent oscillations and proximate destruction.

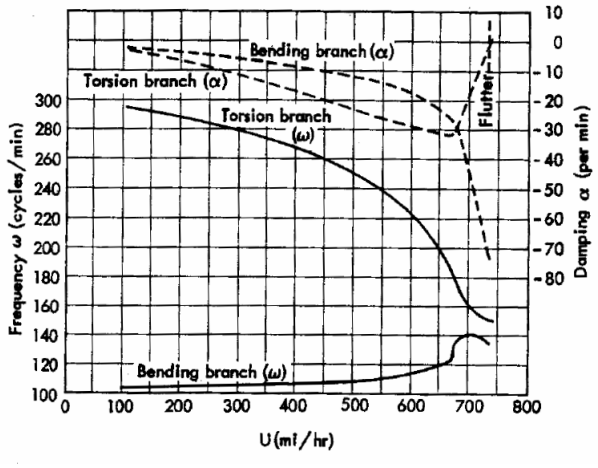

Figure B.4: Frequency and damping of aeroelastic modes vs. airspeed
Figure 9-7 in Bisplinghoff et al. [25]

Figure B.4 illustrates the sudden and violent nature of flutter by reproducing a large aspect ratio wing study by Goland and Luke [73]. The examination of the critical flutter mode relies on the investigation of the lowest frequency natural modes because (a) Aeroelastic modes correspond to the natural vibration modes of the structure; and (b) The stiffness effects with primary significance for large aspect ratios are bending and torsion. Figure B.4 shows a typical development of these fundamental aeroelastic modes. Airspeed is given in miles per hour, damping and frequency represent the real and imaginary part of the exponential complex time dependency of both modes, respectively [25].

Initially, both modes show an increased damping with airspeed. This means energy is extracted from the structure by the airstream and the system is stable. One damping branch will eventually reverse and drop to zero. This crossing of the abscissa denotes the critical flutter speed. Simultaneously, the frequencies of the two coupled modes exercise a merging behavior. Up to the actual reversal point of the critical torsion branch there is no indication of the imminent danger. Prediction of the aeroelastic threat is possible only within a few percent of the flutter speed. In contrast, 5 mph above the critical speed, the wing in Figure B.4 will experience total destruction within two or three cycles of oscillation [25].

B.3.1 Classical Flutter Analysis

For illustration, consider the rigid airfoil in two-dimensional flow in Figure B.5. The airfoil has a pitching degree of freedom θ and a plunging degree of freedom h, representing torsional and bending deformation of the corresponding three-dimensional lifting surface. The two linear springs take the cross sectional place of wing torsional and bending stiffness.

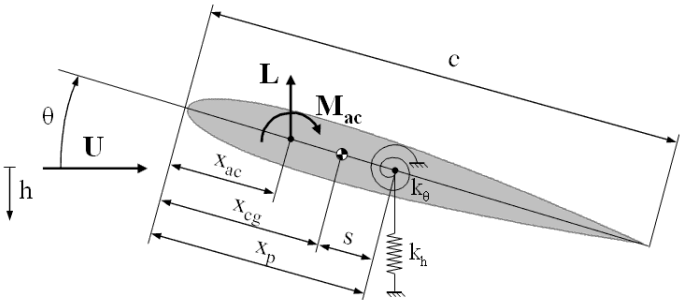

Figure B.5: Rigid airfoil with two degrees of freedom

The derivation of the equations of motion starts with the realization that θ and h are generalized coordinates. That is, θ and h are independent and can be varied without affecting one another. Thus, the application of Lagrange's equation yields

$$m\ddot{h} + S_\theta \ddot{\theta} + k_h h = -L \tag{B.7}$$

$$I_\theta \ddot{\theta} + S_\theta \ddot{h} + k_\theta \theta = M, \tag{B.8}$$

where

m = mass per unit span,

$S_\theta = ms$ = static mass moment per unit span about axis $x = x_p$, with $s = x_{cg} - x_p$, and

$I_\theta = I_{cg} + ms^2$ = mass moment of inertia per unit span about axis $x = x_p$

Steady amplitude oscillations in either the pitching or the plunging mode constitute the flutter boundary. Oscillations are initially excited by dynamic airloads, caused by unsteady flow phenomena such as time-varying wind and shed vorticity in the wake. In accordance with the self-sustained oscillations at the flutter boundary, it is admissible to presume a simple harmonic time dependency for both aerodynamic forces and resulting modes of motion.

$$L(t) = \overline{L} \cdot e^{i\omega t}, \qquad M(t) = \overline{M} \cdot e^{i\omega t} \tag{B.9}$$

$$h(t) = \overline{h} \cdot e^{i\omega t}, \qquad \theta(t) = \overline{\theta} \cdot e^{i\omega t} \tag{B.10}$$

The a priori assumption of simple harmonic motion is the essence of classical flutter analysis. While this assumption disables the calculation of any off-stability-boundary condition, it allows for the unsteady airloads to be determined in a comparatively simple way. Assuming fully attached flow and small amplitudes of motion, linear flow theory may be used to obtain the airload amplitudes.

$$\overline{L} = -\pi \rho_\infty b^3 \omega^2 \left(L_h \frac{\overline{h}}{b} + L_\theta \overline{\theta} \right) \tag{B.11}$$

$$\overline{M} = \pi \rho_\infty b^4 \omega^2 \left(M_h \frac{\overline{h}}{b} + M_\theta \overline{\theta} \right) \tag{B.12}$$

The parameter $b = \frac{c}{2}$ denotes the airfoil semi chord customary in unsteady aerodynamics. L_h, L_θ, M_h, and M_θ are complicated functions of the reduced frequency k and the free stream Mach number M_∞ [25, 82].

$$k = \frac{b\omega}{V} \tag{B.13}$$

$$M_\infty = \frac{V}{a_\infty} \tag{B.14}$$

Upon substitution of Equations B.9 and B.10 into the equations of motion, Equations B.7 and B.8 can be recast.

$$-\omega^2 m \overline{h} - \omega^2 S_\theta \overline{\theta} + k_h \overline{h} = -\overline{L} \tag{B.15}$$

$$-\omega^2 I_\theta \overline{\theta} - \omega^2 S_\theta \overline{h} + k_\theta \overline{\theta} = \overline{M} \tag{B.16}$$

It is convenient praxis to introduce the natural frequencies of the uncoupled modes. They are easily found by setting the inertial coupling terms on the left hand side and the forcing terms on the right hand side in Equations B.7 and B.8 to zero. Taking advantage of the simple harmonic motion of θ and h, the uncoupled natural torsional and bending frequencies can be evaluated.

$$\omega_\theta = \sqrt{\frac{k_\theta}{I_\theta}}, \qquad \omega_h = \sqrt{\frac{k_h}{m}}. \tag{B.17}$$

Using the developed expressions for aerodynamic load amplitudes and natural mode frequencies, the equations of motions can be further rearranged to yield an algebraic set of two linear and homogeneous equations for the mode amplitudes $\overline{\theta}$ and $\overline{h}$.

$$\left[\frac{m}{\pi \rho_\infty b^2} \left(1 - \frac{\omega_h^2}{\omega^2} \right) + L_h \right] \frac{\overline{h}}{b} + \left(\frac{S_\theta}{\pi \rho_\infty b^3} + L_\theta \right) \overline{\theta} = 0 \tag{B.18}$$

$$\left(\frac{S_\theta}{\pi\rho_\infty b^3}+M_h\right)\frac{\overline{h}}{b}+\left[\frac{I_\theta}{\pi\rho_\infty b^4}\left(1-\frac{\omega_\theta^2}{\omega^2}\right)+M_\theta\right]\overline{\theta}=0 \tag{B.19}$$

The coefficients in Equations B.18 and B.19 can be expressed in terms of dimensionless parameters. Introducing the mass ratio μ, the radius of gyration r, and the natural frequency ratio σ,

$$\mu=\frac{m}{\pi\rho_\infty b^2},\qquad r=\sqrt{\frac{I_\theta}{mb^2}},\qquad \sigma=\frac{\omega_h}{\omega_\theta} \tag{B.20}$$

the flutter problem presents itself as follows.

$$\left\{\mu\left[1-\sigma^2\left(\frac{\omega_\theta}{\omega}\right)^2\right]+L_h\right\}\frac{\overline{h}}{b}+\left(\mu\frac{s}{b}+L_\theta\right)\overline{\theta}=0 \tag{B.21}$$

$$\left(\mu\frac{s}{b}+M_h\right)\frac{\overline{h}}{b}+\left\{\mu r^2\left[1-\left(\frac{\omega_\theta}{\omega}\right)^2\right]+M_\theta\right\}\overline{\theta}=0 \tag{B.22}$$

The trivial solution of the above eigenvalue problem is of no physical relevance. The non-trivial solution requires a rather cumbersome iterative procedure. The solution of the flutter boundary evaluates to the flutter determinant in Equation B.23.

$$\begin{vmatrix} \mu\left[1-\sigma^2\left(\frac{\omega_\theta}{\omega}\right)^2\right]+L_h & \mu\frac{s}{b}+L_\theta \\ \mu\frac{s}{b}+M_h & \mu r^2\left[1-\left(\frac{\omega_\theta}{\omega}\right)^2\right]+M_\theta \end{vmatrix}=0 \tag{B.23}$$

The resulting polynomial is quadratic in the unknown $\left(\frac{\omega_\theta}{\omega}\right)^2$, giving a first impression of a simple linear system of equations. However, there are three more unknowns representing the flight condition. Because of the backbone of classical flutter analysis, i.e. the assumption of simple harmonic motion at the flutter boundary, the main quest is to find the very flight condition at which the presumed simple harmonic motion is indeed valid. The additional unknowns are mass ratio μ, free stream Mach number M_∞, and reduced frequency k, leaving only one equation for a total of four unknowns.

Partial relief is provided by the complex aerodynamic coefficients L_h, L_θ, M_h, and M_θ, making the polynomial a complex equation. Recognizing that both real and imaginary

part need to be zero in order to satisfy the characteristic polynomial, two equations are now available. The mathematically still underdetermined system is solved iteratively by specifying an initial guess for two of the four unknowns.

B.3.2 The V-g Method

Equations B.7 and B.8 disregard structural dissipation. While the internal friction of aircraft is very small, corresponding forces are important to the accuracy of stability calculations [59, 64]. Expanding the equations of motion for the two-dimensional example in Figure B.5 to include structural damping results in

$$m\ddot{h} + S_\theta\ddot{\theta} + k_h h = -L + D_h \tag{B.24}$$

$$I_\theta\ddot{\theta} + S_\theta\ddot{h} + k_\theta\theta = M + D_\theta. \tag{B.25}$$

Structural damping was found to be proportional to the elastic force and in phase with the velocity of the corresponding oscillatory motion [59, 160]. The damping forces in Equations B.24 and B.25 can thus be derived as a complex quantity by employing a non-dimensional coefficient on the restoring force term.

$$D_h = ig_h k_h \overline{h} \cdot e^{i\omega t} \tag{B.26}$$

$$D_\theta = ig_\theta k_\theta \overline{\theta} \cdot e^{i\omega t} \tag{B.27}$$

The equations of motion can now be formulated as

$$-\omega^2 m\overline{h} - \omega^2 S_\theta\overline{\theta} + (k_h - ig_h)\overline{h} = -\overline{L} \tag{B.28}$$

$$-\omega^2 I_\theta\overline{\theta} - \omega^2 S_\theta\overline{h} + (k_\theta - ig_\theta)\overline{\theta} = \overline{M}. \tag{B.29}$$

Expressing the spring constants k_h and k_θ in terms of the uncoupled natural frequencies (Equation B.17), the flutter eigenvalue problem can be developed by following the steps outlined in classical flutter analysis.

$$\left\{\mu\left[1-\sigma^2\left(\frac{\omega_\theta}{\omega}\right)^2(1+ig_h)\right]+L_h\right\}\frac{\overline{h}}{b}+\left(\mu\frac{s}{b}+L_\theta\right)\overline{\theta}=0 \tag{B.30}$$

$$\left(\mu\frac{s}{b}+M_h\right)\frac{\overline{h}}{b}+\left\{\mu r^2\left[1-\left(\frac{\omega_\theta}{\omega}\right)^2(1+ig_\theta)\right]+M_\theta\right\}\overline{\theta}=0 \tag{B.31}$$

Smilg and Wasserman [170] are referenced to first have introduced the assumption of equal damping [25, 64]. Applied to Figure B.5, the artificial structural damping in both modes is then represented by a single damping coefficient g.

$$g=g_h=g_\theta \tag{B.32}$$

Because of the lack of quantitative information on structural damping, and because of the convenient grouping of the damping coefficient with the flutter frequency, both g and ω are treated as unknowns in a single complex expression.

$$Z=\left(\frac{\omega_\theta}{\omega}\right)^2(1+ig) \tag{B.33}$$

The flutter determinant,

$$\begin{vmatrix} \mu(1-\sigma^2 Z)+L_h & \mu\frac{s}{b}+L_\theta \\ \mu\frac{s}{b}+M_h & \mu r^2(1-Z)+M_\theta \end{vmatrix}=0 \tag{B.34}$$

then leads to a quadratic equation with two complex solutions.

$$Z_{1,2}=\left(\frac{\omega_\theta}{\omega_{1,2}}\right)^2(1+ig_{1,2}) \tag{B.35}$$

The roots of the flutter polynomial (Equation B.35) are obtained in a fashion similar to classical flutter analysis. The difference and advantage of the *V-g* solution process is the absence of iteration requirements on k. Instead, the flutter solution is determined for a specified combination of altitude and reduced frequency, thus the alternate name *k method*, and damping g and frequency ω of the modes are plotted against the airspeed. As a result, *V-g* and *V-f* plots similar to Figure B.4 are obtained.

However, the determined flutter speed can disagree with the preselected flight condition. Only an iterative procedure of performing the flutter analysis for multiple densities

can ensure that $V_F = {}^{b\omega_F}/_k = Ma$ Such a matched point solution gains imperative when compressibility effects need to be accounted for.

Also, it is important to recall that g has been introduced as artifice to model structural damping in simple harmonic motion. Thus, g and ω have no physical meaning except at the fluttery boundary, where structural damping is assumed to vanish. In fact, the *V-g method* has shown faulty predictions of modal coupling and the potentially unstable mode; but produces consistent flutter speed results [80].

B.3.3 The p-k Method

The equations of motion for the two-dimensional airfoil in Figure B.5 (Equations B.7 and B.8) can also be expressed in terms of matrices.

$$\begin{bmatrix} m & S_\theta \\ S_\theta & I_\theta \end{bmatrix} \begin{Bmatrix} \ddot{h} \\ \ddot{\theta} \end{Bmatrix} + \begin{bmatrix} k_h & 0 \\ 0 & k_\theta \end{bmatrix} \begin{Bmatrix} h \\ \theta \end{Bmatrix} = \begin{Bmatrix} -L \\ M \end{Bmatrix} \tag{B.36}$$

The generalized coordinates h and θ result in a total of $n = 2$ degrees of freedom. Introducing ξ_i as the i^{th} generalized coordinate, Equation B.36 can be written as

$$[M] \left\{ \ddot{\xi} \right\} + [K] \{\xi\} = \{F\} \tag{B.37}$$

The force vector on the right hand side of Equation B.37 represents the external loading by means of aerodynamic forces that can be derived as linear function of the generalized coordinates and derivatives thereof.

$$F_i = q_\infty \sum_{j=1}^{n} (a_{ij}\xi_j + b_{ij}\dot{\xi}_j + c_{ij}\ddot{\xi}_j) \qquad i, j = 1, ..., n \tag{B.38}$$

On a side note, if the two-dimensional airfoil in Figure B.5 is stationary, the generalized coordinates $\xi_1 = h$ and $\xi_2 = \theta$ do not change with time, i.e., $\dot{\xi}_i = 0$ and $\ddot{\xi}_i = 0$. The magnitude of F_1 then reduces to the well known steady state lift $L = q_\infty 2\pi\theta S$, with 2π being the lift curve slope from thin airfoil theory resulting in $a_{11} = 0$ and $a_{12} = -2\pi S$.

The general solution of Equation B.37 can be expressed as exponential function of time.

$$\xi_i(t) = \overline{\xi}_i \cdot e^{p\frac{V}{b}t} \tag{B.39}$$

Substitution of this expression into Equations B.37 and B.38 yields a linear system of n algebraic equations with the unsteady aerodynamic matrix $[A(p)] = p^2[c] + p[b] + [a]$ that defines the generalized aerodynamic forces.

$$\left[\frac{V^2}{b^2}[M]p^2 + [K] - q_\infty[A(p)]\right]\{\bar{\xi}\} = 0 \tag{B.40}$$

For a non-trivial solution, the determinant of the above coefficient matrix must be zero.

$$\left|\frac{V^2}{b^2}[M]p^2 + [K] - q_\infty[A(p)]\right| = 0 \tag{B.41}$$

Equation B.41 is solved for n complex conjugate pairs of p (Equation B.42), with k being the reduced frequency, and γ being the rate of decay expressed as function of successive amplitudes of the oscillatory motion.

$$p = \gamma k \pm ik \tag{B.42}$$

$$\gamma = \frac{1}{2\pi} ln\left(\frac{a_{n+1}}{a_n}\right) \tag{B.43}$$

The above system describes transient motion and airloads by means of the complex eigenvalue p, which gave the solution procedure the name *transient method* or *p method*

The assumption of simple harmonic motion in the *k method* on the other hand resets the rate of decay. The complex eigenvalue reduces to $p = ik$, and Equation B.41 becomes

$$\left|-\frac{V^2}{b^2}[M]k^2 + [K] - q_\infty[A(ik)]\right| = 0. \tag{B.44}$$

In traditional Amercian form, Equation B.44 reads

$$\left|-\frac{1}{b^2}[M]k^2 + \frac{1}{V^2}[K] - \frac{\rho}{2}[A(ik)]\right| = 0. \tag{B.45}$$

Equation B.41 is solved directly for p by specifying a combination of speed and altitude. In contrast, Equation B.45 is solved for the complex roots of $1/V^2$ by preselecting values of k and altitude. Hence, free stream velocity and Mach number are unknown and need to be iterated on in order to accurately capture compressibility effects.

The advantage of the *p method* of having available the correct Mach number at the outset enables the direct determination of the coefficients in $[A(p)]$. The disadvantage is that transient aerodynamic loads are far more delicate than simple harmonic ones. A compromise is offered by the *p-k method*, which is based on the assumption that the aerodynamics for oscillatory motion with slowly changing amplitudes can be approximated very well with constant amplitudes [80]. The flutter determinant then reads

$$\left| \frac{V^2}{b^2} [M] p^2 + [K] - q_\infty [A(ik)] \right| = 0. \tag{B.46}$$

Equation B.46 is solved for p using determinant iteration. Starting with an initial guess for k, the unsteady aerodynamic matrix $[A(ik)]$ can be computed, and an initial solution for p can be determined. The corresponding values for reduced frequency and damping for one of the n complex conjugate roots (Equation B.42) evaluate to

$$k_1 = Im(p), \qquad \gamma_1 = \frac{Re(p)}{k_1}. \tag{B.47}$$

The so found reduced frequency k_1 is used in the recalculation of $[A(ik)]$, leading to a new reduced frequency k_2 (Equation B.47). The aerodynamic matrix is successively updated and used in the solution of Equation B.46 until the k values converge [80].

B.4 Epilogue

Aeroelasticity is a field of great diversity with complex phenomena affronting the general idea of simplification. A true capture of aeroelastic events in all physical detail requires elaborate analyses such as full FEA coupled with sound CFD. However, a legitimate set of simplifying assumptions can greatly expedite computational implementations by enabling rapid calculations sufficient for the coarse localization of potential instabilities. The transparency of such calculations not only contributes to a better understanding of physical mechanisms, but also enables a rapid detection of respective stability margins. Conservative results are typically enough to assure freedom from instability, but also provide a starting point for high fidelity analyses.

The preceding chapter provided a basic notion of the complexity of aeroelasticity. It presented a very limited selection of aeroelastic phenomena with solution techniques that are frequently used in literature. For a broader coverage and further references the reader is referred to Bisplinghoff, Ashley, and Halfman [25]; Fung [64]; and Hodges et al. [82].

Appendix C

FIRST ORDER PERTURBATION EQUATION

Given a baseline structure with unsatisfactory natural mode characteristics, the uncoupled equations of motion are expressed with a generalized mass and a generalized stiffness matrix.

$$[K] = [M]\left[\omega^2\right] \tag{C.1}$$

$$[K] = [\phi]^T [k] [\phi], \qquad [M] = [\phi]^T [m] [\phi] \tag{C.2}$$

The baseline system is fully known in terms of its structural and modal properties. The modal properties, however, fail to agree with desired vibratory response criteria. That is, the natural frequencies and mode shapes of the baseline system do not meet a set of specified values. The objective system on the other hand, features all the desired natural mode characteristics, but is unknown in its structural properties.

$$\left[\hat{K}\right] = \left[\hat{M}\right]\left[\hat{\omega}^2\right], \tag{C.3}$$

$$\left[\hat{K}\right] = \left[\hat{\phi}\right]^T \left[\hat{k}\right] \left[\hat{\phi}\right], \qquad \left[\hat{M}\right] = \left[\hat{\phi}\right]^T [\hat{m}] \left[\hat{\phi}\right] \tag{C.4}$$

Substitution of Equations 3.7 - 3.10 into the objective equations of motion yields

$$\begin{gathered}([\phi] + [\triangle\phi])^T ([k] + [\triangle k]) ([\phi] + [\triangle\phi]) = \\ ([\phi] + [\triangle\phi])^T ([m] + [\triangle m]) ([\phi] + [\triangle\phi]) \left(\left[\omega^2\right] + \left[\triangle\omega^2\right]\right)\end{gathered} \tag{C.5}$$

Expanding the left hand side,

$$\begin{gathered}lhs = [\phi]^T [k] [\phi] + [\phi]^T [k] [\triangle\phi] + [\phi]^T [\triangle k] [\phi] + [\phi]^T [\triangle k] [\triangle\phi] + \\ [\triangle\phi]^T [k] [\phi] + [\triangle\phi]^T [k] [\triangle\phi] + [\triangle\phi]^T [\triangle k] [\phi] + [\triangle\phi]^T [\triangle k] [\triangle\phi]\end{gathered}$$

eliminating all higher order terms,

$$lhs = [K] + [\phi]^T [k] [\triangle\phi] + [\phi]^T [\triangle k] [\phi] + [\triangle\phi]^T [k] [\phi]$$

and making use of $[\triangle\phi] = [\phi] [C]^T$ bears

$$lhs = [\phi]^T [\triangle k] [\phi] + [K] + [K] [C]^T + [C] [K] . \tag{C.6}$$

Similarly, the right hand side of Equation C.5 is expanded, all higher order terms are eliminated, and $[\triangle\phi]$ is replaced by $[\phi] [C]^T$.

$$rhs = [M] \left[\omega^2\right] + [M] [C]^T \left[\omega^2\right] + [\phi]^T [\triangle m] [\phi] \left[\omega^2\right] + [M] \left[\triangle\omega^2\right] + [C] [M] \left[\omega^2\right] \tag{C.7}$$

Reuniting and rearranging left and right hand side,

$$[\phi]^T [\triangle k] [\phi] - [\phi]^T [\triangle m] [\phi] \left[\omega^2\right] = [M] \left[\triangle\omega^2\right] + [M] \left[[C]^T \left[\omega^2\right] - \left[\omega^2\right] [C]^T \right] . \tag{C.8}$$

leads to the general form of the first order perturbation equation in matrix form (Equation C.9).

$$[\phi]^T [\triangle k] [\phi] - [\phi]^T [\triangle m] [\phi] \left[\omega^2\right] = [\triangle] \tag{C.9}$$

$$\Delta_{ij} = \begin{cases} M_j \triangle \omega_j^2 & \forall i = j \\ M_i C_{ji} \left(\omega_j^2 - \omega_i^2\right) & \forall i \neq j \end{cases}$$

An alternative form can be written in terms of n^2 scalar equations.

$$\{\psi_i\}^T [\Delta k] \{\psi_j\} - \omega_j^2 \{\psi_i\}^T [\Delta m] \{\psi_j\} = \begin{cases} M_j \triangle \omega_j^2 & \forall i = j \\ M_i C_{ji} \left(\omega_j^2 - \omega_i^2\right) & \forall i \neq j \end{cases} \tag{C.10}$$

Making use of the elemental structural changes introduced in Equations 3.11 and 3.12,

$$\sum_{e=1}^{\sigma} \{\psi_i\}^T [k_e] \{\psi_j\} \alpha_e^k - \omega_j^2 \{\psi_i\}^T [m_e] \{\psi_j\} \alpha_e^m = \Delta_{ij}$$

Equation C.10 can be rearranged to a compact expression in matrix form,

$$\left\{P^k\right\}^T \left\{\alpha^k\right\} + \left\{P^m\right\}^T \left\{\alpha^m\right\} = \Delta_{ij}$$

with

$$P_e^k = \left\{\psi_i\right\}^T [k_e] \left\{\psi_j\right\}$$

$$P_e^m = -\omega_j^2 \left\{\psi_i\right\}^T [m_e] \left\{\psi_j\right\}$$

such that

$$[P]_{Sx2\sigma} \{\alpha\}_{2\sigma x1} = \{\triangle\}_{Sx1} \tag{C.11}$$

Equation C.11 represents a linear system of algebraic equations. The choice of solution algorithm depends on the number of modal objectives S, and the number of structural elements σ subject to change. Equation C.10 illustrates that for $i = j$ the structural changes exclusively relate to the change in natural frequency. Similarly, for $i \neq j$ only mode shape changes are addressed.

The modal objectives on the right hand side of the first order perturbation equation require the specification of admixture coefficients C_{ji}. The computation of these coefficients constitutes a separate optimization problem that may not always have a clear solution. Sandstrom and Anderson conceived a clever manipulation of the perturbation equations resolving that problem [158].

For the derivation of this modification lets expand the modal objectives on the right hand side of Equation C.11 and focus on changes of the j^{th} natural mode, only. The objective associated with the natural frequency change is placed first for ease of subsequent manipulations.

$$\{\Delta_{ij}\} = \begin{Bmatrix} M_j \triangle \omega_j^2 \\ M_1 C_{j1} \left(\omega_j^2 - \omega_1^2\right) \\ \vdots \\ M_{j-1} C_{j,j-1} \left(\omega_j^2 - \omega_{j-1}^2\right) \\ M_{j+1} C_{j,j+1} \left(\omega_j^2 - \omega_{j+1}^2\right) \\ \vdots \\ M_n C_{jn} \left(\omega_j^2 - \omega_n^2\right) \end{Bmatrix} \tag{C.12}$$

Introducing the transformation matrix $[T_j]$,

$$[T_j] = \begin{bmatrix} \frac{1}{M_j} & 0 & \cdots & 0 & 0 & \cdots & 0 \\ 0 & \frac{\psi_{11}}{M_1\left(\omega_j^2-\omega_1^2\right)} & \cdots & \frac{\psi_{j-1,1}}{M_{j-1}\left(\omega_j^2-\omega_{j-1}^2\right)} & \frac{\psi_{j+1,1}}{M_{j+1}\left(\omega_j^2-\omega_{j+1}^2\right)} & \cdots & \frac{\psi_{n1}}{M_n\left(\omega_j^2-\omega_n^2\right)} \\ \vdots & \vdots & \ddots & & & & \vdots \\ 0 & \frac{\psi_{1,j-1}}{M_1\left(\omega_j^2-\omega_1^2\right)} & & \frac{\psi_{j-1,j-1}}{M_{j-1}\left(\omega_j^2-\omega_{j-1}^2\right)} & & & \frac{\psi_{n,j-1}}{M_{j-1}\left(\omega_j^2-\omega_{j-1}^2\right)} \\ 0 & \frac{\psi_{1,j+1}}{M_1\left(\omega_j^2-\omega_1^2\right)} & & & \frac{\psi_{j+1,j+1}}{M_{j+1}\left(\omega_j^2-\omega_{j+1}^2\right)} & & \frac{\psi_{n,j+1}}{M_{j+1}\left(\omega_j^2-\omega_{j+1}^2\right)} \\ \vdots & \vdots & & & & \ddots & \vdots \\ 0 & \frac{\psi_{1n}}{M_1\left(\omega_j^2-\omega_1^2\right)} & \cdots & \frac{\psi_{j-1,n}}{M_{j-1}\left(\omega_j^2-\omega_{j-1}^2\right)} & \frac{\psi_{j+1,n}}{M_{j+1}\left(\omega_j^2-\omega_{j+1}^2\right)} & \cdots & \frac{\psi_{nn}}{M_n\left(\omega_j^2-\omega_n^2\right)} \end{bmatrix} \tag{C.13}$$

premultiplying $[T_j]$ to Equation C.12, an expression free of admixture coefficients can be arrived at. Recall that C_{ji} denotes the participation of the i^{th} baseline mode to the change in the j^{th} mode shape.

$$[T_j]\{\Delta_{ij}\} = \begin{Bmatrix} \triangle\omega_j^2 \\ \psi_{11}C_{j1} + \cdots + \psi_{j-1,1}C_{j,j-1} + \psi_{j+1,1}C_{j,j+1} + \cdots + \psi_{n1}C_{jn} \\ \vdots \\ \psi_{1n}C_{j1} + \cdots + \psi_{j-1,n}C_{j,j-1} + \psi_{j+1,n}C_{j,j+1} + \cdots + \psi_{nn}C_{jn} \end{Bmatrix} = \begin{Bmatrix} \triangle\omega_j^2 \\ \Delta\psi_{j1} \\ \vdots \\ \Delta\psi_{jn} \end{Bmatrix}$$

Application of the transformation matrix $[T_j]$ to both sides of Equation C.11 then yields a first order perturbation equation for changes associated with the j^{th} natural mode, that allows an explicit specification of the modal objectives on the right hand side.

$$[T_j]_{NxS}\left\{\left[P^k\right]_{Sx\sigma}\left\{\alpha^k\right\}_{\sigma x1}+\left[P^m\right]_{Sx\sigma}\left\{\alpha^m\right\}_{\sigma x1}\right\}=\left\{\begin{array}{c}\triangle\omega_j^2\\ \Delta\psi_{j1}\\ \vdots\\ \Delta\psi_{jn}\end{array}\right\}_{Nx1} \tag{C.14}$$

N specifies the number of actual physical objectives for the j^{th} natural mode, expressed in terms of explicit shape and frequency change specifications. S represents the number of non-physical modal objectives as expressed in Equation C.10, i.e., constraints that rely on admixture coefficients. As before, σ is the number of structural elements subject to change.

REFERENCES

[1] *NIST/SEMATECH Engineering Statistics Handbook.* www.itl.nist.gov/div898, July 18, 2006.

[2] Abarcar, R. and Cuniff, P., "The vibration of cantilever beams of fiber reinforced material," *Journal of Composite Materials*, vol. 6, no. 10, pp. 504–517, 1972.

[3] Agarwal, B. D. and Broutman, L. J., *Analysis and Performance of Fiber Composites.* John Wiley & Sons, Inc., 1990.

[4] Akaflieg Braunschweig e.V., TU Braunschweig, Germany. www.af-bs.de.

[5] Alexandrov, N., "On managing the use of surrogates in general nonlinear optimization and mdo," *AIAA Paper*, 1998-4798.

[6] Baker, A., Dutton, S., and Kelly, D., *Composite Materials for Aircraft Structures.* American Institute of Aeronautics and Astronautics, 2nd ed., 2004.

[7] Balling, R. and Sobieszczanski-Sobieski, J., "Opimization of coupled systems: A critical overview of approaches," *AIAA Journal*, vol. 34, pp. 6–17, January 1996.

[8] Bandte, O., *A probabilistic multi-criteria decision making technique for conceptual and preliminary aerospace systems design.* PhD thesis, Georgia Institute of Technology, 2000.

[9] Banerjee, J., "Flutter characteristics of high aspect ratio tailless aircraft," *Journal of Aircraft*, vol. 21, pp. 733–736, September 1984.

[10] Banerjee, J., "Flutter modes of high aspect ratio tailless aircraft," *Journal of Aircraft*, vol. 25, pp. 473–476, May 1988.

[11] Bauchau, O. A., *DYMORE-2 User's Manual.* Georgia Institute of Technology, School of Aerospace Engineering, Atlanta, GA, September 18, 2006.

[12] Bauchau, O. A., *AE 6100 Structural Dynamics.* Georgia Institute of Technology, School of Aerospace Engineering, Atlanta, GA 30332, July 2008. Class Notes.

[13] Bauchau, O. A., *DYMORE-3 User's Manual.* Georgia Institute of Technology, School of Aerospace Engineering, Atlanta, GA, February 27, 2008.

[14] Bauchau, O. A. and Craig, J. I., *AE 6107 Aerospace Structural Analysis.* Georgia Institute of Technology, School of Aerospace Engineering, Atlanta, GA 30332, May 2007. Class Notes.

[15] Bauchau, O. A. and Hodges, D. H., "Analysis of nonlinear multi-body systems with elastic couplings," *Multibody System Dynamics*, vol. 3, pp. 168–188, 1999.

[16] Behdinan, K., Perez, R., and Liu, H., "Multidisciplinary design optimization of aerospace systems," in *2nd CDEN International Conference on Design Education, Innovation, and Practice*, July 2005.

[17] Berdichevsky, V., "On the energy of an elastic rod," *PMM*, vol. 45, pp. 518–529, 1982.

[18] Berger, B., "Despite helios mishap nasa to pursue solar-powered uavs," *Space News*, July 7 2003. www.space.com.

[19] Bernitsas, M. M. and Blouin, V. Y., "Structural redesign for forced response with proportional damping by large admissible perturbations," *AIAA Journal*, vol. 37, no. 11, pp. 1506–1513, 1999.

[20] Bernitsas, M. M. and Kang, B., "Admissible large perturbations in structural redesign," *AIAA Journal*, vol. 29, no. 1, pp. 104–113, 1991.

[21] Bernitsas, M. M. and Kristanto, B. M., "Static stress redesign of structures by large admissible perturbations," *Journal of Offshore Mechanics and Arctic Engineering*, vol. 127, no. 2, pp. 122–129, 2005.

[22] Bernitsas, M. M. and Rim, C. W., "Redesign of plates by large admissible perturbations," *AIAA Journal*, vol. 32, pp. 1021–1028, May 1994.

[23] Bernitsas, M. and Suryatama, D., "Structural redesign by large admissible perturbations with static mode compensation," *Journal of Offshore Mechanics and Arctic Engineering*, vol. 121, pp. 39–46, February 1999.

[24] Bishop, D., "Qinetiq's zephyr uav exceeds official world record for longest duration unmanned flight," *Qinetiq News Releases*, September 10 2007. www.qinetiq.com.

[25] Bisplinghoff, R., Ashley, H., and Halfman, R., *Aeroelasticity*. Dover Publications, Inc., 1983.

[26] Blanchard, B., *System Engineering Management*. John Wiley & Sons, Inc., 3rd ed., 2004.

[27] Braun, R., Gage, P., Kroo, I., and Sobieski, I., "Implementation and performance issues in collaborative optimization," *AIAA Paper*, 1996-4017.

[28] Buede, D., *The Engineering Design of Systems*. John Wiley & Sons, Inc., 2000.

[29] Butler, R., Hansson, E., Lillico, M., and Van Dalen, F., "Comparison of multidisciplinary design optimization codes for conceptual and preliminary wing design," *Journal of Aircraft*, vol. 36, pp. 934–940, November-December 1999.

[30] Butler, T. and D., M., *NASTRAN - Summary of the functions and capabilities of the NASA structural analysis computer system*. National Aeronautics and Space Administration, 1971.

[31] Carty, A., "An approach to multidisciplinary design, analysis & optimization for rapid conceptual design," *AIAA Paper*, 2002-5438.

[32] Chandra, R. and Chopra, I., "Experimental and theoretical analysis of composite i-beams with elastic couplings," *AIAA Journal*, vol. 29, no. 12, pp. 2197–2206, 1991.

[33] Chandra, R. and Chopra, I., "Experimental-theoretical investigation of the vibration characteristics of rotating composite box beams," *Journal of Aircraft*, vol. 29, pp. 657–664, July-August 1992.

[34] Chandra, R., Stemple, A., and Chopra, I., "Thin-walled composite beams under bending, torsional, and extensional loads," *Journal of Aircraft*, vol. 27, pp. 619–626, July 1990.

[35] Chattopadhyay, A., Jha, R., and Seeley, C., "Application of hubrid optimization technique for improved aeroelastic performance of composite wings," *AIAA Paper*, 1996-4015.

[36] Chen, H.-P., "Nonlinear perturbation theory for structural dynamics systems," *AIAA Journal*, vol. 43, pp. 2412–2421, November 2005.

[37] Chen, P., Sarhaddi, D., and Liu, D., "Integration of a steady/unsteady wing-body aerodynamic module into astros," *AIAA Paper*, 1998-1867.

[38] Chen, P., Sarhaddi, D., and Liu, D., *Development of the Aerodynamic/Aeroservoelastic Modules in ASTROS, Volume 4: ZAERO Theoretical Manual.* Air Force Research Laboratory, February 1999. AFRL-VA-WP-TR-1999-3052.

[39] Chen, P., Sarhaddi, D., Liu, D., and Karpel, M., "Unified aerodynamic-influence-coefficient approach for aeroelastic/aeroservoelastic and mdo applications," in *Collection of Technical Papers - AIAA/ASME/ASCE/AHS/ASC Structures, Structural Dynamics & Materials Conference*, vol. 2, (Kissimmee, FL, USA), pp. 1271–1277, AIAA, New York, NY, USA, 1997.

[40] Church, C., "Composite structures for high altitude uavs," *AIAA Paper*, 2003-6508.

[41] Cifuentes, A., *Using MSC/NASTRAN - Statics and Dynamics.* Springer Verlag, 1989.

[42] Collar, A., "The expanding domain of aeroelasticity," *Journal of the Royal Aeronautical Society*, vol. 50, pp. 613–636, 1946.

[43] de Visser, J., "Aeroelastic and strength optimization of a composite wing using a multilevel approach," *AIAA Paper*, 1999-1258.

[44] DeBaets, P., *A Methodology for Aeroelastic Constraint Analysis in a Cenceptual Design Environment.* PhD thesis, School of Aerospace Engineering, Georgia Institute of Technology, March 2004.

[45] DeBaets, P. and Mavris, D., "Potential formulation for aeroelastic constraint analysis in a conceptual design environment," *AIAA Paper*, 2002-1295.

[46] DeBaets, P., Mavris, D., and Sobieszczanski-Sobiesky, J., "Aeroelastic design by combining conventional practice with bi-level integrated system synthesis," *AIAA Paper*, 2004-4431.

[47] Dieter, G., *Engineering Design: A Materials and Processing Approach*. McGraw-Hill Companies, Inc., 2000.

[48] Dubbel, H., *Handbook of Mechanical Engineering*. Springer-Verlag, 1994.

[49] Dufresne, S., "A methodology for requirements identification and definition of complex systems." PhD Proposal, Georgia Institute of Technology, 2006.

[50] Dugundji, J., "Personal perspective of aeroelasticity during the years 1953-1993," *Journal of Aircraft*, vol. 40, pp. pp. 809–812, September-October 2003.

[51] D'Vari, R. and Baker, M., "Aeroelastic loads and sensitivity analysis for structural loads optimization," *Journal of Aircraft*, vol. 36, pp. 156–166, January-February 1999.

[52] Eagan, R. J., Allen, B. E., Caudill, C. D., Howard, R. A., Hunter, J. S., Magee, C. L., Ostrach, S., and Rouse, W. B., "Approaches to improve engineering design," tech. rep., The National Academies Press, Washington, D.C., 2001. www.nap.edu.

[53] Eastep, F., Tischler, V., Venkayya, V., and Khot, N., "Aeroelastic tailoring of composite structures," *Journal of Aircraft*, vol. 36, pp. 1041–1047 1041–1047, November-December 1999.

[54] Eldred, M. and Dunlavy, D., "Formulations for surrogate-based optimization with data fit, multifidelity, and reduced-order models," *AIAA Paper*, 2006-7117.

[55] Fabrycky, W. and Blanchard, B., *Life-Cycle Cost and Economic Analysis*. Prentice Hall, 1991.

[56] Fang, H. and Horstemeyer, M., "Metamodeling with radial basis functions," *AIAA Paper*, 2005-2059.

[57] Fletcher, R. and Powell, M., "A rapidly convergent descent method for minimization," *Computer Journal*, vol. 6, pp. 163–168, 1963.

[58] Forsberg, K. and Mooz, H., *Software Requirements Engineering (System Engineering Overview)*. IEEE Computer Society Press, 2nd ed., 1997.

[59] Freberg, C. R. and Kemler, E. N., *Aircraft Vibration and Flutter*. John Wiley & Sons, 1944.

[60] French, M., *Engineering Design: The Conceptual Stage*. Heinemann Educational Books, 1971.

[61] Friedmann, P. P. and Hodges, D. H., "Rotary wing aeroelasticity - a historical perspective," *Journal of Aircraft*, November-December 2003.

[62] Friedmann, P. P. and Hodges, D. H., "Rotary wing aeroelasticity - a historical perspective (draft)," *Journal of Aircraft*, November-December 2003.

[63] Friedmann, P., "Renaissance of aeroelasticity and its future," *Journal of Aircraft*, vol. 36, pp. 105–121, January-February 1999.

[64] Fung, Y., *An Introduction to the Theory of Aeroelasticity*. Dover Publications, Inc., 1993.

[65] Galvanetto, U., Surace, C., and Tassotti, A., "Structural damage detection based on proper orthogonal decomposition: Experimental verification," *AIAA Journal*, vol. 46, pp. 1624–1630, July 2008.

[66] Ganguli, R., "Survey of recent developments in rotorcraft design optimization," *Journal of Aircraft*, vol. 41, pp. 493–510, May-June 2004.

[67] Gano, S., Agarwal, H., and Renaud, J., "Reliability based design using variable fidelity optimization," *AIAA Paper*, 2005-2135.

[68] Gans, H. D. and Anderson, W. J., "Structural optimization incorporating centrifugal and coriolis effects," *AIAA Journal*, vol. 29, no. 10, pp. 1743–1750, 1991.

[69] Garrick, I., "Aeroelasticity - frontiers and beyond," *Journal of Aircraft*, vol. 13, no. 9, pp. 641–657, 1976.

[70] Giesing, J. and Barthelemy, J., "A summary of industry mdo applications and needs," *AIAA Paper*, 1998-4737.

[71] Giles, G. L., "Equivalent plate analysis of aircraft wing box structures with general planform geometry," in *Collection of Technical Papers - AIAA/ASME/ASCE/AHS Structures, Structural Dynamics & Materials*, vol. 1, (San Antonio, TX), pp. 333–342, AIAA (CP863), New York, NY, USA, 1986.

[72] Goebel, G., *Unmanned Aerial Vehicles*. www.vectorsite.net/twuav.html.

[73] Goland, M. and Luke, Y., "A study of the bending-torsion aeroelastic modes for airplane wings," *Journal of the Aeronautical Sciences*, vol. 16, July 1949.

[74] Goldfarb, D., "A family of variable metric updates derived by variational means," *Mathematics of Computing*, vol. 24, pp. 23–26, 1970.

[75] Goraj, Z. e. a., "High altitude long endurance unmanned aerial vehicle of a new generation - a design challenge for a low cost, reliable and high performance aircraft," *Bulletin of the Polish Academy of Sciences*, vol. 52, no. 3, pp. 173–194, 2004.

[76] Grandhi, R., "Structural optimization with frequency constraints - a review," *AIAA Journal*, vol. 31, pp. 2296–2303, December 1993.

[77] Guo, S., Cheng, W., and Cui, D., "Optimization of composite wing structures for maximum flutter speed," *AIAA paper*, 2005-2132.

[78] Haftka, R. and Yates, E., "Repetitive flutter calculations in structural design," *Journal of Aircraft*, vol. 13, no. 7, pp. 454–461, 1976.

[79] Hall, D., Fortenbach, C., Dimiceli, E., and Parks, R., "A preliminary study of solar powered aircraft and associated power trains," Tech. Rep. CR 3699, NASA, December 1983.

[80] Hassig, H., "An approximate true damping solution of the flutter equation by determinant iteration," *Journal of Aircraft*, vol. 8, pp. 885–889, November 1971.

[81] Hodges, D. H., *Nonlinear Composite Beam Theory*. American Institute of Aeronautics and Astronautics, 2006. Volume 213: Progress in Astronautics and Aeronautics.

[82] Hodges, D. H., Pierce, G. A., Bauchau, O. A., and Smith, M. J., *AE 6200 Aeroelasticity*. Georgia Institute of Technology, Atlanta, GA 30332, 2006. Class Notes.

[83] Hodges, D., Atilgan, A., Fulton, M., and Rehfield, L., "Free-vibration analysis of composite beams," *Journal of the American Helicopter Society*, pp. 36–47, July 1991.

[84] Hoenlinger, H., Krammer, J., and Stettner, M., "Mdo technology needs in aeroelastic structural design," *AIAA Paper*, 1998-4731.

[85] Hoff, C., Bernitsas, M., Sandstrom, R., and Anderson, W., "Nonlinear incremental inverse perturbation method for structural redesign," *AIAA Paper*, 1983-0892.

[86] Hoff, C. J. and Bernitsas, M. M., "Dynamics redesign of marine structures.," *Journal of Ship Research*, vol. 29, no. 4, pp. 285–295, 1985.

[87] Hoff, C. J., Bernitsas, M. M., Sandstrom, R. E., and Anderson, W. J., "Inverse perturbation method for structural redesign with frequency and mode shape constraints," *AIAA Journal*, vol. 22, no. 9, pp. 1304–1309, 1984.

[88] Hollowell, S. J. and Dugundji, J., "Aeroelastic flutter and divergence of stiffness coupled graphite/epoxy cantilevered plates," *Journal of Aircraft*, vol. 21, pp. 69–76, January 1984.

[89] Hunten, K. and Blair, M., "The application of the mistc framework to structural design optimization," *AIAA Paper*, 2005-2127.

[90] INCOSE International Council on Systems Engineering, *A Consensus of the INCOSE Fellows*, Last Updated: October 2006. http://www.incose.org/practice/fellowsconsensus.aspx.

[91] Isogai, K., "Direct search method to aeroelastic tailoring of a composite wing under multiple constraints," *Journal of Aircraft*, vol. 26, no. 12, pp. 1076–1080, 1989.

[92] Jung, S. and Kim, S., "Aeroelastic response of composite rotor blades considering transverse shear and damping," *AIAA Journal*, vol. 32, pp. 820–827, April 1994.

[93] Jung, S., Nagaraj, V., and Chopra, I., "Assessment of composite rotor blade modelling techniques," *Journal of the American Helicopter Society*, vol. 44, pp. 188–205, July 1999.

[94] Jung, S., Nagaraj, V., and Chopra, I., "Refined structural model for thin- and thick-walled composite rotor blades," *AIAA Journal*, vol. 40, pp. 105–116, January 2002.

[95] Jung, S. N., Nagaraj, V. T., and Chopra, I., "A refined structural dynamics model for composite rotor blades," *AIAA Paper*, 1999-1485.

[96] Kang, B. and Bernitsas, M., "Stress redesign by large admissible perturbations," *Proceedings of BOSS'94 Conference*, vol. 3, pp. 201–212, July 1994. Cambridge, MA.

[97] Karpel, M., Moulin, B., and Love, M. H., "Modal-based structural optimization with static aeroelastic and stress constraints," in *Collection of Technical Papers - AIAA/ASME/ASCE/AHS/ASC Structures, Structural Dynamics & Materials Conference*, vol. 3, (Salt Lake City, UT, USA), pp. 1494–1503, AIAA, New York, NY, USA, 1996.

[98] Karpel, M., Moulin, B., and Love, M., "Modal-based structural optimization with static aeroelastic and stress constraints," *Journal of Aircraft*, vol. 34, no. 3, pp. 433–440, 1997.

[99] Kim, C. and White, S., "Analysis of thick hollow composite beams under general loadings," *Composite Structures*, vol. 34, pp. 263–277, 1996.

[100] Kim, H., Malone, B., and Sobieszczanski-Sobieski, J., "A distributed, parallel, and collaborative environment for design of complex systems," *AIAA Paper*, 2004-1848.

[101] Kim, K.-O., Anderson, W. J., and Sandstrom, R. E., "Nonlinear inverse perturbation method in dynamic analysis.," *AIAA Journal*, vol. 21, no. 9, pp. 1310–1316, 1983.

[102] Kirby, M. R., *A Methodology for Technology Identification, Evaluation, and Selection in Conceptual and Preliminary Aircraft Design*. PhD thesis, Georgia Institute of Technology, March 2001.

[103] Klimmek, T., Kiessling, F., and Hoenlinger, H., "Multidisciplinary wing optimization using a wing box layout concept and a parametric thickness model," *AIAA Paper*, 2002-5657.

[104] Kodiyalam, S. and Sobieszczanski-Sobieski, J., "Bilevel integrated system synthesis with response surfaces," *AIAA Journal*, vol. 38, August 2000.

[105] Kodiyalam, S. and Sobieszczanski-Sobieski, J., "Multidisciplinary design optimization - some formal methods, framework requirements, and application to vehicle design," *International Journal of Vehicle Design*, pp. 3–22, 2001. Special Issue.

[106] Komarov, V. and Weisshaar, T., "Aircraft structural design - improving conceptual design level fidelity," *AIAA Paper*, 1998-4885.

[107] Kroo, I., "Distributed multidisciplinary design and collaborative optimization," in *VKI lecture series on Optimization methods & Tools for Multicriteria/Multidisciplinary Design*, November 15-19 2004.

[108] Ku, J., *A hybrid optimization scheme for helicopters with composite rotor blades*. PhD thesis, Georgia Institute of Technology, August 2007.

[109] Ku, J., Volovoi, V. V., and Hodges, D. H., "Multilevel-multiphase optimization of composite rotor blade with surrogate model," *AIAA Paper*, 2007-1900.

[110] Kumano, T., Jeong, S., Obayashi, S., Ito, Y., Hatanaka, K., and Morino, H., "Multidisciplinary design optimization of wing shape for a small jet aircraft using kriging model," *AIAA Paper*, 2006-0932.

[111] Lillico, M., Butler, R., Banerjee, J. R., and Guo, S., "Aeroelastic optimization of high aspect ratio wings using an exact dynamic stiffness matrix method," *AIAA Paper*, 1994-4401.

[112] Lillico, M., Butler, R., and Holden, M., "Conceptual design optimization of composite wings with aeroelastic and strength contraints," *AIAA Paper*, 1996-4004.

[113] Lillico, M. and Butler, R., "Finite element and dynamic stiffness methods compared for modal analysis of composite wings," *AIAA Journal*, vol. 36, no. 11, pp. 2148–2151, 1998.

[114] Liu, B., Haftka, R., and Akgun, M., "Composite wing structural optimization using genetic algorithms and response surfaces," *AIAA Paper*, 1998-4854.

[115] Liu, B., Haftka, R., and Akgun, M., "Two-level composite wing structural optimization using response surfaces," *Structural Multidisciplinary Optimization*, vol. 20, pp. 87–96, 2000.

[116] Liu, H., Wu, Z., and Raymer, D., "Auotmated scheme adjustment for conceptual aircraft design and optimization," *AIAA Paper*, 2005-0532.

[117] Livne, E., Schmit, L., and Friedmann, P., "Integrated structure/control/aerodynamic synthesis of actively controlled composite wings," *Journal of Aircraft*, vol. 30, no. 3, pp. 387–394, 1993.

[118] Livne, E. and Weisshaar, T., "Aeroelasticity of nonconventional airplane configurations - past and future," *Journal of Aircraft*, vol. 40, pp. 1047–1065, November-December 2003.

[119] Lombardi, G., Mengali, G., and Beux, F., "A hybrid genetic based optimization procedure for aircraft conceptual analysis," *Optim Eng*, vol. 7, pp. pp. 151–171, 2006.

[120] Lophaven, S. N., Nielsen, H. B., and Sondergaard, J., *DACE - A Matlab Kriging Toolbox*. Technical University of Denmark, August 1 2002. Technical Report IMM-TR-2002-12.

[121] Maghami, P. G. and Sparks, D. W., "Design of neural networks for fast convergence and accuracy," *AIAA Paper*, 1998-1780.

[122] Marks, L. S., *Mark's Standard Handbook for Mechanical Engineers*. McGraw-Hill, 10th ed., 1996.

[123] Mason, B. and Walsh, J., "Coupled aerodynamic and structual sensitivity analysis of a high-speed civil transport," *AIAA Paper*, 2001-1431.

[124] Mavris, D., DeLaurentis, D., Bandte, O., and Hale, M., "A stochastic approach to multi-disciplinary aircraft analysis and design," *AIAA Paper*, 1998-0912.

[125] McCarthy, T. and Chattopadhyay, A., "A refined higher-order composite box beam theory," *AIAA Paper*, 1996-1470.

[126] Meirovitch, L. and Seitz, T. J., "Structural modeling for optimization of low aspect ratio composite wings," *Journal of Aircraft*, vol. 32, pp. 1114–1123, September - October 1995.

[127] Mitra, M., Gopalakrishnan, S., and Bhat, M. S., "A new super convergent thin walled composite beam element for analysis of box beam structures," *International Journal of Solids and Structures*, vol. 41, no. 5-6, pp. 1491–1518, 2004.

[128] MSC Software Corporation. www.mscsoftware.com.

[129] Mullur, A. and Messac, A., "Extended radial basis functions: More flexible and effective metamodeling," *AIAA Paper*, 2004-4573. 10th AIAA/ISSMO Multidisciplinary Analysis and Optimization Conference, Albany, New York, Aug. 30-1, 2004.

[130] NASA, "Pathfinder - introducing solar-powered aircraft for observing the environment without disturbing nature." NASA Educational Materials, 1999.

[131] NASA, "Statement of work for the task order entitled roa sector design and analysis tool development for vehicle systems programs." NASA Langley Research Center Subject Contract with the Aerospace Systems Design Laboratory (ASDL), March 2005.

[132] NASA Dryden Flight Research Center. www.nasa.gov/centers/dryden.

[133] National Air and Space Museum. Smithsonian Institution. www.nasm.si.edu.

[134] Neill, D. and Herendeen, D., *ASTROS Enhancements. Volume I - User's manual*, March 1993.

[135] Newcome, L. R., *Unmanned Aviation: A Brief History of Unmanned Aerial Vehicles*. American Institute of Aeronautics and Astronautics, Inc., 2004.

[136] NIST/SEMATECH, *e-Handbook of Statistical Methods*. 2007. www.itl.nist.gov/div898/handbook.

[137] Noll, T., Brown, J., Perez-Davis, M., Ishmael, S., Tiffany, G., and Gaier, M., "Investigation of the helios prototype aircraft mishap," *NASA Mishap Report*, vol. 1, January 2004.

[138] Paik, J., Volovoi, V., and Hodges, D., "Cross-sectional sizing and optimization of composites blades," *AIAA Paper*, 2002-1322.

[139] Pan, L. and Du, H., "Structural topology optimization for dynamics performance using sqp method," *AIAA Paper*, 2000-4736.

[140] Pandey, A. K., Biswas, M., and Samman, M. M., "Damage detection from changes in curvature mode shapes," *Journal of Sound and Vibration*, vol. 145, no. 2, pp. 321–332, 1991.

[141] Parkinson, C. N., "Parkinson's law," *The Economist*, pp. 635–637, November 19 1955. Retrieved from http://en.wikipedia.org.

[142] Parsch, A., *Directory of U.S. Military Rockets and Missiles*, 2001-2007. Appendices 2 and 4, www.designation-systems.net.

[143] Patil, M., *Nonlinear Aeroelastic Analysis, Flight Dynamics, and Control of a Complete Aircraft*. PhD thesis, Georgia Institute of Technology, May 1999.

[144] Patil, M. and Hodges, D., "On the importance of aerodynamic and structural geometrical nonlinearities in aeroelastic behavior of high-aspect-ratio wings," *Journal of Fluids and Structures*, vol. 19, pp. 905–915, 2004.

[145] Patil, M., Hodges, D., and Cesnik, C., "Nonlinear aeroelasticity and flight dynamics of high-altitude long-endurance aircraft," *Journal of Aircraft*, vol. 38, pp. 88–94, January-February 2001.

[146] Pendaries, C., Boiffier, J., Jeanneau, M., and Barrau, J., "Flexible aircraft in conceptual design hales on the way to ornithopter," *AIAA Paper*, 1998-0505.

[147] Pettit, C., "Uncertainty quantification in aeroelasticity: Recent results and research challenges," *Journal of Aircraft*, vol. 41, pp. 1217–1229, September-October 2004.

[148] Popescu, B. and Hodges, D., "On asymptotically correct timoshenko-like anisotropic beam theory," *International Journal of Solids and Structures*, vol. 37, pp. 535–558, 2000.

[149] Qin, Z. and Librescu, L., "Static/dynamic solutions and validation of a refined anisotropic thin-walled beam model," *AIAA Paper*, 2002-1394.

[150] Rai, M. M. and Madavan, N. K., "Aerodynamic design using neural networks," *AIAA Paper*, 1998-4928.

[151] Ratcliffe, C. P., "Damage detection using a modified laplacian operator on mode shape data," *Journal of Sound and Vibration*, vol. 204, no. 3, pp. 505–517, 1997.

[152] Raymer, D., *Aircraft Design: A Conceptual Approach*. AIAA Educational Series, 1999.

[153] Raymer, D., "Vehicle scaling laws for multidisciplinary optimization," *AIAA Paper*, 2001-0532.

[154] Robinson, D. G., "A survey of probabilistic methods used in reliability, risk and uncertainty analysis: Analytical techniques i," Tech. Rep. SAND98-1189, Sandia National Laboratories, June 1998.

[155] Roehl, P. J., *A multilevel decomposition procedure for the preliminary wing design of a high-speed civil transport aircraft*. PhD thesis, Georgia Institute of Technology, May 1995.

[156] Salawu, O. S., "tion of structural damage through changes in frequency: a review," *Engineering Structures*, vol. 19, no. 9, pp. 718–723, 1997.

[157] Sandstrom, R., "Inverse perturbation methods for vibration analysis," in *NATO-NSF Advanced Study Institute on Optimization of Distributed Parameter Structures*, pp. 1539–1552, 21 May - 4 June 1980.

[158] Sandstrom, R. E. and Anderson, W. J., "Modal perturbation methods for marine structures," *SNAME Transactions*, vol. 90, pp. 41–54, 1982.

[159] Scaled Composites, LCC, Mojave, CA. www.scaled.com.

[160] Scanlan, R. H. and Rosenbaum, R., *Introduction to the Study of Aircraft Vibration and Flutter*. Dover Publications, 1968.

[161] Schuhmacher, G., Murra, I., Wang, L., Laxander, A., O'Leary, O., and Herold, M., "Multidisciplinary design optimization of a regional aircraft wing box," *AIAA Paper*, 2002-5406.

[162] Schuster, D. M., Liu, D., and Huttsell, L. J., "Computational aeroelasticity: Success, progress, challenge," *Journal of Aircraft*, vol. 40, pp. 843–856, September - October 2003.

[163] Schutte, J., Haftka, R., and Watson, L., "Decomposition and two-level optimization of structures with discrete sizing variables," *AIAA Paper*, 2004-1541.

[164] Schweiger, J., Krammer, J., and Hoernlein, H., "Development and application of the integrated structural design tool lagrange," *AIAA Paper*, 1996-4169.

[165] Schweiger, J., Sensburg, O., and Berns, H., "Aeroelastic problems and structural design of a tailless cfc-sailplane," *2nd International Symposium on Aeroelasticity and Structural Dynamics*, vol. Aachen, West Germany, pp. pp. 457–468, 1-3 April 1985.

[166] Schweiger, J., Suleman, A., Kuzmina, S., and Chedrik, V., "Mdo concepts for an european research project on active aeroelastic aircraft," *AIAA Paper*, 2002-5403.

[167] Seeley, C. and Chattopadhyay, A., "Development of a hybrid technique for continuous/discrete optimization," *AIAA Paper*, 1996-4149.

[168] Shirk, M., Hertz, T., and Weisshaar, T., "Aeroelastic tailoring - theory, practise, and promise," *Journal of Aircraft*, vol. 23, no. 1, pp. pp. 6–18, 1986.

[169] Simpson, T., Korte, J., Mauery, T., and Mistree, F., "Comparison of response surface and kriging models for multidisciplinary design optimization," *AIAA Paper*, 1998-4755.

[170] Smilg, B. and Wasserman, L., "Application of three-dimensional flutter theory to aircraft structures," tech. rep., Air Force Technical Report 4798, 1942.

[171] Smith, E. and Chopra, I., "Formulation and evaluation of an analytical model for composite box-beams," *Journal of the American Helicopter Society*, vol. 36, pp. 23–35, July 1991.

[172] Smith, E. and Chopra, I., "Aeroelastic response and blade loads of a composite rotor in forward flight," *AIAA Paper*, 1992-2566.

[173] Smith, M. J. and Hutton, S. G., "Frequency modification using newton's method and inverse iteration eigenvector updating," *AIAA Journal*, vol. 30, no. 7, pp. 1886–1891, 1992.

[174] Sobester, A. and Keane, A., "Multidisciplinary design optimization of uav airframes," *AIAA Paper*, 2006-1612.

[175] Sobieski, I., Manning, V., and Kroo, I., "Response surface estimation and refinement in collaborative optimization," *AIAA Paper*, 1998-4753.

[176] Sobieszczanski-Sobieski, J., Agte, J., and Sandusky, R., "Bilevel integrated system synthesis," *AIAA Journal*, vol. 38, pp. pp. 164–172, January 2000.

[177] Sobieszczanski-Sobieski, J., Altus, T., Phillips, M., and Sandusky, R., "Bilevel integrated system synthesis for concurrent and distributed processing," *AIAA Journal*, vol. 41, pp. pp. 1996–2003, October 2003.

[178] Sobieszczanski-Sobieski, J. and Haftka, R., "Multidisciplinary aerospace design optimization: survey of recent developments," *Structural Optimization*, vol. 14, no. 1, pp. pp. 1–23, 1997.

[179] Sobieszczanski-Sobieski, J., Altus, T. D., Phillips, M., and Sandusky, R., "Bi-level integrated system synthesis (bliss) for concurrent and distributed processing," *AIAA Paper*, 2002-5409.

[180] Stetson, K. A., "Perturbation method of structural design relevant to holographic vibration analysis," *AIAA Journal*, vol. 13, April 1975.

[181] Stetson, K. A. and Palma, G. E., "Inversion of first order perturbation theory and its application to structural design," *AIAA Journal*, vol. 14, no. 4, pp. 454–460, 1976.

[182] Stettner, M., *Tiltrotor Multidisciplinary Optimization*. PhD thesis, Georgia Institute of Technology, August 1995.

[183] Suh, N. P., *The Principles of Design*. Oxford University Press, 1990.

[184] Suh, N. P., *Axiomatic Design*. Oxford University Press, 2001.

[185] Taylor, J. and Butler, R., "Optimum design and validation of flat composite beams subject to frequency constraints," in *Collection of Technical Papers - AIAA/ASME/ASCE/AHS/ASC Structures, Structural Dynamics & Materials Conference*, vol. 4, (Salt Lake City, UT, USA), pp. 2335–2343, AIAA, New York, NY, USA, 1996.

[186] Taylor, J. and Butler, R., "Optimum design and validation of flat composite beams subject to frequency constraints," *AIAA Journal*, vol. 35, no. 3, pp. 540–545, 1997.

[187] Tedford, N. and Martins, J., "On the common structure of mdo problems: A comparison of architectures," *AIAA Paper*, 2006-7080.

[188] Thimbleby, H., "Computerised parkinson's law," *Computing and Control Engineering Journal*, pp. 197–198, 1993.

[189] U.S. Department of Defense, *MIL-STD-499 Military Standard on Systems Engineering Management*, July 1969.

[190] Vanderplaats, G. N., *Numerical Optimization Techniques for Engineering Design.* Vanderplaats Research & Development, Inc., 3rd ed., 1999.

[191] Venkataraman, S. and Haftka, R., "Structural optimization: What has moore's law done for us?," *AIAA Paper*, 2002-1342.

[192] Vicini, A. and Quagliarella, D., "Airfoil and wing design through hybrid optimization strategies," *AIAA Journal*, vol. 37, pp. pp. 634–641, May 1999.

[193] Volovoi, V. V., Hodges, D. H., Cesnik, C. E. S., and Popescu, B., "Assessment of beam modeling methods for rotor blade applications," *Mathematical and Computer Modelling*, vol. 33, no. 10-11, pp. 1099–1112, 2001.

[194] Volovoi, V., Ku, J., and Hodges, D., "Coupling global and local aspects of cross-sectional optimization for rotor blades," *AIAA Paper*, 2006-1822.

[195] Volovoi, V., Li, L., Ku, J., and Hodges, D., "Multi-level structural optimization of composite rotor blades," *AIAA Paper*, 2005-2282.

[196] Volovoi, V., Yoon, S., Lee, C., and Hodges, D., "Structural optimization of composite rotor blades," *AIAA Paper*, 2004-1837.

[197] Wang, L., Beeson, D., Wiggs, G., and Rayasam, M., "A comparison of meta-modeling methods using practical industry requirements," *AIAA Paper*, 2006-1811.

[198] Weisshaar, T. A. and Foist, B. L., "Vibration tailoring of advanced composite lifting surfaces," *Journal of Aircraft*, vol. 22, pp. 141–147, February 1985.

[199] WEU - Interparliamentary European Security and Defence Assembly, *Unmanned combat air vehicles and military aeronautics of the future.*, November 2004. www.assembly-weu.org.

[200] Yu, W., "An integrated approach for efficient high-fidelity analysis of composite structures," *AIAA Paper*, 2005-1911.

[201] Yu, W., Volovoi, V., Hodges, D., and Hong, X., "Validation of the variational asymptotic beam sectional analysis (vabs)," *AIAA Paper*, 2001-1530.

[202] Yu, W., *Variational Asymptotical Modeling of Composite Dimensionally Reducible Structures.* PhD thesis, School of Aerospace Engineering, Georgia Institute of Technology, 2002.

[203] Yu, W., *An Tutorial of VABS.* Utah State University, Logan, Utah 84322, June 2005. VABS 2.1.

[204] Yu, W., *Variational Asymptotic Beam Sectional Analysis (VABS).* Utah State University, Logan, Utah 84322-4130, June 2005. VABS 2.1.

[205] Yu, W. Email correspondence, March 2006.

[206] Yu, W., *Manual of VABS Lite.* Utah State University, Logan, Utah 84322, November 2008.

[207] Zink, P., *A Methodology for Robust Structural Design with Application to Active Aeroelastic Wings*. PhD thesis, Georgia Institute of Technology, June 2001.

[208] Zink, P., DeLaurentis, D., Hale, M., Volovoi, V., Schrage, D., Craig, J., Fulton, R. E., Mistree, F., Mavris, D., Chen, W., Röhl, P., Lewis, K., Koch, P., Cesnik, C., and Simpson, T., "New approaches to high speed civil transport multidisciplinary design and optimization," in *Presented at the 2000 IEEE Aerospace Conference, Big Sky, Montana*, March 18-25, 2000.

[209] ZONA Technology, Scottsdale, AZ, *ZAERO Version 7.0*, November 2003. Theoretical Manual.